



The
University
Of
Sheffield.

Exploring KNO_3 behaviour and Formation through Simulation

Vittoria Fantauzzo

A thesis submitted in partial fulfilment of the requirements for the degree of
Doctor of Philosophy

The University of Sheffield
Faculty of Engineering
Department of Materials Science and Engineering

2023

List of contents

Declaration	3
Acknowledgements.....	5
Abstract	7
List of Tables	9
List of Figures.....	13
Table of Contents.....	25

Declaration

I, Vittoria Fantauzzo, confirm that the Thesis is my own work. I am aware of the University's Guidance on the Use of Unfair Means (www.sheffield.ac.uk/ssid/unfair-means). This work has not been previously been presented for an award at this, or any other, university.

I confirm that the work submitted is their own, except where work that has formed part of jointly authored publications has been included. The contribution of the candidate and the other authors to this work has been explicitly indicated below. The candidate confirms that appropriate credit has been given within the thesis where reference has been made to the work of others.

Publications

- V. Fantauzzo, S.R. Yeandel, C.L. Freeman, J.H. Harding, *A transferable force-field for alkali metal nitrates*, J. Phys. Commun., 2022, **6** 05501;
- J.H. Harding, C.L. Freeman, V. Fantauzzo, E. Armstrong, V. Marinova, S.R. Yeandel, *Controlling mineral polymorphs: insights from computer simulation*, Goldschmidt2021, 04 Jul 2021-09 Jul 2021. Goldschmidt2021 abstracts. European Association of Geochemistry. 2021

Acknowledgments

In the following section, I would like to acknowledge all the people that have contributed to the completion of this work.

I would like to start by expressing my gratitude to the ‘Crystallisation in the Real World’ consortium and all the members from Leeds, Warwick and UCL. In particular, I would like to thank Thomas Dunn (soon to be Dr.) and Prof Fiona Meldrum, from University of Leeds, for the constructive discussion that lead to the work included in Chapter 6. I am grateful for allowing me to use part of their unpublished work. I would also thank Dr. Aaron Finney and Prof. Matteo Salvalaglio for hosting me in London and helping me develop the work included in Chapter 7.

I would like to express my gratitude to Dr. Colin Freeman and Prof John Harding, for being an invaluable source of information for me, and for offering assistance, direction, and expert advice throughout the course of my PhD. I owe a great deal of gratitude to them, for not just making this opportunity available to me in the first place but also for being such a wonderful guide all the way through it.

I would like to thank Dr. Stephen Yeandel and Dr. Veselina Marinova for being resourceful, constant guides during my PhD. In particular, I should acknowledge Dr. Stephen Yeandel for his help in the development of the work published and included in Chapter 3 (methodology for the free energy of hydration calculation) and Dr. Veselina Marinova for providing the theoretical background, methodology and structures used in Chapter 7.

During the course of my PhD, I have supervised a master student, Georgia Lea, whose work constitutes the very start of Chapter 7, and I would like to thank her as well for the material we have together developed.

I would like to express my gratitude to all the people in my office, in particular a friend, Emma. Our library days have been fundamental in the writing process of this work. Thanks to the C-14 office and the post-doc office, as well as the entire MESAS group.

And in the end, a huge thanks to my family, James and his family, as well as all my friends for helping me going through this big journey. Thank you.

Abstract

Alkali metal nitrates are both of industrial and scientific interest. In this thesis, we present a new rigid-ion force-field for the alkali metal nitrates that is suitable for simulating solution chemistry, crystallisation and polymorphism. We show that it gives a good representation of the crystal structures, lattice energies, elastic and dielectric properties of these compounds over a wide range of temperatures. Since all the alkali metal nitrates are fitted together using a common model for the nitrate anion, the force-field is also suitable for simulating solid solutions.

We utilise our model by exploring, in particular, KNO_3 behaviour in a range of systems. Because the ultimate goal is to model the nucleation, and subsequent crystallisation, of KNO_3 we have explored a few possible scenarios, from an homogeneous to an heterogeneous one. We have started by attempting to nucleate KNO_3 from pure, supersaturated solutions. Because of the statistically rare nature of the event, we tried to make the process possible to investigate in a time frame that is also optimal for simulation, by putting said solutions in contact with a slab of KNO_3 . We add a constant chemical potential method ($C\mu$ -MD) to our model to try to determine growth mechanisms and rates. At this stage of this work no clear growth behaviour has been observed.

We then swapped the slab of KNO_3 for a self-assembled monolayer (SAM) surface to investigate the effect of functional groups, charges and defects on the nucleation process. In this case, the results were not comparable with the ones obtained for CaCO_3 because the nucleation was not significantly accelerated by the presence of the defects.

List of Tables

3.1 Absolute free hydration energies for the ions used in this work	98
3.2 Data required for the corrections	107
3.3 Droplet corrections.....	108
3.4 Ewald corrections.....	109
4.1 Interactions between alkali metal ions ^[26] $q_M = 1.0$ for $M = \text{Li-Cs}$ where ϵ and R_{\min} are defined as the energy and interatomic distance at the minimum, i.e. we use the Lennard-Jones potential in the form $V(r) = \epsilon \left[\left(\frac{R_{\min}}{r} \right)^{12} - 2 \left(\frac{R_{\min}}{r} \right)^6 \right]$	122
4.2 Force-field Parameters for the nitrate ion ($q_N = 0.7802 e $, $q_O = -0.5934 e $)	124
4.3 Interactions between alkali metal ions and water ^[26] $q_M = 1.0$ for $M = \text{Li-Cs}$ where ϵ and R_{\min} are defined as the energy and interatomic distance at the minimum, i.e., the Lennard-Jones potential is written as $V(r) = \epsilon \left[\left(\frac{R_{\min}}{r} \right)^{12} - 2 \left(\frac{R_{\min}}{r} \right)^6 \right]$	125
4.4 SPE/Fw parameters for the water molecule ($q_H = 0.41 e $, $q_O = -0.82 e $) Wu et al.[39] The water-water interaction is given in Table 4.3	125
4.5 Buckingham parameters fitted for a rigid ion force-field (unit charge for all metal ions)	127
4.6 Comparison between dielectric constants calculated using various force-fields and experimental values for the aragonite phase of potassium nitrate (KNO_3). *Note that the axes have been changed from the original references to conform to the crystallographic axes used for the Pnma space group in ref [18].	129
4.7(a) Comparison of the lattice parameter ‘a’ using this work L-J force-field, DFT and experimental data. All the values are expressed in Å.	129
4.7(b) Comparison between elastic stiffness constants (GPa), calculated using various force-fields and density functional calculations and experimental values for the aragonite phase of potassium nitrate (KNO_3). *Note that the axes (and hence the Voigt notation) for the elastic constants has been changed from the original references to conform to the crystallographic axes used for the Pnma space group in ref [18]. \$Values extrapolated back from the measured values at 293 K to 0 K using the thermo-elastic constants reported in the same paper ^[32]	130

4.8 Interactions between water and the nitrate anion using a Buckingham potential form $V(r) = A\exp(-r/\rho) - C/r^6$	131
4.9 Comparison with structural data for $\text{LiNO}_3 \cdot 3\text{H}_2\text{O}$ (space group Cmcm (63)) ^[46] . Comparison of the atomic positions can be found in Section 4.3.5.	131
4.10 Comparison of current force-field with experimental data (in italics; corrected to a static lattice) and previous force-fields	132
4.11 Comparison of force-field prediction with structural data for $\text{LiNO}_3 \cdot 3\text{H}_2\text{O}$ ^[71]	133
4.12 Comparison of experimental ^[72] crystal structure of $\text{NaRb}_2(\text{NO}_3)_3$ and force-field.....	134
4.13 Energy of polymorphs with respect to the most stable one (kJ mol^{-1}) as predicted by different force-fields. Dashes indicate the failure of a force-field to optimise a particular structure. The most stable polymorph is emphasised in bold	135
4.14 Lattice energies (kJ mol^{-1}) for alkali metal nitrates compared with those obtained from those obtained from the NBS Tables ^[70] . Values quoted for the stable polymorph at standard temperature and pressure (STP). Dashes mean either that no force-field is available or that the force-field could not produce a stable minimised structure	136
4.15 Elastic stiffness constants for LiNO_3 calculated with different force-fields and compared with experimental data. (C_{14} is omitted from the goodness of fit calculation)	137
4.16 Elastic constants for NaNO_3 calculated with force-field and compared with experiment	137
4.17 Comparison between lattice parameter ‘a’ for various alkali metal nitrates, obtained using this ff Lennard-Jones, Buckingham and experimental values. All the values are expressed in Å.	140
4.18 Energy values of the two different polymorphs of NaNO_3 (R3c and R3m) at 600K	143
4.19 Thermodynamic properties for alkali metal nitrates systems	146
5.1 Comparison between $r_{\text{max}}(\text{N-O}_w)$ obtained in this work and available data in literature.....	157
5.2 Comparison between coordination number obtained in this work and available data in literature	158
5.3 Comparison of density values, for pure water at room temperature	159

5.4 Coordination number for K in respect to O of the nitrate group and O of the water for different molality boxes	162
5.5 Cluster size (number of potassium ions) as a function of the radius of gyration (expressed in Å) for a 6 molal clustered solution of KNO ₃	166
5.6 Schematic representation of cluster organisation and their number of connection (absolute and average).....	168
5.7 Schematic representation of cluster organisation and their number of connection (average)	174
5.8 Mean fractions of the Manhattan distance difference for calcite and aragonite within 1 and 3 standard deviation from the mean.....	182
6.1 CASTEP parameters	199
6.2 Comparison between surface energy obtained with DFT and force-field from this work. Surfaces are listed by their energy values (ranked from the lowest to the highest).....	200
7.1 Concentrations expressed in number of moles per litre of solution for the boxes containing different amount of KNO ₃	235
7.2 Coordination number for the nitrogen of the nitrate group in respect of the oxygen of the water and oxygen of the carboxylic head group of the 16-MDHA chains, for the various concentration solutions	240
7.3 Coordination number for the nitrogen of the nitrate group in respect of the oxygen of the water and oxygen of the carboxylic head group of the 16-MDHA chains, for the various concentration solutions	242
7.4 Coordination number for the nitrogen of the nitrate group in respect of the oxygen of the water and oxygen of the carboxylic head group of the 16-MDHA	245
7.5 Statistics about the cluster connection in a potassium nitrate solution sitting on a flat SAM surface	250
7.6 Statistics about the cluster connection in a potassium nitrate solution sitting on a flat SAM surface	257

7.7 Non-bonded interactions.....	260
7.8 Bonded interactions	262

List of Figures

1.1 KNO ₃ aragonite, top and ferroelectric, bottom. Images supplied by F Meldrum, T Dunn (Leeds University) ^[2]	34
1.2 Different polymorphs of calcium carbonate. Top left shows the only amorphous form of calcium carbonate, while vaterite (top-right), aragonite (bottom left) and calcite (bottom right) represent the crystal forms in crescent order of thermodynamic stability (http://www.ruhr-uni-bochum.de/sediment/forschung.html) ^[29]	35
1.3 Behaviour of a monotropic (right) and enantiotropic (left) systems ^[7] . Green lines represent the contributions to the free energy and the blue lines to the enthalpy. Reproduced with the publisher's permission	36
1.4 Free energy profiles as function of the number of precipitated formulae units. If $\Delta\mu$ (black curve) is equal to zero, the energy barrier is not overcome and the system does not nucleate. In the other 2 cases (red and grey curve) the system overcomes the critical radius and as a function of the depth of the free energy well it manages to nucleate a proportional amount of formulae units ^[13]	38
1.5 The potential paths and physical mechanisms by which monomers create a stable bulk crystal might have thermodynamic (A, B, C) or kinetic (D, E) origins (A) The traditional monomer-by-monomer addition. (B) Metastable particle aggregation (aggregation of liquid, amorphous, or weakly crystalline particles, or aggregation of oriented [and nearly orientated] metastable nanocrystals). (C) Crystallisation by metastable bulk phase creation (i.e., liquid or solid polymorph). (D) Cluster or oligomer aggregation dominated by kinetics. (E) Aggregation of unstable particles with different interior structures than equilibrium phases [35]. All the rights to the authors.....	41
2.1 Resonance structure of the nitrate anion	47
2.2 LiNO ₃ (along the <010> direction) ^[1] . Reproduced with the publisher's permission.....	48
2.3 BFDH theoretical crystal growth morphology of LiNO ₃ (calculated) ^[1] . Reproduced with the publisher's permission	49
2.4 . Left: II-NaNO ₃ crystal structure ^[15] . Right: I-NaNO ₃ crystal structure ^[15] . Grey spheres represent sodium atoms, red spheres oxygens from the nitrate group. Reproduced with the publisher's permission	50

2.5 Theoretical and experimental crystal growth morphology of NaNO_3 ^[1] . Reproduced with the publisher's permission	51
2.6. Left: α - KNO_3 , Middle: β - KNO_3 , Right: γ - KNO_3 crystal structures ^[1] . All structures are viewed along $\langle 010 \rangle$ direction Reproduced with the publisher's permission.....	53
2.7 RbNO_3 phases and its transition temperatures (Rao at al.) IV- RbNO_3 (Pohl et al.) and III- RbNO_3 , II- RbNO_3 , and I- RbNO_3 (Ahtee et al.). The scale of unit cells is not the same. All structures are viewed along the $\langle 010 \rangle$ direction. ^[1] . Reproduced with the publisher's permission.....	55
2.8 BFDH growth morphology of RbNO_3 calculated by Benages ^[1] . Reproduced with the publisher's permission	57
2.9 CsNO_3 unit cell. Left: phase II and right phase I. All viewed along the $\langle 100 \rangle$ direction. ^[1] . Reproduced with the publisher's permission.....	57
3.1 The four main components of a molecular mechanic force-field are represented schematically as bond stretching (a), angle bending (b), torsional terms (c), and non-bonded interactions (d) and (e).....	67
3.2 (a) Lennard Jones potential and its parameters	70
3.2 (b) Lennard-Jones potential with cut-off highlighted	75
3.3 Jacob's ladder of DFT functionals. The functionals are ordered from the bottom to the top based on their accuracy and computational cost ^[78]	80
3.4 Schematic representation of PBCs.....	89
3.5 The minimum image convention within PBCs.....	90
3.6 Schematic representation of the charge compensation obtained by using corrections to the simulation. Credits to the author [115]	100
3.7 Single point-multipole particle (left) describing a point-charge distribution (right). Credits to the authors [115]	102
3.8 Radially averaged electric potential $\Phi(r)$ in units of volts as a function of the radial distance r from the center of water clusters with $N = 256$ (magenta) and 1024 (green) SPC water molecules at 298 K. Extracted from ref [116], see reference for further details. Reproduced with the author's permission.....	104

4.1 Structures of the phases of the alkali metal nitrates that are used in the fitting. Purple spheres are the alkali metal ions; light blue spheres are the nitrogen atoms; red spheres are the oxygen atoms	122
4.2 Lattice energies for possible polymorphs of alkali metal nitrates as indicated by filled symbols. Different crystal structures are shown in different colours: calcite (blue), aragonite (red), RbNO ₃ phase IV structure (yellow) ferroelectric trigonal (purple). The stable low temperature polymorphs are calcite (Li, Na), aragonite (K) and RbNO ₃ phase IV (Rb, Cs). The ionic radii come from Shannon ^[44] ; Roman numerals denote the coordination number to which they refer	128
4.31 Lattice parameter fits for potassium nitrate (aragonite and trigonal (ferroelectric) structure)	130
4.4 Phonons NaNO ₃ obtained with this force-field (black lines) compared with experiment ^[32] (red symbols)	138
4.5 Phonons for KNO ₃ (Σ direction) obtained with this force-field (black curves) compared with experiment ^[73] (red symbols).....	138
4.6 Phonons for KNO ₃ (Δ direction) obtained with this force-field (black curves) compared with experiment ^[73] (red symbols).....	139
4.7 Phonons for KNO ₃ (Λ direction) obtained with this force-field (black curves) compared with experiment ^[73] (red symbols).....	139
4.8 Radial distribution functions for Li-O (top) and Li-N (bottom) in LiNO ₃	141
4.9 Radial Distribution Function for Na - O (top) and Na - N (bottom) in NaNO ₃	142
4.10 Radial Distribution Function for Na - N in NaNO ₃ for the two different polymorphs (R3c, blue line and R3m, orange line) extracted at 300K	143
4.11 Radial Distribution Function for K - N in KNO ₃ as the temperature increases. The yellow line represents the system at 100 K, the blue line at 300 K and the green line at 500 K.....	144
4.12 Radial Distribution Function for K - N in KNO ₃ as the temperature decreases. The yellow line represents the system at 100 K, the blue line at 300 K and the green line at 500 K.....	144
4.13 Radial Distribution Function for K - O in KNO ₃ as the temperature increases. The yellow	

line represents the system at 100 K, the blue line at 300 K and the green line at 500 K, the dotted line (same colours) represent the cooling down of the system	145
4.14 Radial Distribution Function for K-O in KNO ₃ obtained by cooling down the simulation at 500 K (blue) and the RDF of the polymorph obtained from cooling down the aragonite structure (red). Dotted lines represent the positions of XRD ^[75] peaks for the experimental R3m structure ^[13]	145
4.15 Scheme of the fitting process using GULP for this force field.....	150
5.1 Radial distribution function (RDF) for nitrogen of nitrate- oxygen of the water at 300K	158
5.2 Comparison between experimental density of KNO ₃ solution and the values obtained using force-field from this work ^[2]	159
5.3 6 molal box of potassium nitrate.....	159
5.4 RDF for the K to O(NO ₃) solid potassium nitrate (aragonite) at 0K	161
5.5 RDF for the K to O(NO ₃) solid potassium nitrate (aragonite) at 300K.....	161
5.6 Snapshot of a KNO ₃ -aragonite box in two different moment of the simulation. Black circle highlights how the same nitrate group changes position though the simulation	162
5.7 Unit cell of potassium nitrate (aragonite)	164
5.8 A collection of tip types and crystalline products at a variety of KNO ₃ concentrations. (a) Canine hair producing two prismatic Phase II crystals at 4.25 M. (b) An APTES-treated (amine-terminated silane) glass tip producing a 5-6 prismatic Phase III crystals. (c) Human hair nucleating a single, prismatic Phase III crystal. (d) The feline whisker with a frayed tip creates many contact points with the droplet resulting in fast, dendritic growth of a Phase II crystal aggregate. ^[8] . Images supplied by F Meldrum, T Dunn (Leeds University).....	164
5.9 KNO ₃ aragonite. Images supplied by F Meldrum, T Dunn (Leeds University) ^[2]	165
5.10 KNO ₃ ferroelectric. Images supplied by F Meldrum, T Dunn (Leeds University) ^[2]	165
5.11 Cluster size vs radius of gyration.....	166
5.12 Fractal dimension of the largest finite cluster in solution for a 6 molal clustered box.....	167

5.13 8 molal solution: probability of connection versus number of connection for each potassium in the solution	169
5.14 8 molal solution: (a) average number of potassium unit included in a finite size cluster though the 10 ns of simulation; (b) average number of potassium unit included in the largest detected cluster though the 10 ns of simulation; (c) average number of potassium unit not showing any connection at all though the 10 ns of simulation normalised as a function of the total number of potassiums	170
5.15 Fractal dimension of the largest finite cluster in solution for an 8 molal box	170
5.16 10 molal solution: probability of connection versus number of connection for each potassium in the solution	171
5.17 Collection of dimer and triangular-shaped cluster	172
5.18 10 molal solution: (a) average number of potassium unit included in a finite size cluster though the 10 ns of simulation; (b) average number of potassium unit included in the largest detected cluster throughout the 10 ns of simulation; (c) average number of potassium unit not showing any connection at all though the 10 ns of simulation, normalised as a function of the total number of potassiums	172
5.19 Fractal dimension of the largest finite cluster in solution for a 10 molal box	173
5.20 12 molal solution: probability of connection versus number of connection for each potassium in the solution	174
5.21 12 molal solution: (a) average number of potassium unit included in a finite size cluster though the 10 ns of simulation; (b) average number of potassium unit included in the largest detected cluster though the 10 ns of simulation; (c) average number of potassium unit not showing any connection at all though the 10 ns of simulation, normalised as a function of the total number of potassiums	175
5.22 Fractal dimension of the largest finite cluster in solution for a 12 molal box	175
5.23 Percentage of 'single unit' cluster as a function of total number of potassium ions	176
5.24 Isolated medium-sized cluster. Picture shows only potassiums in green	177
5.25 Collection of clusters in various shapes and sizes, with potassium ions shown in green. At the top of the figure, highlighted in a black circle is an isolated ion, the middle of the figure	

shows the biggest cluster, a long chain with a few folds. At the bottom of the figure, highlighted in black circles, are a pair and a triangle-shaped cluster.....	177
5.26 Orange Euclidean distance, green, light blue and yellow Manhattan distances	178
5.27 Angles reference	180
5.28 Distances reference K-N	180
5.29 Distances reference N-N	181
5.30 $s(\alpha)$ vs $s(\beta)$ for calcite in a 8 molal solution after 2 and 10 ns of simulation. The areas of more intense blue represent the combination of standard deviation with the highest occurrence of polymorph resemblance.	183
5.31 $s(\alpha)$ vs $s(\beta)$ for aragonite in a 8 molal solution after 2 and 10 ns of simulation. The areas of more intense blue represent the combination of standard deviation with the highest occurrence of polymorph resemblance.	184
5.32 $s(\alpha)$ vs $s(\beta)$ for calcite in a 10 molal solution after 2 and 10 ns of simulation. The areas of more intense blue represent the combination of standard deviation with the highest occurrence of polymorph resemblance.....	186
5.33 $s(\alpha)$ vs $s(\beta)$ for aragonite in a 10 molal solution after 2 and 10 ns of simulation. The areas of more intense blue represent the combination of standard deviation with the highest occurrence of polymorph resemblance.	187
5.34 $s(\alpha)$ vs $s(\beta)$ for calcite in a 12 molal solution after 2 and 10 ns of simulation. The areas of more intense blue represent the combination of standard deviation with the highest occurrence of polymorph resemblance.....	189
5.3535 $s(\alpha)$ vs $s(\beta)$ for aragonite in a 12 molal solution after 2 and 10 ns of simulation. The areas of more intense blue represent the combination of standard deviation with the highest occurrence of polymorph resemblance.	190
5.36 Intermediate coordination 8 oxygen of NO_3 and 3 water oxygens.....	191
5.37 Calcite like with only monodentate binder oxygens. Total oxygen coordination 11	192
5.38 Coordination polyhedron of Fig. 5.37.....	192
5.39 Mono and bi-dentate calcite on xy plane	193

5.40 Mono and bi-dentate calcite on z axis.....	193
5.41 Aragonite-like structure. Total coordination sums up to 11	194
6.1 Definition of the three types of surfaces according to Tasker ^[3,5]	199
6.2(a) ferroelectric potassium nitrate, (b) aragonite potassium nitrate	200
6.3 Simulation box of $\langle 0\ 0\ 1 \rangle$ KNO_3 surface in contact with high concentration KNO_3 solution	202
6.4. Simulation box of $\langle 0\ 0\ 1 \rangle$ KNO_3 surface in contact with a high concentration KNO_3 solution after 2 picoseconds run in the NVT ensemble	202
6.5 RDF for the zone 1 reported in Figure 6.4.....	203
6.6 RDF for the zone 2 reported in Figure 6.4.....	203
6.7 Scheme of a standard constant chemical potential molecular dynamics simulation. Reproduced with permission from [12]	205
6.8 $\text{C}\mu$ -MD simulation of a KNO_3 -calcite slab, at the beginning of the application of the forces and after 0.25 ns. Red line on the left hand side shows the centre of the slab while the two parallel lines in the middle show the control region (concentration set to 5 M). For clarity, figure shows only the potassium cores (red balls).....	208
6.9 Evolution over time (ps) of water (purple symbols), potassium (green symbols) and nitrogen (light blue symbols) concentration expressed as number of ions per cubic nanometre. The potassium and nitrate lines are constantly equal to zero and therefore overlap perfectly	209
6.10 Evolution over time (ps) potassium (green symbols) and nitrogen (light blue symbols) potential bias (kJ/mol). The potassium and nitrate lines are constantly equal to zero and therefore overlap perfectly.....	209
6.11 $\text{C}\mu$ -MD simulation of a KNO_3 -calcite slab, at the beginning of the application of the forces and after 1 ns. Red line on the left hand side shows the centre of the slab while the two parallel lines in the middle show the control region (concentration set to 5 M). For clarity, figure shows only the potassium cores (red balls).....	210

6.12. Evolution over time (ps) of water (purple symbols), potassium (green symbols) and nitrogen (light blue symbols) concentration expressed as number of ions per cubic nanometre	211
6.13 Evolution over time (ps) potassium (green symbols) and nitrogen (light blue symbols) potential bias (kJ/mol).....	211
6.14 q_6 mean (anion-cation) of the system depicted in Figure 6.11 at the beginning of the simulation	212
6.15 q_6 mean (anion-cation) of the system depicted in Figure 6.11 after 1 ns.....	213
6.16 Set up for a C_{μ} -MD simulation of a KNO_3 -aragonite slab. On the left- hand side we can see the slab, in contact with a low concentration solution (5 M) and then the reservoir (15M). Because of the system's periodicity the reservoir is in the middle of two low concentration solutions	214
6.17 C_{μ} -MD simulation of a KNO_3 -aragonite slab, at the beginning of the application of the forces and after 3 ns. Black lines underline the very last layer of the surface. Black box on the right hand-side enhances the dissolution process	215
6.18. z-density as a function of the number of bins for hydrogen (yellow lines) and oxygen of the water (blue line). Green line represents the hydrogen bond density.....	216
6.19 Close up next to the surface of the z-density as a function of the number of bins for hydrogen (yellow lines) and oxygen of the water (blue line). Green line represents the hydrogen bond density.....	216
6.20 Close up next to the Fermi wall of the z-density as a function of the number of bins for hydrogen (yellow lines) and oxygen of the water (blue line). Green line represents the hydrogen bond density.....	217
6.21 Close up next to the surface of the z-density as a function of the number of bins at the beginning of the application of the forces and after 3 ns of simulation, for hydrogen (light green, beginning, dark green after 3ns) and oxygen of the water ((light blue, beginning, dark blue after 3ns).....	217
6.22. z-density as a function of the number of bins for potassium (yellow lines), nitrogen (orange line) and oxygen of the nitrate (green line)	218

6.23 Close up next to the surface of the z-density as a function of the number of bins for potassium (yellow lines), nitrogen (orange line) and oxygen of the nitrate (green line).....	219
6.24 Close up next to the surface of the z-density as a function of the number of bins for nitrogen. Yellow line represents the system at the beginning of the application of the forces, the green line after 3 ns of simulation.....	219
6.25 C μ -MD simulation of a KNO ₃ -aragonite slab, at the beginning of the application of the forces and after 3 ns. Black lines underline the very last layer of the surface. Black box on the right hand-side enhances the surface's behaviour	220
6.26 z-density as a function of the number of bins at the beginning of the application of the forces and after 3 ns of simulation, for hydrogen (light green, beginning, dark green after 3ns) and oxygen of the water (light blue, beginning, dark blue after 3ns)	221
6.27 Close up next to the surface of the z-density as a function of the number of bins at the beginning of the application of the forces and after 3 ns of simulation, for hydrogen (light green, beginning, dark green after 3ns) and oxygen of the water (light blue, beginning, dark blue after 3ns).....	221
6.28 Close up next to the surface of the z-density as a function of the number of bins for nitrogen. Yellow line represents the system at the beginning of the application of the forces, the green line after 3 ns of simulation.....	222
7.1 Schematic representation of a SAM. Blue balls represents the terminal group, yellow balls the head group, zig-zag lines the organic chains.	228
7.2 Different types of surface defects in SAM surfaces: a) Vacancy and b) Step defect	229
7.3 Schematic representation of the defect on the xy plane	230
7.4 Vacancy defect of 16-MHDA SAM. The three yellow layers represent gold atoms. Their role is to anchor the SAMs at various heights, thus generating the defect. Underneath it is possible to see a red layer (argon) that because of its inert nature blocks the interaction between the bottom of the surface and the periodic image replica of the water box.	231
7.5 Vacancy defect of 16-MHDA SAM on the xy plane	231
7.6 Chain of 16-mercaptohexadecanoic acid	232

7.7 Single chain of 16-mercaptohexadecanoic acid on a SAM surface set-up.....	232
7.8 a) Flat SAM surface and b) Vacancy defect SAM surface with a box of water and Potassium Nitrate. Water is not displayed.....	233
7.9 Example of an MSD plot of an ion broken into x -, y - and z -components. The region used for the calculation of diffusion coefficients is marked in red	236
7.10 Interquartile range analysis on the diffusion coefficients of ions within a cluster. The analysis identifies some outliers, as marked on the plot, which are removed from the mean cluster diffusion coefficient to obtain a corrected mean.....	236
7.11 Figure 7.11: a) Configuration of system after 1 ns with water visualised and configurations containing b) 10, c) 20, d) 30, e) 40, f) 50 Potassium Nitrate Ions before and after 1 ns. For figures b) to f) water molecules not shown for clarity.....	238
7.12 Nitrate on the SAM surface	238
7.13 RDF of the interaction between nitrogen of the nitrate group and oxygen of the water	239
7.14 RDF of the interaction between nitrogen of the nitrate group and oxygen of the carboxylic head group of the 16-MDHA chains.....	240
7.15 (a) Configuration of system after 0.25 ns with water visualised and configurations containing b) 10, c) 20, d) 30, e) 40, f) 50 Potassium Nitrate Ions before and after 0.25 ns. Except for (a), which depicts the whole system, the water molecules have been eliminated for clarity	241
7.16 RDF of the interaction between nitrogen of the nitrate group and oxygen of the water	243
7.17 RDF of the interaction between nitrogen of the nitrate group and oxygen of the carboxylic head group of the 16-MDHA chains.....	243
7.18 Starting configuration, in LAMMPS, for defective SAMs surface and 50 KNO ₃ . Picture does not include water	244
7.19 Clustered KNO ₃ on a flat, charged, SAM surface. Starting configuration for the simulation. Water not displayed for clarity.	246

7.20 Cell of Figure 7.19 after 30 ns of <i>nvt</i> run. Water not displayed for clarity	246
7.21 RDF for the potassium to nitrogen interaction for the solution on top of a flat SAM surface	247
7.22 RDF for the potassium to nitrogen interaction for potassium nitrate – aragonite	247
7.23 MSD of K ions on a flat SAM surface. The blue line represents the x-, the orange line the y- and the green line the z- components. The black line shows the total MSD.....	248
7.24 IQR analysis for K ions on a flat SAM surface. Blue dots represent the data set, red dashed line the mean, purple dashed line the standard deviation, green dashed line the median, brown dashed line the interquartile range and orange dashed the correct mean.....	248
7.25 MSD of nitrogen ions on a flat SAM surface. The blue line represents the x-, the orange line the y- and the green line the z- components. Black line shows the total MSD	249
7.26 IQR analysis for nitrogen ions on a flat SAM surface. Blue dots represent the data set, red dashed line the mean, purple dashed line the standard deviation, green dashed line the median, brown dashed line the interquartile range and orange dashed the correct mean	249
7.27 Radius of gyration over time.....	251
7.28 Fractal dimension of the average finite cluster in solution for a solution of KNO_3 sitting on a flat SAM surface	251
7.29 Number of potassium in a cluster vs probability (normalised).....	252
7.31 Clustered KNO_3 on a defective, charged, SAM surface. Starting configuration for the simulation.....	252
7.31 Cell of Figure 7.30 after 30 ns <i>nvt</i> run	253
7.32 Cell of Figure 7.30 after 30 ns <i>nvt</i> run. Only KNO_3 displayed. Black line show the defects on the <i>xy</i> plane	253
7.33 RDF for the potassium to nitrogen interaction for the solution on top of a defective SAM surface.....	254
7.34 RDF for the potassium to nitrogen interaction for potassium nitrate – calcite.....	254
7.35 MSD of K ions on a defective SAM surface. The blue line represents the x-, the orange line the y- and the green line the z- components. Black line shows the total MSD	255

7.36 IQR analysis for K ions on a flat SAM surface. Blue dots represent the data set, red dashed line the mean, purple dashed line the standard deviation, green dashed line the median, brown dashed line the interquartile range and orange dashed the correct mean.....	255
7.37 MSD of nitrate ions on a defective SAM surface. The blue line represents the x-, the orange line the y- and the green line the z- components. Black line shows the total MSD.....	256
7.38 IQR analysis for nitrate ions on a defective SAM surface. Blue dots represent the data set, red dashed line the mean, purple dashed line the standard deviation, green dashed line the median, brown dashed line the interquartile range and orange dashed the correct mean.....	256
7.39 Radius of gyration over time.....	257
7.40 Fractal dimension of the average finite cluster in solution for a solution of KNO_3 sitting on a flat SAM surface	258
7.41 Number of potassium in a cluster vs probability (normalised).....	258

Table of Contents

Chapter 1 - Introduction	33
1.1 Importance of simulating nucleation and crystallisation	33
1.1.1 Crystallisation in the Real World	33
1.2 Crystal	34
1.2.1 Crystal structure	35
1.2.2 Polymorphism	35
1.2.3 Crystallisation.....	36
1.3 Nucleation	36
1.3.1 Classical nucleation theory	37
1.3.1.1 Transient precursor	39
1.3.1.2 Competition of Phases	39
1.3.1.3 Kinetic Trapping of Bulk Metastable or Unstable States	40
1.3.1.4 High Nucleation Density.....	40
1.3.2 Non-classical nucleation theory	40
1.4 Calcium Carbonate as a model	42
1.5 References.....	43
Chapter 2 – Alkali metal nitrates	47
2.1 Introduction.....	47
2.2 Lithium Nitrate.....	48
2.2.1 Crystal structure, polymorphism and phase transition	48
2.3 Sodium Nitrate	49
2.3.1 Crystal structure, polymorphism and phase transition	49
2.3.2 Crystal Growth	51
2.3.3 Crystal Morphology	52
2.4 Potassium Nitrate	52

2.4.1 Crystal structure, polymorphism and phase transition	52
2.4.2 Crystal Growth	54
2.4.3 Crystal Morphology	54
2.5 Rubidium Nitrate	55
2.5.1 Crystal structure, polymorphism and phase transition	55
2.5.2 Crystal Growth	56
2.5.3 Crystal Morphology	56
2.6 Caesium Nitrate	57
2.6.1 Crystal structure, polymorphism and phase transition	57
2.6.2 Crystal Growth	58
2.6.3 Crystal Morphology	58
2.7 References.....	59
Chapter 3 - Methodology.....	65
3.1 Development of the force-field.....	66
3.1.1 Potential modelling	66
3.1.2 Short-Range Non-bonded Interactions	68
3.1.2.1 Lennard-Jones Potential.....	69
3.1.2.2 Buckingham Potential.....	70
3.1.2.3 Many bodies interactions	71
3.1.2.3.1 Force-field for nitrates	72
3.1.3 Long-Range Cut-offs.....	74
3.1.3.1 Mei-Davenport-Fernando taper	75
3.1.3.2 Ewald Decomposition.....	76
3.1.3.3 Particle Mesh Ewald	78
3.2 <i>Ab-initio</i> methods	78
3.2.1 Density functional theory	79

3.2.2.1 Exchange Correlation Functionals	79
3.2.2.2 Basis set	81
3.3 Energy Minimisation	83
3.3.1 Lattice Energy	83
3.3.2 Minimisation Algorithms	84
3.3.2.1 Steepest Descent	84
3.3.2.2 Conjugate Gradient	85
3.3.2.3 Newton-Raphson.....	85
3.3.2.4 BFGS Method	87
3.3.3 Constant Pressure Minimisation.....	87
3.4 Molecular Dynamics	87
3.4.1 Periodic boundary conditions.....	88
3.4.1.1 Minimum Image Convention.....	89
3.4.2 Calculation of Forces	90
3.4.3 Time Integration Algorithms.....	91
3.4.3.1 Verlet Leap-Frog	92
3.4.3.2 Velocity Verlet.....	93
3.4.4 Initialisation.....	93
3.4.5 Equilibration Period	94
3.4.6 Ensembles.....	94
3.4.6.1 Canonical ensemble (NVT)	94
3.4.6.2 Isothermal–isobaric (NPT) ensemble	95
3.5 Free energies of hydration of isolated ions	95
3.5.1 The experimental problem	96
3.5.2 The simulation problem	99
3.5.2.1 Absolute free energy of hydration of a single ion	99
3.5.2.1.1 Corrections of type A	102

3.5.2.1.2 Corrections of type B	102
3.5.2.1.3 Corrections of type C	104
3.5.2.1.4 Corrections of type D.....	106
3.5.2.2 Calculating the corrections for example cases	107
3.5.3 Conclusions	110
3.6 References	112
Chapter 4 – Force-field fitting	121
4.1 Introduction.....	121
4.1.1 Structures of the alkali metal nitrates	121
4.2 Methodologies	122
4.2.1 Fitting procedures	123
4.2.2 Simulation of solution properties	127
4.3 Results and discussion.....	129
4.3.1 Comparison of force-fields with crystal structures.....	132
4.3.2 Stability of polymorphs	135
4.3.3 Comparison with crystal properties	137
4.3.4 The Lattice thermal expansion	141
4.3.5 Simulation of the crystal structures at high temperature	141
4.3.6 Calculating the corrections to the free energy of hydration	147
4.3.7 Solubility	147
4.4 Conclusions	148
4.5 Appendix – Force-field fitting details	149
4.6 References	151
Chapter 5 - Supersaturated Solutions of Potassium Nitrate.....	157
5.1 Behaviour of KNO ₃ solutions	157
5.1.1 Classical molecular dynamics	159
5.1.1.1. Radial Distribution Functions	160

5.2 Cluster Analysis	162
5.2.1 6 molal solution clustered	165
5.2.2 8 molal solution	168
5.2.3 10 molal solution	171
5.2.4 12 molal solution	173
5.2.5 Comparison of molalities	176
5.3 Manhattan Distances	178
5.3.1 Reference Systems	179
5.3.2 Average Polymorphs	181
5.3.3 8 molal solution	182
5.3.4 10 molal solution	185
5.3.5 12 molal solution	188
5.3.6 Polymorphs resemblance	191
5.3.7 Conclusions	194
5.4 References	195
Chapter 6 - Growth of KNO₃	197
6.1 Purpose of this work	197
6.2 Creation of KNO ₃ 's slabs	197
6.2.1 Methodology	198
6.2.2 Results	199
6.3 Classical Molecular Dynamics	201
6.3.1 Methodology	201
6.3.2 Results	201
6.3.2.1 Analysis of the radial distribution function (RDF)	203
6.4 Constant Chemical Potential Molecular Dynamic (C μ -MD)	204
6.4.1 Methodology	204
6.4.2 Moving interface	207

6.4.2.1 KNO ₃ ferroelectric	207
6.4.3 Fixed interface.....	209
6.4.3.1 KNO ₃ ferroelectric	210
6.4.3.1.1 Collective variables analysis.....	212
6.4.3.1.2 Results.....	213
6.4.3.2 KNO ₃ aragonite.....	213
6.4.3.2.1 Control Region 2 <i>M</i>	214
6.4.3.2.1.1 Water ordering	215
6.4.3.2.1.2 z-density analysis	218
6.4.3.2.2 Control Region 7 <i>M</i>	220
6.4.3.2.2.1 Water ordering	221
6.4.3.2.2.2 z-density analysis	222
6.5 Final considerations and future work.....	223
6.6 References.....	224
Chapter 7 - Behaviour of Potassium Nitrate on Self-Assembled Monolayer surfaces ..	227
7.1 Introduction.....	227
7.1.1 Self-Assembled Monolayers (SAMs)	227
7.1.2 SAMs with calcium carbonate	229
7.2 Methodology.....	230
7.2.1 Introduction of defects.....	230
7.2.2 Simulation set-up.....	232
7.2.2.1 Force-field parameters	233
7.2.2.2 Molecular dynamics set-up	234
7.2.2.2.1 SAMs-water simulations.....	234
7.2.2.2.1 Ion cluster at SAMs defect in water.....	234
7.2.3 Diffusion coefficient calculations	235
7.3 Results.....	237

7.3.1 Neutral SAMs, Preliminary Studies - Flat SAM	237
7.3.1.1 Analysis of the radial distribution function (RDF)	239
7.3.2 Neutral SAMs, Preliminary Studies - Defective SAM	241
7.3.2.1 Analysis of the radial distribution function (RDF)	242
7.3.3 Further studies on defective SAM	244
7.3.3.1 Analysis of the radial distribution function (RDF)	244
7.3.4 Charged SAMs	245
7.3.4.1 Flat SAM.....	245
7.3.4.1.1 Analysis of the radial distribution function (RDF).....	247
7.3.4.1.2 Mean-square displacement analysis.....	248
7.3.4.1.3 Cluster analysis	250
7.3.4.2 Defective SAM	252
7.3.4.2.1 Analysis of the radial distribution function (RDF).....	253
7.3.4.2.2 Mean-square displacement analysis.....	254
7.3.4.2.3 Cluster analysis	256
7.4 Conclusions.....	259
7.5 Appendix: force-field parameters	260
7.6 References.....	264
Chapter 8 – Conclusions and future work.....	267

Chapter 1

Introduction

This chapter will outline the fundamentals behind this thesis, which explores alkali metal nitrates through simulation, to understand their nucleation and crystallisation processes. The following sections will give an in-depth explanation of why it is important to possess effective tools for simulating nucleation and crystallisation, along with the origin of this project, and to highlight its place in the consortium ‘Crystallisation in the Real World’^[1] to which the PhD position was linked.

1.1 Importance of simulating nucleation and crystallisation

Nucleation, and crystallisation, are challenging processes to study because of the timescales: most experimental techniques available are not able to detect the first steps due to the speed and localised nature, especially if the compound of study possesses a high solubility level. In these cases, simulation is an important tool to study the missing steps of the process. Simulation, by its own nature, is able to cover small time-intervals. However, the nucleation process can be classified as a rare event as it is projected to occur infrequently, with a probability in the order of 10^{-3} s^{-1} . Calculating these rare-event probabilities is challenging as they are beyond the general time of atomic scale simulations.

Alkali metal nitrates are characterised by a simple structure, which makes the simulation theoretically easy to perform, but they are not exempt from the above challenges (that will be outlined in the following chapters).

1.1.1 Crystallisation in the Real World

‘Crystallisation in the Real World: Delivering Control via Theory and Experiment’ is an EPSRC-funded project started in 2018. Three experimental groups and five modelling groups from the universities of Leeds, Sheffield, Warwick, and UCL are involved.

The goal of this research is to create new methods for understanding and controlling crystallisation through integrated experimental and computational work.

Crystallisation has long caught the attention of many researchers. The dynamic, molecular-scale mechanisms that underpin nucleation and growth are only now being understood

because we have the necessary instruments and theoretical tools. We are examining the nanoscale changes that take place in the solid and solution during crystallisation by fusing modelling approaches that address length-scales, time-scales, and environments relevant to real-world conditions with carefully crafted multi-scale experiments that range from the purposefully basic to cutting-edge. This new insight holds the key to the synthesis of crystal polymorphs, either with the help of pre-selected soluble additives that can generate particles with the required sizes and shapes, or by merely modifying the reaction conditions. When and where we want crystal formation to occur, we can choose particles that can promote nucleation, possibly even of a specific polymorph, or create surfaces that can either encourage or inhibit it. These new additives can be used in a variety of industries, including the chemical industry, environment, healthcare, formulated products, oil and gas, water, mining, and sophisticated materials^[48].

1.2 Crystals

A crystal is defined as a solid material in which the atoms possess a highly ordered structure. This highly ordered structure is repeated in all the directions and is called a lattice. In contrast, a lack of organisation leads to the formation of a structure called “amorphous”. A crystal can be identified by its shape, which means by flat faces characterised by specific orientations. *Figure 1.1* shows two different types of KNO_3 crystals, as an example.

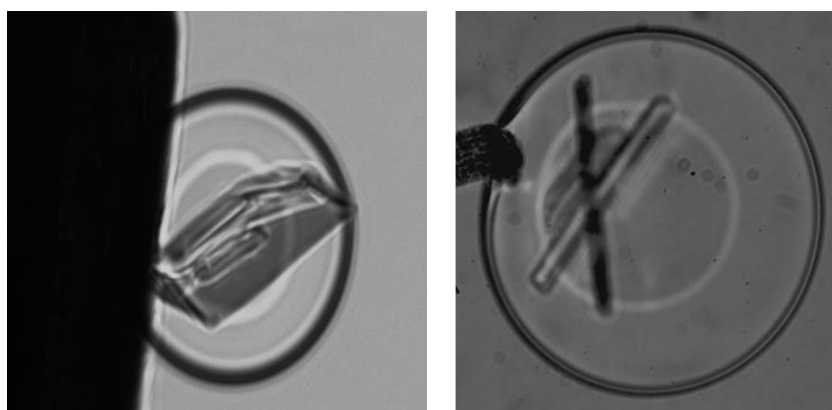


Figure 1.1. KNO_3 ferroelectric, left hand-side and aragonite, right hand-side. Images supplied by F Meldrum, T Dunn (Leeds University)^[2]

1.2.1 Crystal structure

A crystal structure is the array of the particles that generates a crystal. Normally, a parallelepiped is used in order to define the unit cell, and is characterised by the length of the cell on the three cartesian directions (a , b , c) and the angles (α , β , γ). Starting from a chosen point, every atom's position is identified by fractional coordinates (x_i , y_i , z_i)^[3]. Every crystal is identified, as well, by all the possible symmetry operations, that together describe the space group that a particular crystal belongs to^[4].

1.2.2 Polymorphism

Polymorphism is the phenomenon by which a material can exist in more than one crystalline shape or can be completely amorphous. If the same crystal can be differently packed, it is called packing polymorphism, otherwise if the crystals are formed by different conformers of the same molecule is called conformational polymorphism.

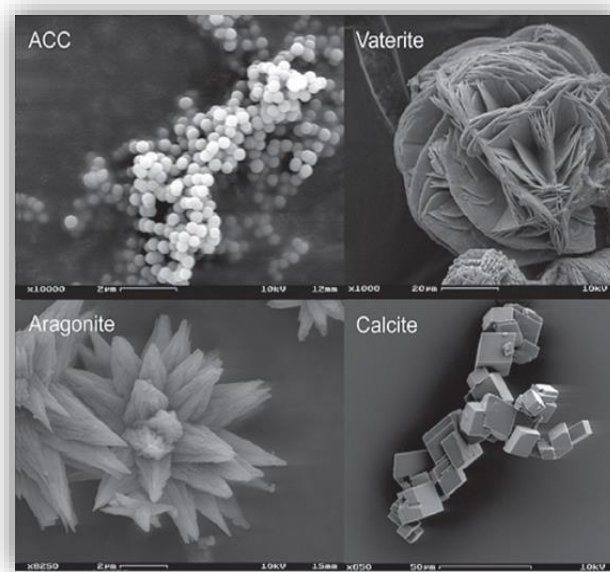


Figure 1.2. Different polymorphs of calcium carbonate. Top left shows the only amorphous form of calcium carbonate (ACC), while vaterite (top-right), aragonite (bottom left) and calcite (bottom right) represent the crystal forms in crescent order of thermodynamic stability (<http://www.ruhr-uni-bochum.de/sediment/forschung.html>)^[29]

For example, as shown in *Figure 1.2*, calcium carbonate exists in three different crystalline forms and one amorphous form. Based on the behaviour of the curve of free energy as a function of the temperature it is possible to distinguish two different trends: monotropic^[7], where the different curves of the polymorphs do not cross before the melting point, meaning an irreversible transition between polymorphs, and enantiotropic where the curves cross and the transition is reversible.

Polymorphism can be controlled by the solvent impurities, the level of supersaturation, the temperature and variation in the stirring conditions.^[8] Usually, a species with different polymorphs follows the Ostwald rule, by which the first polymorph formed is the most unstable.^[9]

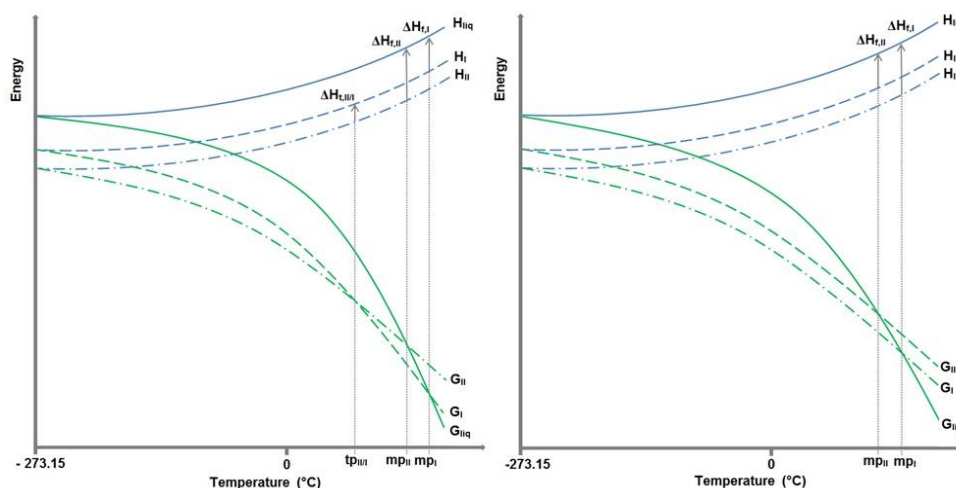


Figure 1.3. Behaviour of a monotropic (right) and enantiotropic (left) systems^[7]. Green lines represent the contributions to the free energy and the blue lines to the enthalpy. Reproduced with the publisher's permission.

1.2.3 Crystallisation

Crystallisation is the process that, starting from a fluid or a solution, creates a crystal. Different crystals possess different properties and qualities; therefore, it is vital for industry to be able to control and understand the whole range of parameters to obtain a specific crystal. Crystallisation can be simplified as a two-step process: nucleation and growth. Nucleation is the formation of the first cluster; growth is the increase in the size of the first nucleus until the critical size is reached, thus leading to an indefinite growth of the system. Usually, the driving force of this process is the level of supersaturation of the system.

1.3 Nucleation

Nucleation is the first step of crystallisation that, starting from building blocks, leads to the formation of a new structure by self-assembly and/or self-organisation. Starting from ions in solutions, progressive organising generates intermediary phases, for example high-disorder species like multi-ion clusters, dense liquid droplets, transient crystalline or amorphous phases. By analysing the intermediate species, it is usually possible to understand the kinetics and thermodynamics of formation for what will be the actual crystal generated from this

process. It is possible to define two kinds of nucleation: primary and secondary. In primary nucleation, the events occur without needing any external crystal to initiate the process. It can be homogeneous, when the particles assemble themselves without any help from the external environment or heterogeneous if a catalyst is needed.

Secondary nucleation, requires pre-existing nuclei acting as catalysts. Secondary nucleation is usually more efficient than primary nucleation, mainly because it is characterised by a low kinetic order, which is proportional to the supersaturation and because it happens with low levels of supersaturation, thus leading to the formation of good quality crystals^[10].

1.3.1 Classical nucleation theory

Classical nucleation theory represents a general framework to model nucleation, crystal growth and/or decay and crystal stability on the basis of thermodynamics. This theory leads on the foundation of Gibbs' assumption of this process being the results of the balance of two forces, growth and dissolution ^[11,12]. In order to take place, nucleation should overcome the barrier of free energy ($\Delta G_{bulk} < 0$). The free energy for a bulk crystal can be described as

$$\Delta G_{bulk} = \Delta E_{pot} - T\Delta S + p\Delta V \quad (1.1)$$

where ΔE_{pot} represents the potential energy, $p\Delta V$ is the volume variation depending on the pressure (p). Both those terms represent the enthalpic contribution to the Gibbs free energy. The entropic contribution is $-T\Delta S$, and is linearly dependent on the temperature. Therefore, for the nucleation process to be spontaneous the ΔG just needs to be negative; the sign of the components does not matter. When the condition

$$\Delta E_{pot} + p\Delta V = T\Delta S \quad (1.2)$$

is reached, so is the transition point, which implies having defined the saturation concentration as a function of temperature and pressure.

There are, potentially, multiple barriers that the system has to overcome in order to undergo a phase transition. These could be the disruption of the solute-solvent interactions and the formation of a crystalline surface. In most interpretations of classical nucleation theory, the assumption is made to simplify the equations, to assume that growing crystals have a spherical shape, therefore

$$\Delta G_{cry} = \Delta G_{bulk} + \Delta G_{surf} \quad (1.3)$$

Which means that the total free energy of the crystal is made up of a bulk term, which depends on the radius of the crystal as r^3 in the bulk phase and as r^2 in the surface term. A more general way to describe the free energy of formation of a crystal, however, does not involve a reference to the particle geometry, but instead takes into account only the number of particles involved in the process

$$\Delta G_{cryst}(N) = \Delta\mu \cdot N + \sigma_{surface} \cdot N^{2/3} \quad (1.4)$$

where $\Delta\mu \cdot N$ represents the equivalent term for the bulk free energy in equation (1.4) and takes in account how the potential energy changes whilst the system evolves from one phase to another one. Given the shape of the system (1.4) can be rewritten as

$$\sigma_{surface} \cdot N^{2/3} = \sigma_{100} \cdot A_{100} + \sigma_{110} \cdot A_{110} + \dots \quad (1.5)$$

In (1.5) A is the term related with the known faces and σ is related with the free energy needed to observe such faces.

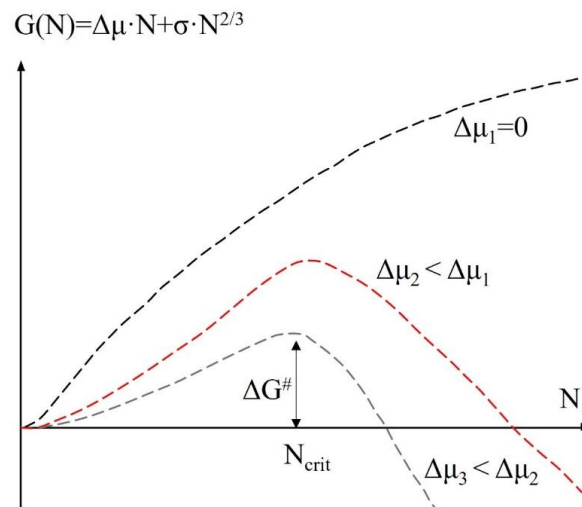


Figure 1.4. Free energy profiles as function of the number of precipitated formulae units. If $\Delta\mu$ (black curve) is equal to zero, the energy barrier is not overcome and the system does not nucleate. In the other 2 cases (red and grey curve) the system overcomes the critical radius and as a function of the depth of the free energy well it manages to nucleate a proportional amount of formulae units ^[13]

As shown in *Figure 1.4*, the different curves represent the variation of chemical potential during the formation of the crystal, and each represents a different driving force in the process (concentrations, temperature, etc.). If $\Delta\mu < 0$ and the energy barrier is crossed ($\Delta G^\# = G(N_{crit})$) growth should occur continuously (until the saturation level changes significantly). If N tends to infinity, the free energy converges to the variation of chemical potential. Classical nucleation theory allows us to describe the meaning of the nucleation barrier in a

thermodynamic sense, but also provides a way to interpret multi-step nucleation and Ostwald ripening^[14]. In the cases where classical nucleation theory might seem not to be applicable, their non-adherence can be explained with one of the cases listed in the following subsections.

1.3.1.1 Transient Microscopic Precursors

According to CNT, the energy penalty associated with cluster formation can be derived by the bulk surface energy. This, however, ignores the fact that, for small-sized clusters, the contribution of the difference in energy for different types of surfaces is actually highly substantial, and specific atomic configurations of the expanding cluster may therefore become more beneficial than others^[30]. Based on the classical formulas, assuming spherical nuclei with constant surface energy, the relative abundance of these transitory species will be larger than expected. Such local minima in free energy associated with specific monomer configurations will result in transitory species. Due to kinetic or thermodynamic considerations, these species, which can only exist in limited amounts because they are still more unstable than free monomers, may offer the simplest route to the final state.

1.3.1.2 Competition of Phases

While polymorphs and related phases may not be the most stable in ambient conditions, they may be stable bulk phases in specific regions of the phase diagram and have a lower energy than the solution (or vapour) state at sufficient applied chemical potential. If the energy barrier to nucleation is lower than that of the stable phase, they are more likely to form initially and then convert to the stable phase either directly or, more commonly, via dissolution and re-precipitation once the stable phase nucleates^[30].

Ostwald's Rule of Stages is based on this type of nucleation, which frequently occurs in multiphase systems^[31]. This mechanism is a good fit for CNT and, in many ways, supports the veracity of the theory. Metastable phases tend to present, most of the time, surface energy values that are lower than the stable phase.^[32]

$$\Delta G^* \propto \frac{\alpha^3}{\sigma^2} \quad (1.6)$$

Equation (1.6) expresses the relationship between the classical free energy barrier (ΔG^*), the surface energy (α) and the supersaturation (σ).^[31, 32] According to CNT, then

$$\frac{\sigma_{stable}}{\sigma_{metastable}} < \left(\frac{\alpha_{stable}}{\alpha_{metastable}} \right)^{\frac{3}{2}} \quad (1.7)$$

If the condition described in (1.7) is met and the kinetic prefactors are comparable, then the metastable phase will initiate first.

1.3.1.3 Kinetic Trapping of Bulk Metastable or Unstable States

If the formation of the metastable phase does take place, this can be pushed to the point that the system might reach a level of supersaturation so low that inhibits the formation of the stable polymorphs. This is one example of how the metastable phase, through the reduction of the monomer's mobility can prevent the polymorph's conversion over time. That is usually the case for the two less-stable polymorphs of calcium carbonate (vaterite and aragonite), as well as the amorphous form (amorphous calcium carbonate, ACC). All those forms can remain stable, as biominerals, until calcification (formation of calcite) occurs. [33]

1.3.1.4 High Nucleation Density

The conditions that have to be met in order for a supersaturated system to transition are:

1. only one particle exists in equilibrium with the depleting solution (or vapour);
2. the morphology that minimises the surface's energy gets generated first

This describes the simplest process, however, if the chemical potential is high enough it is possible to obtain multiple, simultaneous nucleation events. The products of these separate events can then, over time, have reciprocal interactions, which will eventually lead to the formation of either subcritical clusters, which can aggregate with each other to form, or directly form, stable nuclei.

1.3.3 Non-classical nucleation theory

It has been suggested, though the use of novel experimental techniques, that, starting from solution, the crystallisation process occurs through various intermediate stages, before the thermodynamically stable phase gets formed (so-called rule of stages) [34].

According to the Oswald's rule of stages [34] an unstable (or metastable) system evolves into a slightly more stable conformation, which has the closest free energy to the original one and through a chain of transformations it reaches the final, most stable, state. If the mechanism of

transformation cannot be assimilated into one included in the Section 1.3.1.4, then it may be interpreted as a non-classical pathway. (as shown in *Figure 1.5, B to E*)

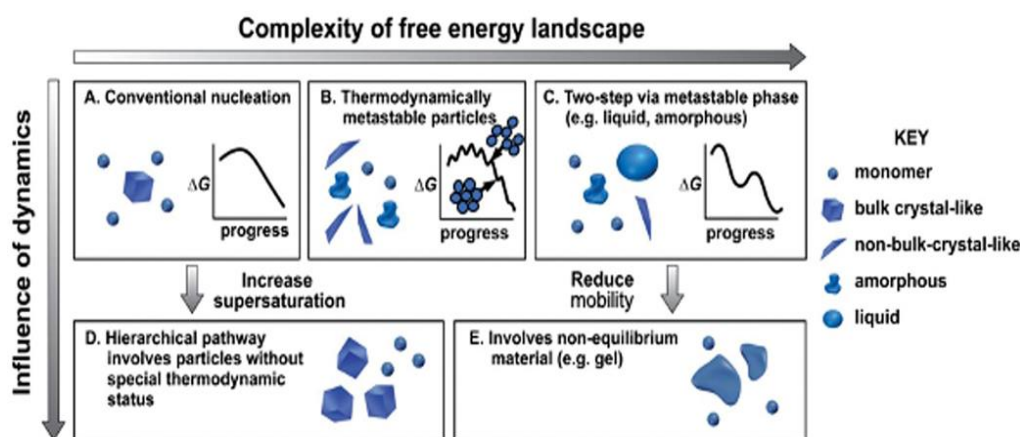


Figure 1.5 The potential paths and physical mechanisms by which monomers create a stable bulk crystal might have thermodynamic (A, B, C) or kinetic (D, E) origins (A) The traditional monomer-by-monomer addition. (B) Metastable particle aggregation (aggregation of liquid, amorphous, or weakly crystalline particles, or aggregation of oriented [and nearly orientated] metastable nanocrystals). (C) Crystallisation by metastable bulk phase creation (i.e., liquid or solid polymorph). (D) Cluster or oligomer aggregation dominated by kinetics. (E) Aggregation of unstable particles with different interior structures than equilibrium phases^[35]. All the rights to the authors.

One of those cases is the formation of a disordered precursor particle^[36, 37], whose order and density increase over time though recurring, multiple, transformations. Hydrated ACC particles may crystallise this way. Recent in situ TEM studies on Mg-doped CaCO₃ solutions revealed that once Mg-containing ACC first developed, it eventually transformed into calcite without changing its original spheroidal shape and with the loss of structural water^[38]. By adding more water to the ACC structure, Mg is crucial in destabilising the ionic bonding network, according to MD simulations^[38]. Systems that quickly polymerise into initially disordered networks or build complex frameworks belong to another class of systems that are difficult to fully fit within the context of CNT. The classic example comes from silicates^[39–42], but other systems as different as peptides^[43], calcium carbonates^[46, 47], phosphates^[45], and iron oxides have also been implicated in this process^[44]. Those species are usually referred as “prenucleation clusters”.

1.4 Calcium carbonate as a model

Most of the existing literature regarding nucleation and crystallisation uses calcium carbonate as a starting point^[15,16]. This compound has previously been chosen as a model because it shows a high natural recurrence, with both inorganic and organic roles: it is the constituent of

biological scaffolds, and a pure mineral both in earth and extra-terrestrials environments^[17,18]. It shows a rich polymorphism as well, with three different forms: vaterite, aragonite, and calcite (listed in reverse order of stability). Despite its relevance, calcium carbonate is still a topic of discussion^[19] as in the last years many mechanisms involving non-classical pathways have been proposed^[20], starting from the analysis of microstructures and biominerals^[21] or unusual geological mineral deposits^[22]. This involves the formation of prenucleation clusters (thermodynamically stable) or dense liquid precursor via liquid-liquid phase separation^[19]. On the other hand, not only crystallisation seems to be problematic, as calcium carbonate shows variation of solubility connected with CO₂ pressure^[23,24], variation of pH, temperature^[25,26] and salinity (e.g. interaction with magnesium ions)^[27,28]. All these reasons, therefore, lead to the necessity to find a new, simpler system to model nucleation and growth.

1.5 Aims and Objectives of this Thesis

The main focus of this work is a computational study of the nucleation process of KNO₃. In order to do so, for the reasons highlighted in Chapter 4, we had to make sure to use the appropriate force-field.

In a progressive order we have started with Chapter 5 by considering a pure, homogeneous nucleation process. Being the nucleation from solution a stochastic process, this goal was ambitious, for the time limitation of the project and the computational resources needed.

The following chapters, therefore, have progressively added a nucleating element.

In Chapter 6 we have attempted secondary homogeneous nucleation (slab of KNO₃) and in Chapter 7 we have attempted heterogeneous nucleation by adding a self-assembled monolayer.

1.6 References

- [1] <https://realworldcrystals.leeds.ac.uk/>;
- [2] T. Dunn, F. Meldrum, 2023, to be submitted;
- [3] J.R. Hook, H.E. Hall, *Solid State Physics. Manchester Physics Series (2nd ed.)*, John Wiley & Sons, 2010, ISBN 978047192804;
- [4] A.R. West, *Basic Solid State Chemistry (2nd ed.)*, Wiley. p. 1., 1999, ISBN 978-0-471-98756-7;
- [5] International Tables for Crystallography (2006). Volume A, Space-group symmetry;
- [6] R.G. Lerner, G.L. Trigg, *Encyclopaedia of Physics (2nd Edition)*, VHC publishers, 1991, ISBN (Verlagsgesellschaft) 3-527-26954-1, ISBN (VHC Inc.) 0-89573-752-3;
- [7] A. Carletta, *Solid-State Investigation of Polymorphism and Tautomerism of Phenylthiazole-thione: A Combined Crystallographic, Calorimetric, and Theoretical Survey*, *Crystal Growth & Design.*, 2015, **15**, 2461–2473;
- [8] K.R. Seddon, M. Zaworotko, *Crystal Engineering: The Design and Application of Functional Solids*, **539**, 1999;
- [9] W. Ostwald, *Studien über die Bildung und Umwandlung fester Körper. 1. Abhandlung: Übersättigung und Überkaltung*, *Zeitschrift für Physikalische Chemie*, 1897, **22**, 289–330;
- [10] N. S. Tavaré, *Industrial Crystallization*, Plenum Press, New York, 1995;
- [11] J. W. Gibbs, *On the Equilibrium of Heterogeneous Substances* *Trans. Conn. Acad. Art Sci.* 1876, **3**, 108–248;
- [12] J. W. Gibbs, *On the Equilibrium of Heterogeneous Substances*, *Trans. Conn. Acad. Art Sci.* 1876, **16**, 343–524;
- [13] P. Duchstein, P. Ectors, D. Zahn, *Molecular simulations of crystal growth: From understanding to tailoring*, *Advances in inorganic chemistry*, 2019, **73**, 507-529;
- [14] D. Zahn, *Chapter Thirteen - Molecular simulations of crystal growth: From understanding to tailoring*, *ChemPhysChem* 2015, **16**, 2069–2075;
- [15] D.N. Petsev, K. Chen, O. Gliko, P.G. Vekilov, *Diffusion-limited kinetics of the solution-solid phase transition of molecular substances*, *Proc Natl Acad Sci USA*, 2003, **100**, 792–796;
- [16] P.J.M. Smeets, K.R. Cho, R.G.E. Kempen, N.A.J.M. Sommerdijk, J.J. De Yoreo, *Calcium carbonate nucleation driven by ion binding in a biomimetic matrix revealed by in situ electron microscopy*, *Nat Mater*, 2015, **14**, 394–399;
- [17] W. V. Boynton, D. W. Ming, S. P. Kounaves, et al., *Evidence for Calcium Carbonate at the Mars Phoenix Landing Site*, *Science*, 2009, **325** (5936), 61–64.;
- [18] B. C. Clark, R. E. Arvidson, R. Gellert, ; et al., *Evidence for montmorillonite or its compositional equivalent in Columbia Hills, Mars*, *Journal of Geophysical Research*, 2007, **112** (E6): E06S01;
- [19] P. Smeets, A. Finney, W. Habraken, F. Nudelman, H. Friedrich, J. Laven, J. De Yoreo, P. Rodger, N. Sommerdijk, *A classical view on non classical nucleation*, *Proceedings of the National Academy of Sciences of the United States of America*, 2017, **114** (38), E7882-E7890;
- [20] J.J. De Yoreo, et al., *CRYSTAL GROWTH. Crystallization by particle attachment in synthetic, biogenic, and geologic environments*, *Science*, 2015, **349**, 6760;
- [21] H.A. Lowenstam, S. Weiner, *On Biomineralization*, Oxford Univ Press, 1989, Oxford;

- [22] J.P. Grotzinger, N.P. James, *Carbonate Sedimentation and Diagenesis in the Evolving Precambrian World*(SEPM, Tulsa, OK), 2000, 75– 90;
- [23] D. R. Lide, CRC Handbook of Chemistry and Physics (86th ed.), Boca Raton (FL): CRC Press, 2005;
- [24] D. Hills, *Selected Solubility Products and Formation Constants at 25 °C*, California State University;
- [25] X. Wang, W. Conway, R. Burns, N. McCann, M. Maeder, *Comprehensive Study of the Hydration and Dehydration Reactions of Carbon Dioxide in Aqueous Solution*, The Journal of Physical Chemistry A., 2010, **114** (4), 1734–40;
- [26] W. Mook, *Chemistry of carbonic acid in water, Environmental Isotopes in the Hydrological Cycle: Principles and Applications*, Paris: INEA/UNESCO, 2000, 143–165;
- [27] J.A. Wojtowicz, *Factors affecting precipitation of calcium carbonate*, Journal of the Swimming Pool and Spa Industry, 1998, **3** (1), 18–23;
- [28] J.A. Wojtowicz, *Corrections, potential errors, and significance of the saturation index*, Journal of the Swimming Pool and Spa Industry, 1998, **3** (1), 37–40;
- [29] N. K. Dhami, M. S. Reddy, A. Mukherjee, *Biom mineralization of calcium carbonates and their engineered applications: a review*, 2013, **4**, 314;
- [30] S. Karthika, T. K. Radhakrishnan, P. Kalaichelvi, *A Review of Classical and Nonclassical Nucleation Theories*, Cryst. Growth Des, 2016, **16**, 6663–6681;
- [31] X. Ma, S. Zhang, F. Jiao, C.J. Newcomb, Y.L. Zhang, A. Prakash, Z.H. Liao, M.D. Baer, C.J. Mundy, J. Pfaendtner, A. Noy, C.L. Chen, J.J. De Yoreo, *Tuning crystallization pathways through sequence engineering of biomimetic polymers*, Nat. Mater., 2017, **16**, 767–774;
- [32] H. Konno, T. Watanabe-Nakayama, T. Uchihashi, M. Okuda, L.W. Zhu, N. Kodera, Y. Kikuchi, T. Ando, H. Taguchi, *Dynamics of oligomer and amyloid fibril formation by yeast prion Sup35 observed by high-speed atomic force microscopy*, Proc. Natl. Acad. Sci. U. S. A, 2020, **117**, 7831–7836;
- [33] S. Weiner, L. Addadi, *Crystallization pathways in biomineralization*, Annu. Rev. Mater. Res., 2011, **41**, 21–40;
- [34] J. C. Burleya, M. J. Duera, R. S. Steina, R. M. Vrcelj, *Enforcing Ostwald's rule of stages: Isolation of paracetamol forms III and II*, European journal of pharmaceutical science, 2007, **31**, 271-276;
- [35] J. J. De Yoreo, E. Nakouzi, B. Jaehun, C. J. Mundy, *Spiers Memorial Lecture: Assembly-based pathways of crystallization*, Faraday Discuss., 2022, **235**, 9-35;
- [36] L. Houben, H. Weissman, S.G. Wolf, B. Rybtchinski, *A mechanism of ferritin crystallization revealed by cryo-STEM tomography*, Nature, 2020, **579**, 540–543;
- [37] J.H. Zhou, Y.S. Yang, Y. Yang, D.S. Kim, A. Yuan, X.Z. Tian, C. Ophus, F. Sun, A.K. Schmid, M. Nathanson, H. Heinz, Q. An, H. Zeng, P. Ercius, J.W. Miao, *Observing crystal nucleation in four dimensions using atomic electron tomography*, Nature, 2019, **570**, 500–503;
- [38] Z.M. Liu, Z.S. Zhang, Z.M. Wang, B. Jin, D.S. Li, J.H. Tao, R.K. Tang, J.J. De Yoreo, *Shape-preserving amorphous-to-crystalline transformation of CaCO₃ revealed by in situ TEM*, Proc. Natl. Acad. Sci. U. S. A., 2020, **117**, 3397–3404;
- [39] J.D. Rimer, M. Tsapatsis, *Nucleation of open framework materials: Navigating the voids*, MRS Bull, 2016, **41**, 393–398;

- [40] J.D. Rimer, D.G. Vlachos, R.F. Lobo, *Evolution of self-assembled silicatetrapropylammonium nanoparticles at elevated temperatures*, J. Phys. Chem. B, 2005, **109**, 12762–12771;
- [41] P.E.A. de Moor, T.P.M. Beelen, R.A. van Santen, *In situ observation of nucleation and crystal growth in zeolite synthesis. A small-angle X-ray scattering investigation on Si-TPA-MFI*, J. Phys. Chem. B, 1999, **103**, 1639–1650;
- [42] M. Maldonado, M.D. Oleksiak, S. Chinta, J.D. Rimer, *Controlling crystal polymorphism in organic-free synthesis of Na-zeolites*, J. Am. Chem. Soc., 2013, **135**, 2641–2652;
- [43] M. Kellermeier, R. Rosenberg, A. Moise, U. Anders, M. Przybylski, H. Colfen, *Amino acids form prenucleation clusters: ESI-MS as a fast detection method in comparison to analytical ultracentrifugation*, Faraday Discuss., 2012, **159**, 23–45;
- [44] J. Scheck, M. Drechsler, X. Ma, M.T. Stockl, J. Konsek, J.B. Schwaderer, S.M. Stadler, J.J. De Yoreo, D. Gebauer, *Polyaspartic acid facilitates oxolation within iron(III) oxide prenucleation clusters and drives the formation of organic-inorganic composites*, J. Chem. Phys. 2016, **145**, 211917;
- [45] A. Dey, P.H.H. Bomans, F.A. Mueller, J. Will, P.M. Frederik, G. deWith, N.A.J.M. Sommerdijk, *The role of prenucleation clusters in surface-induced calcium phosphate crystallization*, Nat. Mater., 2010, **9**, 1010–1014;
- [46] D. Gebauer, M. Kellermeier, J.D. Gale, L. Bergstrom, H. Colfen, *Pre-nucleation clusters as solute precursors in crystallisation*, Chem. Soc. Rev., 2014, **43**, 2348–2371;
- [47] D. Gebauer, A. Volkel, H. Colfen, *Stable prenucleation calcium carbonate clusters*, Science, 2008, **322**, 1819–1822.
- [48] <https://realworldcrystals.leeds.ac.uk/>

Chapter 2

Alkali metal nitrates

2.1 Introduction

The alkali metal nitrates are the subject of this study, and this chapter will provide information about each member of this family of compounds, highlighting their morphology, polymorphism, crystal structure and uses. Alkali metal nitrates have the generic formula XNO_3 ($X=Li, Na, K, Rb, Cs$). The nitrate group is a polyatomic anion with a single central nitrogen atom and three oxygens connected to the central atom with a trigonal planar structure. The three oxygen formally carry the charge equally, each with a value of $-2/3$, while the nitrogen carries a formal charge of $+1$. This results in a total formal charge of -1 . Three resonance structures are formally used to describe the nitrate anion, shown in *Figure 2.1*. Being the conjugate base of a strong acid (nitric acid, HNO_3) the nitrate group tends to create salts that are mildly acidic in solution.

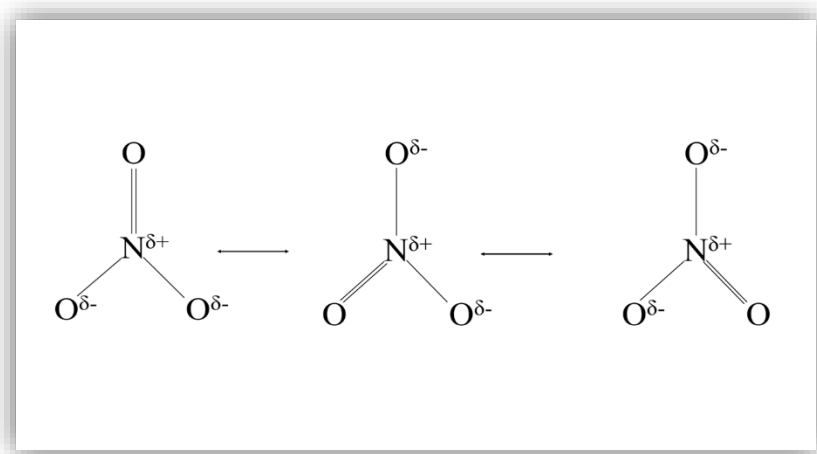


Figure 2.1. Resonance structures of the nitrate anion.

Alkali metal nitrates are commonly used as fertiliser and food preservatives. Nitrates are often added to food with the purpose of generating *in-situ* nitrites (NO_2^-) which is the active preservative ingredient. They are usually added in the form of sodium and potassium salts, labelled as E251 and E252 respectively. They prevent the growth of *Clostridium botulinum* and other bacteria, and

are also used to maintain the natural colour of meat and avoid the development of unpleasant odours and flavours^[2]. As fertiliser, nitrates are commonly used because of their high solubility and biodegradability. The most common forms are ammonium, sodium, potassium, and calcium nitrate. Another use is as heat transfer fluids in concentrated solar power plants^[3].

2.2 Lithium nitrate

Lithium nitrate is the lithium salt of nitric acid and the first of the family of alkali nitrates. It is commercially used as oxidising agent in the manufacture of red-coloured fireworks and flares^[6].

2.2.1 Crystal structure, polymorphism and phase transitions

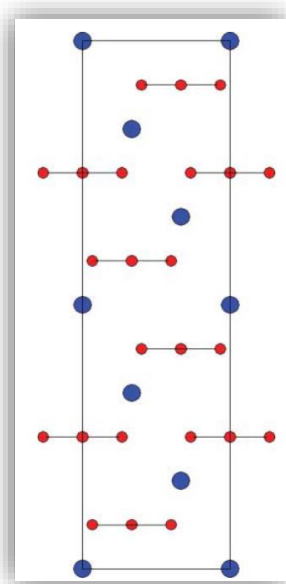


Figure 2.2. LiNO_3 (along the $\langle 010 \rangle$ direction)^[1]. Reproduced with the publisher's permission.

At 298 K, LiNO_3 crystallises in the rhombohedral $R\bar{3}c$ group^[1] with $Z=6$, $a=4.692$. According to Wu *et al*^[7] lithium nitrate is isostructural with calcite and nitratine (NaNO_3). Being isostructural with calcite^[8] and nitratine^[9], lithium nitrate is expected to have a Bravais-Friedel-Donnay-Harker (BFDH) morphology with $\{012\}$, $\{01\bar{2}\}$ and $\{001\}$ forms, shown in *Figure 2.3*.

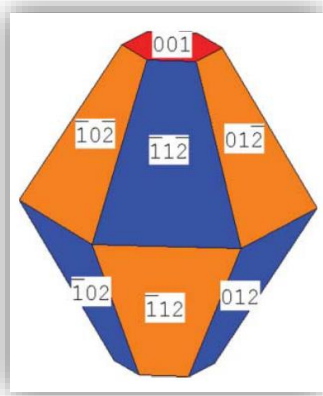


Figure 2.3. BFDH theoretical crystal growth morphology of LiNO_3 (calculated)^[1]. Reproduced with the publisher's permission.

2.3 Sodium nitrate

Sodium nitrate is a white solid with high solubility in water. It has been used in industrial applications as a readily available source of NO_3^- .

2.3.1 Crystal structure, polymorphism, and phase transitions

Sodium nitrate crystallises in the rhombohedral (calcite type $R\bar{3}c$ group^[10]) at 298 K with $Z=6$, $a=5.0396 \text{ \AA}$ and $c=16.829 \text{ \AA}$ and transforms into a high-temperature disordered phase ($R\bar{3}m$) around 548.5 K. This polymorph has $Z=3$, $a=5.0889 \text{ \AA}$ and $c=8.868 \text{ \AA}$. The nitrate group appears to be static in the low temperature phase (II- NaNO_3) and becomes rotationally disordered in the high temperature phase (I- NaNO_3)^[11]. Phase transitions in sodium nitrate have been extensively studied because of its analogy with calcite. Despite much effort, it has not been possible to correlate the transitions with currently existing standard models^[12]. However, both carbonate and nitrate groups show orientationally disordered high temperature phases. Starting from a pure solution it is possible to grow single $\{10.4\}$ rhombohedral crystals^[13] whilst adding Li^+ and K^+ ions allow to grow $\{00.1\}$ crystals.^[14]

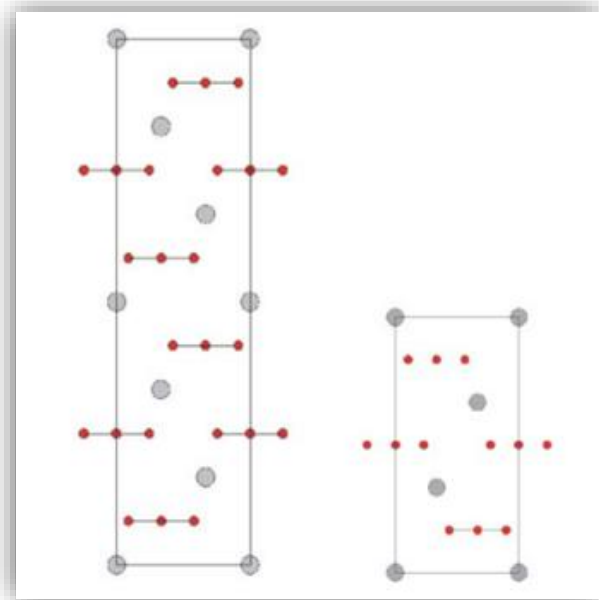


Figure 2.4. Left: II- NaNO_3 crystal structure^[15]. Right: I- NaNO_3 crystal structure^[15]. Both viewed along the $\{010\}$ direction. Grey spheres represent sodium atoms, red spheres oxygens from the nitrate group. Reproduced with the publisher's permission.

Figure 2.4 shows a projection of the crystal structures for phase I and II along the $\{010\}$ direction. Phase II of sodium nitrate ($R\bar{3}c$ group) is stable between 100 and 550 K. It is made up of layers of sodium ions and nitrate groups, rotated by 60° around the triad axis. In this conformation sodium has an octahedral coordination with respect to the oxygens. Phase II converts into phase I ($R\bar{3}m$ group) at temperature above 550 K and below the melting point (581 K). Each cell contains three formula units, and can be distinguished from the more stable phase II as the nitrate ions show rotational disorder. The existence of these two polymorphs has been confirmed by different studies^[16]. Teo *et al*^[17] identified a new phase above 14 Kbar that, because of a slight volume shift during the phase transition, would mimic the II- NaNO_3 phase. Some authors^[71] propose expanding the second-order (order-disorder) transition that separates the low- and high-temperature forms of NaNO_3 by about 100 K. According to many authors^[18], the cell loses the c glide plane and all nitrate planes become equivalent. This occurs as a result of the NO_3 anion becoming rotationally disordered. Fermor and Kjekshus^[19], who conducted an extensive study on the electric properties of NaNO_3 , asserted that the apparent energy gap shifts at 433 K, which causes the second order transition to begin. The activation of the nitrate group's rotation around its trigonal axis is suggested as the reason of this order-disorder transition by all the data collected by Rao *et al*^[20]. Spectroscopic studies, however, seem to suggest that NO_3 is not capable of free rotation above the

transition temperature. This could be due to a lack of the methodology in the detection of said process. Since sodium nitrate is a chemical that can be manufactured in a high purity condition and has a lengthy transition, it has been considered to be an especially appropriate system for testing various hypotheses and relations presented for higher order transitions.^[21] Harris^[22] summarises the two potential models for this second-order transition as the "free rotation" model first put forth by Kracek^[23] and the "two-position disorder" model first put forth by Ketalaar and Strijk.^[24]

2.3.2 Crystal growth

A few authors have looked into how NaNO_3 crystals are formed. The first investigation to measure crystal formation as a function of temperature (273-323 K) at a continuous supercooling of $T_{\text{equilibrium}} = 0.3$ K was carried out by Sipyagin and Chernov^[32].

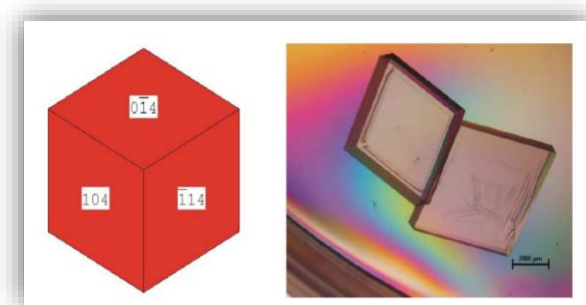


Figure 2.5. Theoretical and experimental crystal growth morphology of NaNO_3 ^[41]. Reproduced with the publisher's permission.

Figure 2.5 shows the theoretical and experimental morphology of sodium nitrate, with the lowest surface in energy being the {104}.

Kirkova and Nikolaeva^[33] examined the growth rate of nitratine faces as a function of flow rate at various supersaturations.^[32] These observations suffered from two flaws: first, both examples' rising face indexes were unclear, and second, the sources do not assess the isothermal growth rate required to identify the NaNO_3 crystal development process. Treivus^[34] drew attention to the fact that under a free convection regime, the expansion of the NaNO_3 solution occurs in accordance with the dislocation process. It is important to draw attention to the work of Benages-Vilau *et al*^[35], who constructed an instrument to study the development of isothermal NaNO_3 crystals. The authors operated at very low supersaturation levels of 0.005, and the growth rate on the {104} form was continuously lower than $R_{\{104\}} < 2.5 \mu\text{m}\cdot\text{min}^{-1}$. This prevented unwanted nucleation.

Even though the growth rate results were of a similar order of magnitude to those of Ristic *et al*^[36], separate calculated supersaturations demonstrated that a crossover was still true^[1]. The authors' final conclusion was that the growing process is influenced by the relative placement of a (corresponding) face in reference to the flow direction. Additionally, the same authors demonstrate in a previous work^[37] how the addition of LiNO₃ or KNO₃ impurities affects the growth rate.

2.3.3 Crystal morphology

According to an early investigation by Benages *et al*^[38], single {10.4} rhombohedral crystals are consistently formed in pure solutions, whereas rhombohedra, or truncated {001} were produced in solutions including K⁺ and Li⁺ ions. According to Punin and Fanke^[39], the inclusion of certain impurities, such as KH₂PO₄, KHSO₄, KF, LiCl, and KIO₈, causes the growth of curved {00.1} pinacoid faces on NaNO₃ crystals. A straightforward cleavage rhombohedron is used to construct the athermal equilibrium morphology (at 0 K) while accounting for the surface energy estimated at the density functional theory (DFT) level^[39].

2.4 Potassium nitrate

2.4.1 Crystal structure, polymorphism and phase transition

Potassium nitrate has been studied and extensively used in industry as a source of nitrogen^[40] and it is also a major constituents of gunpowder^[41]. KNO₃ exists in three different polymorphic forms at atmospheric pressure^[42]:

- Phase II, α -KNO₃ orthorhombic *Pm $\bar{c}n$* aragonite type, stable at 299 K;
- Phase III γ -KNO₃, rhombohedral, *R3m*, ferroelectric, stable at 397 K, with $a=5.43$ Å and $c=9.112$ Å;
- Phase I, β -KNO₃ rhombohedral *R $\bar{3}c$* , calcite type, stable at 403 K with $a=5.42$ Å and $c=19.41$ Å;

α -KNO₃ has the stacking sequence *ABCABC*... In this sequence A corresponds to the K⁺ ions layer, while *B* and *C* to the NO₃⁻ layers. The sum of the ions in the B and C layer equals the number of the A layer to guarantee the electrical neutrality of the system.

β -KNO₃, presents a stacking similar to I-NaNO₃.^[41] This phase is characterised by the nitrate group not being planar, but twisted on the same flat plane, therefore a vibrational disorder seems to be more plausible^[42].

γ -KNO₃ phase presents a stacking that is similar to the β -KNO₃ phase, but the spacing between the layers appears to be different.

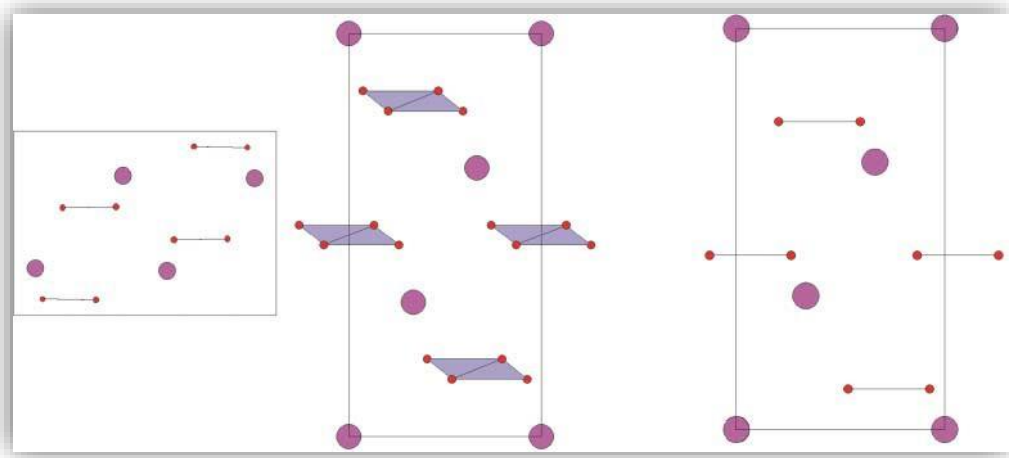


Figure 2.6. Left: α -KNO₃, Middle: β -KNO₃, Right: γ -KNO₃ crystal structures.^[1] All structures are viewed along $\langle 010 \rangle$ direction. Reproduced with the publisher's permission.

Further studies by Nimmo and Lucas^[41,42] confirmed the lattice parameter previously obtained by Rao, with the exception of the c parameter in β -KNO₃, where their value is half of the original one. Not all authors agree about the possibility of obtaining γ -KNO₃ at room temperature and pressure^[43]. A mixture of α -KNO₃ and γ -KNO₃ phases^[45] have also been produced for concentrations higher than 5.52 molar. Because the high temperature form has been shown to have a NO₃⁻ rotational disorder, the α -KNO₃ \rightarrow β -KNO₃ transition may also be considered as an order-disorder transition. This transition appears to be first order, as references suggest a single temperature transition. Some authors^[47] argued that, while functioning in the 400-397 K temperature range, it is reversible. They made a connection between this result and anomalies in the dielectric and lattice constants of KNO₃. Nagase *et al*^[48] further discovered that heating during the transition from α -KNO₃ \rightarrow β -KNO₃ altered the Brillouin shift, line width, and mode number. It appeared as though the authors had found an "intermediate phase" as a consequence. Additionally, Cornelison *et al*^[49] showed that KNO₃ displays significant reflection losses when the temperature approaches the order-disorder transition point of 401 K. Simulations of the phase

transition have also been conducted by Swaminathan and Srinivasan ^[50] concluding that the three polymorphic transitions can be described as martensitic-like and twinning of the parent phase and the transition starting by the rotation of the nitrate ions about their triad axes. Aidynol *et al* ^[51] performed *ab-initio* simulations where they made a comparison between the structures and calcite. The paraelectric to ferroelectric transition (β -KNO₃ \rightarrow γ -KNO₃) was interpreted by Rao *et al* ^[20] as being caused by the electrostriction effect. The α -KNO₃ \rightarrow β -KNO₃ transition is abrupt, as determined by Raman scattering^[52].

2.4.2 Crystal growth

At a growth temperature between 296 and 298 K, Chernov and Sipyagin calculated the growth rates of the {111} and {110} faces of KNO₃ ^[53]. In a ternary KNO₃-NaNO₃-H₂O environment, the authors found a decrease in the growth rate for the same faces^[54]. The biggest difference between the growth rates reported by these authors and those of previous research ^[55,56] is nearly two orders of magnitude. This disagreement is mostly caused by the different experimental setups, but it is also related to the crystal quality. The literature suggest a disagreement with some authors preferring a random fluctuation model^[57] and others proposing a constant crystal growth model ^[58], in some cases indicated as linear ^[59]; whereas other authors ^[60] propose a diffusion controlled growth, for specific industrial set-ups.

2.4.3 Crystal morphology

Van der Voort investigated the morphology of KNO₃ crystals both theoretically ^[61] and experimentally ^[62]. In experiments, the author found that, while maintaining the same sub-cooling of $T_{equilibrium} - T_{growth} = 0.15$ K, the growth habit varies as the crystallisation temperature is raised. Below 305 K^[63] potassium nitrates mostly shows the {110}, {111}, {010} and {021} surfaces. They pointed out that there was good agreement between the estimated and experimental morphologies of KNO₃.

The {001} cut has the lowest surface energy, according to Lovik *et al*'s ^[64] *ab-initio* DFT estimate of the surface stability of numerous KNO₃ faces. Simple parallelepipeds made by {100}, {010}, and {001} are obtained when drawing the shape with unrelaxed surface energy values.

2.5 Rubidium nitrate

Rubidium nitrate is utilised in industry as a colourant and oxidizer in pyrotechnics^[65]. It is also utilised as a raw material in the production of various rubidium compounds and rubidium metal, as well as in the production of catalysts and scintillation counters.

2.5.1 Crystal structure, polymorphism and phase transition

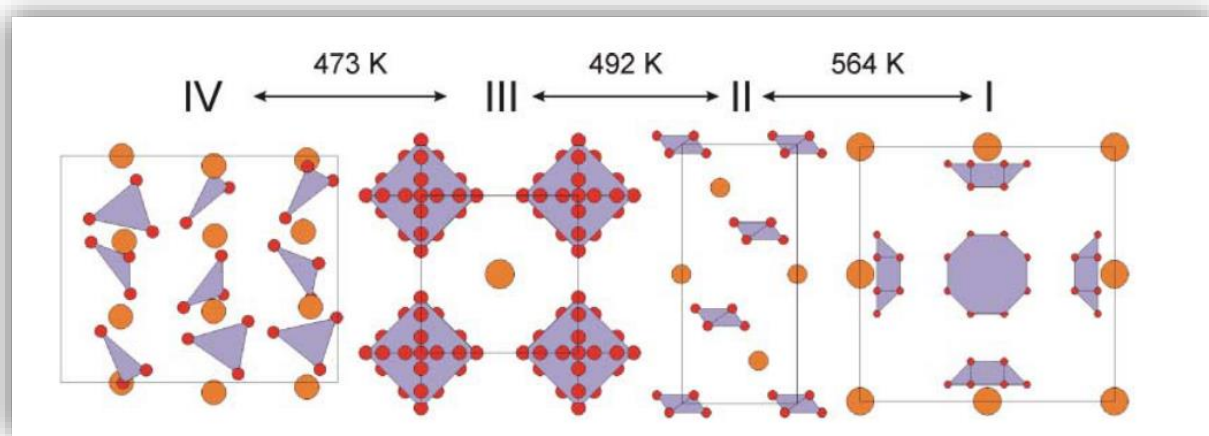


Figure 2.7 Phases of RbNO₃ and their transition temperatures (Rao et al.) III-RbNO₃, II-RbNO₃, and I-RbNO₃ (Pohl et al) and IV-RbNO₃ (Ahtee et al). The scale of unit cells is not the same. All structures are viewed from the 010> side^[1]. Reproduced with the publisher's permission.

Rubidium nitrate presents four different phases:

- Phase IV, trigonal $P3_1m$, stable at 298 K, with $Z=9$, $a=10.479$ Å and $c=7.452$ Å, isostructural with II-CsNO₃^[66];
- Phase III, cubic (CsCl type), $Pm\bar{3}m$, stable between 437 and 492 K, with $Z=1$, $a=4.39$ Å^[67];
- Phase II, rhombohedral, $R\bar{3}m$, stable around 520 K, with $Z=1$, $a=4.8$ Å and $\gamma=70^\circ20'$ (angle between a and b) despite belonging to the $R\bar{3}m$ group^[68, 69];
- Phase I, cubic (NaCl type), $Fm\bar{3}m$, stable between 557 and 583 K, with $Z=4$ ^[70] and $a=7.32$ Å

Rao *et al* ^[20] reported on phase transitions and found that crystals heated from phase IV-RbNO₃ to phase III-RbNO₃ become isotropic. However, crystals shatter and revert to being anisotropic when heated from phase III-RbNO₃ to phase II-RbNO₃. Rb⁺ positional randomisation appears to change throughout the transition between the IV-RbNO₃, III-RbNO₃, and II-RbNO₃ phases, which can be derived from XRD analyses. According to Ahtee and Hewat ^[71], however, these transformations can be attributed to the rotational disorder of the nitrate group; this does not work in the case of the II-RbNO₃ → I-RbNO₃, as the randomisation is not present, with the free rotation disorder being excluded as a cause for all the phases. According to Shamsuzzoha and Lucas ^[72] the transition can be defined by a switch from pseudo-cubic to cubic of sublattices of the Rb. This suggests the existence of an order-disorder shift of the nitrate group, backed up by the simulation work performed by Liu *et al* ^[73], which also exclude any possibility of free rotation for the NO₃⁻ group. In contrast, Yamamoto *et al* ^[16], suggested that because both structures have an eight-fold orientational disorder.

2.5.2 Crystal growth

Chernov and Sipyagin ^[53] studied the evolution of the {124} and {114} faces of RbNO₃ and provide kinetic coefficients, exchange fluxes, and other information. The only other information available in literature ^[74] on the kinetics report a linear relationship between the growth rate (V) and the excess of mass in the temperature range of 301.2 - 297.6 K for the forms {110} and {100}: $V = (8.76 \pm 0.75) \cdot 10^{-7} \Delta m$, where Δm is the excess of mass expressed in mol·kg⁻¹ H₂O. At this time, it is important to emphasise that the growth mechanism cannot be studied using this methodology to calculating growth rate.

2.5.3 Crystal morphology

The only information available regarding rubidium nitrate's morphology comes from the experiments of Franke *et al* ^[54] where a pseudo-hexagonal habit is described. This is in good agreement with the BFDH calculated growth morphology of *Figure 2.8*.

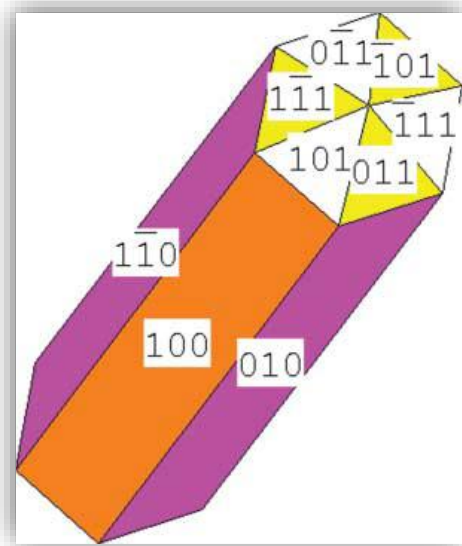


Figure 2.8 BFDH growth morphology of RbNO_3 calculated by Benages^[1]. Reproduced with the publisher's permission.

2.6 Caesium nitrate

Caesium nitrate is used in industry mainly in pyrotechnic compositions, as a colorant and an oxidiser, e.g., in decoys and illumination flares^[70]. Prisms are used in infrared spectroscopy, in X-ray phosphors, and in scintillation counters.

2.6.1 Crystal structure, polymorphism and phase transition

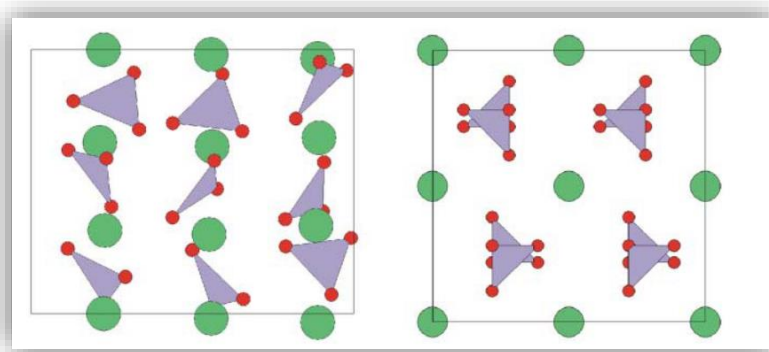


Figure 2.9. CsNO_3 unit cell. Left: phase II and right phase I. All viewed along the $\langle 100 \rangle$ direction.^[1]. Reproduced with the publisher's permission.

It shows two different phases:

- Phase II, pyroelectric, trigonal $P3_1m$, stable at 296 K, with $Z=9$, $a=10.87 \text{ \AA}$, and $c=7.76 \text{ \AA}$, isostructural with IV-RbNO₃^[75]
- Phase I cubic has been described as $Pm\bar{3}m$, around 400 K, with $Z=1$, and $a=8.96 \text{ \AA}$, but also as, $Pa\bar{3}$ with $Z=8$ and $a=8.98 \text{ \AA}$ ^[76]

At about 434 K, the II-CsNO₃ phase converts into the I-CsNO₃ phase. Charrier *et al*^[77] measured the equilibrium temperature for the transition, which was found to be $427 \pm 10 \text{ K}$ together with the transition enthalpy. Near the phase transition, these authors^[78] discovered an abnormality in the dielectric constant. Kawashima *et al*^[79] and Kawashima^[80], who discovered a discontinuity in the phase transition, made similar conductivity measurements from room temperature to the melt. Additionally, Tagaki *et al*^[81] determined that II-CsNO₃ is a true ferroelectric phase after studying the phase transition using Brillouin scattering. Research on the high pressure polymorphism of CsNO₃ was conducted by Dean *et al*^[82] and references therein. The three CsNO₃ high pressure polymorphs discovered by Kalliomäki and Meisalo^[83] are highlighted here. These are the III, IV, and V-CsNO₃ phases; while having differing axial ratios, all three phases displayed the same Pmmn space group.

2.6.2 Crystal growth

Chernov and Sipyagin about the evolution of the {124} and {114} faces of CsNO₃^[53]. Treivus and Franke^[74] found a linear relationship between the growth rate (V) and the excess mass (m) in the temperature range of 299.3-297 K for the forms {110} and {100}: $V=(18 \pm 2\text{K}) \cdot 10^{-7} \Delta m$, where Δm is the excess mass expressed in $\text{mol} \cdot \text{kg}^{-1} \text{ H}_2\text{O}$.

2.6.3 Crystal morphology

Pohl^[84] describes the crystal as hexagonal shaped c-axis needles. The BFDH morphology calculated by Benages *et al*^[1] is the same as RbNO₃, as the two compounds are isostructural.

2.7 References

- [1] R. Benages-Vilau, T. Calvet, M.À. Cuevas-Diarte, *Polymorphism, crystal growth, crystal morphology and solid-state miscibility of alkali nitrates*, Crystallography Reviews, 2014, **20**:1, 25-55;
- [2] https://www.fsai.ie/faq/use_and_removal_of_nitrite.html
- [3] S. Bajpai, N. Alam, P. Biswas, *Chapter 4 - Present and Potential Water-Quality Challenges in India*, Separation Science and Technology, 2019, **11**, 85-112;
- [4] R.W. Bradshaw, D.A. Brosseau, *Low-melting point inorganic nitrate salt heat transfer fluid*, US 78,588,694 B1. 2009 Sep 15;
- [5] P.J. Shamberger, T. Reid, *Thermophysical Properties of Lithium Nitrate Trihydrate from (253 to 353) K*, Journal of Chemical & Engineering Data, 2012, **57** (5),1404–11;
- [6] M. Kenisarin, K. Mahkamov, *Salt hydrates as latent heat storage materials: Thermophysical properties and costs*. Solar Energy Materials and Solar Cells, 2016, **145** (3), 255–86;
- [7] X. Wu, F. Fronczek, L. Butler, *Structure of LiNO₃– point-charge model and sign of the Li–7 quadrupole coupling-constant*, Inorg Chem., 1994, **33**, 1363–1365;
- [8] D. Aquilano, R. Benages-Vilau, M. Bruno, M. Rubbo, F.R. Massaro, *Positive and negative form of calcite crystal (CaCO₃) in the light of Bravais-Friedel-Donnay-Harker and Hartman-Perdok*, Approach. Cryst Eng Comm., 2013, **15**, 4465–4472;
- [9] R. Benages-Vilau, T. Calvet, L. Pastero, D. Aquilano, M.À. Cuevas-Diarte, *Morphology Change of Nitratine (NaNO₃) from Aqueous Solution, in the Presence of Li⁺ and K⁺ Ions*, Crystal Growth & Design, 2015, **15** (11), 5338-5344;
- [10] C.N.R. Rao, B. Prakash, M. Natarajan, *Crystal structure transformations in inorganic nitrites, nitrates, and carbonates*, Washington: National Standard Reference Data System-National Bureau of Standards; 1975;
- [11] G. Gonschorek, H. Weitzel, G. Mieke, W. Schmahl, *The crystal structure of NaNO₃ at 100 K, 120 K, and 563 K*, Z Krist., 2000, **215**, 752–756;
- [12] M.J. Harris, *A new explanation for the unusual critical behaviour of calcite and sodium nitrate, NaNO₃*, Am Min., 1999, **84**, 1632–1640;
- [13] C.W. Lan, M.C. Su, M.C. Liang, *A visualization and computational study of horizontal Bridgman crystal growth*, J Cryst Growth. 2000, **208**, 717–725;
- [14] R. Benages-Vilau, M. Rubbo, T. Calvet, D. Aquilano, M.À. Cuevas-Diarte, *Growth Kinetics of the {10.4} Faces of Nitratine (NaNO₃)*, Cryst. Growth Des. 2013, **13**, 8, 3419-3428;
- [15] A.C. McLaren, *Thermal Transformations in Nitrates of Univalent Ions*, Rev. P. App. Chem., 1962, **12**, 54-68;
- [16] S. Yamamoto, Y. Suematsu, Y. Shinnaka, *X-ray study of phase-transition in RbNO₃*, J Phys Soc Jpn., 1977, **43**, 1962–1967;
- [17] K.L. Teo, Z.X. Shen, M.H. Kuok, S.H. Tang, *High pressure phase transition study of NaNO₃ by Raman spectroscopy*, J Mol Struct., 1993, **294**, 163–166.

- [18] G. Gonschorek, H. Weitzel, G. Miehe, W. Schmahl, *The crystal structure of NaNO₃ at 100 K, 120 K, and 563 K*, Z Krist., 2000, **215**, 752–756;
- [19] J.H. Fermor, A. Kjekshus, *On the electrical properties of NaNO₃*, Acta Chem Scand., 1968, **22**, 1628–1636;
- [20] C.N.R. Rao, B. Prakash, M. Natarajan, *Crystal structure transformations in inorganic nitrites, nitrates, and carbonates*, Washington: National Standard Reference Data System-National Bureau of Standards, 1975;
- [21] N.G. Parsonage, L.A.K. Staveley, *Disorder in crystals*. Oxford: Clarendon Press; 1978.
- [22] M.J. Harris, *A new explanation for the unusual critical behaviour of calcite and sodium nitrate, NaNO₃*, Am Min., 1999, **84**, 1632–1640;
- [23] F.C. Kracek, *Gradual transition in crystalline sodium nitrate. II. The structure at various temperatures and its bearing on molecular rotation*, J Am Chem Soc., 1931, **53**, 3339–3348;
- [24] J.A.A. Ketelaar, B. Strijk, *The atomic arrangement in solid sodium nitrate at high temperatures*, Recueil des Travaux Chimiques des Pays-Bas, 1945, **64**, 174–182;
- [25] W.W. Schmahl, E. Salje, *X-ray diffraction study of the orientational order-disorder transition in NaNO₃ – evidence for order parameter coupling*, Phys Chem Min., 1989, **16**, 790–798;
- [26] S.J. Paynet, M.J. Harris, M.E. Hagen, M.T. Dove, *A neutron diffraction study of order-disorder phase transition in sodium nitrate*, J Phys Cond Mat., 1997, **9**, 2423–2432;
- [27] W.C.K. Poon, E. Salje, *The excess optical birefringence and phase transition in sodium nitrate*, J Phys C., 1988, **21**, 715–729;
- [28] R.J. Reeder, S.A.T. Redfern, E. Salje, *Spontaneous strain at the structural phase transition in NaNO₃*, Phys Chem Min., 1988, **15**, 605–611;
- [29] P. Ballirano, *Laboratory parallel-beam transmission X-ray powder diffraction investigation of the thermal behavior of nitratine NaNO₃: spontaneous strain and structure evolution*, Phys Chem Min., 2011, **38**, 531–541;
- [30] J. Liu, C. Duan, M. Ossowski, W.N. Mei, R.W. Smith, J.R. Hardy, *Simulation of structural phase transition in NaNO₃ and CaNO₃*, Phys Chem Min., 2001, **28**, 586–590;
- [31] R.M. Lyndell-Bell, M. Ferrario, I.R. McDonald, E. Salje, *A molecular dynamics study of orientational disordering in crystalline sodium nitrate*, J Phys Cond Mat., 1989, **1**, 6523–6542;
- [32] V.V. Sipyagin, A.A. Chernov, *Anomalies of temperature dependence of growth-rates of faces of crystals KNO₃, NaNO₂, NaNO₃, NaClO₄ and Rochelle salt from aqueous-solutions*, Kristallografiya, 1972, **17**, 1003–1009;
- [33] E. Kirkova, R. Nikolaeva, *Influence of the flow velocity, supersaturation and temperature on the crystal-growth from solutions*, Cryst Res Tech., 1983, **18**, 743–754;
- [34] E.B. Treivus, *The oscillations of crystal growth rates at their formation in the regime of free convection of a solution; statistical investigation*, Cryst Res Tech., 1997, **32**, 963–972;
- [35] R. Benages-Vilau, T. Calvet, M.A. Cuevas-Diarte, M. Rubbo, D. Aquilano, *Growth kinetics of the (10.4) faces of nitratine (NaNO₃)*, Cryst Growth Des., 2013, **13**, 3419–3428;
- [36] R.I. Ristic, B.Y. Shekunov, J.N. Sherwood, *The influence of synchrotron radiation-induced strain on the*

- growth and dissolution of brittle and ductile materials*, J Cryst Growth, 1997, **179**, 205–212;
- [37] R. Benages-Vilau, T. Calvet, M.A. Cuevas-Diarte, M. Rubbo, D. Aquilano, *Effect of impurities in the morphology and growth rate of NaNO₃*, in preparation.
- [38] C.W. Lan, M.C. Su, M.C. Liang, *A visualization and computational study of horizontal Bridgman crystal growth*, J Cryst Growth, 2000, **208**, 717–725;
- [39] Y.O. Punin, V.D. Franke, *Curved-face growth of NaNO₃ crystals*, Cryst Rep. 2001, **49**, 256–260;
- [40] G. Adiwidjaja, D. Pohl, *Superstructure of α -phase of potassium nitrate*, Acta Cryst. 2003, C59:i139– i140;
- [41] J.K. Nimmo, B.W. Lucas, *A neutron diffraction determination of the crystal structure of α -phase potassium nitrate at 25°C and 100°C*, J Phys C., 1973, **6**, 201–211;
- [42] J.K. Nimmo, B.W. Lucas, *The crystal structures of γ - and β -KNO₃ and the α - γ - β phase transformations*, Acta Cryst., 1976, **B-32**, 1968–1971;
- [43] E.J. Freney, L.A.J. Garvie, T.L. Groy, P.R. Buseck, *Growth and single-crystal refinement of phase-III potassium nitrate, KNO₃*, Acta Cryst., 2009, **B-65**, 659–663;
- [44] C. Viedma, M. Prieto, J.M. Garcia Ruiz, J.L., Amosos, *Cristalización polimórfica del KNO₃ (nitro) a partir de soluciones*, I Congreso Español de Geología, 1984, **II**, 305–316;
- [45] J. Tuech, S. Combet, *Étude Thermodynamique des Solutions Aqueuses de Nitrate de Potassium jusq'au dela Saturation, III. Cas de Cristallisation en deux Étapes en Solution Sursaturée*, J. Chim Phys., 1977, **74**, 137–142;
- [46] R. Benages, T. Calvet, M.A. Cuevas-Diarte, H.A.J. Oonk, *The NaNO₃ – KNO₃ phase diagram*, in preparation.
- [47] Y.G. Asadov, V.I. Nasirov, G.A. Jarailova, *Morphology of crystal growth and polymorphic transformations in KNO₃, AgNO₃ and NH₄NO₃ single crystals*, J Cryst Growth, 1972, **15**, 45–50;
- [48] A. Nagase, Y. Takeuchi, Y. Takagi, *Brillouin scattering study on KNO₃ crystal: appearance of intermediate phase on heating*, Jpn J Appl Phys, 1996, **35**, 2903–2906;
- [49] S.G. Cornelison, A. Gauss, J. Krane, J.R. Hardy, *Centimeter-wave reflection in the nitrates and nitrites of sodium and potassium: experiment and theory*, J Appl Phys, 1997, **81**, 1451–1456;
- [50] S. Swaminathan, S. Srinivasan, *A probable crystallographic path for the thermal phase transition in single crystal of KNO₃*, Acta Cryst, 1975, **A31**, 628–634;
- [51] M.K. Aydinol, J.V. Mantese, S.P. Alpay, *A comparative ab-initio study of the ferroelectric behaviour in KNO₃ and CaCO₃*, J Phys. 2007, **19**, 496210 [23 p.];
- [52] R. Murugan, P.J. Huang, A. Ghule, H. Chang, *Studies on thermal hysteresis of KNO₃ by thermo-Raman spectroscopy*, Thermochem Acta, 2000, **346**, 83–90;
- [53] A.A. Chernov, V.V. Sipyagin, *Peculiarities in crystal growth from aqueous solutions connected with their structures*, In: Kaldis E, editor. Current topics in materials science, Vol. 5. Amsterdam: North-Holland; 1980, p. 279–334;
- [54] V.D. Franke, E.B. Treivus, V.K. Filippov, V.A. Antonova, *Crystallization of nitrates in the presence of HNO₃ and its relation to physical and chemical properties of the systems*, J Cryst Growth, 1981, **52**, 795–800;
- [55] A. Herden, R. Lacmann, *The crystallization of potassium nitrate. 2. Growth rate dispersion*, J Cryst

- Growth, 1997, **179**, 592–604;
- [56] J.E. Helt, M.A. Larson, *Effects of temperature on the crystallization of potassium nitrate by direct measurement of supersaturation*, AIChE, 1977, **23**, 822–830;
- [57] J. Rolfs, R. Lacmann, S. Kipp, *Crystallization of potassium nitrate (KNO₃) in aqueous solution. 1. Growth kinetics of the pure system*, J Cryst Growth, 1997, **171**, 174–182;
- [58] S. Wang, A. Mersmann, *Initial-size-dependent growth rate dispersion of attrition fragments and secondary nuclei*, Chem Eng Sci, 1992, **47**, 1365–1371;
- [59] P. Huang, D.C. Huang, N.P. Xu, J. Shi, *Quantitative identification of nucleation and crystal growth stages in batch crystallization from solution*, Chem J Chin Univ, 2004, **25**, 589–595;
- [60] T.A. Graber, M.E. Taboada, M.N. Alvarez, E.H. Schmidt, *Determination of mass transfer coefficients for crystal growth of nitrate salts*, Cryst Res Tech, 1999, **34**, 1269–1277;
- [61] E. van der Voort, *The theoretical growth form of potassium nitrate from an aqueous solution*, J Cryst Growth, 1991, **110**, 653–661,
- [62] E. van der Voort, *Observations on growth forms and habits of potassium nitrate as a function of temperature*, J Cryst Growth, 1990, **100**, 539–544;
- [63] L.Z. Soltzberg, O. Carneiro, G.S. Joseph, Z. Khan, T.M. Meretsky, M.M. NG, S.A. Ofek, *Prediction of early- and late-growth morphologies of ionic crystals*, Acta Cryst B. 1998, **54**, 384–390;
- [64] Lovik OM, Jensen TL, Moxnes JF, Swang O, Unneberg E. Surface stability of potassium nitrate (KNO₃) from density functional theory. Comp Mat Sci. 2010; **50**, 356–362.
- [65] W. Lenk, H. Prinz, A. Steinmetz, *Rubidium and Rubidium Compounds*, Ullmann's Encyclopedia of Industrial Chemistry, 2010 Wiley-VCH Verlag GmbH & Co. KGaA, Weinheim.;
- [66] M. Shamsuzzoha, B.W. Lucas, *Structure (neutron) of phase-IV rubidium nitrate at 298 K and 403 K*, Acta Cryst B., 1982, **38**, 2353–2357;
- [67] R.W. Bradshaw, D.A. Brosseau, *Low-melting point inorganic nitrate salt heat transfer fluid*. US 78,588,694 B1. 2009;
- [68] M. Ahtee, A.W. Hewat, *Structures of the high temperature phases of rubidium nitrate*, Phys State Solids., 1980, **58**, 525–531;
- [69] K. Stromme, *Crystal structures of high-temperature phases of rubidium nitrate, cesium nitrate, and thallium nitrate*, Acta Chem Scand. 1971;25:211–215;
- [70] S. Budavari, *The Merck Index: An Encyclopedia of Chemicals, Drugs, and Biologicals (13th ed.)*, Merck, 2001, p. 345;
- [71] G. Gonschorek, H. Weitzel, G. Mieke, G.W. Schmahl, *The crystal structure of NaNO₃ at 100 K, 120 K, and 563 K*, Z Krist, 2000, **215**, 752–756;
- [72] M. Shamsuzzoha, B.W. Lucas, *Polymorphs of rubidium nitrate and their crystallographic relationships*, Can J Chem, 1988, **66**, 819–823;
- [73] J.K. Nimmo, B.W. Lucas, *The crystal structures of γ - and β -KNO₃ and the α - γ - β phase transformations*, Acta Cryst., 1976, **B-32**, 1968–1971.

- [74] E.B. Treivus, V.D. Franke, *Crystallization kinetics of some anhydrous nitrates*, Kristallografiya, 1976, **21**, 1002–1005;
- [75] B.W. Lucas, *The structure (neutron) of phase-II cesium nitrate at 298 K*, $CsNO_3$, Acta Cryst C., 1983, **39**, 1591–1594;
- [76] C.N.R. Rao, B. Prakash, M. Natarajan, *Crystal structure transformations in inorganic nitrites, nitrates, and carbonates*, Washington: National Standard Reference Data System-National Bureau of Standards; 1975;
- [77] E. Charrier, E.L. Charsley, P.G. Laye, H.M. Markham, T.T. Griffiths, *Determination of the temperature and enthalpy of solid-solid phase transition of caesium nitrate by differential scanning calorimetry*, Thermochim Acta. 2006, **445**, 36–39;
- [78] A.S. Chary, S.N. Reddy, T. Chiranjivi, *Structural phase-transition in $CsNO_3$ – dielectric studies*, Solid State Ionics, 1993, **62**, 3–4;
- [79] R. Kawashima, K. Hirai, *Electrical-properties near the structural phase-transition of crystalline caesium nitrate*, Phil Mag B, 1988, **58**, 663–669;
- [80] R. Kawashima, *AC conductivities near the structural phase-transition point of caesium nitrate crystal*, J. Phys. Soc. Jpn., 1989, **58**, 3236–3242;
- [81] Y. Takagi, S. Kimura, Y. Takeuchi, *Structural phase transition of $CsNO_3$ crystal-spontaneous polarization*, Ferroelectrics, 2003, **284**, 303–309;
- [82] C. Dean, T.W. Hambley, M.R. Snow, *Structures of phase-IV rubidium nitrate, $RbNO_3$, and phase-II cesium nitrate, $CsNO_3$* , Acta Cryst. C, 1984, **40**, 1512–1515.
- [83] M.S. Kalliomäki, V.P.J. Meisalo, *Structure determination of the high pressure phases $RbNO_3$ V, $CsNO_3$ III, and $CsNO_3$ IV*, Acta Cryst., 1979, **B35**, 2829–2835;
- [84] D. Pohl, T. Gross, *Cesium nitrate (II) at 296 K*, Acta Cryst C., 1993, **49**, 316–318.

Chapter 3

Methodology

This chapter will cover the theoretical background of all the methods used in this work. Step number one was fitting a force-field able to describe equally well alkali metal nitrates both as ions in solution and as crystals. To do this a wide set of programs and levels of theory have been applied. Some of these have also been used further during this work. This chapter will start by giving a brief overview of essential concepts behind the general simulation methodology.

Energy minimisation has been widely performed, therefore we need to say a few words about concepts such as lattice energy, various types of minimisation algorithms, and in particular the ones that have been used in this work, these are the conjugate gradient method and the quasi Newton-Raphson method. A brief outline of constant pressure minimisation and the purpose of its use will also be given.

A major part of this chapter will be dedicated to the level of theory most extensively used in this work: molecular dynamics (MD). A section will cover concepts such as the calculation of the forces and time integration algorithms with details of the ones used in this work (Verlet Leap-Frog and Velocity Verlet). What parameters are important to set-up for the rest of the simulation, such as initial velocities, time-step, equilibration period, neighbour lists and Verlet lists will also be considered.

The major ensembles will be described (NVE, NVT, NpT) and rules that need to be accounted for whilst performing MD will be discussed.

Wherever possible, some parameters calculated to validate the force-field have also been tested against density functional theory (DFT) results. This chapter will also include a brief description of this level of theory, the program used and the parameters that have to be considered.

To conclude this chapter, a detailed outline of the free energy of hydration methods used in the force-field validation process will be presented, alongside with a literature review of the topic to explain the position of this work in comparison with previous work.

3.1 Development of force-fields

3.1.1 Potential Modelling

This work has made use of so-called ‘interatomic potentials’. The advantage of this choice is that there is no need to solve the entire electronic structure of the system; instead, it is possible to make use of parametrised equations, which are much simpler to solve. While lacking the accuracy intrinsic to *ab-initio* methods, potential models, allow the simulation of longer timescales and significantly bigger systems. In molecular modelling, we call the form of the equations and their parameters used to determine the potential interaction between atoms, molecules or particles, the force-field. Usually, the force-field can either simulate all the atoms present in the system, or treat a group of them as a single entity (e.g. organic moieties, where non-polar H- atoms are grouped with their parent carbon). The first case is called ‘all atom’, the second case ‘united atom’ and they are mainly used in coarse-grained simulations. In this work ‘all atom’ force-fields were used exclusively.

A relatively simple four-component description (see *Figure 3.1*) of intramolecular and intermolecular forces inside the system can be utilised to comprehend a range of commonly used molecular modelling force-fields. Chemical bonds are represented by functions, bonds and angles that move away from their equilibrium values are energetically penalised, and the force-field incorporates terms that simulate the interaction of the non-bonded constituents of the system.

The appealing feature of this representation is that different expressions, such as bond lengths, angles, bond rotations, or movements of atoms in relation to one another, may be linked to changes in certain internal coordinates. This simplifies the parametrisation procedure and makes it easier to comprehend the effect of the force-field parameter on the simulation performance. One such

force-field that can be helpful for simulating single molecules or collections of atoms and/or molecules is the following:

$$\begin{aligned}
 E(r^N) = & \sum_{\text{bonds}} \frac{k_i}{2} (l_i - l_{i,0})^2 + \sum_{\text{angles}} \frac{k_i}{2} (\theta_i - \theta_{i,0})^2 & (3.1) \\
 & + \sum_{\text{torsions}} \frac{E_n}{2} (1 + \cos(n\omega - \gamma)) \\
 & + \sum_{i=1}^N \sum_{j=i+1}^N \left(4\epsilon_{ij} \left[\left(\frac{\sigma_{ij}}{r_{ij}} \right)^{12} - \left(\frac{\sigma_{ij}}{r_{ij}} \right)^6 \right] + \frac{q_i q_j}{4\pi\epsilon_0 r_{ij}} \right)
 \end{aligned}$$

Where the first term accounts for the bond energy (*Figure 3.1 (a)*), the second for the angle bending (*Figure 3.1 (b)*), the third for the bond rotation (or torsion) (*Figure 3.1 (c)*) and the fourth for non-bonded interaction (both electrostatic and Van der Waals) (*Figure 3.1 (d), (e)*).

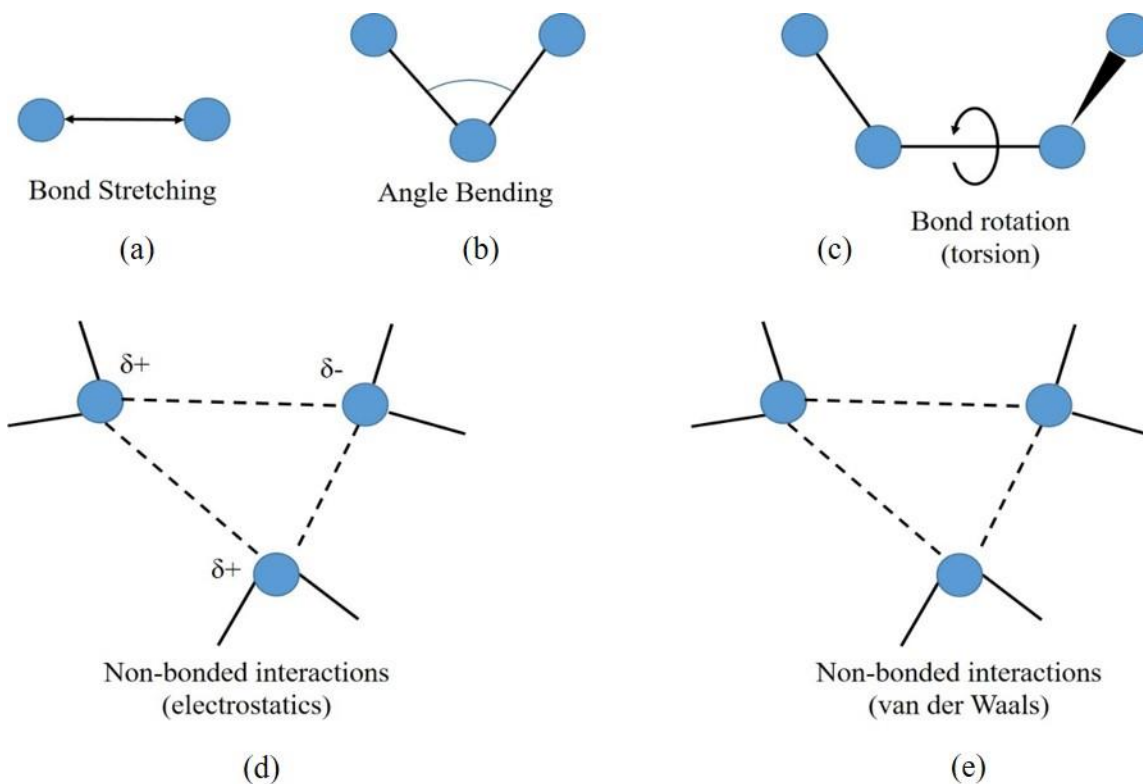


Figure 3.1 The four main components of a molecular mechanic force-field are represented schematically as bond stretching (a), angle bending (b), torsional terms (c), and non-bonded interactions (d) and (e)

The potential energy, or $E(r^N)$, is a function of the positions (\mathbf{r}) of the N particles. Figure 3.1 shows the various contributions schematically. The interaction between pairs of bonded atoms is modelled in the first term of Equation 3.1 by a harmonic potential, which results in an increase in energy as the bond length l_i deviates from the reference value $l_{i,0}$. The second term, which is also described using a harmonic potential, is a summation of all valence angles in the molecule (a valence angle is the angle formed between three atoms A-B-C in which A and C are both bonded to B). The third term in Equation 3.1, the torsional potential, simulates how the energy changes as a bond rotates. The non-bonded component is the fourth contribution. This is calculated for all atom pairs (i and j) that are in different compounds or that are in the same molecule but are separated by at least three bonds. In a straightforward force-field, the non-bonded component is often represented by a Lennard-Jones potential for van der Waals interactions and a Coulomb potential term for electrostatic interactions^[114].

3.1.2 Short-Range Non-bonded Interactions

An important parameter to discuss during the evaluation of energies and forces of a system is the short-range terms. The first one is considered the Pauli term, to account for electric clouds interacting at small atomic separations. Because two electrons cannot have the same quantum numbers, one has to be forced into a higher energetic state to solve this issue. This leads to an increased repulsion between species for short distances. The other contribution to be considered is the London dispersion. This term comes from the formation of a localised, instantaneous dipole, that leads to the formation of another dipole. It is usually attractive, but decays rapidly over distance. Usually the term for the cation-cation interaction is disregarded, whilst the anion-anion and anion-cation terms are considered^[4]. This is because anion-cation interactions are typically more prevalent and have a more significant impact on chemical behaviour than cation-cation interactions. Anion-cation interactions have a substantial impact on the behaviour and properties of chemical compounds. When cations and anions come together, they form ionic bonds due to electrostatic attraction. These ionic bonds are strong and stable, leading to the formation of

crystalline structures in many cases. The strength of these bonds can affect various chemical properties such as melting and boiling points, solubility, and conductivity.

Anion-cation interactions play a crucial role in determining the solubility of ionic compounds in solvents. For instance, in aqueous solutions, the interaction between water molecules (which are polar) and ions (cation-anion interactions) is vital for dissolving ionic compounds. This is why some salts dissolve readily in water while others do not.

A full set of potentials have been parametrised for the description of these interactions. They all differ in the way the attraction and repulsion curves are shaped. Depending on the system of interest, it is possible to decide which one works best. They all depend, however, on the parameters used to fit the potential equation. Those data usually come from either experiments, *ab-initio* simulations or both.

3.1.2.2 Lennard-Jones Potential

There are multiple short-range terms that can be used. We have specifically made use of the whole Lennard-Jones term^[5], especially whilst determining metal ion-metal ion interactions.

$$V_{LJ} = 4\varepsilon \left[\left(\frac{\sigma}{r} \right)^{12} - \left(\frac{\sigma}{r} \right)^6 \right] \quad (3.2)$$

Where ε is the depth of the potential well, σ is the radius of the rigid sphere that approximates the atomic size and r is the distance between the particles.

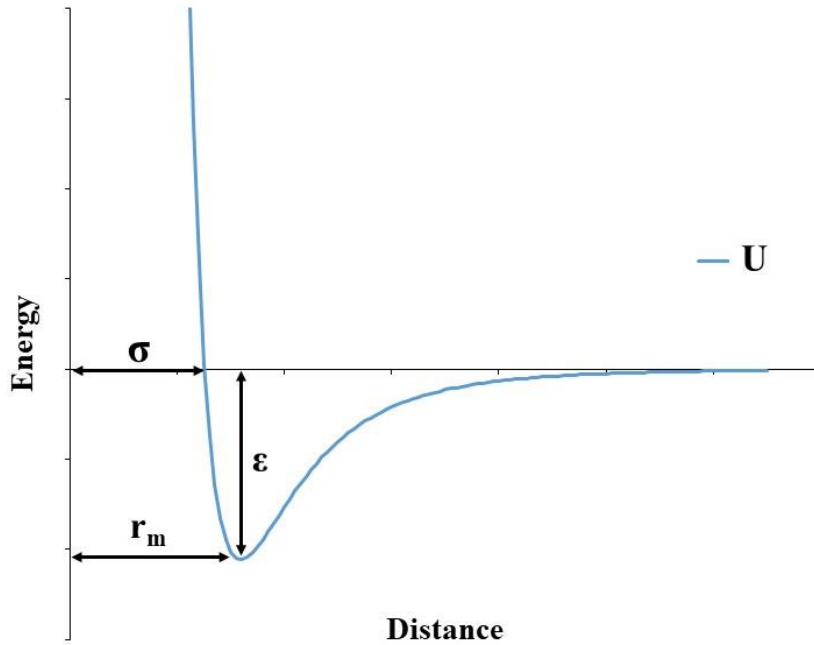


Figure 3.2(a) Lennard Jones potential and its parameters. ϵ represents the depth of the potential well, σ is the radius of the rigid sphere that approximates the atomic size and r_m is the distance between the particles.

For our implementation, we used the 12-6 representation of the potential:

$$V_{LJ}(r) = \frac{A}{r^{12}} - \frac{B}{r^6} \quad (3.3)$$

Where

$$A = 4\epsilon \cdot \sigma^{12} \quad (3.4) \quad B = 4\epsilon \cdot \sigma^6 \quad (3.5) \quad \sigma = \sqrt[6]{\frac{A}{B}} \quad (3.6) \quad \epsilon = \frac{B^2}{4A} \quad (3.4)$$

3.1.2.1 Buckingham Potential

This potential describes the repulsion term using an exponential type form, while the attraction is described in a similar fashion to the Lennard-Jones, r^{-6} .

$$E = A \cdot e^{\frac{-r}{\rho}} - \frac{C}{r^6} \quad (3.5)$$

In this expression A is expressed in units of eV, ρ in Å, C in eV·Å⁶

3.1.2.3 Many-bodies interactions

Additional potential terms are added to account for bonding-based interactions. These interactions can be visualised in Figure 3.1. For this force-field, a harmonic set of terms are used for direct bonds.

$$E = \frac{1}{2} K_2 \cdot (r - r_0)^2 \quad (3.6)$$

Where K_2 is expressed in eVÅ⁻², r and r_0 in Å.

To describe the interaction in the nitrate group a three-body potential has been used which describes the preferred angle between the bonds. It is defined as

$$E(\text{three}) = \frac{1}{2} k(\theta - \theta_0)^2 \quad (3.7)$$

Where k is the spring constant related to the stiffness of the angle and is expressed in eVrad⁻², θ is the current angle, θ_0 is the equilibrium angle, and both are expressed in rad.

Four this force-field in particular, to maintain the correct geometry of the nitrate group further torsional intermolecular interactions were added as well using a bond-bond cross term three body potential^[7], defined as

$$E(\text{three}) = K \cdot (r_{12}^0 - r_1) \cdot (r_{13}^0 - r_2) \quad (3.8)$$

In the expression, the units of K are eVÅ⁻², r_1 and r_2 in Å.

The bond-angle cross term three body potential^[7] has been inserted as well, in the form

$$E(three) = [K_1(r_{12}^0 - r_1) + K_2(r_{13}^0 - r_2)] \cdot (\theta - \theta_0) \quad (3.9)$$

Here K_1 and K_2 are expressed in eV/(Å·rad), r_1 and r_2 in Å, θ_0 is the equilibrium angle, and is expressed in rad.

As the nitrate group is planar, it was decided to add an out of plane energy term, which considers the harmonic energy penalty for atom 1 (nitrogen) lying out of the plane of atoms 2, 3 and 4 (oxygens)^[7].

$$E = k \cdot d^2 + k_4 \cdot d^4 \quad (3.10)$$

Where d represents the distance to the plane. k is defined in eVÅ⁻², k_4 is defined in eVÅ⁻⁴. Coulomb subtraction was applied within all the nitrate molecules.

3.1.2.3.1 Force-field for nitrates

In this work, to fit the force-field for the nitrate group, as described in the previous section, the carbonate force-field from Raiteri *et al*^[8] has been used as a starting point. It was created to study the properties of pre-nucleation clusters and provides a correct description of the solution chemistry. For those systems, particularly, in the case of *ab-initio* techniques, where the simulation size limit is a few nanometers, they may be simulated for only tens to hundreds of picoseconds, and direct simulation of ion aggregation, nucleation, and growth for those systems is well beyond what can be performed with the currently available computational tools. Force-field simulations are substantially less expensive from a computational point of view and are already being used to create microsecond-long atomistic trajectories for systems with sizes and concentrations comparable to experiment^[9]. The total simulation length, however, depends on factors such as number of particles and system size, therefore the bigger the system (higher number of particles simulated), the higher the computational cost associated. In this work, given the size of the systems investigated, we have only been able to simulate nanoseconds.

Although lacking the accuracy of *ab-initio* methods, if a force-field is properly calibrated against experimental thermodynamic data, it can be a very powerful tool for studying the very early stages of aggregation and, with the aid of cutting-edge sampling techniques, of the nucleation process itself. To create accurate force-field simulations of any system, the choice of the functional form and its parametrisation is a crucial first step. There are numerous parameter sets for alkaline-earth cations in water that have already been published in the literature^[10–16], and numerous force-fields for their carbonate salts in solid form^[17–23]. There are, however, fewer models that can adequately capture the characteristics of the ions in both the solid state and aqueous solution^[24–28].

The key point from Raiteri *et al* is that because the entropic contribution cannot be ignored, it is essential to calibrate for the free energy rather than enthalpies for ions in aqueous solution. As a result, their force-field attempts to reproduce the solubility of alkaline-earth carbonates observed in experiments and it is based on the free energies of the pertinent systems. Using the software GULP^[1] and a relaxed fit^[29] to the structures and experimental bulk moduli, the interactions between the cations and carbonate were identified.

Fit procedures using the simplex or BFGS minimization algorithms are embedded in GULP. In addition to these two minimization algorithms, GULP contains genetic algorithms for generating sets of initial parameters for subsequent refinement. Although tests showed that the BFGS algorithm in general provides calculated results in a good agreement with the observed data, using little computing time, some limitations were observed. As the BFGS algorithm uses gradients calculated numerically, the effect of noise in the gradients may make it difficult to fit the potential parameters. In this case, methods that require only function evaluations are a good choice. Although, GULP does allow some bounds on potentials by using the “absolute” keyword, which can restrict values that should be positive, it is not possible to specify the lower and upper bounds for each the adjustable parameter. As a consequence, it is possible to obtain good results from potential parameters that do not make physical sense and prevent the transferability of the potential parameters for other similar compounds. In cases where the fitting methods of GULP do not provide good results, it is common to adjust the parameters by means of a process of trial and error.

In their work, the free energies of the crystalline carbonate phases at 298.15 K were also included in the observables after the thermodynamics of the ions in solution were properly fitted, ensuring that the solubility products of these minerals would be as close to the experimental values as is practical.

3.1.3 Long-Range Cut-offs

For every inter- and intra-molecular interaction, we consider the value of its potential to be zero at distances greater than a cut-off, as the values will effectively be almost zero. This is done to save computational expense. *Figure 3.3* shows the cut-off set for Lennard-Jones type of potential. If the goal is to simulate dispersion or repulsion interactions, a new term must be taken in account, the so-called switching function, $S(r)$. Setting an arbitrary cut-off can lead to discontinuities in the forces and therefore a function is applied to the potential to smooth its decay to zero.

$$V(r) = \begin{cases} v(r) & \text{for } r < r_{\text{switch}} \\ v(r) \cdot S(r) & \text{for } r_{\text{cut-off}} \leq r \leq r_{\text{switch}} \\ 0 & \text{for } r > r_{\text{cut-off}} \end{cases} \quad (3.11)$$

In this case, we must define a new distance, the so-called switch distance. It is usually set a couple of angstroms (\AA) before the zero cut-off. We must ensure that $S(r)$, $\frac{dS(r)}{dr}$ and preferably $\frac{d^2S(r)}{dr^2}$ are continuous at r_{switch} , $r_{\text{cut-off}}$. The role of the switching function is to allow the potential to move more gently to zero, which avoids an unphysical description of the system without having to deal with a discontinuity in the forces.

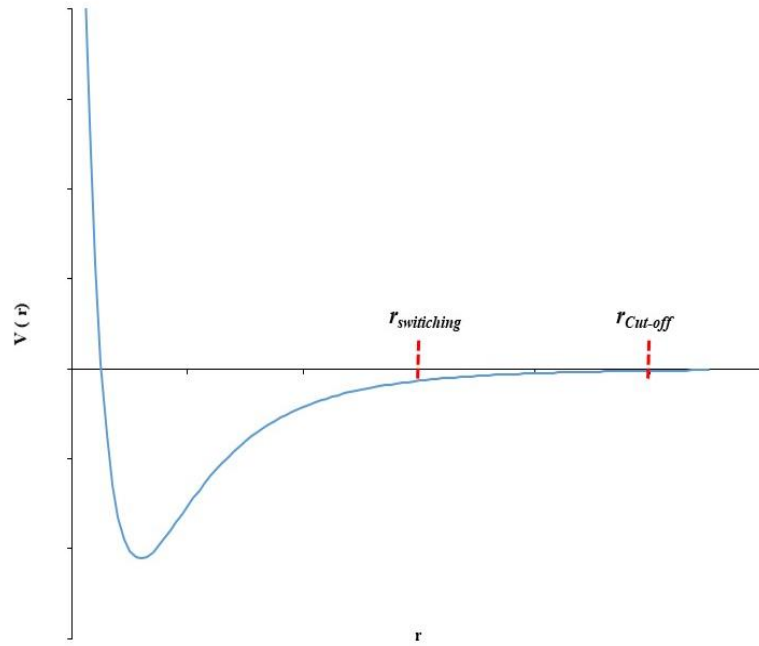


Figure 3.2(b) Lennard-Jones potential with cut-off highlighted

3.1.3.1 Mei-Davenport-Fernando taper

The MDF^[32](Mei-Davenport-Fernando) taper was applied in all our cases with the form

$$E_{smooth}(r) = E(r) \cdot f_{cut}(r) \quad (3.12)$$

With $f_{cut} = 1$ for $r < r_m$ and $f_{cut} = 0$ for $r \geq r_{cut}$ ^[33]. In between, the value is obtained by

$$f_{cut}(r) = ((1 - x)^3) \cdot (1 + 3x + 6x^2) \quad (3.13)$$

Where

$$x = \frac{(r - r_m)}{(r_{cut} - r_m)} \quad (3.14)$$

In this case, r_m represents the taper range. In this case, r was set at 9.0 Å and r_{cut} as 3.0 Å.

3.1.3.2 Ewald Decomposition

Ewald summation accounts for the long-range (φ_1), short-range (φ_2), and self-interaction (φ_3) terms^[73, 74].

$$\varphi = \varphi_1 + \varphi_2 + \varphi_3 \quad (3.15)$$

According to this method, all the charges are wrapped in diffuse charge densities, whose role is neutralising them. This charge is commonly represented with a Gaussian charge density, $\rho_i(\mathbf{r})$:

$$\rho_i(\mathbf{r}) = \frac{q_i \alpha^3}{\pi^{3/2}} e^{-\alpha^2 r^2} \quad (3.16)$$

where \mathbf{r} is the point in space that is in relation to the charge distribution's centre and α determines the width of the Gaussian.

The interaction between each charge and its respective opposite-sign Gaussian counterpart is left out. Equation 3.16.a contains the complementary error function.

$$erfc(x) = \frac{2}{\sqrt{\pi}} \int_x^\infty e^{-t^2} dt \quad (3.16.a)$$

The Fourier components in reciprocal space can then be added to find the value of φ_1 :

$$\varphi_1 = \frac{1}{2} \sum_{k \neq 0} \sum_{i=1}^N \sum_{j=1}^N \frac{1}{\pi V} \frac{q_i q_j}{4\pi \epsilon_0} \frac{4\pi^2}{k^2} \exp\left(\frac{-k^2}{4\alpha^2}\right) \cos(k \cdot r_{ij}) \quad (3.17)$$

where, according to Equations 3.23 and 3.24, \mathbf{k} is the volume of the cell and the sums in equation (3.17) are over the reciprocal lattice vectors (k) and the ions in the simulation cell (i, j).

$$\mathbf{k} = \frac{2\pi n}{\lambda} \quad (3.18)$$

$$k = |\mathbf{k}| = \sqrt{\sum_{i=1}^n k_i^2} \quad (3.19)$$

For a neutral simulation cell, the term for $k=0$ in Equation 3.17 can be ignored.

Charged cells, dipoles, and multipoles can all be incorporated into the Ewald approach^[75].

The analytical expressions for the two terms, into which the interactions are divided, are respectively:

$$\operatorname{erf}(x) = \frac{2}{\sqrt{\pi}} \int_0^x e^{-t^2} dt \quad (3.20)$$

$$\operatorname{erfc}(x) = 1 - \frac{2}{\sqrt{\pi}} \int_0^x e^{-t^2} dt \quad (3.21)$$

Those two functions are defined in a way that

$$\operatorname{erf}(x) + \operatorname{erfc}(x) = 1 \quad (3.22)$$

This allows decomposing the Coulombic interaction potential into:

$$\frac{1}{r} = \frac{1}{r} [\operatorname{erf}(\alpha r) + \operatorname{erfc}(\alpha r)] = \frac{\operatorname{erf}(\alpha r)}{r} + \frac{\operatorname{erfc}(\alpha r)}{r} \quad (3.23)$$

The variable α has been introduced to make sure that the interaction, will, in fact, go down to zero at the right r value. The Ewald method is the most commonly used; it divides electrostatic interactions in two groups:

1. Short-range components: in real space it rapidly decays to zero, therefore it can be treated as a Lennard-Jones potential.
2. Long-range components: because of their nature, these components have to be calculated in reciprocal space. To do so a so-called Gauss error function (erf) and complementary error function (erfc) are employed^[30].

3.1.3.3 Particle Mesh Ewald

A method that further approximates the Ewald one is the Particle Mesh Ewald^[31]. It works by smoothing the charges through a defined finite-sized group of lattice points; on a so-called ‘mesh’, that covers the entire simulation cell. This significantly reduces the dimensionality of the charge distribution across the entire simulation cell and its infinite periodic images, thus reducing the computational cost. This is not, however, connected with a diminished accuracy. By using fast-Fourier-transform on the charges, it is possible to calculate the long-range terms of the potential. For all the benefits described above, this tends to be, the preferred method.

3.2 *Ab-initio* methods

By considering the electronic structure of the system it is possible to obtain reliable results. This is, unfortunately, also connected with an increased computational cost. When talking about rare-events such as crystallisation *ab-initio* methods will struggle to access the necessary time. There are other cases, however, such as the calculation of solid-state properties (for example, the elastic stiffness constant), which can be calculated from a small cell, therefore making a system that can be modelled with an *ab-initio* approach. Through this work, we made use of these methods to make a comparison between the values obtained with *ab-initio* methods, widely considered, more accurate, and the results obtained with a classical approach. Simulations were all performed with the CASTEP^[65] code (Cambridge Serial Total Energy Package).

3.2.1 Density functional theory

One of the most popular quantum mechanical modelling techniques in the fields of physics, chemistry, and materials science is density functional theory (DFT). This method may be used to study many-body systems, such as atoms, molecules, and condensed phases.

The Born-Oppenheimer approximation states that all the details needed to characterise a molecular system are included in the electron density (i.e. considering the electronic and nuclear movements

independently). The wave function, which depends on $3N$ position variables and N spin variables, is replaced by the electronic density (which depends on just three variables) to describe an N -electron system, which is the foundation of DFT. The density $\rho(r_1)$ may be calculated by integrating the wave function ψ using the spatial and spin variables of electrons x and merely the spin variable of electron 1 σ :

$$\rho(\vec{r}_1) = N \int \dots \int |\psi(\vec{x}_1 \vec{x}_2 \dots \vec{x}_n)|^2 d\sigma_1 d\vec{x}_2 \dots d\vec{x}_N \quad (3.24)$$

The Hohenberg-Kohn theorems^[76], on which DFT^[66] is founded, demonstrate that the properties of a many-electron system may be predicted using functionals of the electron density. A functional is defined as a function of other functions. In this theory all the system properties (e.g. total energy) are defined as a function of the electron density. In this context, the total energy of a system is defined as:

$$E_{tot}[n] = E_{kin}[n] + E_{ext}[n] + E_H[n] + E_{XC}[n] \quad (3.25)$$

where $E_{kin}[n]$ is the quantum-mechanics (QM) kinetic energy of electrons, $E_{ext}[n]$ is the energy due to the external potential, $E_H[n]$ is the Hartree repulsion, and $E_{xc}[n]$ is the exchange correlation functional.

3.2.2.1 Exchange Correlation Functionals

“Exchange” is a quantum mechanical effect regarding identical particles, and originates from the fact that two particles, when subject to exchange symmetry, can see their wave function remaining the same (symmetry) or change sign (antisymmetric).

“Correlation” is the interaction between electrons that is not accounted for by a mean field approximation (as in Hartree-Fock theory). The effect of the instantaneous positions matters because the mean field underestimates the ability of electrons to avoid each other. In DFT, the principle is to approximate these components in the best way possible, as the exact analytical form is not known. A useful tool to visualise the concept of efficiency for DFT exchange-correlation

(XC) functionals is the Jacob's ladder shown in Figure 3.3^[77]. The local density approximation (LDA), states that the XC energy function only depends on the density at that point and is that of the uniform electron gas of that density, and is the simplest way to model the exchange-correlation term. This functional frequently makes errors, including overestimating lattice parameters, underestimating binding energies, and overlooking magnetic material energies^[67].

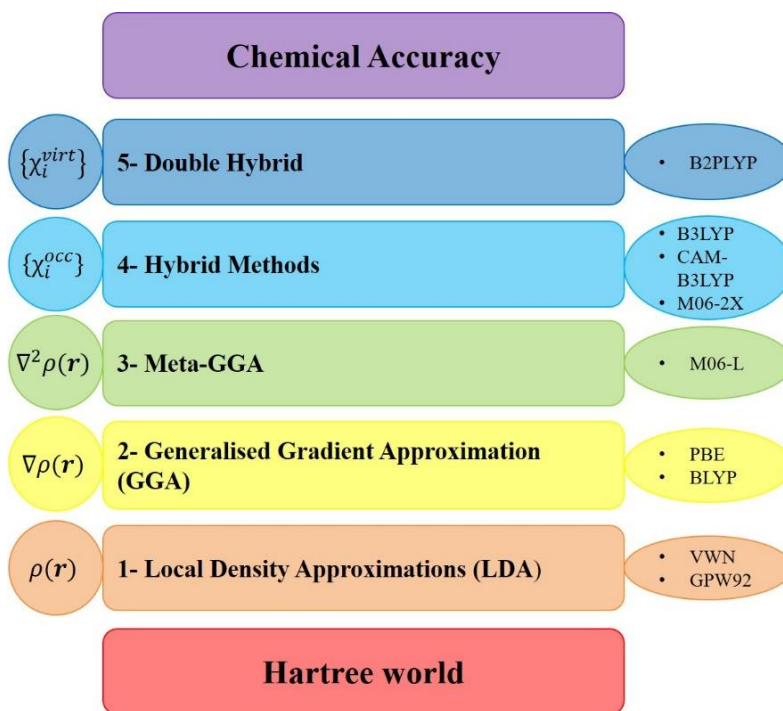


Figure 3.3 Jacob's ladder of DFT functionals. The functionals are ordered from the bottom to the top based on their accuracy and computational cost^[78].

The class of generalised gradient approximations (GGA^[68]), employs both the density and its gradient at each point. They are often more accurate than LDA since they have more information. PBE^[69] is not one of the most computationally expensive methods and can be highly accurate, it offers good potential for utilisation. However, it is well known to underestimate the band gap in a periodic system or the HOMO-LUMO gap.

Hybrid functionals combines a precise exchange potential (Hartree-Fock) with an experimentally or *ab-initio*-calculated correlation potential.

3.2.2.2 Basis set

When performing a DFT computation, the basis set is a parameter that must be selected. The partial differential equations of the model are transformed into algebraic equations by the basis set, a set of functions that represents the electronic wave function and is employed for quick computer processing. A single particle's states are then represented as linear combinations of the basic functions (molecular orbitals). STO- n G is the most prevalent minimum basis set which makes use of a linear combination of gaussian type orbitals. The quantity n represents how many basic Gaussian functions there are in a single basis function. In addition to localised basis sets, plane-wave basis sets can also be used in quantum-chemical simulations. These basis sets are the ones that are most commonly used for periodic calculations^[79]. According to the Bloch equation, a periodic system's periodic cell and plane wave components can be combined to form the wavefunction, u , of an electron in band n . The periodic portion is defined using a plane wave basis set, and u may then be represented as

$$u_n(\vec{r}) = \sum_{\vec{G}} \vec{G} c_{n,\vec{G}} e^{i\vec{G}\vec{r}} \quad (3.26)$$

where the reciprocal lattice vectors \vec{G} are picked to respect the lattice's periodicity and $c_{n,\vec{G}}$ is a coefficient. Combining Bloch's equation with (3.26), we can now define

$$\psi_n(\vec{r}) = \sum_{\vec{G}} \vec{G} c_{n,(\vec{k}+\vec{G})} e^{i(\vec{k}+\vec{G})\vec{r}} \quad (3.27)$$

The k -points and cut-off energy are two significant factors that affect how precisely the method works. A new wavefunction is generated for each value of k . However, it is feasible to identify a small set of k -points (depending on the system's symmetry) that accurately captures the structure. In principle, an endless number of k -points could be chosen, and the computation could be carried out anywhere in space. For geometry optimisation, k -point sample densities with low computing

cost are around $0.05 \ 2\pi \ 1/\text{\AA}$. The computation's upper estimate, or cut-off energy, is typically between 350 and 650 eV, with the higher value being more accurate.

To test the reliability of the force-field fitted with the previously defined terms, the same static lattice has been investigated using CASTEP^[2]. In CASTEP every single calculation is parallelised over a defined number of cores; it is possible to know the number of computationally required resources by performing a so-called “dry run”^[34]. A “dry run” gives as a result not only the amount of memory needed by the calculation, but also the number of k -points examined. Knowing the number of k -points is valuable information, as every single one can be used to parallelise the calculation, which means that every CPU works on a single k -point (i.e. no data exchange). In this case a geometry optimisation was performed, in order to determine lattice constants, energy of the polymorph and elastic constants.

All the calculations were performed using DFT-D method^[70], which adds the corrections of dispersion to a classic density functional theory calculation. This method improves the previous one, giving a result with less than 1% error in the calculation of energy, compared with the same experimental values.

$$E_{inter} = E_{Pauli} - E_{rep} + E_{ES} + E_{pol} + E_{(disp,short)} + E_{(disp,London)} \quad (3.28)$$

This is performed by adding a long-range correlation effect (London term)^[71].

In equation 3.23 E_{Pauli} is the Pauli repulsion, E_{rep} the electrostatic repulsion, E_{ES} is electrostatic energy and E_{pol} the energy associated with the polarisation effect. The PBE^[68] exchange correlation functional was used, whilst the pseudopotentials were generated “on the fly” by the CASTEP program.

Since the basis set for plane waves does not consist entirely of electrons, it is necessary to employ a pseudopotential, which is specified by the functional used. The pseudopotential attempts to replace the effects of the motion of the core electrons of an atom and its nucleus with a so-called pseudopotential, in order for the Schrödinger equation to contain a modified effective potential term rather than the Coulombic potential term for core electrons typically found in the Schrödinger

equation. For core electrons, pseudopotentials are produced to replace the Coulombic potential term.

3.3 Energy Minimisation

The goal of energy minimisation is to find the global minimum energy of a system. Whilst performing an energy minimisation one must take into account that a system far from equilibrium or a non-rational starting configuration is unlikely to lead to a proper optimisation. An additional source of error is connected with the presence of local minima, because the algorithm is likely to pick the closest minimum, which might not be the global minimum for the system. Whilst, usually, a structure is minimised at zero kelvin, this can lead to the errors by not accounting for any vibrational modes.

Energy minimisations in this work have been performed using different levels of theory and a range of programs. *Ab-initio* minimisation has been performed using CASTEP^[34], classical minimisations have been performed using GULP^[1], DL_POLY^[36-38] (both classic and 4) and LAMMPS^[39]. While METADISE^[35] has been used for surface cleavage minimisation.

3.3.1 Lattice Energy

The general protocol for energy minimisation involves moving the atoms with the final aim of minimising the forces they are subject to.

$$F = \frac{-\delta U(\mathbf{r})}{\delta(\mathbf{r})} = 0 \quad (3.29)$$

Where U is the total energy and \mathbf{r} are the coordinates at equilibrium.

The process consists of reducing the energy of the system iteratively where its form is a Taylor expansion as a function of the atomic coordinates \mathbf{r} .

$$U(\mathbf{r} + \delta r) = U(r) + \frac{\delta U(r)}{\delta r} \delta r + \frac{1}{2!} \frac{\delta^2 U(r)}{\delta r^2} \delta r^2 + O(\delta r^3) \quad (3.30)$$

In (3.30) $U(r)$ represents the minimum of the lattice energy. Usually, the first two terms are essential whilst the following ones are incorporated into the term $O(\delta r^3)$ and disregarded.

3.3.2 Minimisation Algorithm

The following section will give an overview of the most used minimisation algorithms, including this work.

3.3.2.1 Steepest Descent

The steepest descent^[40] method uses the gradient of the energy function, which is connected to the forces in the form:

$$g_n = \frac{\delta U}{\delta r_n} \quad (3.31)$$

$$F_n = -g_n \quad (3.32)$$

In (3.34) \mathbf{F} is the force and \hat{F}_n its unit vector (in 3.33).

$$|F_n| = \sqrt{\sum_{i=1}^n F_i^2} \quad (3.33)$$

$$\hat{F}_n = \frac{F_n}{|F_n|} \quad (3.34)$$

The positions of the atoms are updated by:

$$r_{n+1} = r_n + \alpha_n \hat{F}_n \quad (3.35)$$

The advantage of this method is the computational simplicity, as the calculations require little memory. The disadvantage is that it might require additional steps in order to find the minimum. It is efficient in the case where only a few strong interatomic forces are present, as these are responsible for the direction of the gradient.

3.3.2.2 Conjugate Gradient

Following the first step, which is a steepest descent step^[41], the step size and direction are both then modified. The direction is expressed as a vector in the form:

$$F_n = -g_n + \gamma_n F_{n-1} \quad (3.36)$$

$$\gamma_n = \frac{g_n \cdot g_n}{g_{n-1} \cdot g_{n-1}} \quad (3.37)$$

The term γ_n is a scalar coefficient and gives information on how the gradient should be corrected systematically. From the values derived by (3.36) combined with (3.37) it is possible to obtain information regarding the new position.

3.3.2.3 Newton-Raphson

When information about the second derivative of the energy (W) is included, the method will account for the change of the gradient of the energy, not just the gradient itself. The Newton-

Raphson^[42] method is one of these, so-called, second order methods. Starting from the Taylor expansion

$$W(r) = W(r_n) + (r - r_n)W'(r_n) + \frac{(r - r_n)^2 W''(r_n)}{2} + \dots \quad (3.38)$$

The first derivative of $W(r)$ is

$$W'(r) = rW'(r_n) \quad (3.39)$$

For a purely quadratic function the second derivative does not depend on the position, namely

$$W''(r) = W''(r_n)$$

At the minimum (r^*) the first derivative is null, therefore

$$r^* = r_n - W'(r_n)/W''(r_n) \quad (3.40)$$

To solve this algorithm it is required to calculate the Hessian (second derivative matrix) and invert it:

$$W_n = \left(\frac{\delta^2 U}{\delta r_n^2} \right) \quad (3.41)$$

Then the positions are updated with

$$r_{n+1} = r_n - g_n W_n \quad (3.42)$$

Because of its nature and the involvement of quadratic equations, this method can be used to locate the minimum in a single step, assuming that U is quadratic. It is usually referred to as the harmonic approximation. Because of the need to calculate and invert the Hessian matrix the method is usually very expensive from a computational point of view and requires a reliable minimisation algorithm to approach the minimum. This first approach can then be followed by the application of the Newton-Raphson method to better locate the true minimum.

3.3.2.4 BFGS Method

The Broyden-Fletcher-Goldfarb-Shanno (BFGS) algorithm is an iterative approach for addressing unconstrained nonlinear optimisation problems in numerical optimisation. It is a quasi-Newton Raphson method. This is much less expensive since, instead of calculating the inverse Hessian at each step, it approximates the inverse Hessian using gradient information for most optimisation steps. It only performs a full calculation of the inverse Hessian occasionally, Full details can be found in reference [80].

3.3.3 Constant Pressure Minimisation

Alongside the atomic positions, it is also possible to optimise the simulation cell itself. This methodology is usually referred to as ‘constant pressure’ because of the equivalence of said pressure with the forces. In this method, it is necessary to consider the cell parameters as new additional variables. The variation of the lattice parameter as a consequence of the application of a defined pressure can be seen as a strain of said lattice vector, which follows from Hooke’s law in the form^[40]:

$$\varepsilon = C^{-1} \cdot \sigma \quad (3.43)$$

In (3.43) C is the elastic stiffness matrix.

3.4 Molecular dynamics

Molecular dynamics^[43] is a simulation technique which aims to reproduce the dynamic behaviour of atoms in a system. By using the energy function, as described Section 3.1.2.3.1, it is possible to calculate the force on any atom.

$$F_a = \frac{-\partial U}{\partial r_a} \quad (3.44)$$

The forces can be used to calculate each atom's motion by Newton's second law. Each Molecular dynamics simulation is divided in time into discrete time steps, no more than a few femtoseconds (10^{-15} s) each.

3.4.1. Periodic boundary conditions

Real crystals have different properties and behaviour at the interfaces. Usually the size of a crystal is such that one can consider modelling the behaviour of the bulk while ignoring the surfaces' effect. In order to avoid having to take in account these effects for each simulation, unless explicitly required, it is possible to use a number of approximations. Here, the ones that have been actively used during this work are listed and described. Periodic Boundary Conditions (or PBCs)^[44] make use of a 'simulation cell', which does not necessarily correspond to the crystal primitive cell, to simulate, in a convenient way, the periodicity inside an infinite lattice. This cell is then reproduced around the original one, in a way such that every object leaving the simulation cell is then reintroduced at the opposite side of the cell, see Figure 3.4. This type of periodicity does not account for the presence of defects and it can be considered, therefore, artificial. In order to overcome possible problems deriving from this induced artificial periodicity it is important to choose a cell with a size that accounts for this effect, without disrupting the computational efficiency.

When calculating size-dependent properties, such as diffusion or dynamical properties, thermal expansion, heat capacity and thermal conductivity it is necessary to use a unit cell that is several times bigger than the primitive cell of the crystal.

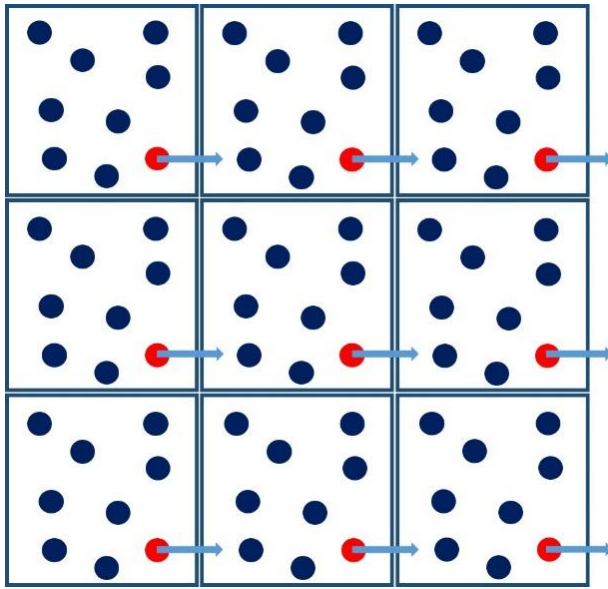


Figure 3.4. Schematic representation of PBCs

3.4.1.1 Minimum Image convention

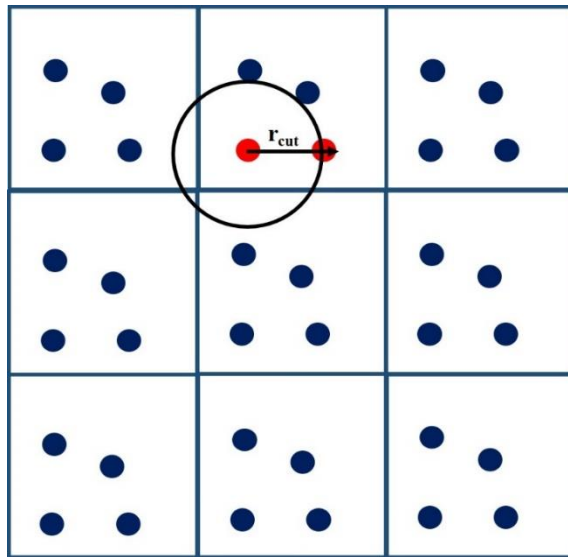


Figure 3.5 The minimum image convention within PBCs.

The minimum image convention^[45] states that the cut-off distance for two different particles should be at least half the length of the shortest cell vector. The goal of this condition is to prevent a particle from colliding with another particle twice, resulting in artificial effects.

3.4.2 Calculation of Forces

Calculation of the forces using molecular dynamics is performed with the following route: the first step is to estimate the interatomic distances, using the atomic Cartesian coordinates with

$$r_{ij} = r_i - r_j \quad (3.45)$$

In (3.45) r_i and r_j are the coordinate for atoms i and j

$$r_{ij} = |r_{ij}| = \sqrt{x_{ij}^2 + y_{ij}^2 + z_{ij}^2} \quad (3.46)$$

In (3.46), r_{ij} is the distance between atoms i and j , its modulus refers to the value being made positive (i.e. the positive root). Because the equation calculates the interatomic distances, it comes that when calculating forces they will also be interatomic ones. This is done by using

$$F_{ij} = \frac{-dU}{dr_{ij}} \quad (3.47)$$

After that, by utilising the distance unit vector to divide the force into components from each dimension:

$$\mathbf{F}_{ij} = F_{ij} \frac{\mathbf{r}_{ij}}{|r_{ij}|} = - \frac{dU}{dr_{ij}} \quad (3.48)$$

By adding up all the forces operated by all the atoms on a single atom, it is possible to obtain the total as:

$$F_i = \sum_{j=1}^N F_{ij} \quad (3.49)$$

with $i \neq j$

The derivation of acceleration from force is done by applying Newton's second law. In (3.50) t represents the time, \mathbf{a} the acceleration, and m the mass.

$$F = \frac{d^2 r}{dt^2} = m \cdot \mathbf{a} \quad (3.50)$$

3.4.3 Time Integration Algorithms

Once the force acting on an atom has been calculated, it is possible to build equations that update the position and velocities of atoms based on accelerations and prior positions and velocities using a Taylor expansion:

$$\mathbf{r}(t + \Delta t) = \mathbf{r}(t) + \mathbf{v}(t)\Delta t + \frac{\mathbf{a}(t)\Delta t^2}{2} \quad (3.51)$$

$$\mathbf{v}(t + \Delta t) = \mathbf{v}(t) + \mathbf{a}(t)\Delta t \quad (3.52)$$

In (3.51) \mathbf{r} represents the position, \mathbf{v} represents the velocity and \mathbf{a} the acceleration of the atoms.

In molecular dynamics, because the timestep is finite, discrete equations (3.51) and (3.52) cannot be used as these equations do not include the higher terms of the Taylor expansions and therefore their accuracy is poor^[46].

3.4.3.1 Verlet Leap-Frog

Verlet Leap-frog algorithm^[47] estimates the velocities at the half-time step. These velocities are then used to re-estimate the current one. The half-time step velocities in this method are determined by:

$$v\left(t + \frac{\Delta t}{2}\right) = v\left(t - \frac{\Delta t}{2}\right) + a(t)\Delta t \quad (3.53)$$

For each timestep, then, the velocities are extrapolated by using the time-average of neighbouring velocities

$$v(t) = \frac{v\left(t + \frac{\Delta t}{2}\right) + v\left(t - \frac{\Delta t}{2}\right)}{2} \quad (3.54)$$

From (3.53) and (3.54) it is possible to derive the position as

$$r(t + \Delta t) = r(t) + v\left(t + \frac{\Delta t}{2}\right)\Delta t \quad (3.55)$$

Leapfrog integration has two key benefits when utilised to resolve mechanics problems. The time-reversibility of the Leapfrog approach is the first. One can integrate forward n steps to reach the same starting point, and then integrate backward n steps by switching the direction of integration. The second benefit is its symplectic nature, which occasionally enables the energy (slightly modified) of a dynamical system to be conserved (only true for certain simple systems).

3.4.3.2 Velocity Verlet

The Velocity Verlet^[48] method can be summarised as the following:

$$r(t + \Delta t) = r(t) + v(t)\Delta t + a(t)\frac{\Delta t^2}{2} \quad (3.56)$$

By using (3.56) it is possible to use the current positions, velocities and accelerations of a particle to calculate its new position.

$$v\left(t + \frac{\Delta t}{2}\right) = v(t) + \frac{a(t)\Delta t}{2} \quad (3.57)$$

By knowing the new position is then, straightforward, to derive new forces and accelerations.

$$v(t + \Delta t) = v\left(t + \frac{\Delta t}{2}\right) + \frac{a(t + \Delta t)\Delta t}{2} \quad (3.58)$$

By using (3.58) it is possible to update accelerations and velocities.

3.4.4 Initialisation

Velocity Verlet algorithm requires the knowledge of the initial coordinates and velocities for each particle.

$$\sum_{i=1}^N m_i v_i^2 = 3Nk_b T \quad (3.59)$$

By using (3.59) it is possible to correlate the average atom velocities to the temperature. In this equation, m_i is the mass and v_i is the velocity of any given particle; N is the total number of particles and k_b is the Boltzmann constant.

$$p = \sum_{i=1}^N m_i v_i = 0 \quad (3.60)$$

As stated in (3.60), an essential requirement is, also, that the linear momentum, and the angular momentum, of the system is zero.

3.4.5 Equilibration Period

Before analysing a trajectory, one must make sure to run the simulation for an extended period to avoid including any initialisation effects.

A large force will be created quickly if the atoms start too near to one another. The substantial acceleration and force will cause the molecule to split. As a result, it can be concluded that the system under investigation is not the desired original molecule. If a maximum force restriction is used, the initial molecule might outlast equilibration. After the equilibration has taken place, the system can be examined.

3.4.6 Ensembles

By *ensemble*, we mean a set of parameters with the purpose of controlling the particular system conditions. For each *ensemble*, we must specify a different Hamiltonian, whose role is to account for the invariant quantities of the system itself. All the ensembles that this work has made use of are described in the following paragraphs.

3.4.8.1 Canonical ensemble (NVT)

The so-called “canonical ensemble” simulates a system by retaining the amount of substance (N), volume (V) and temperature (T). In NVT, the simulation box is connected to a reservoir much larger than itself, which maintains the system at a constant temperature. The energy exchange in a MD simulation box can be simulated by a range of algorithms, approximating the canonical ensemble. Popular methods to control temperature include velocity rescaling, the Nosé–Hoover thermostat^[55,56], Nosé–Hoover chains, the Berendsen thermostat^[57], the Andersen thermostat^[58,59]

and Langevin dynamics^[60]. It is not trivial to obtain a canonical ensemble distribution of conformations and velocities using these algorithms. The dependence of the algorithm from the system size, thermostat choice, thermostat parameters, time step and integrator is currently still studied.

3.4.8.2 Isothermal–isobaric (NPT) ensemble

In the isothermal–isobaric ensemble, the amount of substance (N), pressure (P) and temperature (T) are conserved. To do so a thermostat and a barostat are needed^[61]. The temperature is kept constant in a similar way as done for the NVT ensemble. To keep the pressure constant the cell is allowed to adjust itself and expand/contract. This can occur in multiple ways, and there are various options to do so: the cell can be let free to change isotropically, anisotropically, retain or vary the angles in between the cell vectors.

3.5 Free energies of hydration of isolated ions

It is not possible to experimentally measure the thermodynamic properties of isolated ions. Experiment (values of the free energy of solution) can give only the value of a neutral combination of ions. To get the value of the free energy of hydration of the isolated ion one value must be fixed. This represents a significant limit, because every value obtained with the simulation will not have an experimental reference counterpart to support it.

Historically, the solution to this problem has been to pick a reference system, the proton, and set its free energy to a standard value of zero, such that all the others could have been scaled starting from this value (conventional values). This results in a non-transferable approach, therefore there is a need to find something more physically based. To do so the Born model of hydration has been used, leading to an estimation of the free energy of the proton of $\Delta G^0([\text{H}^+](\text{aq}) \text{ abs}) = -1056 \pm 6$

kJ mol^{-1} (Marcus^[81]). However, even this approach is not free from errors, and the following section will attempt to give an overview of those problems.

3.5.1 The experimental problem

The approach used by Marcus^[82], quoted in the previous section can be summed up as: the free energy of hydration needed to transfer a solute particle from the gas phase (in its fixed position) to the solvent (in another fixed position). By fixing the ions in a defined position, it is then possible to ignore the translational degrees of freedom of solute particles. In this scenario, the solute is assumed to be at infinite dilution, with no solute-solute interactions considered.

It is necessary to know the difference between the free energies (or enthalpies) required to hydrate the solute in solution and the solute in the gas phase in order to calculate a free energy or enthalpy

$$\Delta H^0(\text{hydration}, M^z, \text{conv}) = \Delta H_f^0(M^z, \text{aq}) - \Delta H_f^0(M^z, \text{g}) + 1536.2z \text{ kJ mol}^{-1} \quad (3.61)$$

$$\Delta G^0(\text{hydration}, M^z, \text{conv}) = \Delta G_f^0(M^z, \text{aq}) - \Delta G_f^0(M^z, \text{g}) + 1516.9z \text{ kJ mol}^{-1} \quad (3.62)$$

$$\Delta S^0(\text{hydration}) = S^\infty(\text{aq}) - S^0(\text{g}) \text{ J mol}^{-1} \text{K}^{-1} \quad (3.63)$$

In (3.61), (3.62) and (3.63) the superscript 0 refers to 298.15 K and atmospheric pressure.

In (3.61), $1536.2 \text{ kJ mol}^{-1}$ is the enthalpy of formation of a gaseous proton^[83] while in (3.70), $1516.9 \text{ kJ mol}^{-1}$ is the free energy of formation of the gaseous proton at 298.15K^[84]. The entropy is $S^\infty(\text{aq})$, the partial molar entropy at infinite dilution.

In this approach, however, an important detail is missing: the ions' movement between the two phases is not taken in account. Hofer and Hünenberger^[85] refer to them as intrinsic quantities rather than bulk or real quantities as a result, since they do not depend on the details of the gas/liquid interface and the experimental values of the solution energies of systems can be obtained by adding up the values of the individual absolute free energies of hydration. According to Marcus, values for the absolute thermodynamic quantities of the proton are

$$\Delta G^0([H^+](aq) \text{ abs}) = -1056 \pm 6 \text{ kJ mol}^{-1} \quad (3.64)$$

$$\Delta H^0([H^+](aq) \text{ abs}) = -1094 \pm 6 \text{ kJ mol}^{-1} \quad (3.65)$$

$$S^\circ([H^+](aq) \text{ abs}) = -22.2 \pm 1.2 \text{ J mol}^{-1} \text{K}^{-1} \quad (3.66)$$

$$S^0([H^+](g)) = 108.85 \text{ J mol}^{-1} \text{K}^{-1} \quad (3.67)$$

$$\Delta S^0([H^+](aq) \text{ abs}) = S^\circ([H^+](aq) \text{ abs}) - S^0([H^+](g)) = -131.05 \pm 1.2 \text{ J mol}^{-1} \text{K}^{-1} \quad (3.68)$$

These numbers are thermodynamically self-consistent, at least to the level of the quoted errors. It is now possible to convert from the conventional scale (conv) to the absolute scale (abs) using the following equations where z is the charge on the ion.

$$\Delta G^0(\text{hyd}, X^z, \text{abs}) = \Delta G^0(\text{hyd}, X^z, \text{conv}) + z\Delta G^0([H^+](aq) \text{ abs}) \text{ kJ mol}^{-1} \quad (3.69)$$

$$\Delta H^0(\text{hyd}, X^z, \text{abs}) = \Delta H^0(\text{hyd}, X^z, \text{conv}) + z\Delta H^0([H^+](aq) \text{ abs}) \text{ kJ mol}^{-1} \quad (3.70)$$

$$\Delta S^0(\text{hyd}, X^z, \text{abs}) = \Delta S^0(\text{hyd}, X^z, \text{conv}) + z\Delta S^0([H^+](aq) \text{ abs}) \text{ kJ mol}^{-1} \quad (3.71)$$

The tabular data in refs ^[81, 82] includes terms accounting for the change in volume that is available to the solute when it goes from the gas to the aqueous phase, therefore corrections are required (details in Marcus^[81, 82]). In every instance, the corrections are the same and are

$$\left. \begin{aligned} \Delta G^*(\text{hydration}) &= \Delta G^0(\text{hydration}) + 7.93 \text{ kJ mol}^{-1} \\ \Delta H^*(\text{hydration}) &= \Delta H^0(\text{hydration}) + 2.29 \text{ kJ mol}^{-1} \\ \Delta S^*(\text{hydration}) &= \Delta S^0(\text{hydration}) - 18.9 \text{ J mol}^{-1} \text{K}^{-1} \end{aligned} \right\} \quad (3.72)$$

Marcus' model is the foundation for the data obtained in Tables 2 and 3 of ref [81], which are the most often utilised free energies of hydration

The values for the absolute thermodynamic quantities for proton hydration have been the subject of considerable research since Marcus created his table. Malloum *et al* review's from six years ago is the most recent^[86]. This leads to the conclusion that the free energy of proton hydration is roughly equal to the estimate made by Hofer and Hünenberger^[85] and much more negative than

Marcus' value. There are fewer figures for the enthalpy of hydration; the one from Tissandier *et al*^[84] based on cluster solvation data is probably the most trustworthy. For 298.15K, the entropy value is calculated by requiring thermodynamic consistency. The result is as follows.

$$\Delta G^0([H^+](aq) \text{ abs}) = -1100 \pm 14 \text{ kJ mol}^{-1}$$

$$\Delta H^0([H^+](aq) \text{ abs}) = -1150 \pm 1 \text{ kJ mol}^{-1}$$

$$\Delta S^0([H^+](aq) \text{ abs}) = -167 \pm 14 \text{ J mol}^{-1} \text{ K}^{-1}$$

These data suggest considerable changes to each of the Marcus values. The hydration free energy of the cations, M^{z+} , shifts from being more negative by -44 kJ mol^{-1} , and the anions, X^{z-} , shift from more positive by $+44 \text{ kJ mol}^{-1}$, assuming that this is the only major correction needed. For the ions being discussed in the project, this results in the following absolute free hydration energies.

Table 3.1 Absolute free hydration energies for the ions used in this work

Li ⁺	-519 kJ mol ⁻¹
Na ⁺	-409 kJ mol ⁻¹
K ⁺	-339 kJ mol ⁻¹
Rb ⁺	-319 kJ mol ⁻¹
Cs ⁺	-294 kJ mol ⁻¹
Mg ²⁺	-1918 kJ mol ⁻¹
Ca ²⁺	-1593 kJ mol ⁻¹
Sr ²⁺	-1468 kJ mol ⁻¹
Ba ²⁺	-1338 kJ mol ⁻¹
F ⁻	-421 kJ mol ⁻¹
Cl ⁻	-296 kJ mol ⁻¹
Br ⁻	-271 kJ mol ⁻¹
I ⁻	-231 kJ mol ⁻¹
NO ₃ ⁻	-256 kJ mol ⁻¹
CO ₃ ²⁻	-1227 kJ mol ⁻¹
SO ₄ ²⁻	-992 kJ mol ⁻¹
H ₂ PO ₄ ⁻	-421 kJ mol ⁻¹
PO ₄ ³⁻	-2633 kJ mol ⁻¹

There is a good agreement with the values from Hofer *et al*^[85, 87], that have been obtained using *ab-initio* methods and correction for the electrostatics.

3.5.2 The simulation problem

All parties agree that Born's solvation model is insufficient and that classical molecular, or wherever possible, quantum simulations are necessary in its place. Experts in the field also concur that these simulations need to be changed. However, the necessary changes and their justifications are disputed. Building on prior research by Hummer *et al*^[93], Hünenberger and McCammon^[92] underlined the importance of restricted size effects and provide guidance on how to account for them. The majority of the field's experts concur on this despite using several nomenclatures to describe them and, worse, embedding them into codes in various ways. Whether it is crucial to consider how the electrostatic sums are computed and how that may affect how the electric potential zero is defined is a matter of dispute. Hünenberger and colleagues often incorporate their methodology into other efforts, as summarised in two papers^[94,95]. Hummer and others list their positions in their original articles (for instance, ref [93]) and further recent work^[96]. In this work, Hünenberger's strategy has been used as a framework in what follows, showing how it differs from Hummer's plan in crucial ways.

3.5.2.1 Absolute free energy of hydration of a single ion

Periodic boundary conditions with either the Ewald summation or one of its close analogues are the most widely used method in the literature for determining $\Delta G^0(\text{hyd}, X^z, \text{abs})$. The Coulomb potential's long-range nature is the root of all the issues. In circumstances where using a charged simulation cell is feasible, these are very difficult. In this context, charged defects in solids and ions in liquids are typical instances. The obvious similarities between the two problems are rarely discussed because few experts cross both fields^[97]. The terms of the infinite sum are added in spherical shells around a central box, and the expanding sphere is immersed in a conducting medium. For further information, see ref [98], which also uses a Gaussian for the cancelling charge distribution.; $q_i \kappa^3 \exp(-\kappa^2 r^2) / \pi^{3/2}$. In addition to summations of the Ewald type, electrostatics can also be solved using periodic boundary conditions and the reaction field approach (e.g. refs

[85, 87]). It is also possible to contain the charged ion inside a large, unlimited water droplet^[94]. There are a number other truncation techniques as well^[94], however they are rarely used.

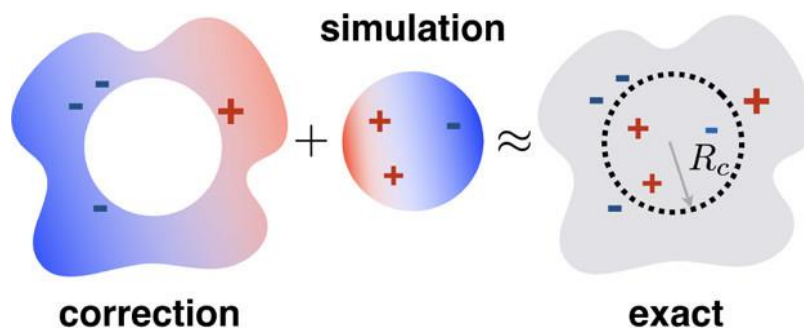


Figure 3.6 Schematic representation of the charge compensation obtained by using corrections to the simulation. Credits to the author [115].

The Ewald summation exhibits a divergence that needs to be eliminated when a charge is added to the periodic cell. To remove the charge, the simplest method is to provide a uniform neutralising adjustment. Two adjustments are involved; they were first defined individually but are now frequently used jointly. First, a straightforward idea of metals with charged ionic cores encased in a neutralising backdrop with an infinite dielectric constant was discussed^[99]. The interaction between the charges and the background, which acts as a neutraliser, is included in the Fuchs correction. The second^[20], the Wigner correction, offers the self-energy of the extra charge through its periodic images. Currently, we ignore the finite dielectric constant of the solvent. The overall correction of a cubic cell is (ref [98], eqⁿ (6.5); ref [101], eqⁿ (2.13))

$$V_{charge} = \frac{-N_A e^2}{8\pi\epsilon_0\kappa^2 L^3} \left| \sum_{i=1}^N q_i \right|^2 \quad (3.73)$$

In (3.81), L is the cell's length, κ is the Gaussian's width parameter, and q_i is the charge of the cell's i^{th} ion. The total Ewald potential energy, EEw , under specified boundary conditions can be expressed as the sum of interionic interactions and self-interactions (with the adjustment for a charged simulation cell included). For a cubic simulation cell of length L ^[92,101,102] can be written as

$$E_{EW} = \frac{1}{8\pi\epsilon_0} \sum_{i \neq j} q_i q_j V_{EW}(r_{ij}) + \frac{M}{8\pi\epsilon_0 L} \sum_i q_i^2 \quad (3.74a)$$

where

$$V_{EW}(r_{ij}) = \sum_m \frac{\text{erfc}(\kappa|r_{ij} + Lm|)}{|r_{ij} + Lm|} + \frac{4\pi}{L^3} \sum_{k \neq 0} \frac{\exp(-k^2/4\kappa^2)}{k^2} \exp(-ik \cdot r_{ij}) - \frac{\pi}{\kappa^2 L^3} \quad (3.74b)$$

In (3.74a) M is the Madelung constant for a group of similar charges, denoted by $M = -2.837297$, and the Wigner potential is the last term. Different formulations are possible and important since they determine which terms are incorporated to standard codes implicitly and which must be explicitly included. The literature contains numerous presentation methods, some of which incorporate discussions of thermodynamic integration^[103,104].

The Wigner potential terms are already present in codes using the P³M (particle-particle-particle-mesh) and SPME (smooth particle mesh Ewald) techniques, however this may not be immediately obvious (see ref [101] especially Appendix A). Examples include DL POLY^[37] (except for the Ewald option in DL POLY Classic^[38]), LAMMPS^[39], AMBER^[105], CHARMM^[106] and GROMACS^[107] (except for the Ewald option and also generally disregarded - see the manual).

According to Hünenberger *et al*^[85,94,95], four fundamental types of correction to the electrostatics mentioned above emerge when we consider an ion dissolved in a solvent. First and second, the ionic charge's representation of the solvent's polarisation may be inaccurate (type A and B corrections below).

Third, when the Born model is employed to correct polarisation problems, mistakes could be produced. As a result, there are no physical boundaries between the parts where the dielectric continuum is modelled and the sections where the solvent is explicitly modelled. These result in the generation of electrostatic potentials, which include the ion (type C corrections).

Fourth are a few minor corrections (collected together as type D). Only certain corrections are necessary; not all simulations require them. This work's approach is in adherence to Hünenberger's categorisation.

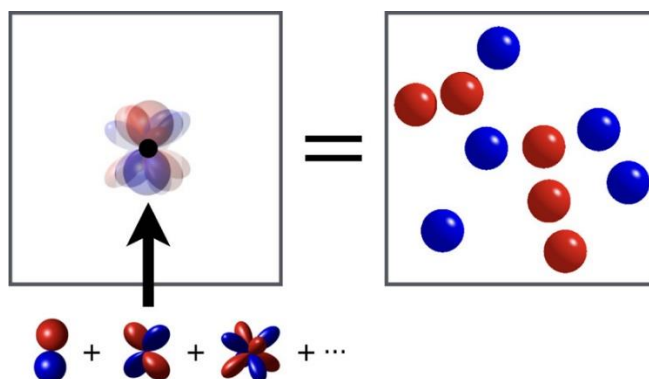


Figure 3.7 Single point-multipole particle (left) describing a point-charge distribution (right). Credits to the authors [115]

3.5.2.1.1 Corrections of type A

Periodic boundary conditions may be used in the system, but type A corrections are needed to account for flaws in precisely capturing the polarisation of the solvent by the charge caused by the use of approximations to the electrostatic interactions (e.g., truncations, shifting, reaction fields). This correction is not required because with the Ewald method as the summation in the limit of infinite system size correctly manages the electrostatics. There is no type A correction for direct Coulombic summations over a finite droplet of solvent or for Ewald-type summations with periodic boundary conditions.

3.5.2.1.2 Corrections of type B

The use of a finite system (such a droplet) or a finite-sized box with periodic boundary conditions that fails to show the polarisation of the solvent by the charge at great distances is corrected by this. The Ewald summation grows the system's size to infinity in the second example, but it does

so by creating periodic images. This calls for a modification. Therefore, rather than being polarised with respect to a single central charge (see Figure 1 of ref [92]) in one of the periodic pictures, the solvent is polarised with respect to the periodic image's representation of the charge. The type B adjustment for the finite droplet includes the estimate of solvent polarisation beyond the droplet's edge from the Born model. This can be expressed as

$$\Delta G_B(\text{droplet}) = -N_A Q^2 e^2 (1 - \epsilon_S^{-1}) / 8\pi\epsilon_0 S \quad (3.75)$$

In (3.83) S is the radius of the droplet and ϵ_S is the dielectric constant of the solvent predicted by the model. The correction for the Ewald summation using periodic boundary conditions is

$$\Delta G_B(\text{Ewald}) = \frac{-N_A Q^2 e^2}{8\pi\epsilon_0 L} \left[\frac{-M}{\epsilon_S} + (1 - \epsilon_S^{-1}) \left\{ \frac{4\pi}{3} \left(\frac{R_I}{L} \right)^2 - \frac{16\pi^2}{45} \left(\frac{R_I}{L} \right)^5 \right\} \right] \quad (3.76)$$

In (3.84) R_I represents the radius of the ion, L represents the length of the (cubic) box.

$M = -2.837297$ is the Madelung constant for a cubic array of like charges. In this formulation, the equation does not account for the basic Wigner correction term, $V_{Wigner} = \frac{-N_A Q^2 e^2}{8\pi\epsilon_0 L} M$,

while only describing the term the effect of dielectric screening on the Wigner potential.

This is due to the fact that V_{Wigner} is already taken into account^[87]. Since the adjustment is already accounted for in Simonson and Roux's free energies, they also omit it from equation (17). Since many codes (as mentioned above) already include this term, the type B adjustment for results produced using such codes is low and the dependency of the raw results (i.e., with no corrections at all) on the simulation box size is rather weak. The fundamental Wigner correction is specifically addressed in Hünenberger's (and Hummer's) formulations^[94,95] since their programmes either do not contain the basic Wigner correction or (as in ref [94]) explicitly deduct it from the raw data and add it to the correction.

$$\Delta G_B(\text{Ewald}) = \frac{-N_A Q^2 e^2}{8\pi\epsilon_0 L} (1 - \epsilon_S^{-1}) \left[-M + \frac{4\pi}{3} \left(\frac{R_I}{L} \right)^2 - \frac{16\pi^2}{45} \left(\frac{R_I}{L} \right)^5 \right] \quad (3.77)$$

The other terms in powers of R/L in equations (3.83) or (3.84) are negligible for box sizes comparable to the one used in this work.

3.5.2.1.3 Corrections of type C

The consequences of an erroneous electrostatic potential produced by the solvent at the location of the ion are taken into consideration by the C term. The specific summation technique employed for the electrostatics summations is to account for this. There are essentially only two conceivable processes. The electrostatic forces between the molecules are added after the electrostatic forces within the solvent molecule have been summed up (this is also known as the *M*-scheme). Or the alternative is to sum all the charges whether they are in separate molecules [*P*-scheme]. The Ewald summation is one example of a *P*-scheme. The possibility of a dipole at the border is seen to be significant because to the implications it has there (even though the boundary is infinitely far away). (See Figure 1 of reference [116], here reproduced as *Figure 3.8*. Take note that the authors do not come to the same findings as Hünenberger *et al*)

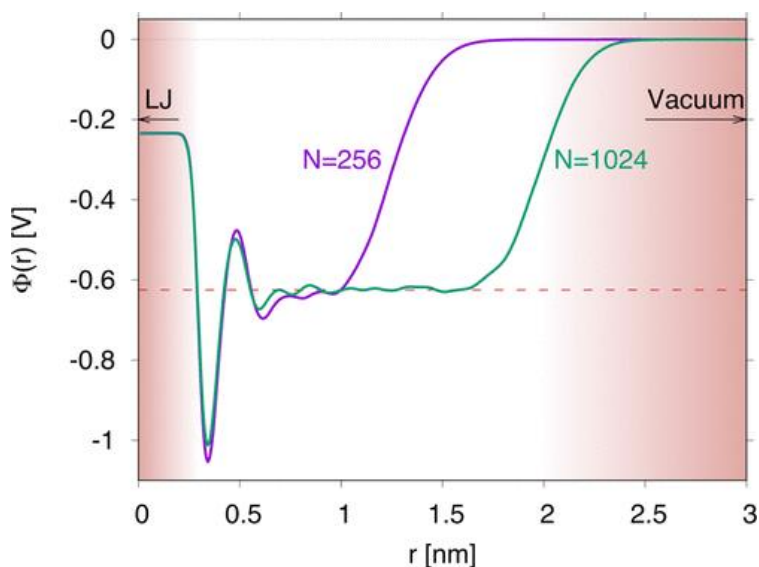


Figure 3.8 Radially averaged electric potential $\Phi(r)$ in units of volts as a function of the radial distance r from the center of water clusters with $N = 256$ (magenta) and 1024 (green) SPC water molecules at 298 K. Extracted from ref [116], see reference for further details. Reproduced with the author's permission

The electrostatic potential of the ion may then be affected, adding an energy term as a result. The following section will give more information about the solvent potentials.

The two issues we started with—the significance of the experimental results and the nature of the corrections needed for the summing methods—are connected by the type C corrections suggested in references^[85,94,95]. The fundamental concepts underlying these modifications are laid out in Appendix A of ref [108].

The transfer of charge into the centre of a large solvent droplet from a distant position in a vacuum results in a shift in potential known as the Galvani potential. An example of this is shown in Figure 1 in reference [96]. This needs to be considered while relating our simulated value to experiment. Three conventions exist for choosing the zero of potential when calculating the absolute potential in a cavity. The first is setting the zero outside of the liquid droplet, ϕ_R , (also called *R* convention), the second is setting the zero as an average over the bulk liquid, ϕ_P , (also called *P*-summation convention), and the third is setting the zero as an average over the bulk liquid but excluding the interior of the solvent molecules, ϕ_M , (*M*-summation convention).

The exclusion potential of the solvent model, ξ , is provided by $\phi_P - \phi_M$. This can be determined if the quadrupole moment trace of the solvent molecule is known. Nevertheless, this figure is totally arbitrary. We wish to carefully establish the exclusion potential so that our model can make an extra-thermodynamic assumption that is consistent with the Born model. The correction can be written as follows. The exclusion potential is given by

$$\xi = N_A \rho_S \gamma_S / 6 M_S \epsilon_0 \quad (3.78)$$

In (3.78) ρ_S represents the solvent density, M_S represents the molar molecular weight of the solvent (see Table below for clarification on units) and γ_S represents the trace of the quadrupole moment of the solvent molecule relative to its molecular centre, M . This can be assumed to be our water model's oxygen atom. Given $\gamma_S = \sum_{i=1}^n q_i \langle r_i^2 \rangle$, q_i is the charge on atom i , and $\langle r_i^2 \rangle$ is the expected value of the square of the H-O distance^[30] if a molecule is flexible. Every atom in the solvent molecule is included in the sum. The method of summing and the shift in potential at the

air-liquid interface lead to two different kinds of C corrections, respectively. This influence must be reduced since we use the natural free energy of hydration to connect with the Marcus numbers.

Since a droplet must contain a whole number of molecules and a straight coulombic summation is M-type, the initial adjustment for the finite droplet is zero. Given by is the overall type C correction (see ref [109] for all the details)

$$\Delta G_C(\text{droplet}; kJmol^{-1}) = -Q \left(70.3 - \frac{107.0}{S} \right) \quad (3.79)$$

In (3.79) Q , which is the cell charge due to a single ion, is expressed in units of $|e|$ and S , which is the droplet radius, is in units of nm. For the Ewald-type summation the total type-C correction is

$$\Delta G_C(\text{Ewald}; kJmol^{-1}) = \frac{-QN_A e f \xi}{1000} + Q(f - 1) \left(70.3 - \frac{10.9}{R_I} \right) \quad (3.80)$$

In (3.80) f represents the fraction of the box occupied by the solvent. If the ion is considered spherical then f can be expressed as

$$f = 1 - \frac{4\pi R_I^3}{3L^3} \quad (3.81)$$

R_I is the Born radius of the ion (and must be in nm in Equation (3.80)).

3.5.2.1.4 Corrections of type D

This accounts for inaccurate solvent permittivity assumptions that lead to inaccurate polarisation results. It is the same for all summation methods and often not significant. Since the thermodynamic parameters for hydration were derived using a unique definition of the standard state, there is also a correction. This holds true for all plans once more.

A Born model is applied to determine the effects of deviations from the forcefield-predicted dielectric constant. It can be expressed in the form^[113].

$$\Delta G_D = -N_A Q^2 e^2 (\varepsilon_{\text{expt}}^{-1} - \varepsilon^{-1}) / 8\pi\varepsilon_0 R_I \quad (3.82)$$

For this purpose, Marcus contains born radii that are accurate enough^[81, 82]. The correction has little influence on the free energies of hydration because of the large dielectric constant of water. The summaries in the cited references^[85,94,95] mention a cavity term. With the exception of the Coulomb terms, this describes all of the immediate effects of introducing a solute ion to a solution. If the thermodynamic integrations already take into account these interactions, this term should be ignored. Corrections stated in equation (3.76) must also be taken into account in order to fit Marcus^[2] and the definition of the standard state given above.

3.5.2.2 Calculating the corrections for example cases

Table 4.3.1 below shows the information needed to calculate the corrections. Also provided are the figures that were utilised to calculate the adjustments for the current study. The necessary adjustments to the present calculations are shown in the tables below.

Table 3.2. Data required for the corrections

Parameter	Value	Comment
q_0 ($ e $)	-0.82	SPC/Fw model; see reference [111] Table I
$\langle r_{OH} \rangle$ (nm)	0.1031	SPC/Fw model; see reference [111] Table II
ρ_S (gm cm ⁻³)	1.012	SPC/Fw model; see reference [111] Table II
M_S (kg)	0.018	Although we use the value of Avogadro's number for the gram molecular weight; M_S must be quoted in kg because the rest of the equation is given in SI units.
γ_S ($ e $ nm ²)	8.58×10^{-3}	Calculated using SPC/Fw data
ξ (V)	0.876	Calculated from Equation (3.90) for SPC/Fw model
ξ_S	79.63	SPC/Fw model; see reference [111] Table II

ϵ_{expt}	80.10	293K; <i>Book of data</i> (Nuffield 1972) ed. R.D. Harrison; p 122.		
L (nm)	4.56	Unit cell length (cubic; 3200 water molecules)		
S (nm)	2.83	Droplet radius (assumed spherical with same number of solvent molecules as the simulation cell).		
R_I (nm) - Na ⁺	0.102	Ionic radius (Marcus ^[2] Table 2)	$f - I$ (Na ⁺)	-4.688 x 10 ⁻⁵
R_I (nm) - K ⁺	0.138		$f - I$ (K ⁺)	-1.161 x 10 ⁻⁴
R_I (nm) - NO ₃ ⁻	0.179		$f - I$ (NO ₃ ⁻)	-2.534 x 10 ⁻⁴
R_I (nm) - Cl ⁻	0.181		$f - I$ (Cl ⁻)	-2.620 x 10 ⁻⁴
R_I (nm) - Br ⁻	0.196		$f - I$ (Br ⁻)	-3.326 x 10 ⁻⁴
R_I (nm) - CO ₃ ²⁻	0.178		$f - I$ (CO ₃ ²⁻)	-2.491 x 10 ⁻⁴
R_I (nm) - SO ₄ ²⁻	0.240		$f - I$ (SO ₄ ²⁻)	-6.107 x 10 ⁻⁴

Table 3.3 Droplet corrections

Ion	Correction	Value (kJ mol ⁻¹)	Ion	Correction	Value (kJ mol ⁻¹)
K ⁺	ΔG_A	0	NO ₃ ⁻	ΔG_A	0
	ΔG_B	-24.3		ΔG_B	-24.3
	ΔG_C	-32.5		ΔG_C	+32.5
	ΔG_{std}	+7.93		ΔG_{std}	+7.93
	TOTAL	-48.9		TOTAL	+16.1

Table 3.4 Ewald corrections

Ion	Correction	Value (kJ mol⁻¹)	Ion	Correction	Value (kJ mol⁻¹)
Na ⁺	ΔG_A	0	Cl ⁻	ΔG_A	0
	ΔG_B	+0.8		ΔG_B	+1.0
	ΔG_C	-84.5		ΔG_C	+84.5
	ΔG_{std}	+7.93		ΔG_{std}	+7.93
	TOTAL	-75.8		TOTAL	+93.4
<hr/>					
Ion	Correction	Value (kJ mol⁻¹)	Ion	Correction	Value (kJ mol⁻¹)
K ⁺	ΔG_A	0	NO ₃ ⁻	ΔG_A	0
	ΔG_B	+1.1		ΔG_B	1.1
	ΔG_C	-84.5		ΔG_C	+84.5
	ΔG_{std}	+7.93		ΔG_{std}	+7.93
	TOTAL	-75.5		TOTAL	+93.5
<hr/>					
Ion	Correction	Value (kJ mol⁻¹)	Ion	Correction	Value (kJ mol⁻¹)
Ca ²⁺	ΔG_A	0	CO ₃ ²⁻	ΔG_A	0
	ΔG_B	+4.4		ΔG_B	+4.4

	ΔG_C	-169		ΔG_C	+169
	ΔG_{std}	+7.93		ΔG_{std}	+7.93
	TOTAL	-156.7		TOTAL	+181.3
Ion	Correction	Value (kJ mol⁻¹)	Ion	Correction	Value (kJ mol⁻¹)
Br ⁻	ΔG_A	0	SO ₄ ²⁻	ΔG_A	0
	ΔG_B	1.1		ΔG_B	+4.4
	ΔG_C	+84.5		ΔG_C	+169
	ΔG_{std}	+7.93		ΔG_{std}	+7.93
	TOTAL	+93.5		TOTAL	+181.3

3.5.3 Conclusions

To summarise all the previous discussions, it is possible to notice that regarding the type A and B adjustments, there is no disagreement. Everyone (in one manner or another) has demonstrated the insignificance of the terms and have included them when it was appropriate. They mostly concern the finite size of the simulation and how that impacts the polarisation effects for charged systems. Finding out which corrections have already been included into a certain software is the main problem.

Type C adjustments are the subject of much more controversy. The core of the issue is what needs to be computed in order to connect with the experiment. Raiteri *et al* claim in their study that they are referring to the *P*-summation from Hummer *et al* but they do not give a further explanation of the form in which they are incorporating said correction. The problem is that whether you choose to include or omit the type C variables depends on the boundary conditions of your computation,

which must coincide with the implicit choice made in the experimental data with which you will be comparing findings. This is the rationale behind Hünenberger *et al*^[85] differentiation between their "intrinsic" and "actual" numbers.

The key distinction in this case is whether or not one considers how the charged ion's potential is impacted by crossing the boundary. These effects are removed from the Ewald-type summations by the type C adjustment because experimentalists often do not include them (creating "intrinsic" values). This is merely a claim that the calculations performed by Hummer *et al*^[96] differ from those that were performed. If the same process is utilised throughout, either summation type can be used to get "real" figures that account for the impacts of the interface potential.

In light of the adjustments to the free energy of hydration for both the Ca^{2+} and CO_3^{2-} ion, we may examine the degree of agreement of the Raiteri *et al* force-field^[8]. Table 4 displays two values for the absolute free energy of hydrating Ca^{2+} : $-1447 \text{ kJ mol}^{-1}$ and $-1503 \text{ kJ mol}^{-1}$ (potential set 1) (potential set 2). The uncorrected values of Marcus^[81] and David^[113] of $-1505 \text{ kJ mol}^{-1}$ and $-1446 \text{ kJ mol}^{-1}$, respectively, might be used to reflect the experimental results in contrast to these.

Marcus and David both use the same absolute free energy value for proton hydration; therefore both values require the same correction, resulting in updated values of $-1534 \text{ kJ mol}^{-1}$ for Marcus and $-1593 \text{ kJ mol}^{-1}$ for David. The Type C adjustment is the main thing Rateri's calculations leave out. These numbers become $-1660 \text{ kJ mol}^{-1}$ (potential set 1, the one from the autor) and $-1604 \text{ kJ mol}^{-1}$ when this is accounted for (potential set 2, the one with included corrections).

Strong agreement between this and the set 2 corrected Marcus value is provided. Marcus's measurements are the only ones available for the carbonate anion, and after correction, they yield a value of $-1227 \text{ kJ mol}^{-1}$. Raiteri's uncorrected results for potential set 1 are $-1175 \text{ kJ mol}^{-1}$ and $-1301 \text{ kJ mol}^{-1}$ (potential set 2). After rectification, these are changed to -994 kJ mol^{-1} (potential set 1) and $-1120 \text{ kJ mol}^{-1}$ (potential set 2). The best forcefield is still Set 2, but it is around 100 kJ mol^{-1} too positive. However, their core argument - that set 2 is generally better than set 1 - is still valid and, if anything, is enhanced, which is a fortunately unexpected development.

3.6 References

- [1] J.D. Gale, *GULP: A computer program for the symmetry-adapted simulation of solids*, J. Chem. Soc., Faraday Trans., 1997, **93**(4), 629-637;
- [2] L. Greengard, V. Rokhlin, *A fast algorithm for particle simulations*, J. Comput. Phys., 1987, **73**, 325–348;
- [3] R. Benages-Vilau, T. Calvet, M.À. Cuevas-Diarte, *Polymorphism, crystal growth, crystal morphology and solid-state miscibility of alkali nitrates*, Crystallography Reviews, 2014, **20**:1, 25-55;
- [4] G.V. Lewis, C.R.A. Catlow, *Potential models for ionic oxides*, Journal of Physics C-Solid State Physics, 1985, **18**(6), 1149-1161.
- [5] J.E. Lennard-Jones, *On the Determination of Molecular Fields*, Proc. R. Soc. Lond., 1924, A, **106** (738): 463–477;
- [6] R.A. Buckingham, *The Classical Equation of State of Gaseous Helium, Neon and Argon*, Proceedings of the Royal Society, 1938, A. **168** (933), 264–283;
- [7] J. D. Gale, *General Utility Lattice Program*, version 5.2, Curtin University;
- [8] P. Raiteri, J.D. Gale, D. Quigley, P.M. Rodger, *Thermodynamically Consistent Force-field for Molecular Dynamics Simulations of Alkaline-Earth Carbonates and Their Aqueous Speciation*, J. Phys. Chem. C, 2010, **114**, 5997–6010;
- [9] R. Demichelis, P. Raiteri, J.D. Gale, D. Quigley, D. Gebauer, *Stable Prenucleation Mineral Clusters Are Liquid-Like Ionic Polymers*, Nat. Commun., 2011, **2**, 590;
- [10] H. Yu, T. Whitfield, E. Harder, G. Lamoureux, I. Vorobyov, V. Anisimov, A. MacKerell, B. Roux, *Simulating Monovalent and Divalent Ions in Aqueous Solution Using a Drude Polarizable Force-field*, J. Chem. Theory Comput., 2010, **6**, 774–786;
- [11] A. Saxena, D. Sept, *Multisite Ion Models That Improve Coordination and Free Energy Calculations in Molecular Dynamics Simulations*, J. Chem. Theory Comput, 2013, **9**, 3538–3542;
- [12] K.M. Callahan, N.N. Casillas-Ituarte, M. Roeselová, H.C. Allen, D.J. Tobias, *Solvation of Magnesium Dication: Molecular Dynamics Simulation and Vibrational Spectroscopic Study of Magnesium Chloride in Aqueous Solutions*, J. Phys. Chem. A, 2010, **114**, 5141–5148;
- [13] D. Jiao, C. King, A. Grossfield, T.A. Darden, P. Ren, *Simulation of Ca^{2+} And Mg^{2+} Solvation Using Polarizable Atomic Multipole Potential*, J. Phys. Chem. B, 2006, **110**, 18553–18559;
- [14] C.S. Babu, C. Lim, *Empirical Force-fields for Biologically Active Divalent Metal Cations in Water*, J. Phys. Chem. A, 2006, **110**, 691–699;
- [15] R.P. Matthews, K.J. Naidoo, *Experimentally Consistent Ion Association Predicted for Metal Solutions From Free Energy Simulations*, J. Phys. Chem. B, 2010, **114**, 7286–7293;

- [16] J. Aqvist, *Ion-Water Interaction Potentials Derived From Free Energy Perturbation Simulations*, J. Phys. Chem., 1990, **94**, 8021–8024;
- [17] A. Pavese, M. Catti, G.D. Price, R.A. Jackson, *Interatomic Potentials for CaCO₃ Polymorphs (Calcite and Aragonite), Fitted to Elastic and Vibrational Data*, Phys. Chem. Miner., 1992, **19**, 80–87;
- [18] D.K. Fidler, J.D. Gale, R.T. Cygan, *A Shell Model for the Simulation of Rhombohedral Carbonate Minerals and Their Point Defects*, Am. Mineral., 2000, **85**, 217–224;
- [19] S. Hwang, M. Blanco, W.A. Goddard III, *Atomistic Simulations of Corrosion Inhibitors Adsorbed on Calcite Surfaces I. Force-field Parameters for Calcite*, J. Phys. Chem. B, 2001, **105**, 10746–10752;
- [20] R.T. Cygan, K. Wright, D.K. Fidler, J.D. Gale, B. Slater, *Atomistic Models of Carbonate Minerals: Bulk and Surface Structures, Defects, and Diffusion*, Mol. Simul., 2002, **28**, 475–495;
- [21] T. Archer, S. Birse, M.T. Dove, S. Redfern, J.D. Gale, R.T. Cygan, *An Interatomic Potential Model for Carbonates Allowing for Polarization Effects*, Phys. Chem. Miner., 2003, **30**, 416–424;
- [22] A. Rohl, K. Wright, J.D. Gale, *Evidence From Surface Phonons for the (2 × 1) Reconstruction of the (10–14) Surface of Calcite From Computer Simulation*, Am. Mineral., 2003, **88**, 921–925;
- [23] S. Xiao, S.A. Edwards, F.A. Grater, *New Transferable Forcefield for Simulating the Mechanics of CaCO₃ Crystals*, J. Phys. Chem. C, 2011, **115**, 20067–20075;
- [24] N.H. de Leeuw, S.C. Parker, *Surface Structure and Morphology of Calcium Carbonate Polymorphs Calcite, Aragonite, and Vaterite: an Atomistic Approach*, J. Phys. Chem. B, 1998, **102**, 2914–2922.
- [25] F. Bruneval, D. Donadio, M. Parrinello, *Molecular Dynamics Study of the Solvation of Calcium Carbonate in Water*, J. Phys. Chem. B, 2007, **111**, 12219–12227;
- [26] P. Raiteri, J.D. Gale, D. Quigley, P.M. Rodger, *Derivation of an Accurate Force-Field for Simulating the Growth of Calcium Carbonate From Aqueous Solution: a New Model for the Calcite– Water Interface*, J. Phys. Chem. C, 2010, **114**, 5997–6010;
- [27] P. Raiteri, J.D. Gale, *Water Is the Key to Nonclassical Nucleation of Amorphous Calcium Carbonate*, J. Am. Chem. Soc., 2010, **132**, 17623–17634;
- [28] H. Tomono, H. Nada, F. Zhu, T. Sakamoto, T. Nishimura, T. Kato, *Effects of Magnesium Ions and Water Molecules on the Structure of Amorphous Calcium Carbonate: a Molecular Dynamics Study*, J. Phys. Chem. B, 2013, **117**, 14849–14856;
- [29] J.D. Gale, *Empirical Potential Derivation for Ionic Materials*, Philos. Mag. B, 1996, **73**, 3–19;
- [30] M.E. Tuckerman, *Statistical Mechanics: Theory and Molecular Simulation*, 2009, Oxford University Press;
- [31] H.D. Herce, A.E. Garcia, T. Darden, *The electrostatic surface term: (I) Periodic systems*, The Journal of Chemical Physics, 2007, **126** (12): 124106;
- [32] J. Mei, J.W. Davenport, G.W. Fernando, *Analytic embedded-atom potentials for fcc metals: Application to liquid and solid copper*, Phys Rev B, 1991, **43**, 4653;

- [33] R. Mittal, S. L. Chaplot, *Lattice dynamical calculation of isotropic negative thermal expansion in ZrW₂O₈ over 0–1050 K*, Phys. Rev., 1999, **B 60**, 7234 ;
- [34] S. Clark, “*Introduction to CASTEP*”, University of Durham, 2012;
- [35] G.W. Watson, P.M. Oliver, S.C. Parker, *Computer simulation of the structure and stability of forsterite surfaces*, Phys Chem Minerals, 1997, **25**, 70–78;
- [36] W. Smith, T.R. Forester, *DL_POLY_2.0: A general-purpose parallel molecular dynamics simulation package*, J. Molec. Graphics, 1996, **14**, 136. 3;
- [37] I.T. Todorov, W. Smith, 2004, *The DL_POLY user manual*, Phil. Trans. R. Soc. Lond. A, **362**, 1835. 3, 227;
- [38] I.T. Todorov, W. Smith, K. Trachenko, M.T. Dove, *DL_POLY*, 2006, J. Mater. Chem., **16**, 1611–1618. 3, 227;
- [39] S. Plimpton, *Fast Parallel Algorithms for Short-Range Molecular Dynamics*, J. Comput. Phys., 1995, 117, 1–19;
- [40] A. Leach, *Molecular Modelling: Principles and Applications (2nd Edition)*, 2001, Prentice Hall;
- [41] R. Fletcher, C.M. Reeves, *Function minimization by conjugate gradients*. The Computer Journal, 1964. **7**(2), 149-154;
- [42] M.J. Norgett, R. Fletcher, *Fast matrix methods for calculating the relaxation about defects in crystals*. Journal of Physics Part C Solid State Physics, 1970, **3**(11), L190-&.
- [43] B. J. Alder, T. E. Wainwright, *Studies in Molecular Dynamics. I. General Method*, The Journal of Chemical Physics, 1959, **31** (2), 459–466;
- [44] D. Frenkel, B. Smit, *Understanding molecular simulation: from algorithms to applications*, 2002, 2nd ed., San Diego. ISBN 978-0-08-051998-2. OCLC 173686073;
- [45] N. Metropolis, A.W. Rosenbluth, M.N. Rosenbluth, A.H. Teller, E.J. Teller, *Equation of State Calculations by Fast Computing Machines*, The Journal of Chemical Physics, 1953, **21**, 1078-1092;
- [46] S. Toxvaerd, O.J. Heilmann, J.C. Dyre, *Energy conservation in molecular dynamics simulations of classical systems*, Journal of Chemical Physics, 2012, **136**(22);
- [47] R.W. Hockney, J.W. Eastwood, *Computer simulations using particles*, 1981, New York: McGraw-Hill;
- [48] W.C. Swope, H.C., Andersen, P.H. Berens, K.R. Wilson, *A computer simulation method for the calculation of equilibrium constants for the formation of physical clusters of molecules: Application to small water clusters*, Journal of Chemical Physics, 1982. **76**(1), 637-649;
- [49] L. Verlet, *Computer" experiments" on classical fluids. I. Thermodynamical properties of Lennard-Jones molecules*, Physical Review, 1967. **159**(1), 98-&;
- [50] S. Nose, *A Unified Formulation of the Constant Temperature Molecular-Dynamics Methods*, Journal of Chemical Physics, 1984. **81**(1), 511-519;

- [51] S. Nose, *A molecular dynamics method for simulations in the canonical ensemble*, *Molecular Physics*, 1984, **52**(2), 255-268;
- [52] W.G. Hoover, *Canonical dynamics: equilibrium phase-space distributions*, *Physical Review A*, 1985, **31**(3), 1695-1697;
- [53] L. Verlet, *Computer "Experiments" on Classical Fluids. I. Thermodynamical Properties of Lennard-Jones Molecules*, *Physical Review*, 1967, **159** (1), 98–103;
- [54] L.D. Landau, E.M. Lifshitz, *Statistical Physics. Course of Theoretical Physics. 5 (3 ed.)*. Oxford: Pergamon Press., 1980;
- [55] H.A. Posch, *Canonical dynamics of the Nosé oscillator: Stability, order, and chaos*, *Physical Review*, 1986, **A. 33** (6), 4253–4265.;
- [56] W.G. Hoover, B.L. Holian, *Kinetic moments method for the canonical ensemble distribution*, *Physics Letters A.*, 1996, **211** (5), 253–257;
- [57] H. J. C. Berendsen, J. P. M. Postma, W. F. van Gunsteren, A. DiNola, J.R. Haak, *Molecular-Dynamics with Coupling to an External Bath*, *Journal of Chemical Physics*, 1984, **81** (8), 3684–3690;
- [58] H. C. Andersen, *Molecular dynamics simulations at constant pressure and/or temperature*, *The Journal of Chemical Physics*, 1980, **72** (4), 2384;
- [59] H. Tanaka, *Constant temperature molecular dynamics calculation on Lennard-Jones fluid and its application to water*, *The Journal of Chemical Physics*, 1983, **78** (5), 2626;
- [60] T. Schlick, *Molecular Modeling and Simulation*, Springer, 2002, 480;
- [61] P. Attard, *On the density of volume states in the isobaric ensemble*, *Journal of Chemical Physics*, 1995, **103** (24), 9884–9885;
- [62] The PLUMED consortium. Promoting transparency and reproducibility in enhanced molecular simulations, *Nat. Methods* 16, 670 (2019);
- [63] G.A. Tribello, M. Bonomi, D. Branduardi, C. Camilloni, G. Bussi, *PLUMED2: New feathers for an old bird*, *Comp. Phys. Comm.*, 2014, **185**, 604, preprint available as arXiv:1310.0980;
- [64] M. Bonomi, D. Branduardi, G. Bussi, C. Camilloni, D. Provasi, P. Raiteri, D. Donadio, F. Marinelli, F. Pietrucci, R.A. Broglia, M. Parrinello, *PLUMED: a portable plugin for free energy calculations with molecular dynamics*, *Comp. Phys. Comm.*, 2009, **180**, 1961, preprint available as arXiv:0902.0874;
- [65] S. J. Clark, M. D. Segall, C. J. Pickard, P. J. Hasnip, M. J. Probert, K. Refson, M. C. Payne, *First principles methods using CASTEP*, *Zeitschrift fuer Kristallographie*, 2005, **220**(5-6), 567-570;
- [66] K. Burke, *Perspective on density functional theory*, *J. Chem. Phys.*, 2012, **136**, 150901;
- [67] D. C. Langreth, M. J. Mehl, *Beyond the local-density approximation in calculations of ground-state electronic properties*, *Phys. Rev.*, 1984, **B 29**, 2310;

- [68] J. P. Perdew, K. Burke, M. Ernzerhof, *Generalized Gradient Approximation Made Simple*, Phys. Rev. Lett., 1996, **77**, 3865;
- [69] M. Ernzerhof, G. E. Scuseria, *Assessment of the Perdew–Burke–Ernzerhof exchange-correlation functional*, J. Chem. Phys., 1999, **110**, 5029;
- [70] S. Ehrlich, L. Goerigk, *DFT-D3: SG*, J. Chem. Phys., 2010, **132**, 154104; J. Antony, H. Krieg, S. Ehrlich, *DFT-D3(BJ): SG*, J. Comput. Chem., 2011, **32**, 1456;
- [71] F. London, *Zur Theorie und Systematik der Molekularkräfte*, Zeitschrift für Physik, 1930, **63** (3–4), 245;
- [72] H. J. Monkhorst, J. D. Pack, *Special points for Brillouin-zone integrations*, Phys. Rev., **B 13**, 1976, 5188;
- [73] P. P. Ewald, *Die Berechnung optischer und elektrostatischer Gitterpotentiale*, Annalen der Physik, 1921, **369**(3), 253-287;
- [74] A. Leach, *Molecular Modelling: Principles and Applications* (2nd Edition), 2001: Prentice Hall;
- [75] A. Aguado, P. A. Madden, *Ewald summation of electrostatic multipole interactions up to the quadrupolar level*, Journal of Chemical Physics, 2003, **119**(14), 7471-7483;
- [76] A. Görling, *Density-functional theory beyond the Hohenberg-Kohn theorem*, Phys. Rev. A, 1999, **59**, 3359–3374;
- [77] J. P. Perdew, K. Schmidt, *Jacob's ladder of density functional approximations for the exchange-correlation energy*, AIP Conference Proceedings, 2001, **577**, 1–20;
- [78] A. Bonvicini, *Theoretical studies of linear and non-linear optical properties of biomolecules*, PhD thesis, 2019, Normandie Université;
- [79] G. Kresse, J. Furthmüller, *Efficient iterative schemes for ab initio total-energy calculations using a plane-wave basis set*, Phys. Rev. B, 1996, **54**, 11169–11186;
- [80] J. E. Dennis, R. B. Schnabel, *"Secant Methods for Unconstrained Minimization"*, *Numerical Methods for Unconstrained Optimization and Nonlinear Equations*, Englewood Cliffs, NJ: Prentice-Hall, 1983, 194–215, ISBN 0-13-627216-9;
- [81] Y. Marcus, *The thermodynamics of solvation of ions. Part 4.—Application of the tetraphenylarsonium tetraphenylborate (TATB) extrathermodynamic assumption to the hydration of ions and to properties of hydrated ions*, J. Chem. Soc. (Faraday), 1987, **83**, 2985;
- [82] Y. Marcus, *A simple empirical model describing the thermodynamics of hydration of ions of widely varying charges, sizes, and shapes*, Biophysical Chemistry, 1994, **51**, 111;
- [83] D. D. Wagman, W. H. Evans, V. B. Parker, R. H. Schumm, I. Halow, S. M. Bailey, K. L. Churney and R. L. Nuttall, *The NBS Tables of Chemical Thermodynamic Properties: Reference Data*, Journal of Physical Chemistry, 1982, **11**, Supplement 2;

- [84] M.D. Tissandier, K.A. Cowen, W. Yong Feng, E. Gundlach, M.H. Cohen, A.D. Earhart, J.V. Coe, T.R. Tuttle, *The Proton's Absolute Aqueous Enthalpy and Gibbs Free Energy of Solvation from Cluster-Ion Solvation Data*, J. Phys. Chem. A, 1998, **102**, 7787;
- [85] T.S. Hofer, P.H. Hünenberger, *First-principles modeling of chemistry in mixed solvents: Where to go from here?*, J. Chem. Phys., 2018, **148**, 222814;
- [86] A. Malloum, J.J. Fifen, J. Conradie, *Determination of the absolute solvation free energy and enthalpy of the proton in solutions*, J. Mol. Liq., 2021, **322**, 114919;
- [87] N. Prasetyo, P.H. Hünenberger, T.S. Hofer, *Single-Ion Thermodynamics from First Principles: Calculation of the Absolute Hydration Free Energy and Single-Electrode Potential of Aqueous Li⁺ Using ab Initio Quantum Mechanical/Molecular Mechanical Molecular Dynamics Simulations*, Journal of Chemical Theory and Computation, 2018, **14** (12), 6443-6459;
- [88] E.H. Byrne, P. Raiteri, J.D. Gale, *Computational Insight into Calcium–Sulfate Ion Pair Formation*, J. Phys. Chem. C, 2017, **121**, 25956;
- [89] Y. Marcus, *The thermodynamics of solvation of ions. Part 2.—The enthalpy of hydration at 298.15 K*, J. Chem. Soc. (Faraday I), 1986, **83**, 339;
- [90] W.R. Cannon, B.M. Petit, J.A. McCammon, *Sulfate Anion in Water: Model Structural, Thermodynamic, and Dynamic Properties*, J. Phys. Chem., 1994, **98**, 6225;
- [91] Y. Marcus, *The hydration entropies of ions and their effects on the structure of water*, J. Chem. Soc. (Faraday I), 1986, **82**, 233
- [92] P.H. Hünenberger, J.A. McCammon, *Ewald artifacts in computer simulations of ionic solvation and ion–ion interaction: A continuum electrostatics study*, J. Chem Phys., 1999, **110**, 856;
- [93] G. Hummer, L.R. Pratt and A.E. Garcia, *Electrostatic Potentials and Free Energies of Solvation of Polar and Charged Molecules*, J. Chem Phys., 1996, **100**, 1206; J. Chem. Phys., 1997, **107**, 1275;
- [94] M.A. Kastholz, P.H. Hünenberger, *Computation of methodology-independent ionic solvation free energies from molecular simulations. II. The hydration free energy of the sodium cation*, J. Chem. Phys., 2006, **124**, 224501;
- [95] M.M. Reif, P.H. Hünenberger, *Computation of methodology-independent single-ion solvation properties from molecular simulations. IV. Optimized Lennard-Jones interaction parameter sets for the alkali and halide ions in water*, J. Chem. Phys., 2011, **134**, 144104;
- [96] T. Simonson, G. Hummer, B. Roux, *Equivalence of M- and P-Summation in Calculations of Ionic Solvation Free Energies*, J. Phys. Chem. A, 2017, **121**, 1525;
- [97] R. Ayala, M. Sprik, *A Classical Point Charge Model Study of System Size Dependence of Oxidation and Reorganization Free Energies in Aqueous Solution*, J. Phys. Chem. B, 2008, **112**, 257;
- [98] M.P. Allen, D.J. Tildesley, *Computer simulation of liquids; 2nd edition* (Cambridge 2017) Chapter 6;

- [99] K. Fuchs, *A quantum mechanical investigation of the cohesive forces of metallic copper*, Proc. Roy. Soc. A, 1935, **151**, 585;
- [100] M. Leslie, M.J. Gillan, *The energy and elastic dipole tensor of defects in ionic crystals calculated by the supercell method*, J. Phys. C, 1985, **18**, 973;
- [101] V. Ballenegger, J.J. Cerda, O. Lenz, C. Holm, *P3M algorithm for dipolar interactions*, J. Chem. Phys., 2008, **128**, 034109;
- [102] T. Darden, D. Pearlman, L.G. Pedersen, *Ionic charging free energies: Spherical versus periodic boundary conditions*, J. Chem. Phys., 1998, **109**, 10921;
- [103] J.S. Hub, B.L. de Groot, H. Grubmüller, G. Groenhof, *Quantifying Artifacts in Ewald Simulations of Inhomogeneous Systems with a Net Charge*, J. Chem. Theo. Comp. 2014, **10**, 381;
- [104] T. Simonson, B. Roux, *Concepts and protocols for electrostatic free energies*, Molec. Sim., 2016, **42**, 1090;
- [105] D. Horinek, S.I. Mamatkulov, R.R. Netz, *Rational design of ion force-fields based on thermodynamic solvation properties*, J. Chem. Phys., 2009, **130**, 124507;
- [106] B.R. Brooks, C.L. Brooks, A.D. MacKerell, Jr., L. Nilsson, R.J. Petrella, B. Roux, Y. Won, G. Archontis, C. Bartels, S. Boresch, A. Caflisch, L. Caves, Q. Cui, A.R. Dinner, M. Feig, S. Fischer, J. Gao, M. Hodoscek, W. Im, K. Kuczera, T. Lazaridis, J. Ma, V. Ovchinnikov, E. Paci, R.W. Pastor, C.B. Post, J.Z. Pu, M. Schaefer, B. Tidor, R.M. Venable, H.L. Woodcock, X. Wu, W. Yang, D.M. York, M. Karplus, *CHARMM: The Biomolecular Simulation Program*, J. Comp. Chem. 2009, **30**, 1545;
- [107] E. Lindahl, M. Abraham, B. Hess, D. van der Spoel, GROMACS Documentation (release 2021.3);
- [108] G. Hummer, L.R. Pratt, A.E. Garcia, B.J. Berne, S.W. Rick, *Hydration Free Energy of Water*, J Phys Chem B, 1997, **101**, 3017;
- [109] M.M. Reif, P.H. Hünenberger, *Origin of Asymmetric Solvation Effects for Ions in Water and Organic Solvents Investigated Using Molecular Dynamics Simulations: The Swain Acity–Basity Scale Revisited*, J Phys Chem B, 2016, **120**, 485;
- [110] T.T. Duignan, M.D. Baer, G.K. Schenter, C.J. Mundy, *Electrostatic solvation free energies of charged hard spheres using molecular dynamics with density functional theory interactions*, J. Chem. Phys., 2017, **147**, 161716;
- [111] M.A. Kastholz, P.H. Hünenberger, *Computation of methodology-independent ionic solvation free energies from molecular simulations: I. The electrostatic potential in molecular liquids*, J. Chem. Phys., 2006, **124**, 124106;
- [112] Y. Wu, H.L. Tepper, G.A. Voth, *Flexible simple point-charge water model with improved liquid-state properties*, J. Chem. Phys., 2006, **124**, 024503;

- [113] F. David, V. Vokhmin, G. Ionova, *Water characteristics depend on the ionic environment. Thermodynamics and modelisation of the aquo ions*, J. Mol. Liq., 2001, **90**, 45;
- [114] M. Feig, *Modelling Solvent Environments: Applications to Simulations of Biomolecules*, Wiley, 2010
- [115] B. Stenqvist, V. Aspelin, M. Lund, *Generalized Moment Correction for Long-Ranged Electrostatics*, J. Chem. Theory Comput., 2020, **16**, 6, 3737-3745
- [116] T. Simonson, G. Hummer, B. Roux, *Equivalence of M- and P-Summation in Calculations of Ionic Solvation Free Energies*, J. Phys. Chem. A, **121** (2017) 1525

Chapter 4

Force-field fitting

A large amount of the work of this chapter is published in

V Fantauzzo et al 2022 *J. Phys. Commun.* 6 055011, <https://doi.org/10.1088/2399-6528/ac6e2b>

4.1 Introduction

Modelling any system relies on good quality force-fields, which must be as accurate and consistent as possible without being computationally expensive. It is essential to balance computational cost against the ability of the simulation to reproduce the observed phenomena. In this chapter, we fit a reliable set of force-fields in order to be able to simulate the nucleation and growth of the alkali metal nitrates and use them to help understand the mechanisms of crystallisation.

The shortcomings of the various existing force-fields, that would affect our use of them, are discussed in detail in this Chapter. Briefly, Ni^[7], Xie^[8] and Mort^[9] fail to obtain the correct order for the relative energy of polymorphs in some nitrates; Ribeiro^[6] fails to optimise several crystal structures; none of the models (except that of Hammond^[5]) predict real values for all the high-symmetry branches of the phonon spectra of the polymorphs to which they were fitted (showing that the true predicted structure must be of lower symmetry than the ones considered). The existing force-fields are adequate for the purposes they were intended for but there is clearly room for improvement. Also, there is no force-field that is suitable for all the alkali metal nitrates, their solution chemistry and their solid state solutions.

4.1.1 Structures of the alkali metal nitrates

As previously mentioned in Chapter 2, all the alkali metal nitrates present various polymorphs and the ones shown in Figure 4.1 will be the main focus of this study.

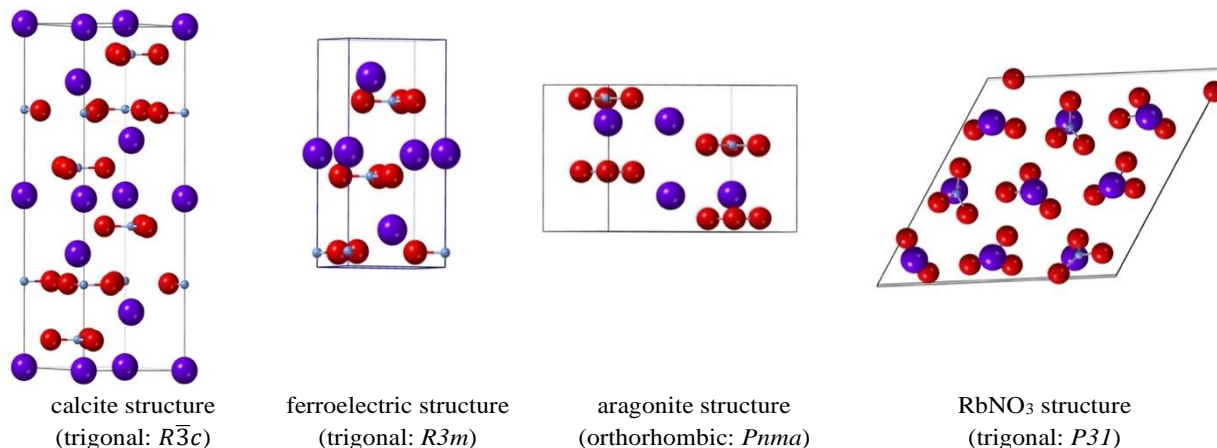


Figure 4.1 Structures of the phases of the alkali metal nitrates that are used in the fitting. Purple spheres are the alkali metal ions; light blue spheres are the nitrogen atoms; red spheres are the oxygen atoms.

4.2 Methodologies

We require a force-field that can describe alkali metal nitrates equally well in a solution and as a solid phase. To keep the costs of molecular dynamics simulations down, a rigid ion model with flexible nitrate ions was used. This type of model has proved successful for many molecular ions, in particular the carbonates and sulphates. Full ionic charges ($q_M = 1$) are used for the alkali metal ions. The fitting of charges on the nitrogen and oxygen atoms is discussed below. Buckingham potentials were used for all intermolecular interactions except for those between the alkali metal cations where the Lennard-Jones form was used for consistency with the model of Joung and Cheatham^[26], frequently used to study solution chemistry of the alkali halides. The parameters for these interactions are given in Table 4.1.

Table 4.1 Interactions between alkali metal ions^[26] $q_M = 1.0$ for $M = \text{Li-Cs}$ where ϵ and R_{min} are defined as the energy and interatomic distance at the minimum, i.e. we use the Lennard-Jones potential in the form

$$V(r) = \epsilon \left[\left(\frac{R_{min}}{r} \right)^{12} - 2 \left(\frac{R_{min}}{r} \right)^6 \right]$$

Alkali ions	ϵ (eV)	R_{min} (Å)
Li-Li	0.01459	1.582
Na-Na	0.01528	2.424
K-K	0.01860	3.186
Rb-Rb	0.01930	3.474
Cs-Cs	0.00390	4.042

A force-field developed by Raiteri *et al.*^[27] for the carbonate anion was used as a starting point for the nitrate but with the initial partial charges adjusted (using charges from electronic structure calculations as a guide) to give the correct overall charge on the nitrate anion and subsequently fitted to the crystal structures and properties as described below. To describe the interactions within the nitrate group, harmonic interactions were used for the N-O bond and three-body bond-angle potentials used to maintain the preferred angle between the bonds. Further many-body interactions were added (as specified by Raiteri *et al.*) to maintain the planarity of the nitrate anion. Coulomb subtraction was applied within all the nitrate molecules. Examination of the Raman lines demonstrated that the internal interactions of the carbonate group could approximate the internal interactions of the nitrate group. The force-field for the nitrate anion is given in Table 4.2. A tapering cut-off for the short-range intermolecular potentials was applied during the fitting. The basic interatomic interaction is multiplied by an additional mathematical function that smooths both its energy and derivatives to zero at the cut-off. In this case, r_m was set at 6.0 Å and r_{cut} at 9.0 Å.

4.2.1 Fitting procedures

The GULP^[29,30] code was used to fit the force-fields using the relaxed fitting algorithm^[31].

Details of the code, including the methods used to calculate the long-range electrostatic summations, can be found in Chapter 3 and Section 4.5 of this chapter. An iterative procedure was used to obtain the charges on the nitrogen and oxygen atoms. First, the individual nitrates were fitted to experimental data to obtain interactions between the alkali metal ions and the atoms of the nitrate anion. Then the nitrogen charge, q_N , and short-range oxygen-oxygen intermolecular interactions were refitted to data for the observed low temperature polymorphs of all the alkali earth nitrates together, assuming that the intramolecular interactions of the nitrate ions and the intermolecular interactions (including electrostatic interactions) between the nitrate ions were the same for all the alkali metal nitrates. The oxygen charge, q_O , is fixed by the requirement that the total charge of the nitrate anion be -1. Then the alkali metal - nitrate interactions were refitted for each compound. This process was iterated until a self-consistent solution was obtained.

A considerable amount of experimental data is available for fitting the force-field. This includes structural data for many of the polymorphs, often at several temperatures (see

the earlier discussion); elastic properties including the thermoelastic constants ($d\log[C_{ij}]/dT$)^[32]; dielectric data^[33] (more details are given in the following sections of this Chapter). Although partial occupancy can be modelled in GULP, using a fractional occupation number, structures with partial occupancy were not used in the fitting process. Corrections need to be made to the available data before they can be compared with simulations. Lattice parameters obtained from experiment will be at a finite temperature and contain zero-point motion effects. Both these must be corrected for to compare with a lattice statics simulation (most often used in fitting). Lattice energies can be obtained from experiment and compared with the simulations, but individual enthalpies of formation are not easily usable since they require a model of the elements in their standard states.

Table 4.2. Force-field Parameters for the nitrate ion ($qN = 0.7802|e|$, $qO = -0.5934|e|$)

Interaction type	Force constants		Distances		Angles
$V_{No}(r) = \frac{1}{2} k_2(r - r_0)^2$	$k_2(\text{eV}\text{\AA}^{-2})$ 40.849		$r_0(\text{\AA})$ 1.255		
$V_{NoO}(\theta) = \frac{1}{2} k_\theta(\theta - \theta_0)^2$	$k_\theta(\text{eVrad}^{-2})$ 13.234				θ_0 (deg) 120.0
$V_{NoO}(r_{12}, r_{13}) = k_{bc}(r_{12} - r_{12}^0)(r_{13} - r_{13}^0)$	$k_{bc}(\text{eV}\text{\AA}^{-2})$ 12.818		$r_{12}^0(\text{\AA})$ 1.255	$r_{13}^0(\text{\AA})$ 1.255	
$V_{NoO}(r_{12}, r_{13}, \theta) = [k_{bca}^{12}(r_{12} - r_{12}^0) + k_{bca}^{13}(r_{13} - r_{13}^0)](\theta - \theta_0)$	$k_{bca}^{12}(\text{eV}\text{\AA}^{-1})$ 1.533	$k_{bca}^{13}(\text{eV}\text{\AA}^{-1})$ 1.533	$r_{12}^0(\text{\AA})$ 1.255	$r_{13}^0(\text{\AA})$ 1.255	θ_0 (deg) 120.0
$V_{NoOO}(d) = k_2^{oop}d^2 + k_4^{oop}d^4$	$k_2^{oop}(\text{eV}\text{\AA}^{-2})$ 13.647	$k_4^{oop}(\text{eV}\text{\AA}^{-4})$ 360.0			

We have performed density functional calculations using the CASTEP^[34] (Cambridge Serial Total Energy Package) program to calculate the structures and properties of selected phases of the nitrates. This program uses a plane wave basis set to perform calculations on periodic systems. All the calculations were performed within the GGA approximation using the PBE functional^[35] and adding dispersion corrections^[36] (employing the DFT-D method^[37]). Pseudopotentials were generated "on the fly". The plane-wave energy cut-off was set at 800 eV; a Monkhorst-Pack grid was used for k-point sampling (8 x 8 x 8 grid, spacing 0.001 \AA^{-1}). Those parameters were chosen after optimisation and convergence testing. Geometry optimisation was performed using the BFGS algorithm^[38]. Since the force-field is needed for aqueous systems, we require a

model for the interactions between water and the alkali earth cations and the nitrate anion. We use the SPC/Fw model for water^[39] since it is cheap on computer resources and performs well in conjunction with the carbonate and sulphate anions.

Amongst the other water models, the most popular are:

1. TIP3P (Transferable Intermolecular Potential 3-Point): TIP3P is known for its simplicity and computational efficiency. It represents water as a rigid molecule with a fixed bond angle and length. Despite its simplicity, it captures many bulk water properties accurately.
2. TIP4P (Transferable Intermolecular Potential 4-Point): TIP4P introduces more complexity by adding a fourth interaction site to represent the lone pairs of electrons on oxygen. This model improves the representation of hydrogen bonding but requires more computational resources.
3. SPC/E (Extended Simple Point Charge): SPC/E is an extension of the SPC model with improved accuracy. It incorporates more parameters to better reproduce water's properties, such as the dielectric constant and vaporization enthalpy.

The SPC/Fw (Simple Point Charge/Flexible Water) model is a popular choice in molecular simulations for representing water molecules. It characterises water as a flexible molecule with three-point charges: one on each hydrogen atom and two on the oxygen atom. This flexibility allows SPC/Fw to more accurately capture the structural properties of water compared to rigid models like SPC, while maintaining computational efficiency by using point charges. SPC/Fw's versatility and balance between simplicity and accuracy make it suitable for a wide range of research applications, from studying bulk water properties to simulating solvation effects in biomolecular systems, where it strikes a balance between accuracy and computational cost.

For completeness, the parameters for the interactions between alkali metal ions and water are listed in Table 4.3 and those for the water model itself are listed in Table 4.4

Table 4.3 Interactions between alkali metal ions and water [26] $q_M = 1.0$ for $M = \text{Li-Cs}$ where ϵ and R_{min} are defined as the energy and interatomic distance at the minimum, i.e., the Lennard-Jones potential is written as

$$V(r) = \epsilon \left[\left(\frac{R_{min}}{r} \right)^{12} - 2 \left(\frac{R_{min}}{r} \right)^6 \right]$$

Alkali ions	ϵ (eV)	R_{min} (Å)
Li-O (H ₂ O)	0.009921	2.5676
Na-O (H ₂ O)	0.010152	2.9886
K-O (H ₂ O)	0.011207	3.3696
Rb-O (H ₂ O)	0.011406	3.5136
Cs-O (H ₂ O)	0.005125	3.7976
H ₂ O-H ₂ O	0.006740	3.553145

Table 4.4 SPE/Fw parameters for the water molecule ($q_H = 0.41|e|$, $q_O = -0.82|e|$) Wu et al.[39] The water-water interaction is given in Table 4.3

Interaction type	Force constants		Distances		Angles	
$V_{HO}(r) = \frac{1}{2}k_2(r - r_0)^2$	$k_2(\text{eV}\text{\AA}^{-2})$	45.93	$r_0(\text{\AA})$	1.012		
$V_{HOO}(\theta) = \frac{1}{2}k_\theta(\theta - \theta_0)^2$	$k_\theta(\text{eVrad}^{-2})$	3.291			θ_0 (deg)	113.24

Molecular dynamics simulations were performed to investigate the high-temperature behaviour of the force-fields. The DL_POLY^[40] code was used to perform canonical ensemble calculations over a temperature interval from 1 to 500 K to model lattice conversion. A Nosé-Hoover thermostat with a relaxation time of 0.1 ps was used. The time step was set to 0.5 fs. The selected number of time steps was 50000 (25 ps), of which 10000 (5 ps) were used as an equilibration period. A temperature-scaling interval of 10 K was used, whilst the radial distribution function (RDF) was collected every 1000 time steps, using a bin width of 0.1 Å to obtain the plot. The Ewald summation real space cut-off was set to 8.0 Å, whilst the width of the Verlet shell was 1 Å. The Ewald sum precision was set to a relative error of 10^{-5} . In order to calculate the long ranged electrostatic (Coulombic) potentials the Smoothed Particle Mesh Ewald (SPME^[41]) summation method was used. The grid for the k-vector summation was set with dimensions of 8x8x8, and α , the Ewald splitting parameter, set to 0.36037 \AA^{-1} . Isothermal-isobaric (NPT) ensemble calculations were performed using the Nose-Hoover NPT ensemble, with the pressure set to 1 atm and the temperature changed from 300 K to 500 K. The thermostat and barostat relaxation times were 0.1 ps. Other parameters were set as for the NVT simulation.

4.2.2 Simulation of solution properties

To obtain the free energies of ion solvation we performed thermodynamic integration (TI) calculations with the LAMMPS code^[42]. To perform a thermodynamic integration we must define a pathway between the two systems of interest, in this case the ion in solution and the ion in vacuum. The pathway must be continuous and reversible. The point along the pathway may be defined by the parameter λ . The free energy may then be obtained by integrating over this pathway. The variation of the free energy is defined as ΔA :

$$\Delta A = \int_{\lambda=0}^{\lambda=1} \left\langle \frac{\partial U(\lambda)}{\partial(\lambda)} \right\rangle_{\lambda} d\lambda \quad (4.1)$$

where $U(\lambda)$ is the potential energy of the system at the point along the pathway given by λ . Hence the term in the angle brackets represents the average of the derivative of the potential energy with respect to λ over the course of a simulation at that λ value. We do not use λ directly but instead use a nonlinear function of λ

$$f(\lambda) = \lambda^5(70\lambda^4 - 315\lambda^3 + 540\lambda^2 - 420\lambda + 126) \quad (4.2)$$

The use of the nonlinear function stabilises the calculation of the system as λ approaches 0 or 1^[43]. Using the $f(\lambda)$ of (4.2) is equivalent to sampling more heavily near the tail end values of λ , with a reweighting scheme given by the derivative of $f(\lambda)$ with respect to λ . The derivative in Equation (4.1) is obtained via the chain rule

$$\frac{\partial U(\lambda)}{\partial(\lambda)} = \frac{\partial U(f(\lambda))}{\partial f(\lambda)} \frac{\partial f(\lambda)}{\partial(\lambda)} \quad (4.3)$$

where the derivative of the nonlinear function with respect to λ is obtained analytically. The derivative of the potential energy with respect to the nonlinear function is obtained numerically by re-analysing the simulation trajectory and recalculating the potential energy with slightly perturbed values of $f(\lambda)$ and entering the result into a central differencing scheme for the computation of the derivative. The perturbed values of $f(\lambda)$ are chosen to be 1% of the value of $f(\lambda)$ to avoid unphysical negative force-field parameters arising in the central differencing scheme.

The pathway we choose between the solvated and desolvated ion is to deactivate all inter-molecular interactions between the ion and the water simultaneously. We construct a cubic simulation cell containing 3,200 water molecules and equilibrate in an NPT

ensemble at 300 K and 0 atm pressure for 1 ns with lattice vectors averaged every 100 fs to get average lattice vectors for the correct density of pure water. We then insert a single ion into the simulation cell (either K or NO₃). This leads to a small additional pressure in the cell when the interactions of the water with the ion are at full strength but is negligible at the simulation cell sizes we use.

Table 4.5. Buckingham parameters fitted for a rigid ion force-field (unit charge for all metal ions)

Interaction	A (eV)	$\rho(A)$	C (eVÅ ⁶)
Li -- O	170.7	0.30063	0.0
Li -- N	1155.8	0.260907	0.0
Na -- O	1842.1	0.24778	0.0
Na -- N	10598.7	0.2376	0.0
K -- O	220.6	0.36777	0.0
K -- N	4.99 x 10 ¹²	0.09385	0.0
Rb -- O	2324.9	0.28467	0.0
Rb -- N	81681.5	0.20626	0.0
Cs -- O	34792.7	0.22944	0.0
Cs -- N	98642.0	0.22721	0.0
O -- O	44806.0	0.20659	31.0

The TI simulations were each run in an NVT ensemble for 100 ns with the trajectory printed for re-analysis every 50 ps. We ran 42 simulations at a λ interval of 0.025 (except below the point at 0.025 where the simulations became unstable, however this represents a small error in our calculation and may be excluded). The integration was performed using the trapezoidal rule to obtain the free energy of solvation.

Comparison of our results with "experimental" tabulations of free energies of solvation is not a simple matter. In addition to ensuring that the results are converged with respect to the size of the simulation cell, it is also necessary to correct for polarisation effects and for the electrostatic potential generated at the site of the ion in a manner consistent with the assumptions that underly the tabulations we wish to compare with. Such issues

have been discussed by various authors^[45-48] who have reached apparently different conclusions. We consider this matter in the following section.

4.3 Results and discussion

We have fitted force-fields for all five alkali metal nitrates using the procedures outlined above. The parameters are given in Table 4.5. We begin by investigating how well the various force-fields can describe the relative stability for all the polymorphs reported for alkali metal nitrates^[4].

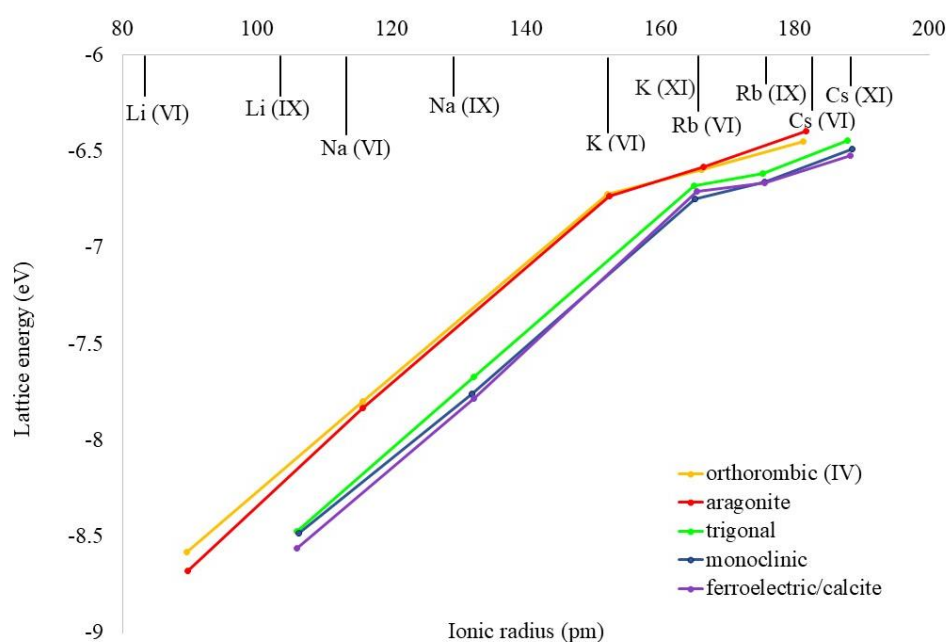


Figure 4.2. Lattice energies for possible polymorphs of alkali metal nitrates as indicated by filled symbols. Different crystal structures are shown in different colours: calcite (blue), aragonite (red), RbNO_3 phase IV structure (yellow) ferroelectric trigonal (purple). The stable low temperature polymorphs are calcite (Li, Na), aragonite (K) and RbNO_3 phase IV (Rb, Cs). The ionic radii come from Shannon^[44]; Roman numerals denote the coordination number to which they refer.

Figure 4.2. shows that the new force-field predicts (qualitatively) the correct stable polymorph for each of the alkali metal nitrates. It also predicts the correct structure for the only case where the crystal structure of a mixed alkali halide is known ($\text{NaRb}_2(\text{NO}_3)_3$). These results give confidence in the transferability of the forcefield. A fuller discussion of these issues, including the behaviour of other force-fields, is given in Section 4.3.3. We compared the predictions of the force-fields with experimental static dielectric constant data (Table 4.6) and with elastic stiffness and crystal structure data obtained both from experiment and from *ab-initio* calculations (Table 4.7). The

lattice parameters are also in excellent agreement with experiment (the experimental lattice parameters are corrected to those for a static lattice i.e. the effects of temperature and zero-point vibrations are removed). The fit for the KNO_3 aragonite phase is shown in Figure 4.3.

Table 4.6 Comparison between dielectric constants calculated using various force-fields and experimental values for the aragonite phase of potassium nitrate (KNO_3). *Note that the axes have been changed from the original references to conform to the crystallographic axes used for the $Pnma$ space group in ref [18].

	ϵ_{11}	ϵ_{22}	ϵ_{33}
Expt [33]	2.28	1.56	2.25
Force-field (this work)	3.6	2.9	2.8
Force-field [6]	1.79	2.55	2.47
Force-field [7]	0.5	2.17	2.11
Force-field [8]	3.5	4.24	3.95
Force-field [9]	2.58	2.22	2.33
Force-field [10]	2.6	2.86	2.66

The agreement with the experimental dielectric^[33] and elastic constants (extrapolated to 0 K)^[32] shown in Tables 4.6 and 4.7 is as good as that obtained with previous sets of parameters where comparison is possible.

Table 4.7(a) Comparison of the lattice parameter ‘a’ using this work L-J force-field, DFT and experimental data. All the values are expressed in Å.

	Lennard-Jones	DFT	experimental
aragonite	6.04	5.93	5.96
trigonal	5.47	4.10	5.41

Table 4.7 also shows that the forcefields compare reasonably well with the results of density functional calculations for the elastic properties. However, the new force-field improves on previous work in its ability to reproduce the experimental lattice dynamics. All previous force-fields show instabilities in the phonon spectra for at least some of the alkali nitrate polymorphs to which they were fitted except for those of Hammond^[5]. This indicates that the structures obtained using previous force-fields were calculated using

the full crystal symmetry and will distort away from the experimental crystal space group if the symmetry constraint is reduced or removed.

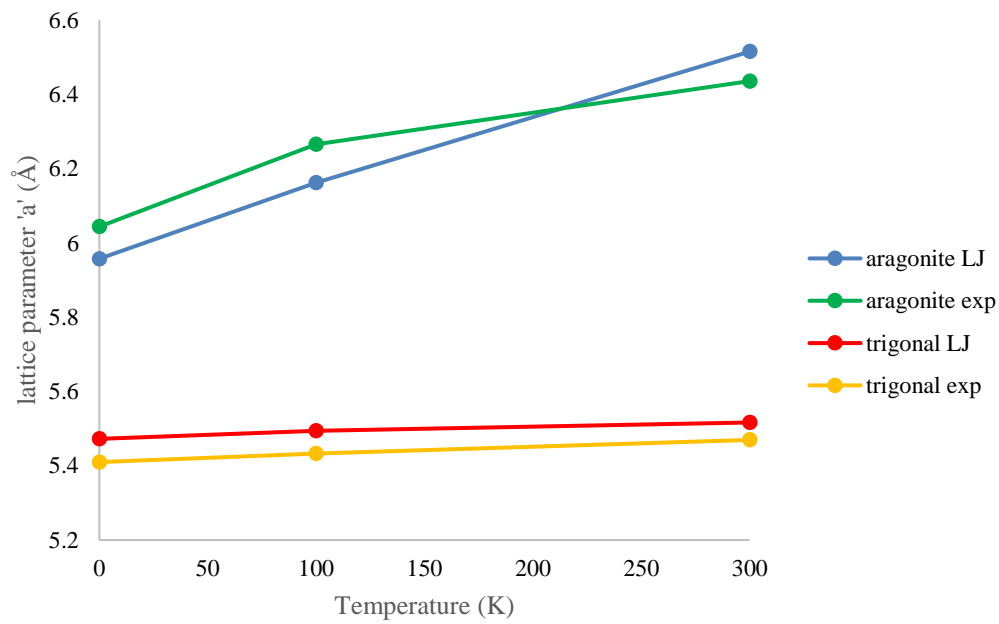


Figure 4.3 Lattice parameter fits for potassium nitrate (aragonite and trigonal (ferroelectric) structure)

Table 4.7(b) Comparison between elastic stiffness constants (GPa), calculated using various force-fields and density functional calculations and experimental values for the aragonite phase of potassium nitrate (KNO_3). *Note that the axes (and hence the Voigt notation) for the elastic constants has been changed from the original references to conform to the crystallographic axes used for the $Pnma$ space group in ref [18]. [§]Values extrapolated back from the measured values at 293 K to 0 K using the thermo-elastic constants reported in the same paper [32].

	C_{11}	C_{22}	C_{33}	C_{44}	C_{55}	C_{66}	C_{12}	C_{13}	C_{23}
Expt (ref [32])^{*§}	26.1	49.7	40.7	10.5	9.6	7.0	12.8	14	22.1
Force-field (this work)	15.3	39.3	28.4	8.4	9.6	8.2	8.5	9.5	16.2
Force-field (ref [6])	18.1	41.3	32.8	10.1	10.3	8.9	9.6	11	17.6
Force-field (ref [7])	44.7	59.9	39.3	11.7	15.1	13.5	20.1	21.9	30.4
Force-field (ref [8])	24.4	42.6	35.1	9.9	12.4	11.1	7.4	9	20
Force-field (ref [9])	9.9	37.6	29.0	8.00	8.0	6.7	13.3	13.3	18.9
Force-field (ref [10])	18.1	39.5	30.6	9.6	10.5	8.8	10.1	11.4	17.2
DFT (this work)	28.7	64.6	37.6	11.3	8.8	7.2	18.4	14.5	34.6
DFT (ref [45])	21.9	40.2	32.9	9.6	8.8	7.3	10.4	12.1	17.3

To obtain the interaction between the nitrate anion and the water molecules, we fit to the experimental crystal structure of the only known hydrate of the alkali metal nitrates, $\text{LiNO}_3 \cdot 3\text{H}_2\text{O}$ ^[46]. We assumed the lithium interactions given in Tables 4.1 and 4.5, the nitrate model of Table 4.2 and the water model of Table 4.4. We use mixing rules for the interactions between the nitrate oxygen and water oxygen atoms. This leaves only the interaction between the hydrogen atoms of water and the oxygen atoms of the nitrate ion to fit. All the parameters for the interactions between water and the nitrate ion are given in Table 4.8 and the comparison with the structure of $\text{LiNO}_3 \cdot 3\text{H}_2\text{O}$ in Table 4.9.

Table 4.8 Interactions between water and the nitrate anion using a Buckingham potential form $V(r) = A\exp(-r/\rho) - C/r^6$

Interactions	A(eV)	ρ (Å)	C(eV Å ⁶)
H(H ₂ O)-O(NO ₃ ⁻)	577.7	0.226352	0.0
O(H ₂ O)-O(NO ₃ ⁻)	225677	0.18661	29.0

Table 4.9 Comparison with structural data for $\text{LiNO}_3 \cdot 3\text{H}_2\text{O}$ (space group $Cmcm$ (63))[46]. Comparison of the atomic positions can be found in Section 4.3.5.

Lattice parameters	expt	force-field
a (Å)	6.8018	6.7756
b (Å)	12.7132	12.7464
c (Å)	5.9990	5.9296

4.3.1 Comparison of force-fields with crystal structures

Previous work on developing force-fields appears to have performed the fit to the experimental data using a lattice statics approach for the simulation but without correcting for the effects of the temperature at which the experiments were performed or for zero temperature vibration effects. Table 4.10 gives a comparison for all these force-fields with the experimental lattice parameters corrected to a zero temperature static lattice to match the conditions of the simulation. The final column of the table gives an indication of the quality of the fit defined as

$$GoF = 100 \sum_i |M_i - E_i| / |E_i| \quad (4.4)$$

where (M_i, E_i) are the i^{th} model prediction and E_i is the corresponding experimental data point. Hence the lower the value of GoF, the better the fit.

Table 4.10 Comparison of current force-field with experimental data (in italics; corrected to a static lattice) and previous forcefields

Nitrate	Phase	a (Å)	b (Å)	c (Å)	Goodness of fit (GoF)
<i>LiNO₃</i>	<i>calcite (expt)[10s]</i>	<i>4.6368</i>	<i>4.6368</i>	<i>14.8373</i>	
This work (DFT including dispersion term)		4.5994	4.5994	14.9582	
This work		4.6016	4.6016	14.9659	2.4
Hammond[5]		4.7108	4.7108	14.8927	3.6
Jayaraman[11]		4.71	4.71	14.9677	3.9
Ni[8]		4.7076	4.7076	14.9678	3.9
Ribeiro[6]		4.7051	4.7051	14.9723	1.1
Xie <i>et al</i> [7]		4.506	4.506	15.2709	8.7
<i>NaNO₃</i>	<i>calcite (expt)[16s]</i>	<i>5.0493</i>	<i>5.0493</i>	<i>16.1893</i>	
This work (DFT including dispersion term)		5.0328	5.0328	16.1856	
This work		5.033	5.033	16.1835	0.6
Mort[9]		4.957	4.957	17.0603	9.0
Jayaraman[11]		5.1335	5.1335	16.3624	4.5
Ni[8]		5.1325	5.1325	16.3638	4.5
Ribeiro[6]		5.1299	5.1299	16.3757	4.2
Xie[7]		4.9013	4.9013	16.5613	8.1
<i>KNO₃</i>	<i>aragonite (expt)[18]</i>	<i>6.044</i>	<i>5.3772</i>	<i>9.104</i>	
This work (DFT including dispersion term)		5.9255	5.3629	9.0147	
This work (forcefield)		5.9576	5.4546	9.132	3.3
Mort[9]		6.6017	5.3516	9.023	10.5
Jayaraman[11]		6.1291	5.4591	9.1297	3.3
Ribeiro[6]		6.0894	5.4528	9.2161	3.3
<i>KNO₃</i>	<i>trigonal ferro-electric (expt)[20]</i>	<i>5.41</i>	<i>5.41</i>	<i>8.67</i>	
This work (DFT including dispersion term)		5.3886	5.3886	8.5514	

This work		5.4726	5.4726	8.5597	3.6
Mort[9]		5.6763	5.6726	7.4723	23.7
Jayaraman[10]		5.4849	5.4849	8.6153	3.3
Ribeiro[6]		5.3666	5.3666	8.8189	3.3
RbNO₃	trigonal (expt)[23]	<i>10.3313</i>	<i>10.3313</i>	<i>7.2282</i>	
This work		10.3061	10.3061	7.251	0.6
Hammond[5]		10.5686	10.5686	7.3849	6.9
CsNO₃	trigonal (expt)[24]	<i>10.642</i>	<i>10.642</i>	<i>7.543</i>	
This work		10.7015	10.7015	7.51	1.5
Ribeiro[6]		10.6526	10.6526	7.574	1.5

Table 4.11 Comparison of force-field prediction with structural data for LiNO₃·3H₂O^[71]

Structure (<i>Cmcm</i>)	expt	forcefield
<i>a</i> (Å)	6.8018	6.7756
<i>b</i> (Å)	12.7132	12.7464
<i>c</i> (Å)	5.9990	5.9296
Li (fractional)	0, 0, 0	0, 0, 0
N (fractional)	0, 0.2176, ¼	0, 0.2098, ¼
O (fractional)	0, 0.1703, 0.0701	0, 0.1605, 0.0667
O (fractional)	0, 0.3161, ¼	0, 0.3074, ¼
O (fractional)	0.2903, 0.4784, ¼	0.2902, 0.4816, ¼
O (fractional)	0, 0.6382, ¼	0, 0.6295, ¼
H (fractional)	0.2169, 0.4144, ¼	0.2278, 0.4085, ¼
H (fractional)	0.3057, 0.0341, ¼	0.3220, 0.0373, ¼
H (fractional)	0, 0.6826, 0.1227	0, 0.6776, 0.1119

The force-field also works well for solid solutions as can be seen from Table 4.12, which shows the ability of the force-field to reproduce the crystal structure of ordered mixed nitrates where the experimental information is available. The Lorenz-Bertholet rules were used to generate the force-fields between unlike cations.

Table 4.12 Comparison of experimental^[72] crystal structure of $\text{NaRb}_2(\text{NO}_3)_3$ and force-field.

Structure ($Pmc2_1$)	expt	force-field
a (Å)	5.313	5.3103
b (Å)	9.077	8.8598
c (Å)	9.700	9.5617
Rb (fractional)	$\frac{1}{2}$, 0.0828, 0.5326	$\frac{1}{2}$, 0.0828, 0.5326
Rb (fractional)	$\frac{1}{2}$, -.3784, 0.7065	$\frac{1}{2}$, -.3803, 0.7087
Na (fractional)	1, 0.2987, 0.7520	1, 0.2943, 0.7612
N (fractional)	1, -.0531, 0.7396	1, -.0625, 0.7456
N (fractional)	$\frac{1}{2}$, -.2517 0.3837	$\frac{1}{2}$, -.2527, 0.3900
O (fractional)	1, 0.0592, 0.6636	1, 0.0574, 0.6756
O (fractional)	0.7910, -.1055, 0.7734	0.7955, -.1208, 0.7816
O (fractional)	0.2975, -.2289, 0.4447	0.2959, -.2276, 0.4503
O (fractional)	$\frac{1}{2}$, -.2987, 0.2620	$\frac{1}{2}$, -.3040, 0.2683
O (fractional)	1, 0.5419, 0.8310	1, 0.5339, 0.8387
O (fractional)	0.7977, 0.3903, 0.5120	0.7970, 0.3805, 0.5219

4.3.2 Stability of polymorphs

The only reliable values for the enthalpy differences between nitrate polymorphs^[32] are for KNO_3 (phase II; aragonite, ($Pnma$) \rightarrow phase I, trigonal ($R\bar{3}m$)); $\Delta H = 5.0 \text{ kJ mol}^{-1}$) and for RbNO_3 (phase IV ($P31$) \rightarrow phase III ($Pm\bar{3}m$)); $\Delta H = 4.0 \text{ kJ mol}^{-1}$). These are small numbers and hence represent a challenge. Of the available force-fields which consider the three nitrates (Li, Na, K), only Jayaraman^[11] and this work get the correct stable polymorph for all cases. Only the current work obtains lattice energies in reasonable agreement with experiment for all five nitrates (Table 4.13).

Table 4.13 Energy of polymorphs with respect to the most stable one (kJ mol^{-1}) as predicted by different force-fields. Dashes indicate the failure of a forcefield to optimise a particular structure. The most stable polymorph is emphasised in bold.

Structures / nitrates	LiNO_3	NaNO_3	KNO_3
Calcite	0.0 (Hammond)[5]	7.7 (Mort)[9]	- (Mort)[9]
	0.0 (Jayaraman)[10]	0.0 (Jayaraman)[10]	1.0 (Jayaraman)[10]
	0.0 (Ni)[8]	6.8 (Ni)[8]	16.4 (Ni)[8]
	0.0 (Ribeiro)[6]	0.0 (Ribeiro)[6]	- (Ribeiro)[6]
	0.0 (Xie)[7]	0.0 (Xie)[7]	0.0 (Xie)[7]
	0.0 (This work)	0.0 (This work)	1.9 (This work)
Trigonal	29.0 (Hammond)[5]	5.8 (Mort)[9]	1.0 (Mort)[9]
	30.0 (Jayaraman)[10]	16.4 (Jayaraman)[10]	6.8 (Jayaraman)[10]
	15.0 (Ni)[8]	0.0 (Ni)[8]	0.0 (Ni)[8]
	38.0 (Ribeiro)[6]	- (Ribeiro)[6]	- (Ribeiro)[6]
	37.0 (Xie)[7]	16.4 (Xie)[7]	0.0 (Xie)[7]
	30.0 (This work)	49.0 (This work)	6.8 (This work)
Aragonite	7.7 (Hammond)[5]	0.0 (Mort)[9]	0.0 (Mort)[9]
	10.6 (Jayaraman)[10]	10.6 (Jayaraman)[10]	0.0 (Jayaraman)[10]
	15.0 (Ni)[8]	3.9 (Ni)[8]	9.6 (Ni)[8]
	38.0 (Ribeiro)[6]	- (Ribeiro)[6]	- (Ribeiro)[6]
	37.0 (Xie)[7]	10.6 (Xie)[7]	0.0 (Xie)[7]
	30.0 (This work)	6.8 (This work)	0.0 (This work)
RbNO₃ (IV) structure	8.0 (Hammond)[5]	6.8 (Mort)[9]	4.8 (Mort)[9]
	8.4 (Jayaraman)[10]	6.8 (Jayaraman)[10]	4.8 (Jayaraman)[10]
	1.0 (Ni)[8]	0.0 (Ni)[8]	19.3 (Ni)[8]
	- (Ribeiro)[6]	- (Ribeiro)[6]	- (Ribeiro)[6]
	2.9 (Xie)[7]	3.9 (Xie)[7]	10.6 (Xie)[7]
	11.6 (This work)	5.8 (This work)	3.9 (This work)

Table 4.14 Lattice energies (kJ mol^{-1}) for alkali metal nitrates compared with those obtained from those obtained from the NBS Tables[70]. Values quoted for the stable polymorph at standard temperature and pressure (STP). Dashes mean either that no forcefield is available or that the forcefield could not produce a stable minimised structure.

Alkali metal nitrate (STP stable polymorph)	LiNO_3 (calcite)	NaNO_3 (calcite)	KNO_3 (aragonite)	RbNO_3 (RbNO_3 IV)	CsNO_3 (RbNO_3 IV)
<i>Experiment</i> [9]	-832.61	-740.91	-672.59	-648.85	-627.63
This work	-836.3	-755.3	-650.0	-642.1	-627.3
Hammond[5]	-734.3	-	-	-523.5	-
Jayaraman[10]	-804.1	-732.1	-675.9	-	-
Ni[8]	-804.4	-732.2	-681.8	-	-
Ribeiro[6]	-804.5	-732.4	-	-	-
Xie[7]	-909.6	-818.4	-731.6	-	-
Mort[9]	-	-1344.4	-1261.2	-	-

4.3.3 Comparison with crystal properties

Most previous forcefields fail to calculate phonon spectra for the stable polymorph at STP. The only exceptions are Hammond^[5] (LiNO_3 and RbNO_3), Jayaraman^[10] and Xie^[8] (both for KNO_3 only). All the other cases where forcefields are available yield negative eigenvalues along at least of one the main symmetry directions of the phonon spectrum. The existence of these imaginary modes means that their predicted structures are stabilised only by the symmetry constraints imposed by the space group used. The figures below show dispersion curves for sodium and potassium nitrate obtained using the force-field fitted here (Figure 4.4-4.7) and the available neutron diffraction data^[73,74]. In this case, no imaginary mode is present and it is possible to see a resemblance with the experimental pattern. Note that the high-frequency modes associated with the vibrations of the nitrate ion are omitted here for reasons of space. They form a narrow band in the range $1350\text{-}1400\text{ cm}^{-1}$ whose position is only weakly dependent on the nitrate in question. The position of the band is consistent with the available Raman data^[75]. There is reasonable agreement between the experimental data available for sodium nitrate and the result obtained with the force-field presented in this work.

Table 4.15 Elastic stiffness constants for LiNO₃ calculated with different force-fields and compared with experimental data.
(C₁₄ is omitted from the goodness of fit calculation)

	C₁₁	C₃₃	C₄₄	C₆₆	C₁₂	C₁₃	C₁₄	GoF
Expt (GPa)[32]	119.2	77.8	23.7	42.6	32.7	19.9	-0.7	
This work	120.7	86.8	21.1	39.1	42.4	21.4	5.6	69.2
Hammond[5]	97.9	48.5	23.2	31.6	34.8	34.7	12.7	164
Jayaraman[10]	79.1	48.9	18.9	27.2	24.8	21.1	8.7	137
Xie[8]	163.0	151.0	32.5	58.6	45.9	36.2	4.8	328

Table 4.16 Elastic constants for NaNO₃ calculated with forcefield and compared with experiment.

	C₁₁	C₃₃	C₄₄	C₆₆	C₁₂	C₁₃	C₁₄	GoF
Expt (GPa)[25]	72	38	17.8	24.1	24	21.7	12.5	
This work	70.9	33	18.1	23.2	24.6	25.3	12.2	41.6
Mort[9]	53.5	23.4	9.1	14.3	24.9	25.8	7.7	341
Jayaraman[10]	55.7	23.4	13.7	18.2	19.4	18.6	8.8	166
Ni[8]	56.4	23.4	13.7	18.4	19.6	18.8	8.9	167
Ribeiro[6]	59.1	23.6	13.7	20	19.2	19.2	9.2	154
Xie[7]	93.9	60.4	25.1	28.4	37	40.6	15	309

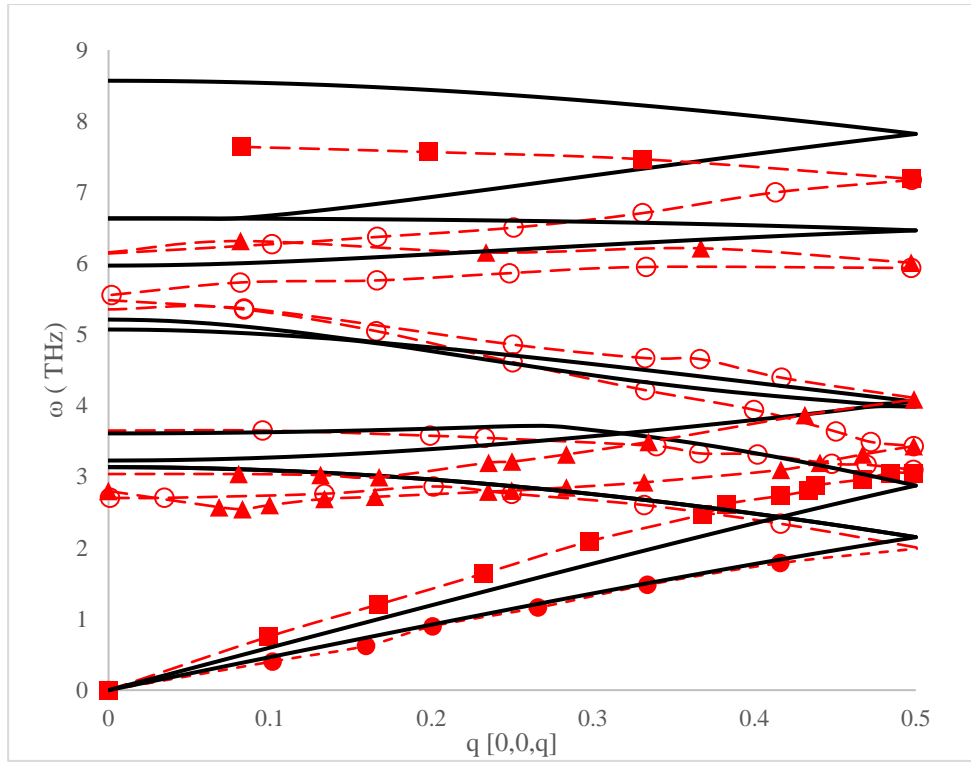


Figure 4.4 Phonons NaNO_3 obtained with this force-field (black lines) compared with experiment[32] (red symbols).

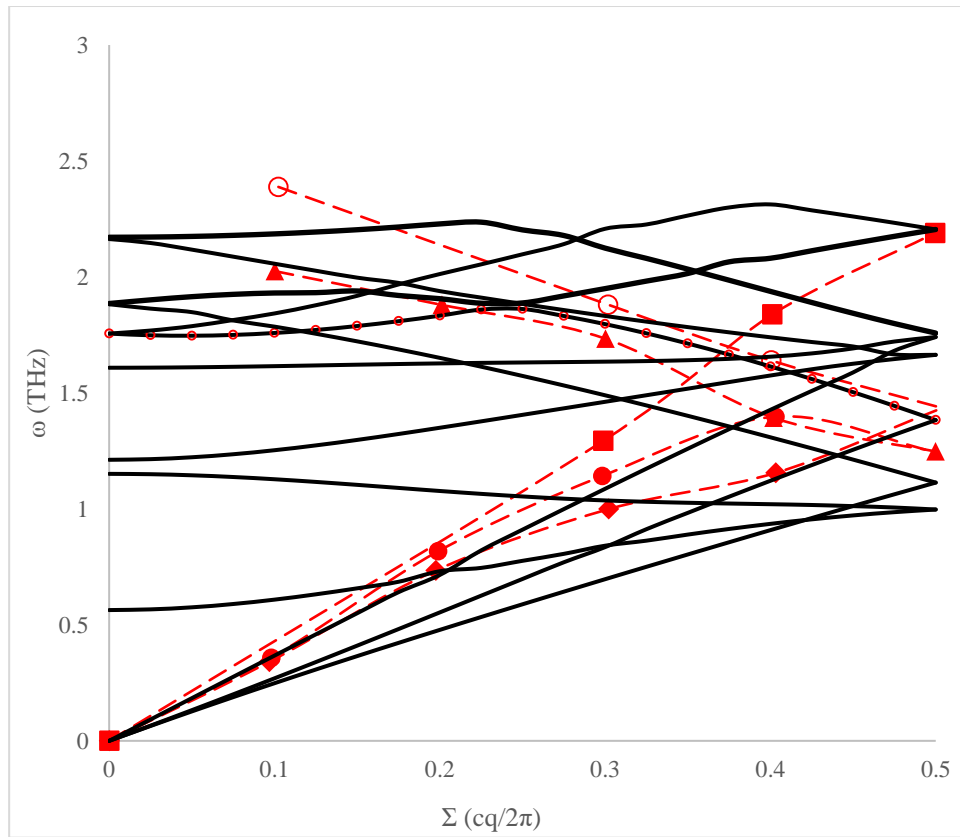


Figure 4.5 Phonons for KNO_3 (Σ direction) obtained with this force-field (black curves) compared with experiment[73] (red symbols)

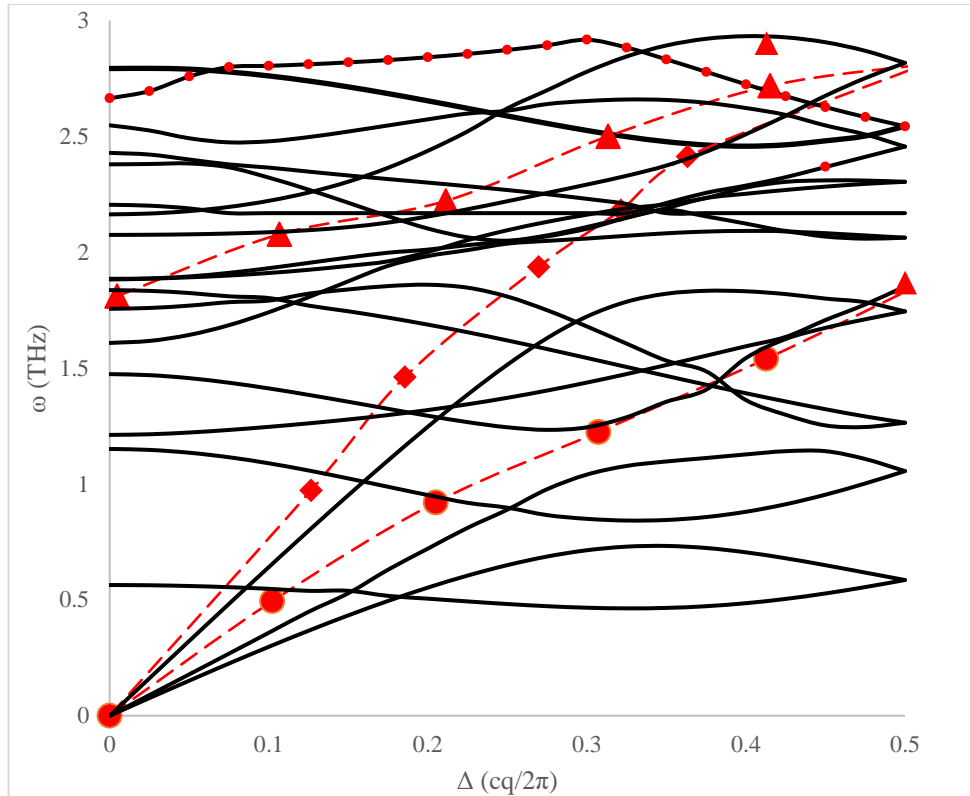


Figure 4.6 Phonons for KNO_3 (Δ direction) obtained with this force-field (black curves) compared with experiment^[73](red symbols).

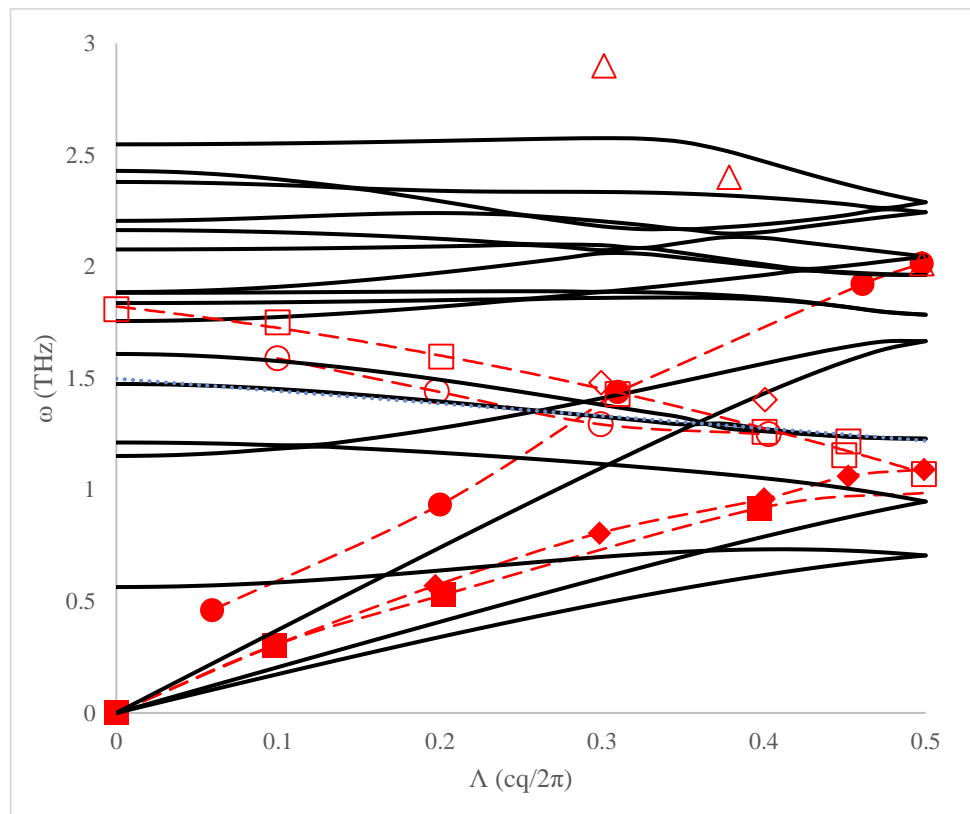


Figure 4.7 Phonons for KNO_3 (Δ direction) obtained with this force-field (black curves) compared with experiment^[73](red symbols).

4.3.4 The Lattice thermal expansion

Table 4.17 Comparison between lattice parameter 'a' for various alkali metal nitrates, obtained using the Lennard-Jones, Buckingham and experimental values. All the values are expressed in Å.

	Lennard - Jones		Buckingham		Experimental	
	0 K	300 K	0 K	300 K	0 K	300 K
LiNO ₃	4.6368	4.692	4.5995	4.6477	4.6016	4.6221
NaNO ₃	5.0493	5.0701	5.0327	5.0552	5.033	5.0491
KNO ₃ - aragonite	6.003	6.4512	6.044	6.436	5.9576	6.5155
KNO ₃ - trigonal	5.4726	5.5168	-	-	5.41	5.469
RbNO ₃	10.3313	10.55	10.3093	10.5516	10.3061	10.5503
CsNO ₃	10.642	11.0093	10.6655	10.9095	10.6546	10.8796

4.3.5 Simulation of the crystal structures at high temperature

We finally turn to a more detailed consideration of the structures predicted by the simulations. NPT molecular dynamics simulations were performed as previously described and showed that for the lithium nitrate system the structure is calcite-like (space group $R\bar{3}c$) at all temperatures and the peaks retain their shape (Figure 4.8). The structure loses some long-range order when the system is heated up from 100 K to 500 K (peaks between 4.5 and 5 Å and between 5 and 7.8 Å merge). However, changes in the polymorph are not visible (lithium nitrate is monotropic as experimentally reported). If the temperature is raised to 600 K the long-range order decays further (peaks shift to the right/broaden and their height decreases). At greater atomic separations, the lack of coherence becomes more evident with more peaks merging (around 6, 7 and 9 Å). The behaviour is similar for sodium nitrate (Figure 4.9). At all temperatures, the structure is calcite-like (space group $R\bar{3}c$); the peaks lose their shape as the temperature rises.

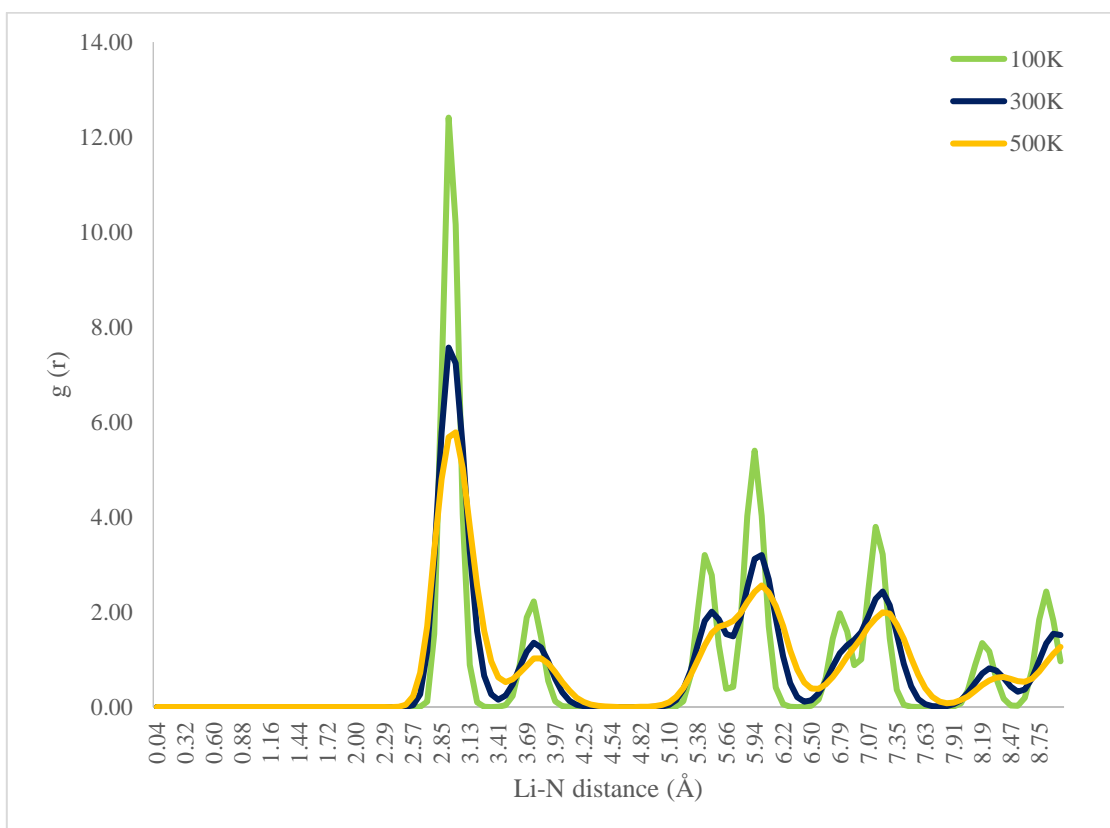
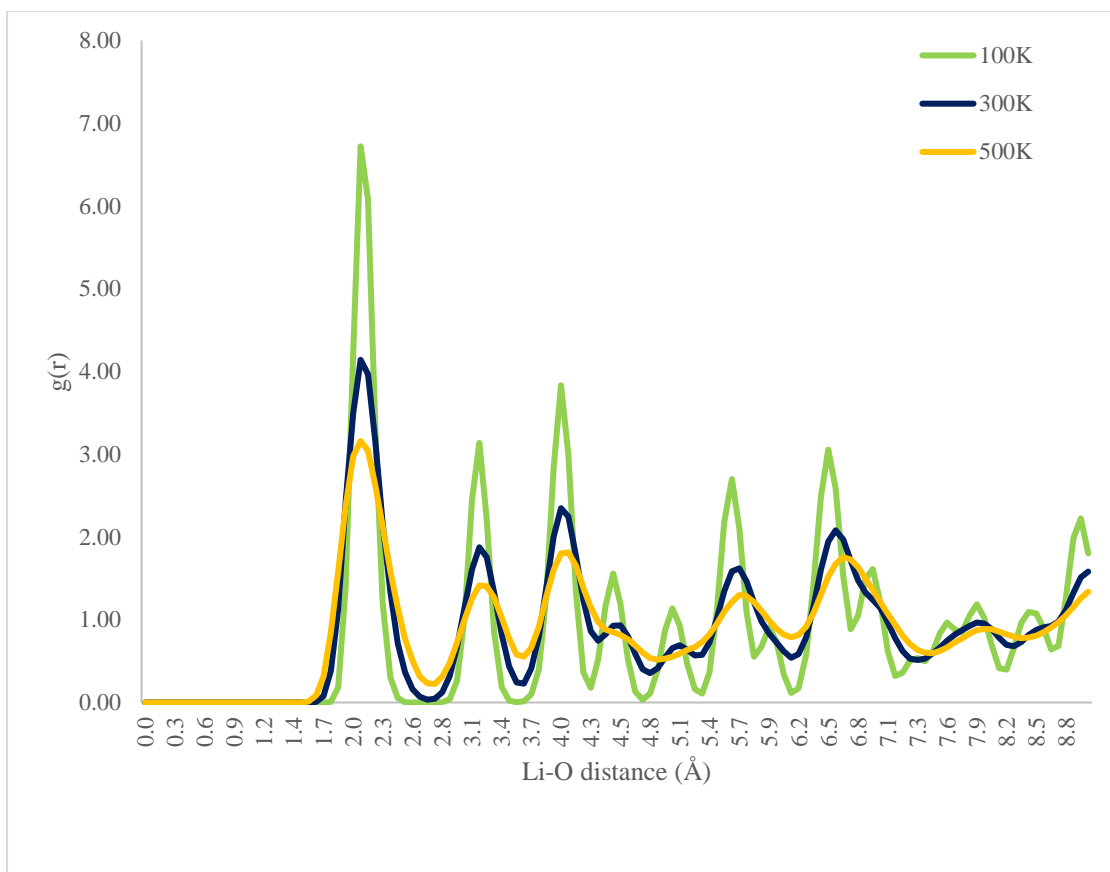


Figure 4.8 Radial distribution functions for Li-O (top) and Li-N (bottom) in LiNO_3 .

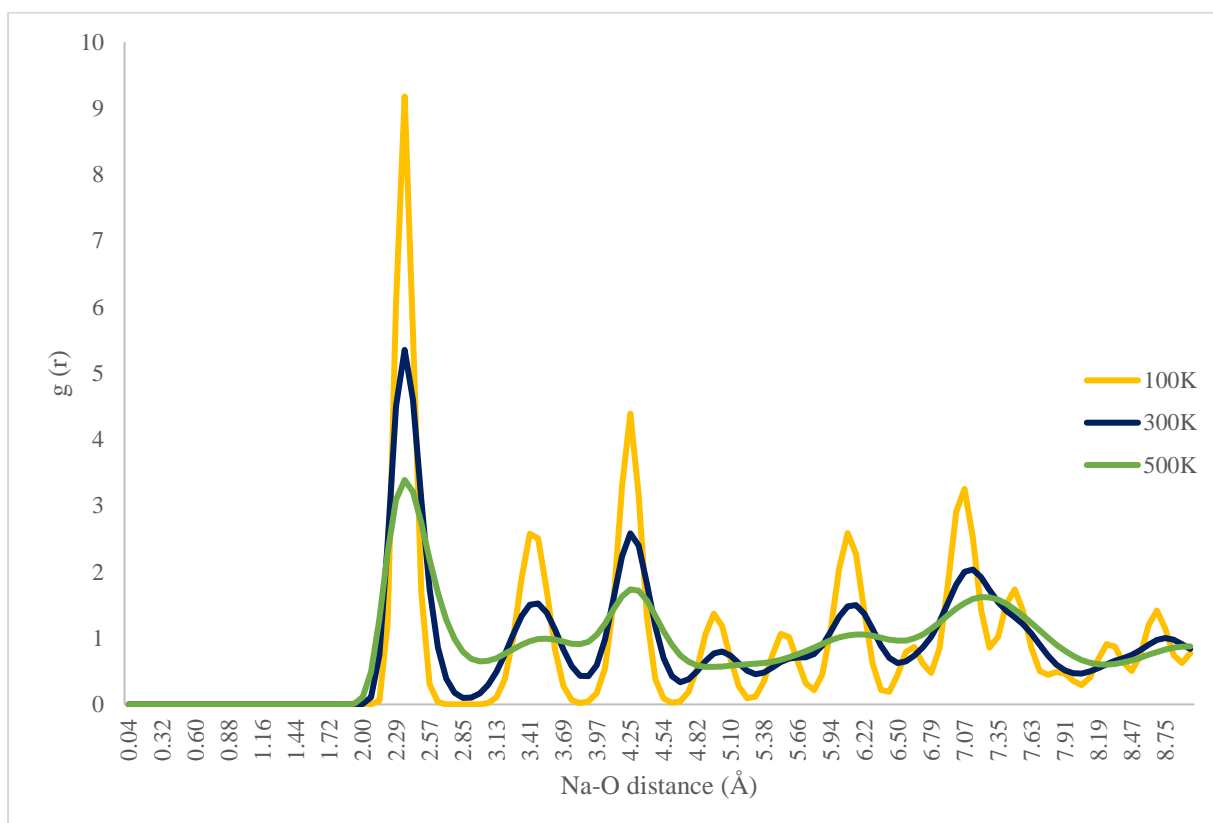
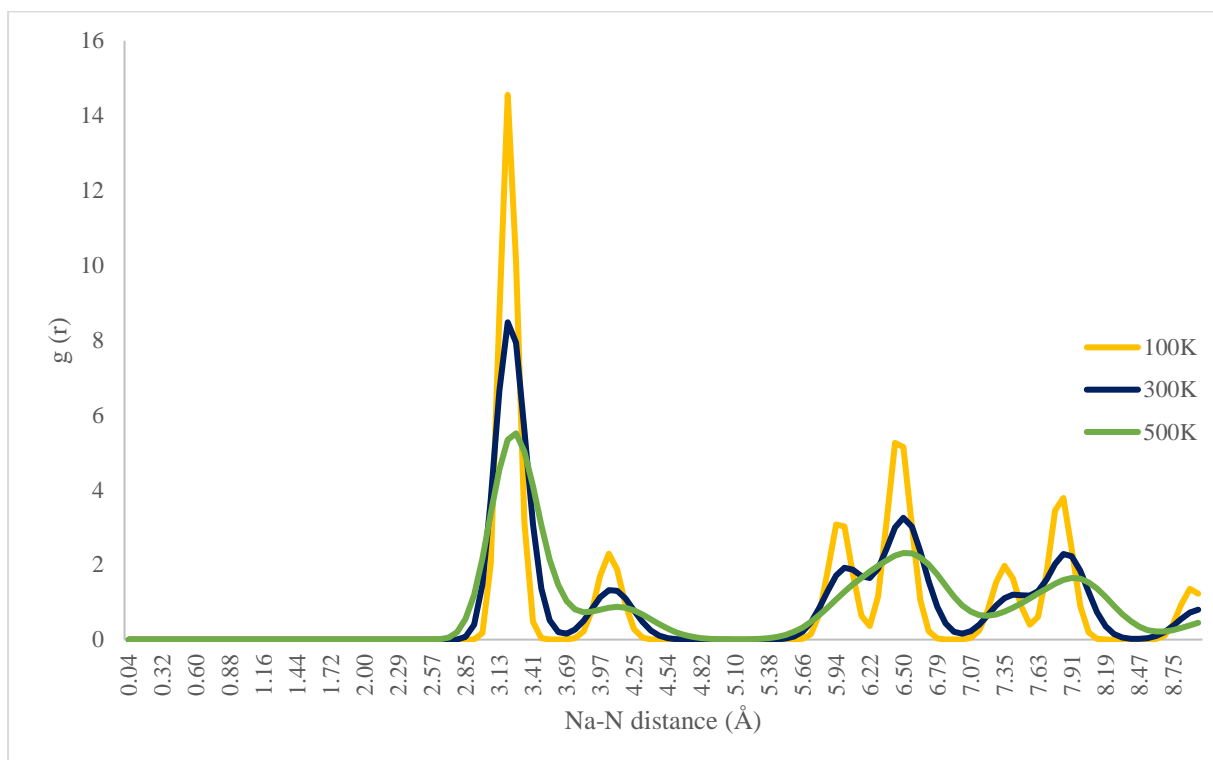


Figure 4.9 Radial Distribution Function for Na - O (top) and Na - N (bottom) in NaNO₃

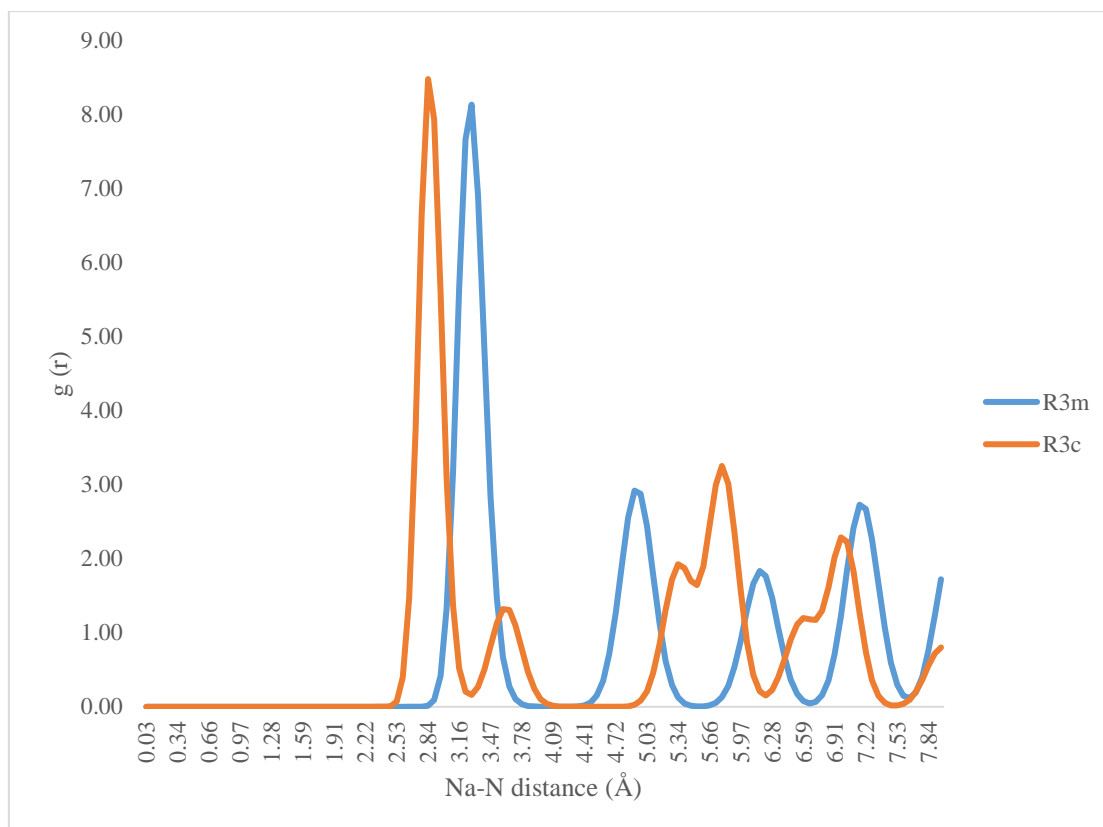


Figure 4.10 Radial Distribution Function for Na - N in NaNO_3 for the two different polymorphs (R3c, blue line and R3m, orange line) extracted at 300K.

Analysing the R3m sodium nitrate structure at different temperatures is possible to notice no interconversion of the structure as well into the previously presented R3c. The energetic order is clearly retained, showing the R3m structure being more stable. This effect can be explained by considering an entropic contribution to the configurational energy.

Table 4.18 Energy values of the two different polymorphs of NaNO_3 (R3c and R3m) at 600K.

	R3m	R3c
600 K	-7.731 eV	-7.528 eV

Potassium nitrate is a more interesting case to study because the RDFs show evidence for three different polymorphs (see Figure 4.13): the ferroelectric trigonal structure (space group R3m) at 100 K; the aragonite structure at 300 K and the trigonal $\overline{R}3m$ structure, (quasi-calcite form) at 500 K. On cooling down the system returns to the original structure but not directly. Cooling down the 500 K trigonal structure gives a distorted aragonite structure, whereas the 300 K structure returns to the ferro-electric

trigonal form on further cooling. This suggests that the force-field is able to reproduce the polymorph changes and shows that those changes are temperature-dependent (potassium nitrate is enantiotropic). Figure 4.14 shows the good agreement between the experimental K-O distances obtained by X-ray diffraction^[75] and those obtained by simulation.

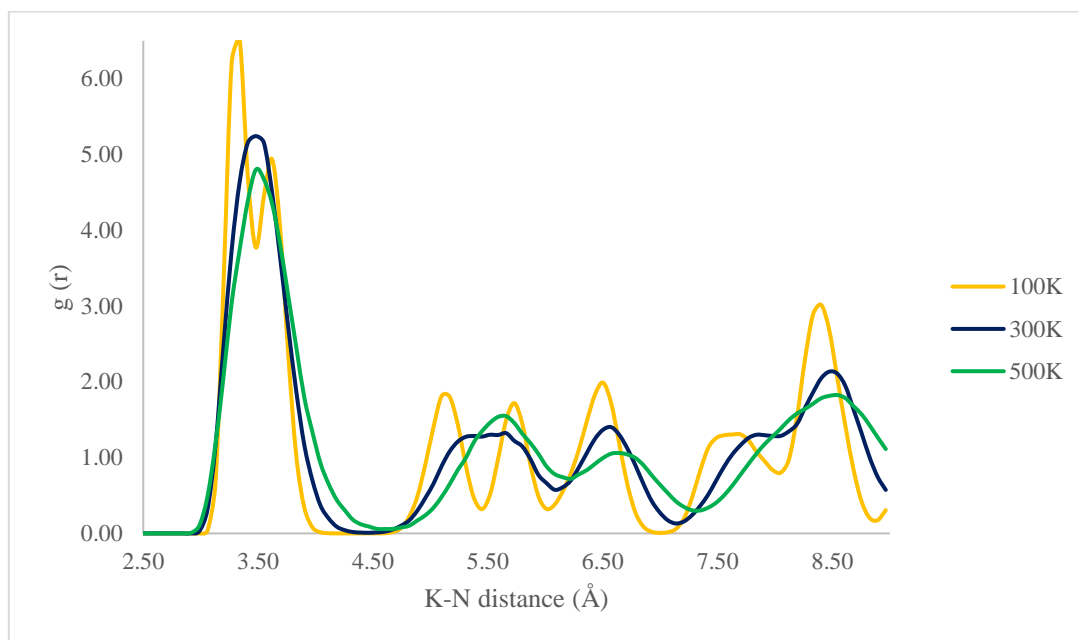


Figure 4.11 Radial Distribution Function for K - N in KNO_3 as the temperature increases. The yellow line represents the system at 100 K, the blue line at 300 K and the green line at 500 K.

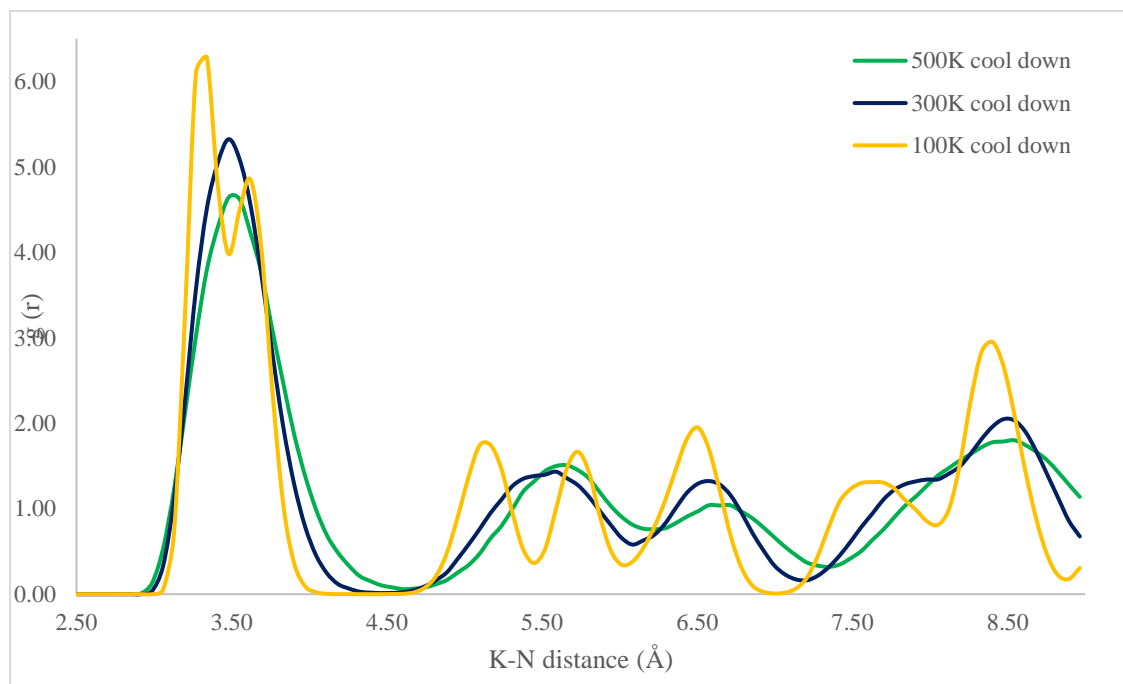


Figure 4.12 Radial Distribution Function for K - N in KNO_3 as the temperature decreases. The yellow line represents the system at 100 K, the blue line at 300 K and the green line at 500 K.

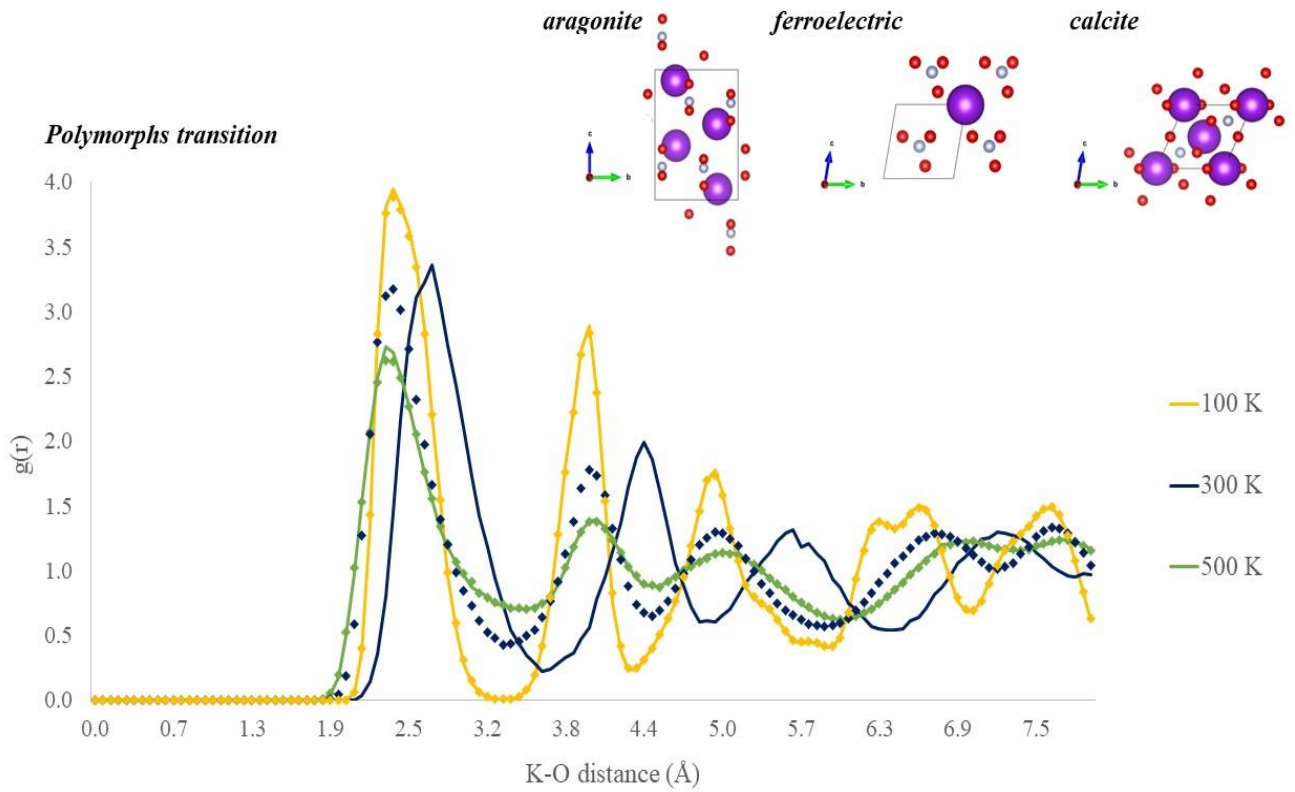


Figure 4.13 Radial Distribution Function for K - O in KNO_3 as the temperature increases. The yellow line represents the system at 100 K, the blue line at 300 K and the green line at 500 K, the dotted line (same colours) represent the cooling down of the system

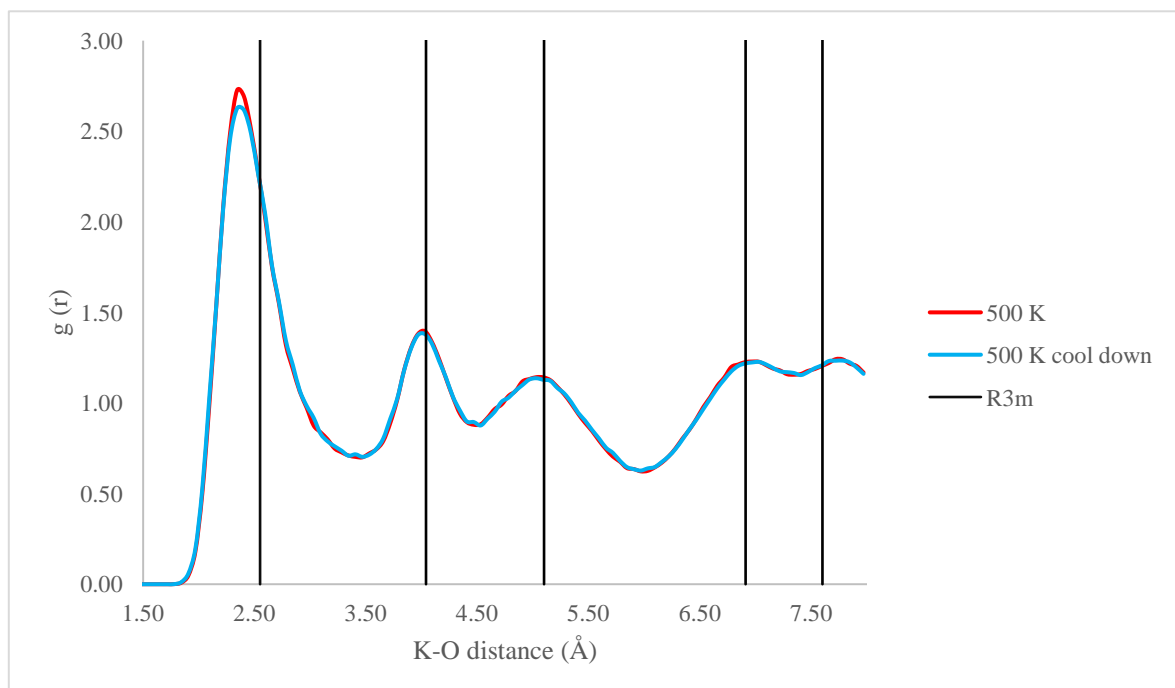


Figure 4.14 Radial Distribution Function for K-O in KNO_3 obtained by cooling down the simulation at 500 K (blue) and the RDF of the polymorph obtained from cooling down the aragonite structure (red). Dotted lines represent the positions of XRD^[75] peaks for the experimental $R3m$ structure^[13].

4.3.6 Calculating the corrections to the free energy of hydration

We considered a small correction for the definition of the standard state used by Marcus^[68] (connected with the change in volume that is available to the solute when it moves from the gas to the aqueous phase). The correction is the same for all ions and is + 7.93 kJ mol⁻¹

The data required to calculating the corrections is given in Table 3.4, Chapter 3, Section 3.5.2.2. The values used to obtain the corrections for the current work also given. More details of the origin of these corrections can be found in the supplementary material of the reference cited in Chapter 3.

The most important correction omitted by Joung and Cheatham is the one involving the electrostatic potential at the site of the cation. When this is added, their result for the free energy of hydration of the potassium ion becomes -371 kJ mol⁻¹.

4.3.7 Solubility

Using the method described by Boothroyd *et al.*^[69] studies regarding the solubility of the alkali metal nitrates systems have been performed. To obtain those data, values for both the free energy of formation of water and the enthalpy of formation of water at 298.15 K have been used, respectively equal to -237.149 kJ/mole and -285.83 kJ/mole. All thermodynamic quantities reported in Table 4.19 are calculated at 298.15 K. Formation enthalpies and free energies are reported with respect to elements in standard states. One needs to apply a correction of +2.29 kJ/mole to enthalpies when going from ideal gas to solution

Table 4.19 Thermodynamic properties for alkali metal nitrates systems

Compound	Solubility (expt) saturation conc	Free energy of formation of salt [70]	Enthalpy of formation of salt [70]	Free energy of formation; dilute solution [70]	Enthalpy of formation; dilute solution [70]
	<i>molality/kg water</i>	<i>kJ/mole</i>	<i>kJ/mole</i>	<i>kJ/mole</i>	<i>kJ/mole</i>
NaCl	6.15	-384.148	-411.153	-393.133	-407.27
LiNO ₃	12.3	-381.1	-483.13	-404.5	-485.85
NaNO ₃	10.8	-367.0	-467.85	-373.15	-447.48
KNO ₃	3.75	-394.86	-494.63	-394.53	-459.74
RbNO ₃	4.45	-395.78	-495.05	-395.24	-458.52
CsNO ₃		-406.54	-505.97	-403.27	-465.52
LiNO ₃ ·3H ₂ O	12.3	-1103.5	-1374.4	-404.5	-485.85

Compound	Free energy of solution [70]	Enthalpy of solution [70]	Lattice enthalpy [70]	Formation Energy; gas cation [70]	Formation Energy; gas anion [70]
	<i>kJ/mole</i>	<i>kJ/mole</i>	<i>kJ/mole</i>	<i>kJ/mole</i>	<i>kJ/mole</i>
NaCl	-9.00	+3.88	-787.38	609.358	-233.13
					Jenkins[63]
LiNO₃	-23.4	-2.72	-832.61	685.783	-336.3
NaNO₃	-6.15	+20.37	-740.91	609.358	-336.3
KNO₃	+0.33	+34.89	-672.59	514.26	-336.3
RbNO₃	+0.54	+36.53	-648.85	490.101	-336.3
CsNO₃	+3.27	+40.33	-627.63	457.964	-336.3
LiNO₃·3H₂O	-12.39	+31.06	-1720.48	685.783	-336.3

Compound	Free energy of cation hydration[64]	Enthalpy of cation hydration[64]	Free energy of anion hydration	Enthalpy of anion hydration[64]	Enthalpy of solution[64]*
	<i>kJ/mole</i>	<i>kJ/mole</i>	<i>kJ/mole</i>	<i>kJ/mole</i>	<i>kJ/mole</i>
NaCl	-365	-415	-340	-365	12.0
LiNO₃	-475	-531	-300	-310	-3.8
NaNO₃	-365	-415	-300	-310	20.5
KNO₃	-295	-334	-300	-310	34.2
RbNO₃	-275	-308	-300	-310	35.5
CsNO₃	-250	-283	-300	-310	40.1
LiNO₃·3H₂O	-475	-530	-300	-310	22.5

The data contained in this section will be used in the work reported in chapter 5. Also, a section containing information about density of the solution and analysis of the behaviour of a pure solution have been included in that chapter, because the rest of the work included there uses those values as a logical starting point.

4.4 Conclusions

In this Chapter, we discussed the need for a reliable, transferable force-field for the alkali metal nitrates that can be used for all the nitrates including solid solutions. Our force-

field reproduces the order of stability of the polymorphs for each alkali nitrate, the crystal structures of the polymorphs together with the elastic and dielectric properties of the materials where these are available. Stable phonon spectra (i.e. no imaginary modes) are obtained in all cases. The model also behaves well as a function of temperature, reproducing the experimental lattice expansion and also showing the transformation of the structures to disordered forms (due to the thermally activated rotation of the nitrate groups) where appropriate. The model is also compatible with the well-known model of Joung and Cheatham[26] for alkali metal ions in solution. Future work will demonstrate the application of this model to aqueous interfaces and crystallisation.

4.5 Appendix – Force-field fitting details

The fitting process begins with a set of crystal structures (e.g. potassium nitrate structures). A range of common functional forms are chosen such as a Lennard-Jones potential, Coulombic interactions for electrostatics, and bond, angle, and dihedral terms to denote bond stretching, angle bending, and torsional rotations. A set of reference data, (experimental observations and/or quantum mechanical computations) are used for the fitting process. This information could be vibrational frequencies, interaction energies, dihedral angles, equilibrium bond lengths, or angles.

The force field parameters (e.g., bond strengths, atomic charges, van der Waals parameters) are adjusted or "fit" to reproduce the reference data as closely as possible. This is done through an iterative optimisation process. An objective function or cost function is defined to quantify the difference between the force field's predictions and the reference data. The goal is to minimise this objective function during the fitting process. GULP employs optimisation techniques, such as nonlinear least-squares fitting or genetic algorithms, to adjust the force field parameters iteratively. The optimisation seeks to minimise the difference between the computed force field properties and the reference data.

The optimisation process continues until certain convergence criteria are met. These criteria could include reaching a minimum value for the objective function or achieving specific tolerances on the fitted parameters. Once the force field parameters are determined, it is essential to validate the force field's predictive accuracy. This is typically done by comparing the force field's predictions to additional reference data that was not used in the fitting process.

The force field should provide good agreement with experimental or high-level quantum mechanical results for a variety of molecular or material properties.

The final set of force field parameters is stored for future use in simulations. These parameters can then be used to model the interactions in molecular dynamics simulations, Monte Carlo simulations, or other types of simulations in GULP and translated into other programs.

Force field fitting in GULP is a crucial step in accurately representing the interactions between atoms or molecules in a system. The success of the force field depends on the quality and diversity of the reference data and the effectiveness of the parameter optimisation process.

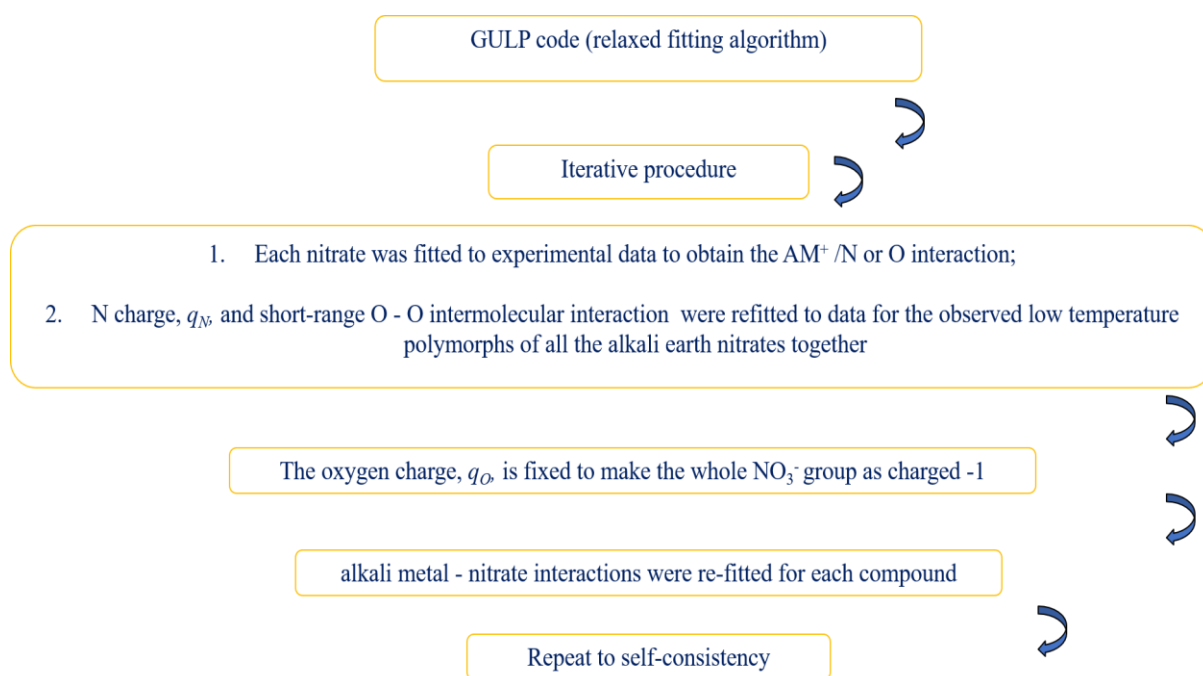


Figure 4.15 Scheme of the fitting process using GULP for this force field

4.6 References

- [1] G.C. Sosso, J. Chen, S.J. Cox, M. Fitzner, P. Pedevilla, A. Zon, A. Michaelides, *Crystal Nucleation in Liquids, Open Questions and Future Challenges in Molecular Dynamics Simulations*, Chem. Rev., 2016, **116**, 7078;
- [2] M. Jehannin, A. Rao, H. Cölfen, *New Horizons of Non-classical Crystallisation*, J. Amer. Chem. Soc., 2018, **141**, 10120;
- [3] J. Berce, M. Zupančič, M. Može, I. Golobič, *A Review of Crystallisation Fouling in Heat Exchangers*, Processes, 2021, **9**,1356;
- [4] R. Benages-Vilau, T. Calvet, M.A. Cuevas-Diarte, *Polymorphism, crystal growth, crystal morphology and solid-state miscibility of alkali nitrates*, Cryst. Rev., 2014, **20**, 25;
- [5] R.B. Hammond, M.J. Orley, K.J. Roberts, R.A. Jackson, M.J. Quayle, *An Examination of the Influence of Divalent Cationic Dopants on the Bulk and Surface Properties of Ba(NO₃)₂ Associated with Crystallization*, Cryst. Growth Des., 2009, **9**, 2588;
- [6] M.C.C. Ribeiro, *On the Chemla effect in molten alkali nitrates*, J. Chem. Phys., 2002, **117**, 266;
- [7] W.J. Xie, Z. Zhang, Y.Q. Gao, *Ion Pairing in Alkali Nitrate Electrolyte Solutions*, J. Phys. Chem. B, 2016, **120**, 2343;
- [8] H. Ni, J. Wu, Z. Sun, G. Lu, J. Yu, *Molecular simulation of the structure and physical properties of alkali nitrate salts for thermal energy storage*, Renew. Energy, 2019, **136**, 955;
- [9] K.A. Mort, P.J. Wilde, R.A. Jackson, *Computer modelling of ammonium nitrate: I. Development of potentials and calculation of lattice properties*, J. Phys. Condens. Matter, 1999, **11**, 3967;
- [10] S. Jayaraman, A.P. Thompson, O.A. von Lilienfeld, E.J. Maginn, *Molecular Simulation of the Thermal and Transport Properties of Three Alkali Nitrate Salts*, Ind. Eng. Chem. Res., 2010, **49**, 559;
- [11] X. Wu, F. Fronczek, L. Butler, *Structure of LiNO₃ – point-charge model and sign of the Li–7 quadrupole coupling-constant*, Inorg Chem., 1994, **33**, 1363;
- [12] D. Aquilano, R. Benages-Vilau, M. Bruno, M. Rubbo, F.R. Massaro, *Positive and negative form of calcite crystal (CaCO₃) in the light of Bravais-Friedel-Donnay-Harker and Hartman-Perdok Approach*, Cryst. Eng. Comm., 2013, **15**, 4465;
- [13] G. Gonschorek, H. Weitzel, G. Mieke, W. Schmahl, *The crystal structure of NaNO₃ at 100 K, 120 K, and 563 K*, Z Krist., 2000, **215**, 752;
- [14] M.J. Harris, *A new explanation for the unusual critical behaviour of calcite and sodium nitrate, NaNO₃*, Am Min., 1999, **84**, 1632;

- [15]R. Benages-Vilau, M. Rubbo, T. Calvet, D. Aquilano, M.A. Cuevas-Diarte, *Growth Kinetics of the {10.4} Faces of Nitratine (NaNO₃)*, Cryst. Growth Des., 2013, **13**, 3419;
- [16]R. Benages-Vilau, T. Calvet, L. Pastero, D. Aquilano, M.A. Cuevas-Diarte, *Morphology Change of Nitratine (NaNO₃) from Aqueous Solution, in the Presence of Li⁺ and K⁺ Ions*, Cryst. Growth Des, 2015, **15**, 5338;
- [17]C.N.R. Rao, B. Prakash, M. Natarajan, *Crystal structure transformations in inorganic nitrites, nitrates, and carbonates*, Washington: National Standard Reference Data System-National Bureau of Standards, 1975;
- [18]M. Fugel, F. Kleemiss, L.A. Malaspina, R. Pal, P.R. Spackman, D. Jayatilaka, G. Grabowsky, *Investigating the resonance in nitric acid and the nitrate anion based on a modern bonding analysis*, Aust. J. Chem., 2018, **71**, 227;
- [19]J.K. Nimmo, B.W. Lucas, *The crystal structures of gamma- and beta-KNO₃ and the alpha-gamma-beta transformations*, Acta Cryst. B, 1976, **32**, 1968;
- [20]E.F. Freney, L.A.J. Garvie, T.L. Groy, P.R. Buseck, *Growth and single-crystal refinement of phase-III potassium nitrate, KNO₃*, Acta Cryst. B, 2009, **65**, 659;
- [21]S. Wolf, N. Alam, C. Feldmann, *delta-KNO₃: synthesis and structure of a new modification of potassium nitrate*, Z. für Anorg. und Allge. Chem., 2015, **641**, 383;
- [22]T.G. Worlton, D.L. Decker, J.D. Jorgensen, R. Kleb, *Structure of high-pressure KNO₃ - IV*, Physica B+C, 1986, **136**, 503;
- [23]M. Shamsuzzoha, B.W. Lucas, *Structure (neutron) of phase IV rubidium nitrate at 298 and 403 K*, Acta Cryst. B, 1982, **38**, 2353;
- [24]D. Pohl, T. Gross, *Cesium nitrate (II) at 296 K*, Acta Cryst. C, 1993, **49**, 316;
- [25]K.J. Rao, C.N.R. Rao, *Crystal structure transformations of alkali sulphates, nitrates and related substances: thermal hysteresis in reversible transformations*, J. Mater. Sci., 1966, **1**, 238;
- [26]S. Joung, T.E. Cheatham, *Determination of Alkali and Halide Monovalent Ion Parameters for Use in Explicitly Solvated Biomolecular Simulations*, J. Phys. Chem. B, 2008, **112**, 9020;
- [27]P. Raiteri, J.D. Gale, D. Quigley, P.M. Rodger, *Thermodynamically Consistent Force-field for Molecular Dynamics Simulations of Alkaline-Earth Carbonates and Their Aqueous Speciation*, J. Phys. Chem. C, 2010, **114**, 5997;
- [28]J. Mei, J.W. Davenport, G.W. Fernando, *Analytic embedded-atom potentials for fcc metals: Application to liquid and solid copper*, Phys Rev B, 1991, **43**, 4653;
- [29]J.D. Gale, *GULP: A computer program for the symmetry-adapted simulation of solids*, J. Chem. Soc. Faraday Trans., 2005, **93**, 629;

- [30]J.D. Gale, *General Utility Lattice Program*, version 5.2 (<https://gulp.curtin.edu.au/gulp/> accessed 10th Feb 2022)
- [31]J.D. Gale, *Empirical potential derivation for ionic materials*, *Philos. Mag. B*, 1996, **73**, 3;
- [32]S. Haussühl, *Elastic properties of the nitrates of lithium, sodium, potassium, cesium, silver and thallium*, *Z. für Kristall.*, 1990, **190**, 111;
- [33]A. Mansingh, A.M. Smith, *Dielectric and conductivity studies in potassium nitrite and potassium nitrate*, *J. Phys. D: Appl. Phys.*, 1971, **4**, 560;
- [34]S.J. Clark, M.D. Segall, C.J. Pickard, P.J. Hasnip, M.J. Probert, K. Refson, M.C. Payne, *First principles methods using CASTEP*, *Z. Kristall.*, 2005, **220**, 567;
- [35]K. Burke, *Perspective on density functional theory*, *J. Chem. Phys.*, 2012, **136**,150901;
- [36]F. London, *Zur Theorie und Systematik der Molekularkräfte*, *Z. für Phys.*, 1930, **63**, 245;
- [37]S. Grimme, J. Antony, S. Ehrlich, H. Krieg, *A consistent and accurate ab initio parametrization of density functional dispersion correction (DFT-D) for the 94 elements H-Pu*, *J. Chem. Phys.*, 2010, **132**,154104;
- [38]J.P. Perdew, K. Burke, M. Ernzerhof, *Generalized Gradient Approximation Made Simple*, *Phys. Rev. Lett.*, 1996, **77**, 3865;
- [39]Y. Wu, H.L. Tepper, G.A. Voth, *Flexible simple point-charge water model with improved liquid-state properties*, *J. Chem. Phys.*, 2006, **124**, 024503;
- [40]W. Smith, T.R Forester, *DL_POLY_2.0: A general-purpose parallel molecular dynamics simulation package*, *J. Molec. Graphics*, 1996, **14**, 136;
- [41]U. Essmann, L. Perera, M.L. Berkowitz, T. Darden, H. Lee, L.G. Pedersen, *A smooth particle mesh Ewald method*, *J. Chem. Phys.*, 1995, **103**, 8577;
- [42]S. Plimpton, *Fast Parallel Algorithms for short-range molecular dynamics*, *J. Comp. Phys.*, 1995, **117**, 1;
- [43]M. de Koning, A. Antonelli, *Einstein crystal as a reference system in free energy estimation using adiabatic switching*, *Phys. Rev. E*, 1996, **53**, 465;
- [44]R.D. Shannon, *Revised Effective Ionic Radii and Systematic Studies of Interatomic Distances in Halides and Chalcogenides*, *Acta Cryst. A*, 1976, **32**, 751;
- [45]D.V. Korabel'nikov, Y.N. Zhuraviev, *First-principles study of the elastic properties of nitrates*, *Russ. Phys. J.*, 2017, **59**, 2122;
- [46]K. Hermansson, J.O. Thomas, I. Olovsson, *Hydrogen Bond Studies. CXXXVIII. Neutron Diffraction Studies of LiNO₃(H₂O)₃ at 120 and 295 K*, *Acta Cryst B*, 1980, **36**, 1032;

- [47] Y. Marcus, *The hydration entropies of ions and their effects on the structure of water*, J. Chem. Soc. (Farad. Trans. 1), 1986, **82**, 233;
- [48] Y. Marcus, *The thermodynamics of solvation of ions Part 2. - The enthalpy of hydration at 298.15 K*, J. Chem. Soc. (Farad. Trans. 1), 1987, **83**, 339;
- [49] Y. Marcus, *Thermodynamics of solvation of ions. Part 5.—Gibbs free energy of hydration at 298.15 K*, J. Chem. Soc. (Farad Trans), 1991, **87**, 2995;
- [50] T.S. Hofer, P.H. Hünenberger, *Absolute proton hydration free energies, surface potential of water, and redox potential of the hydrogen electrode from first principles: QM/MM free-energy simulations of sodium and potassium hydration*, J. Chem. Phys., 2018, **148**, 222814;
- [51] A. Malloum, J.J. Fifen, J. Conradie, *Determination of the absolute solvation free energy and enthalpy of the proton in solutions*, J. Mol. Liq., 2021, **322**, 114919;
- [52] T. Darden, D. Pearlman, L.G. Pedersen, *Ionic charging free energies: Spherical versus periodic boundary conditions*, J. Chem. Phys., 1998, **109**, 10921;
- [53] K. Fuchs, *A quantum mechanical investigation of the cohesive forces of metallic copper*, Proc. Roy. Soc. A, 1935, **151**, 585;
- [54] M. Leslie, M.J. Gillan, *The energy and elastic dipole tensor of defects in ionic crystals calculated by the supercell method*, J. Phys. C, 1985, **18**, 973;
- [55] V. Ballenegger, J.J. Cerda, O. Lenz, C. Holm, *The optimal P^3M algorithm for computing electrostatic energies in periodic systems*, J. Chem. Phys., 2008, **128**, 034109;
- [56] G. Hummer, L.R. Pratt, A.E. Garcia, *Free energy of ionic hydration*, J. Chem. Phys., 1996, **100**, 1206; *ibid* *Ion sizes and finite-size corrections for ionic solvation free energies*, J. Chem. Phys., 1997, **107**, 1275;
- [57] M.A. Kastholz, P.H. Hünenberger, *Computation of methodology-independent ionic solvation free energies from molecular simulations. I. The electrostatic potential in molecular liquids*, J. Chem. Phys. **124** 124106; *ibid*, *II The hydration free energy of the sodium cation*, J. Chem. Phys., 2006, **124**, 224501;
- [58] T. Simonson, G. Hummer, B. Roux, *Equivalence of M- and P-summation in calculations of ionic free energies*, J. Phys. Chem. A, 2017, **121**, 1525;
- [59] R. Caminiti, G. Licheri, G. Piccaluga, G. Pinna G, *On NO_3^- - H_2O interactions in aqueous solutions*, J. Chem. Phys., 1978, **68**, 1967;
- [60] L.X. Dang, T.M. Chang, M. Roeselova, B.M. Garrett, D.J. Tobias, *Rotation driven translational diffusion of polyatomic ions in water: A novel mechanism for breakdown of Stokes-Einstein relation*, J. Chem. Phys., 2006, **124**, 066101;

- [61]P. Banerjee, S. Yashonath, B. Bagchi, *Coupled jump rotational dynamics in aqueous nitrate solutions*, J. Chem. Phys., 2016, **145**, 234502;
- [62]V. Ballenegger, J.J. Cerda, O.Lenz, C. Holm, *P3M algorithm for dipolar interactions*, J. Chem. Phys., 2008, **128**, 034109;
- [63]M.A. Kastenholtz, P.H. Hünenberger, *Computation of methodology-independent ionic solvation free energies from molecular simulations. II. The hydration free energy of the sodium cation*, J. Chem. Phys., 2006, **124**, 224501;
- [64]M.M. Reif, P.H. Hünenberger, *Computation of methodology-independent single-ion solvation properties from molecular simulations. IV. Optimized Lennard-Jones interaction parameter sets for the alkali and halide ions in water*, J. Chem. Phys., 2011, **134**, 144104;
- [65]G. Hummer, L.R. Pratt, A.E. Garcia, B.J. Berne, S.W. Rick, *Electrostatic Potentials and Free Energies of Solvation of Polar and Charged Molecules*, J Phys Chem B, 1997, **101**, 3017;
- [66]T.T. Duignan, M.D. Baer, G.K. Schenter, C.J. Mundy, *Electrostatic solvation free energies of charged hard spheres using molecular dynamics with density functional theory interactions*, J. Chem. Phys., 2017, **147**, 61716;
- [67]Y. Wu, H.L. Tepper, G.A. Voth, *Flexible simple point-charge water model with improved liquid-state properties*, J. Chem. Phys., 2006, **124**, 024503;
- [68]Y. Marcus, *The thermodynamics of solvation of ions. Part 2.—The enthalpy of hydration at 298.15 K*, J. Chem. Soc. (Faraday), 1987, **83**, 2985;
- [69]S. Boothroyd, A. Kerridge, A. Broo, D. Buttar, J. Anwar, *Solubility prediction from first principles: a density of states approach*, Phys. Chem. Chem. Phys., 2018, **20**, 20981;
- [70]D.D. Wagner, W.H. Evans, V.B. Parker, R.H. Schumm, I. Halow, S.M. Bailey, K.L. Churney, R.L. Nuttall, *The NBS Tables of Chemical Thermodynamic Properties*, J. Phys. Chem. Ref. Data, 1982, **11**, Suppl. 2;
- [71]K. Hermansson, J.O. Thomas, I. Olovsson, *Hydrogen bond studies. CXXXVIII. Neutron diffraction studies of $\text{LiNO}_3 \cdot 3\text{H}_2\text{O}$ at 120 and 295 K*, Acta Cryst. B, 1980, **36**, 1032;
- [72]G. Zou, C. Lin, H.G. Kim, H. Jo, K.M. Ok, *$\text{Rb}_2\text{Na}(\text{NO}_3)_3$: A Congruently Melting UV-NLO Crystal with a Very Strong Second-Harmonic Generation Response*, Crystals, 2016, **6**, 1;
- [73]J. Lefebvre, R. Currat, R. Fouret, M. More, *Neutron diffusion studies of lattice vibrations in sodium nitrate*, J. Phys. C, 1980, **13**, 4449;
- [74] H. Bilz, W. Kress, *Phonon Dispersion relations in insulators*, Springer-Verlag, Berlin, 1979, 159
- [75]D.W. James, W.H. Leong, *Vibrational Spectra of Single Crystals of Group I Nitrates*, J. Chem. Phys., 1968, **49**, 5089

Chapter 5

Supersaturated solutions of Potassium Nitrate

This chapter will focus on work examining the behavior of potassium nitrate in a pure, homogeneous, supersaturated solution.

As previously mentioned, nucleation is a rare event, therefore with the use of classical molecular dynamics, the goal was not to see the formation of one or multiple nuclei, but instead to check for clustering, and to see if any of those clusters would resemble a polymorph nucleating in solution.

Calculations have been performed at various concentrations, all above the expected saturation value^[1].

5.1 Behaviour of KNO₃ solutions

Starting from a box of water and potassium nitrate, molecular dynamics simulations using DL_POLY in an NVT ensemble have been performed (2,000 water molecules and 50 potassium nitrate formula units). The radial distribution function (RDF) for KNO₃-water was extracted and analysed (see Figure 5.1). The first maximum in the RDF for the nitrogen and the oxygen in the water molecule ($r_{max}(\text{N-O}_w)$) is at 3.59 Å, shows good agreement with those found in the literature (Table 5.1).

Table 5.1 Comparison between $r_{max}(\text{N-O}_w)$ obtained in this work and available data in literature

	$r_{max}(\text{N-O}_w)$
<i>Experimental</i> ^[59]	3.5 ± 0.311 Å
Xie et al. ^[7]	3.65 Å
Dang et al. ^[60]	3.40 Å
Banerjee et al. ^[61]	3.50 Å
This work	3.59 Å

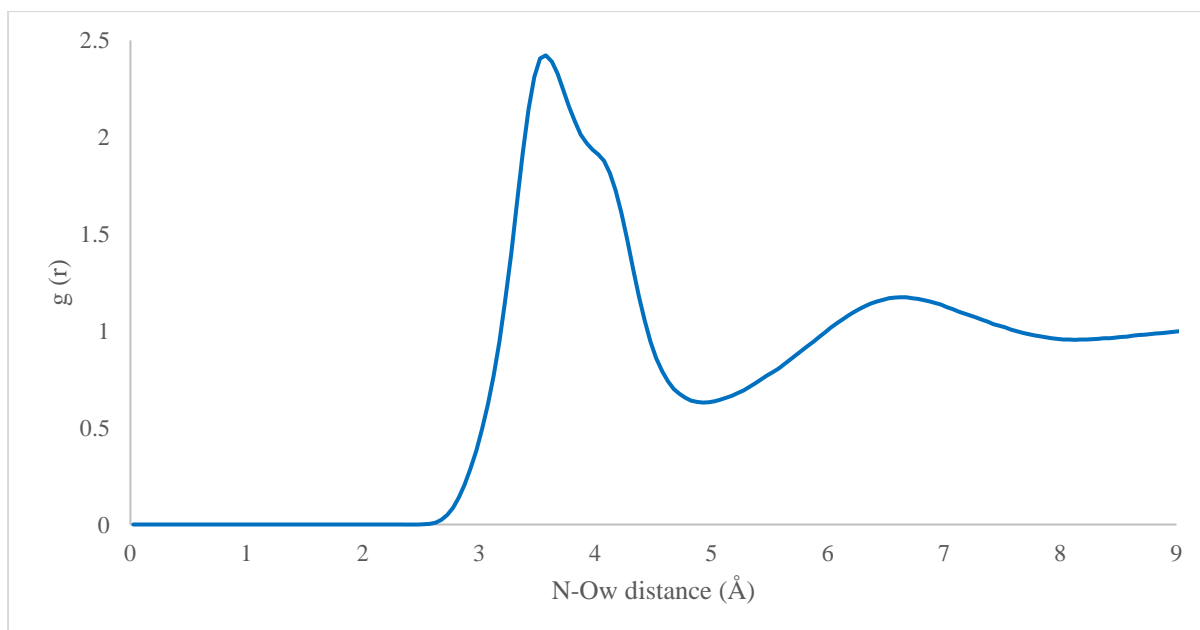


Figure 5.1 Radial distribution function (RDF) for nitrogen of nitrate- oxygen of the water at 300K

The coordination number of water oxygen atoms around the nitrogen has been calculated (9.6), by integrating the RDF and shows good agreement with the values from previous literature as seen in Table 5.2

Table 5.2 Comparison between coordination number obtained in this work and available data in literature.

Coordination number	
Xie <i>et al.</i> ^[7]	10±1
Dang <i>et al.</i> ^[60]	12
Banerjee <i>et al.</i> ^[61]	9.2
This work	9.6

Starting from various boxes containing the theoretically exact calculated value for molality, the true density of the solution has been extracted and plotted in Figure 5.2. The trend is in perfect agreement with the experimental one and the offset visible can be explained by considering that the density of the water model used (SPC-Fw), as highlighted in Table 5.3 is 15 kg/m³ larger than the experimental value.

Table 5.3 Comparison of density values, for pure water at room temperature.

Pure water density, 298.15K	
Wu et al. ^[3]	1012 kg/m ³
Exp.	997 kg/m ³

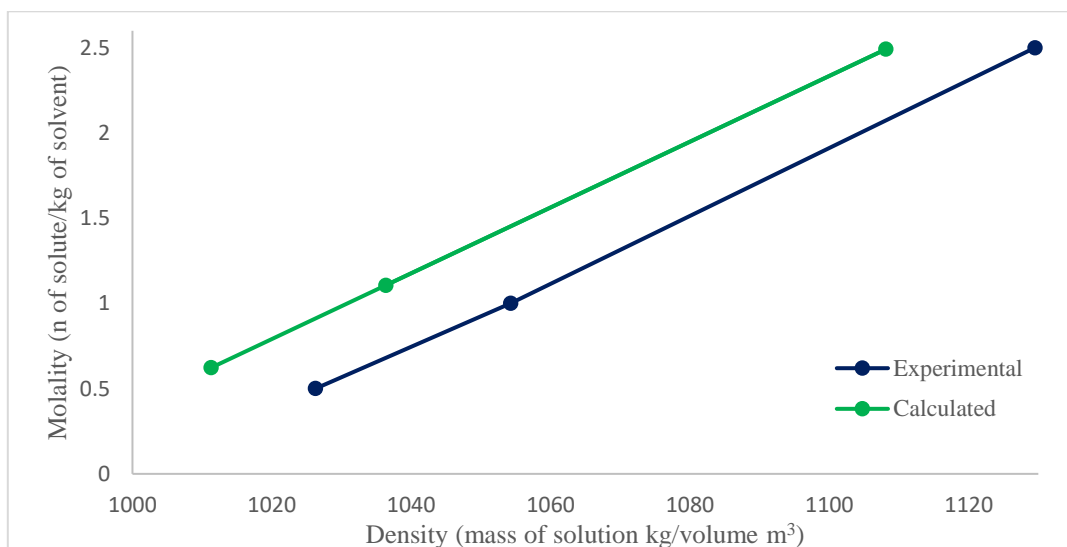


Figure 5.2 Comparison between experimental density of KNO_3 solution and the values obtained using force-field from this work ^[2]

5.1.1 Classical Molecular Dynamics

A set of filled boxes containing various concentrations of potassium nitrate were built using PACKMOL^[4].

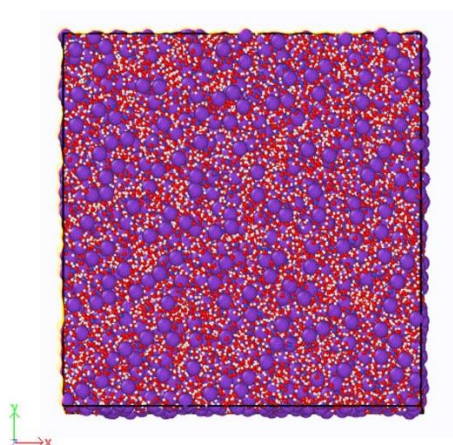


Figure 5.3. 6 molal box of potassium nitrate. Purple balls represent potassium ion, blue ball represent the nitrogen, red balls oxygens from the nitrate group and water, white balls represent the hydrogens from water.

Various numbers of formula units of KNO_3 were randomly packed into a cube with a volume based on the density data extracted from Figure 5.2. Concentration varied from 6 molal to 12 molal (including 8m and 10m). MD simulations were performed using the DL POLY_4 package^[5]. All the boxes have been pre-equilibrated using an *npt ensemble*, with a Nose-Hoover barostat, at 300 K and 1 atmosphere of pressure for 2 ns. There was little to no fluctuation in the volume and the final configuration was used as a starting point.

The MD was performed with a *nvt ensemble* and run with a time step of 0.5 fs for a total of 10 ns, after the system had reached convergence. Potassium nitrate and its interactions with water were modelled using the force-field developed in this work, see Chapter 4^[2].

5.1.1.1 Radial distribution functions

Radial distribution functions have been extracted and analysed for all the different concentrations after the 10 ns runs. In the attempt to find a resemblance in the organisation of the ions in solution, with the polymorph structure, significant guidance can come from the analysis of the RDF: the two different polymorphs of KNO_3 differ from one another in the coordination of K with respect to the oxygens of the nitrate group. This information can be derived by the integration of the first peak of said RDF. The aragonite structure shows a coordination number of 9, and the calcite structure a coordination of 6.

Figure 5.4 shows the RDF of the K to ON (oxygen of the nitrate anion) interaction in a block of solid KNO_3 -aragonite. At 0 K the first peak (first coordination shell) is split in two, as it differentiates the oxygens in the plane between the oxygens perpendicular to the potassium core (the first peak integrates to 3.6, while the second to 5.4).

However, by 300 K the nitrate groups are ‘spinning’, as shown in Figure 5.6, leading to rotational disorder. Their position is no longer stable in time, as captured by the two snapshots, and therefore the RDF peaks now merged and what we obtain is an average of the two, with a non-integer integral number, (instantaneous position of the oxygen might be away from the expected position). The integration of the peak results in a coordination number of 8.6, which can be approximated to the aragonitic structure.

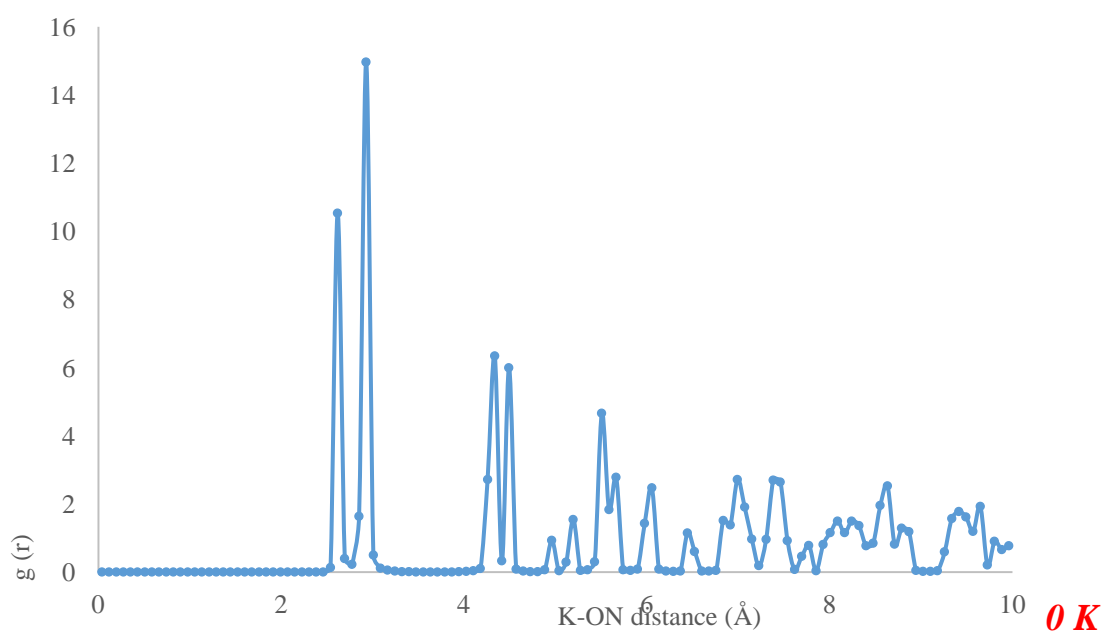


Figure 5.4 RDF for the K to O(NO₃) solid potassium nitrate (aragonite) at 0K

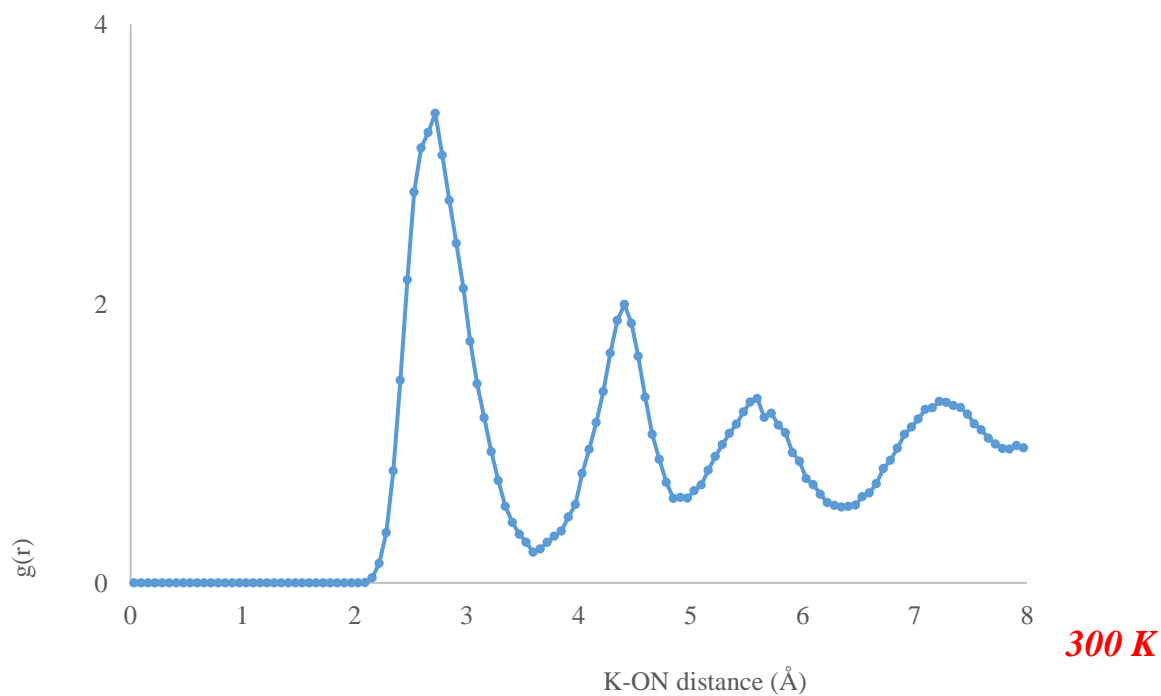


Figure 5.5 RDF for the K to O(NO₃) solid potassium nitrate (aragonite) at 300K.

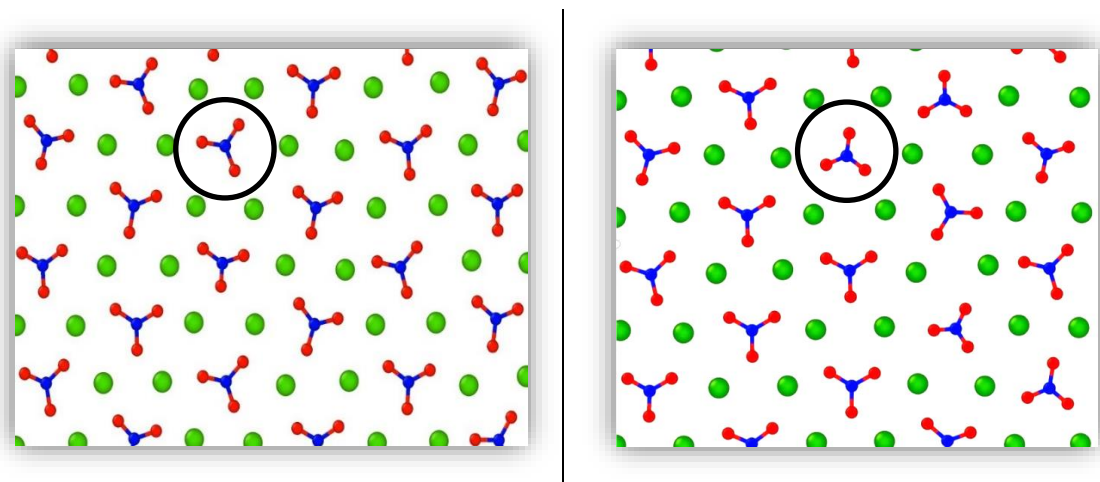


Figure 5.6 Snapshot of a KNO_3 -aragonite box in two different timesteps of the simulation. Black circle highlights how the same nitrate group changes position though the simulation.

The analysis of the RDF for all the different concentrations in solution shows a clear (Table 5.4) coordination maximum of 11 oxygens. As the concentration increases, the number of those oxygens belonging to a nitrate group increases, while the number of oxygens belonging to a water molecule decreases. There is less hydration around the potassium as the concentration increases, which might favour clustering. The following section will explore this possibility in detail.

Table 5.4 Coordination number for K in respect to O of the nitrate group and O of the water for different molality boxes

	Coordination number		
	K-ON	K-OW	total
6 m	4.7	5.3	11
8 m	5	6	11
10 m	6.7	4.3	11
12 m	7.5	3.5	11

5.2 Cluster Analysis

A system behaving according to classical nucleation theory should keep forming and dissolving nuclei until they reach and overcome the critical radius, as previously discussed in Chapter 1, Section 1.3.1.

K ions were recorded as being in a cluster if they were within 4.5 \AA of another K ion.

Clusters fall between small molecules or ions in solution and bulk material. We define a cluster as an aggregate of a countable number of particles (from 2 to 10^n , where n can be up to 6 or 7).

The constituent particles may be identical (homo-atomic) or molecular, (A_a) or contain two or more different species (hetero-atomic or molecular clusters A_aB_b). We might consider defining the clusters by the number of potassium atoms or clusters of potassium and nitrate ions.

Clusters are of importance in the context of nucleation. The fact that clusters cover a vast range of particle sizes, from the molecular (with quantised states) to the microcrystalline, is perhaps one of the strongest arguments for researching clusters (where states are quasi-continuous). Additionally, clusters make up a brand-new class of material called nanoparticles, which may have characteristics that are different from those of single molecules or bulk matter.

Another important fundamental area of research is the evolution of clusters' geometric and electrical structures as well as their chemical and physical characteristics.

What we are interested to capture here, for the chosen system of interest, KNO_3 , is:

- 1) The correlation between a cluster size and the resemblance of its structure to that of the bulk crystal;
- 2) Possible phase transitions;
- 3) The geometric structure of the cluster and its relationship to the cluster size, in order to understand how it relates to crystal growth at the nano level.

The most likely polymorph to develop may be a product of thermodynamic and kinetic aspects of the material growth process. A phase must initially emerge through some sort of nucleation process that involves the creation of an interface with the surrounding solution in order to form. According to classical nucleation theory (CNT), at small sizes interfacial energies dominate the change in free energy of the developing nuclei ^[6]. Therefore, it is more likely for nuclei with relatively low interfacial energy to expand past a certain size before further growth becomes spontaneous.

We can assume that the topological arrangement of atoms will, at some point, match the final crystal structure, even though a developing nucleus is expected to have greater disorder than a typical bulk crystal. We can locate these in a solution of potassium nitrate using the geometric characteristics of the polymorphs, calcite and aragonite. We can also identify prospective candidates for crystal nuclei in the system. The ions that have formed a structure resembling calcite or aragonite may eventually develop into large crystals. We need to determine the

degree to which a particular group of atoms differs structurally from the general ion distribution present in the solution.

The thermodynamically most stable polymorph for potassium nitrate is the aragonite one^[7].

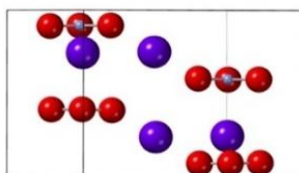


Figure 5.7 Unit cell of potassium nitrate (aragonite)

Work from Meldrum et al.^[8] has proven that under defined experimental conditions it is possible to observe the formation of the ferroelectric phase first. Their set-up consisted of poking microdroplets containing a supersaturated solution of potassium nitrate, using different materials as a stimulant. Those poking elements would vary from a standardised one, such as a functionalised glass rod, to ‘less predictable’ ones, such as human, feline or canine hairs, as shown in Figure 5.8.

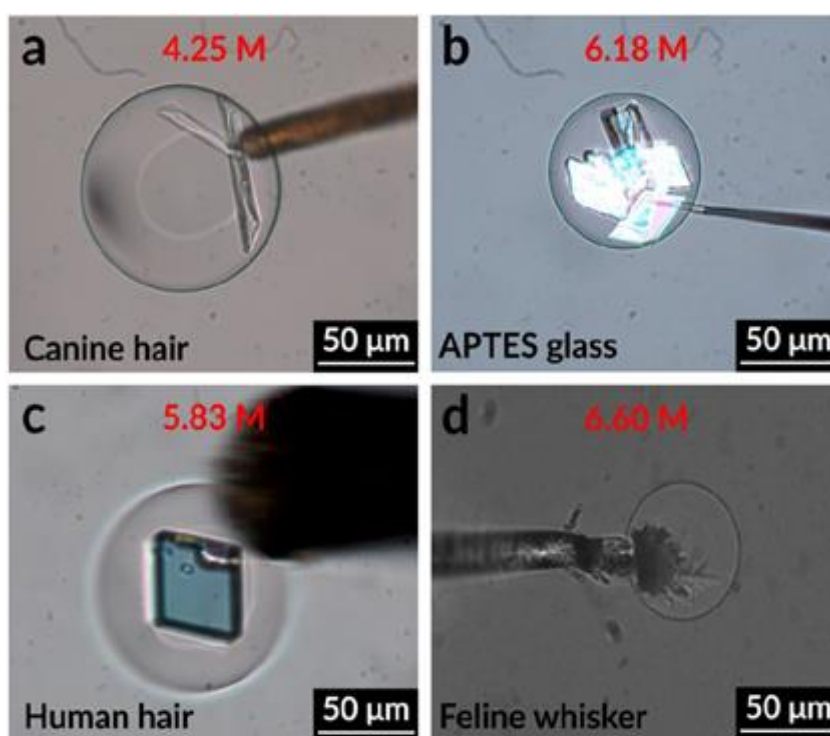


Figure 5.8 A collection of tip types and crystalline products at a variety of KNO_3 concentrations. (a) Canine hair producing two prismatic Phase II crystals at 4.25 M. (b) An APTES-treated (amine-terminated silane) glass tip producing a 5-6 prismatic Phase III crystals. (c) Human hair nucleating a single, prismatic Phase III crystal. (d) The feline whisker with a frayed tip creates many contact points with the droplet resulting in fast, dendritic growth of a Phase II crystal aggregate.^[8] Images supplied by F Meldrum, T Dunn (Leeds University).

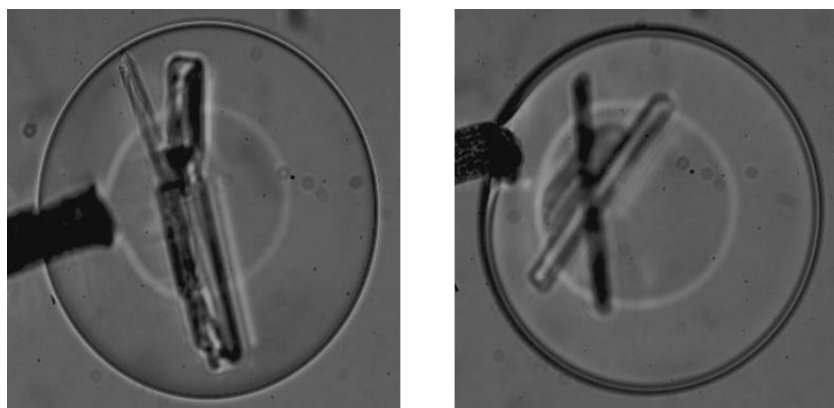


Figure 5.9 KNO_3 aragonite. Images supplied by F Meldrum, T Dunn (Leeds University)^[2]

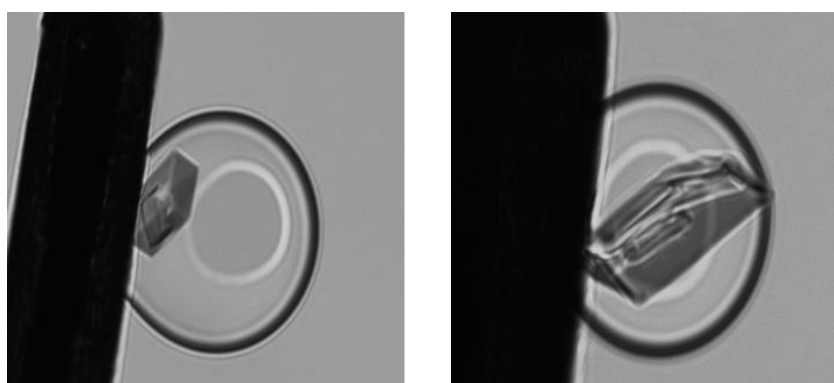


Figure 5.10 KNO_3 ferroelectric. Images supplied by F Meldrum, T Dunn (Leeds University)^[2]

These experiments have also proven that there is no evidence of crystallisation, for concentrations lower than 6 molar, without poking the droplets. Based on the literature^[9] and confirmed by our experimental collaboration we know that the process does not involve a microscopically visible dissolution-recrystallisation process. The following chapter will present the cluster analysis of various solutions of KNO_3 starting from a value sufficient to expect nucleation (6 molal), and boxes with gradually increasing concentration (8, 10 and 12 molal).

5.2.1 6m solution clustered

To induce crystallinity, atoms must begin to adopt the coordination and shape of the crystal. A box of solution corresponding to a 6 molal concentration was been built using Packmol^[4]. The ions were inserted in a limited region of the box, to induce clustering. The results reported here

show that, as expected, all the ions, having being forced together have the tendency to form a cluster.

Table 5.5 Cluster size (number of potassium ions) as a function of the radius of gyration (expressed in Å) for a 6 molal clustered solution of KNO_3

Cluster size	Radius of gyration (Å)
1	0
2	1.46
3	1.86
4	2.24
5	2.65
6	3.43
7	3.80
8	3.45
5843	34.29

The K are nearly all in one cluster of 5843 ions out of the total 6000 ions in solution. These numbers are supported by Figure 5.11, which shows the number of potassium units in a cluster as a function of the radius of gyration (in Å), the actual numbers are clarified in Table 5.5. Apart from a few clusters showing a limited number of units, the system is entirely dominated by a large cluster with a radius of gyration of 34.3 Å, which clearly shows the formation of a single unit.

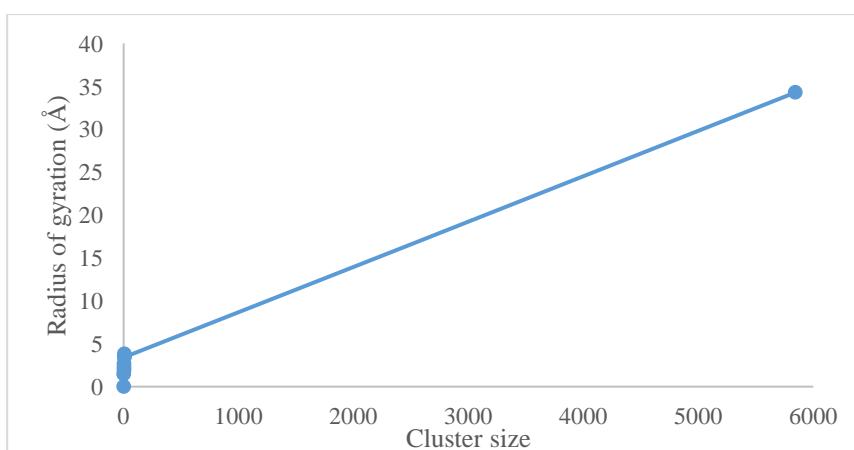


Figure 5.11 Cluster size vs radius of gyration

Figure 5.12 shows the behaviour of the data used to obtain the fractal dimension of the average cluster. The cluster method used is

$$df = \frac{d \ln N(r)}{d \ln(r)} \quad (5.1)$$

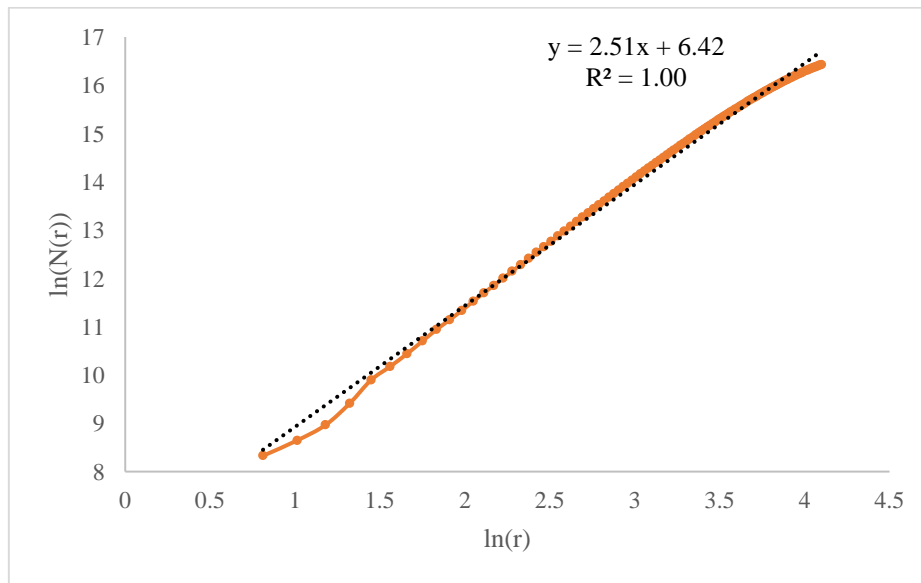


Figure 5.12 Fractal dimension of the largest finite cluster in solution for a 6 molal clustered box.



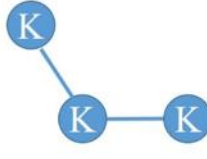
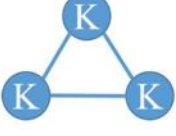
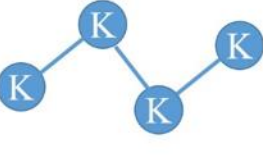
By extracting the logarithm of the number of connections ($\ln N(r)$, where r is the cluster radius), it is possible to obtain the linear trend shown in Figure 5.12. By interpolating this data, it is possible to obtain the fractal dimension of the cluster, which is the slope of the plot.

The expression "fractal dimension" is used to characterise the complexity of fractal patterns or set as a ratio of the change in scale to the change in detail.^{[10][11]} A wide range of objects^[12,13] can be described using fractal dimensions. Theoretically, the topological or Euclidean dimension of a set expressing a common geometric shape is identical to the set's fractal dimension.^[13-16]

Although it might be assumed that the relationship between an increasing fractal dimension and space-filling implies that fractal dimensions measure density, the two are not actually strictly correlated.^[17,18]

Fractal complexity can be quantified by fractal dimensions, even though it is not always easy to break it down into understandable units of size and detail without the use of time-consuming analytical techniques. Table 5.6 shows, for comparison, some integer dimension and some fractal dimensions.

Table 5.6 Schematic representation of cluster organisation and their number of connection (absolute and average)

					
Number of connections	0	1	2	2	3
Average number of connections			1 1/3		1 1/2

In this case, the number 2.5 shows a dimensionality between 2 and 3. The cluster is not linear, a plate, or a solid sphere either. The value of 2.5 suggests “holes” between the potassiums, which can be justified with the presence of water, which, in the previous section of this Chapter, has been shown to be part of the coordination shell of the ions.

5.2.2 8 molal solution

In this section, we are going to discuss the cluster analysis of an 8 molal box of KNO_3 . The box has been built randomly, so unlikely the previous section there is no artificially induced clustering.

Figure 5.13 shows the probability of connection for each potassium in the box. We consider two ions to be connected if their distances is below the first coordination shell in a perfect crystal. Most of the potassium appear to form about 1.7 connections to other potassiums (e.g. they are a single ion that forms and break dimers constantly), while, the total number of connections shows an exponential decrease, as would be expected from a system following classical nucleation theory. For the first 8 ns, there is no noticeable variation over time, while in the last couple of nanoseconds there seems to be a small increases in the number of connections. We would have expected something to happen in this timeframe, therefore running the system for longer seemed unnecessary at this stage.

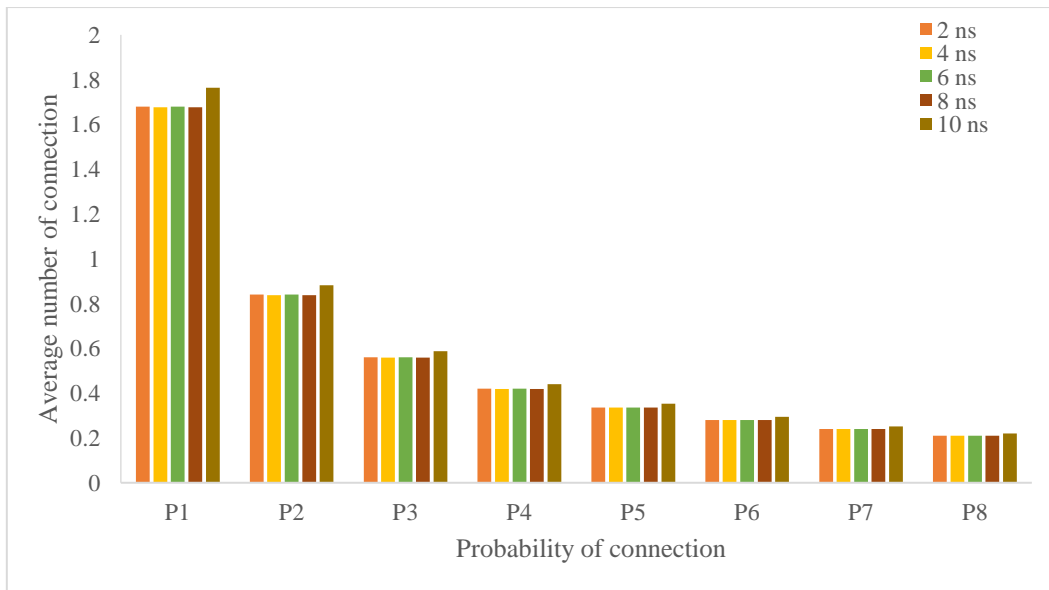


Figure 5.13 8 molal solution: probability of connection versus number of connection for each potassium in the solution.

Figure 5.14(a) shows that the average size for a finite cluster appears to be stable around 1.9 units, with a slight increase at the end of the simulation (1.98). On the other hand, Figure 5.14(b) shows the trend for the largest finite in cluster. This number seems to vary more though the simulation, from a minimum of 20 potassium to a maximum of 22.5.

Figure 5.14(c) shows the number of potassiums with no connections at all (single unit clusters). Out of a total of 8,000 potassiums in the box, an average of 2,240 appears to have no connections at all, with this number slightly decreasing through the simulation time to a minimum of approximately 2,216.

Figure 5.15 shows the logarithm of the number of connections as a function of the radius of a cluster, it presents a slope of 1.7, which indicates that the cluster is probably not a very dense 2-D one, and can be imagined as a flat surface with holes and gaps.

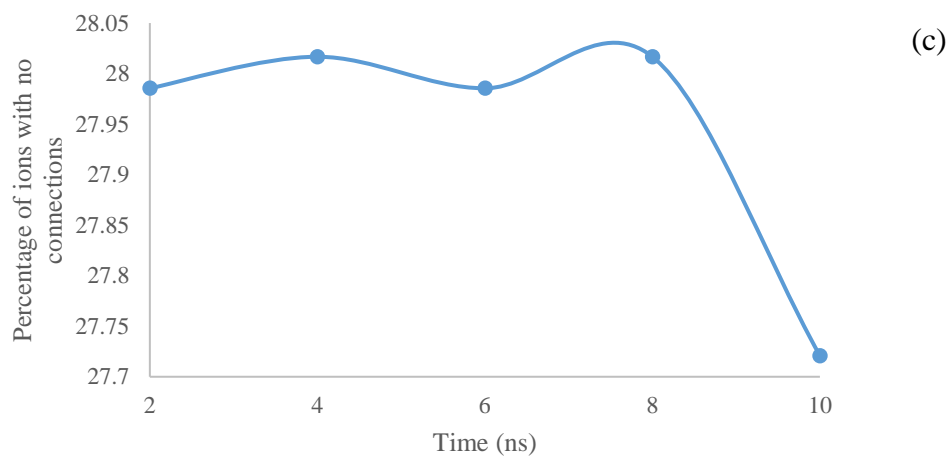
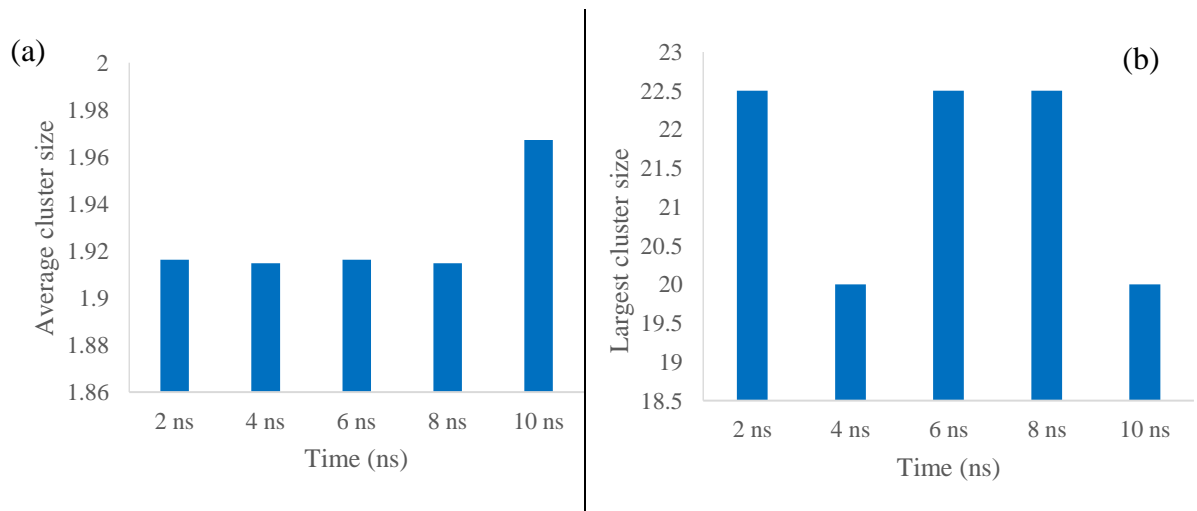


Figure 5.14 8 molal solution: (a) average number of potassium unit included in a finite size cluster though the 10 ns of simulation; (b) average number of potassium unit included in the largest detected cluster though the 10 ns of simulation; (c) average number of potassium unit not showing any connection at all though the 10 ns of simulation normalised as a function of the total number of potassiums.

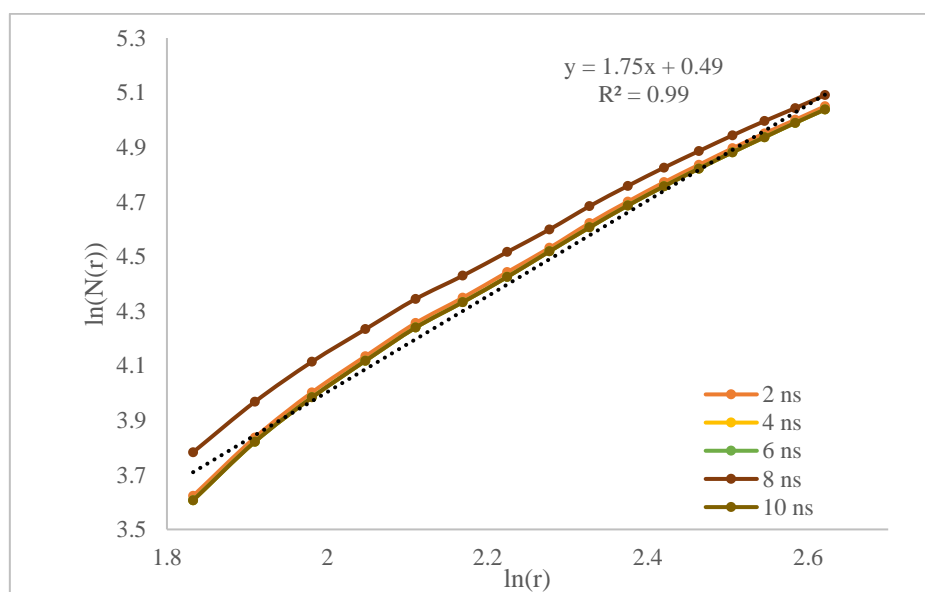


Figure 5.15 Fractal dimension of the largest finite cluster in solution for an 8 molal box

5.2.3 10 molal solution

In this section, we are going to discuss the cluster analysis of a 10 molal box of KNO_3 . Figure 5.16 shows the probability of connection for each potassium in the box. The potassium appear to be forming an average of 1.15 connections (lower than the 8 molal case), and as reported for the previous case the total number of connections, shows an exponential decrease.

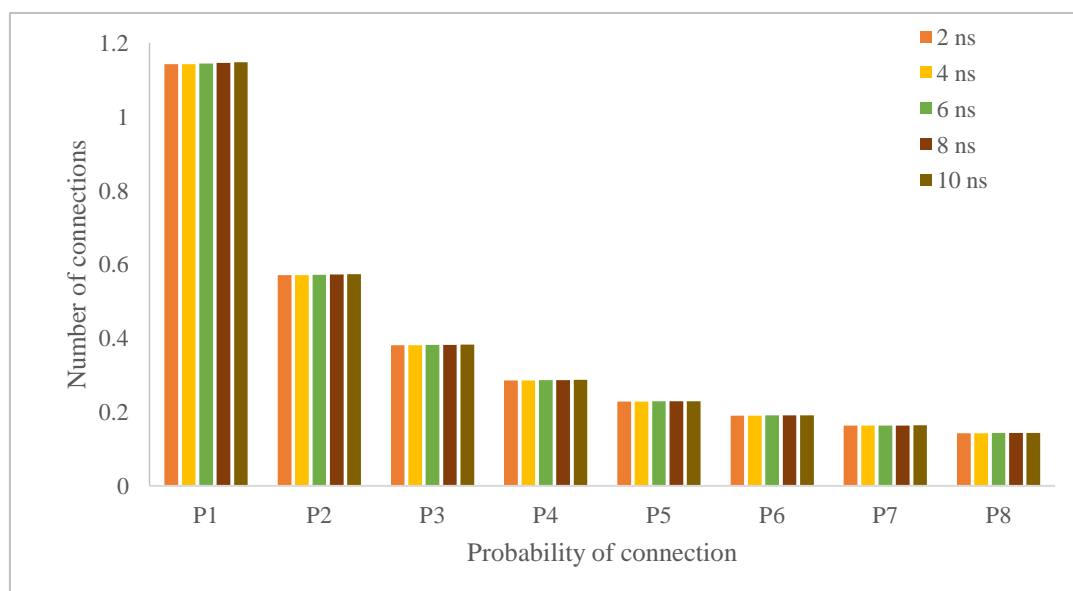


Figure 5.16 10 molal solution: probability of connection versus number of connection for each potassium in the solution.

The reduced average number of connections can be explained, in Figures 5.18(a/c). Figure 5.18(a) shows that the average size for a finite cluster, that appears to be stable is around 2.29 units, indicating that all the ions are involved in the formation of dimers. In fact the average is closer to that for a chain of three potassiums, or sometimes a triangular-shaped cluster. Those different shapes are highlighted in Figure 5.18. Figure 5.18(b) shows the trend for the largest finite cluster, which again appears to be doubled in size in comparison with the 8 molal cell case, it ranges from a minimum of 40.4 to a maximum of 42.3. Figure 5.18(c) shows the number of potassium with no connections at all (single unit clusters). Out of a total of 10,000 potassiums in the box, an average of 2,452 appears to have no connections at all, a similar number compared to the 8 molal box case, but it has to be considered that the total number is also increased, therefore, in this case, a smaller fractions of ions are left with no connections.

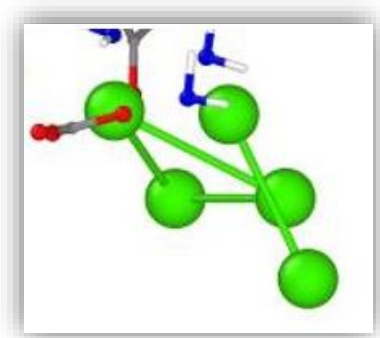


Figure 5.17 Collection of dimer and triangular-shaped cluster.

Figure 5.19 shows the logarithm of the number of connections as a function of the radius of a cluster, it presents a slope of 1.7, which indicates, like the previous case, that the cluster are probably not very dense 2-D one, and can be imagined as a flat surface with holes and gaps (see Figure 5.24).

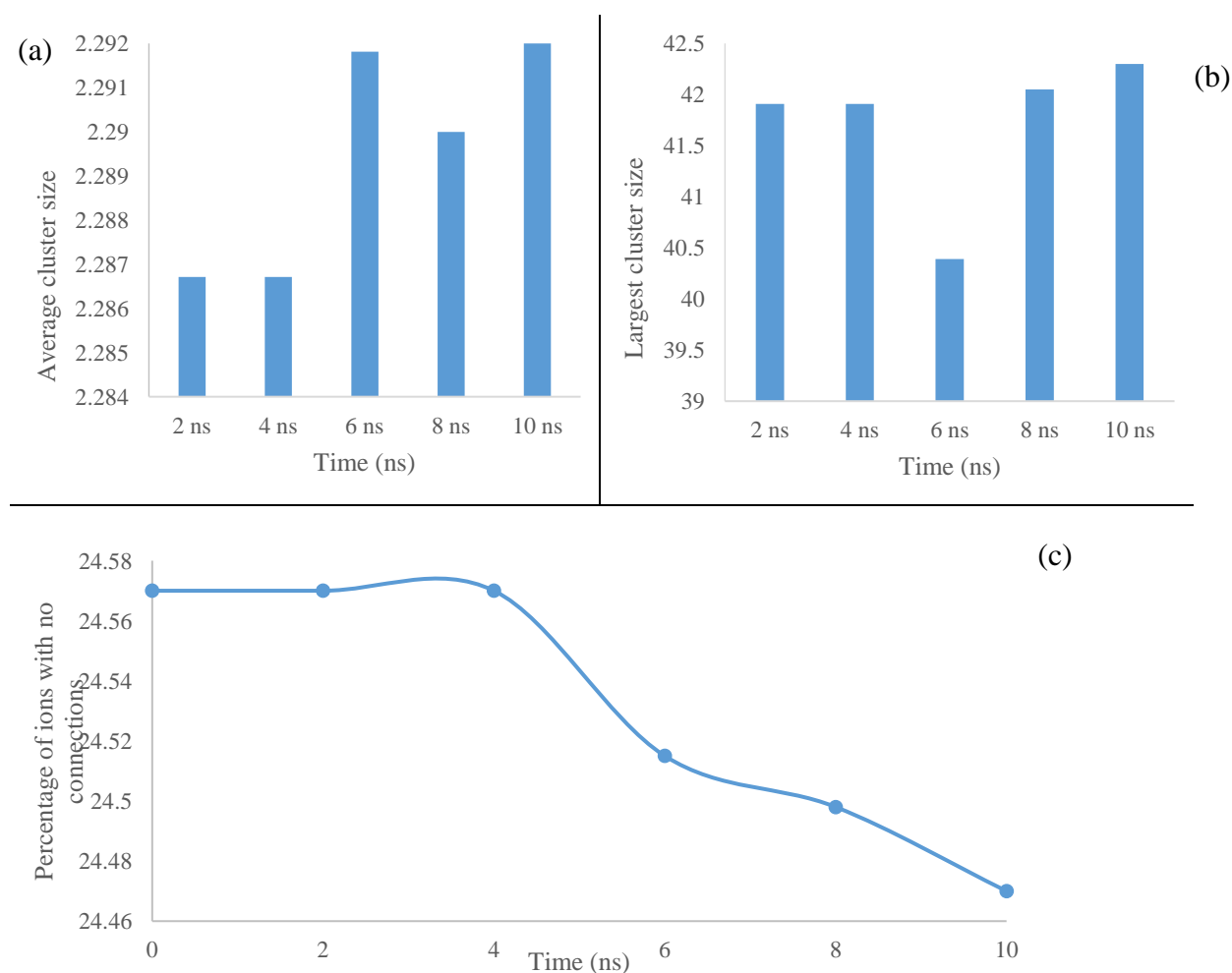


Figure 5.18 10 molal solution: (a) average number of potassium unit included in a finite size cluster though the 10 ns of simulation; (b) average number of potassium unit included in the largest detected cluster throughout the 10 ns of simulation; (c) average number of potassium unit not showing any connection at all though the 10 ns of simulation, normalised as a function of the total number of potassiums.

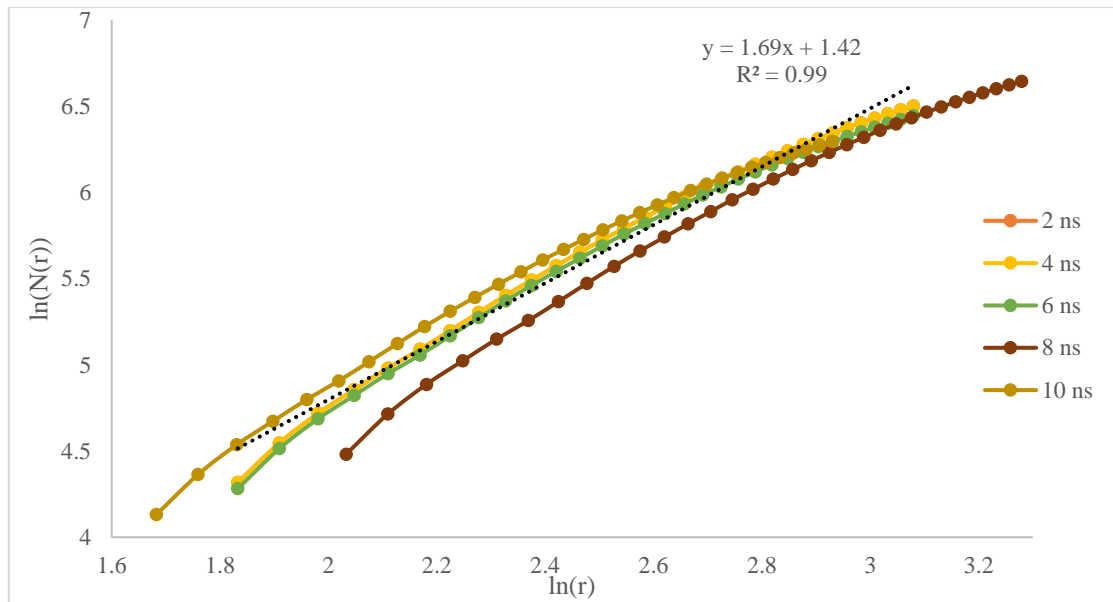


Figure 5.19 Fractal dimension of the largest finite cluster in solution for a 10 molal box.

5.2.4 12 molal solution

As for the previous cases, this box has been built randomly. Figure 5.20 shows the probability of connection for each potassium in the box. Most of the potassium appear to be forming an average of 1.3 connections, which is less than the previous cases for lower concentrations of 8 molal, but more than 10 molal. As before, the total number of connections shows an exponential decrease. There is no significant variation of said trend over time.

Table 5.7 Schematic representation of cluster organisation and their number of connection (average)

Average number of connections	2	2	2
Average number of connections	2	2.5	2

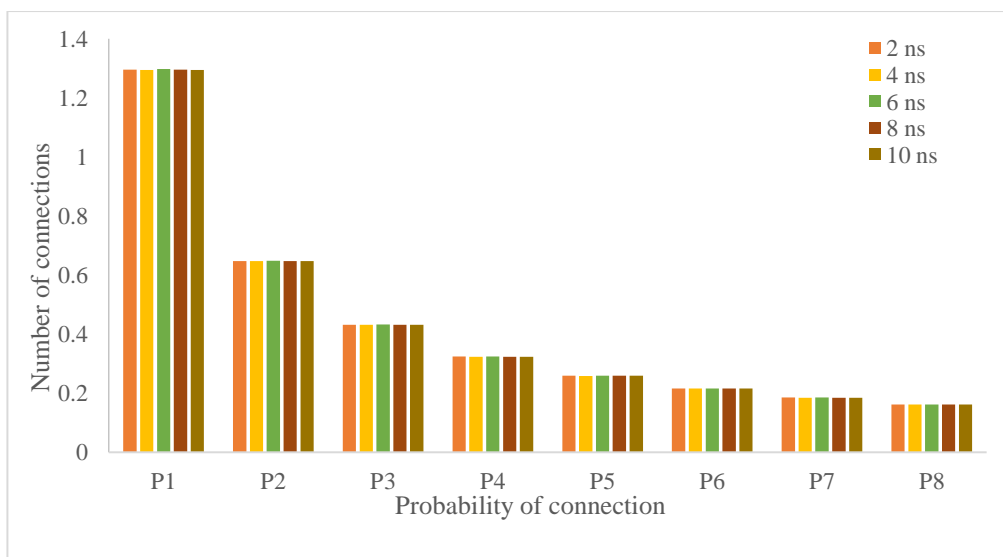


Figure 5.20 12 molal solution: probability of connection versus number of connection for each potassium in the solution.

The reduced average number of connection can be explained, from Figures 5.21(a/c).

Figure 5.21(a) shows the average size of the clusters is around 2.73 units. This number is appreciably bigger than the previous cases. Figure 5.21(b) shows that the average size of the biggest cluster detected in solution is 3.5 times the biggest detected in the 8 molal solution. Figure shows the number of potassiums with no connections at all (single unit clusters). As visible from Figure 5.21(c), out of a total of 12,000 potassiums in the box, an average of 2,356 appears to have no connections at all. This number is comparable with the one estimated for the 8 molal solution (2,216), as there were less potassiums in that box on average more atoms are involved in the formation of less clusters in the 12 molal case so they are bigger in size, which leads to a lower connectivity due to their shape.

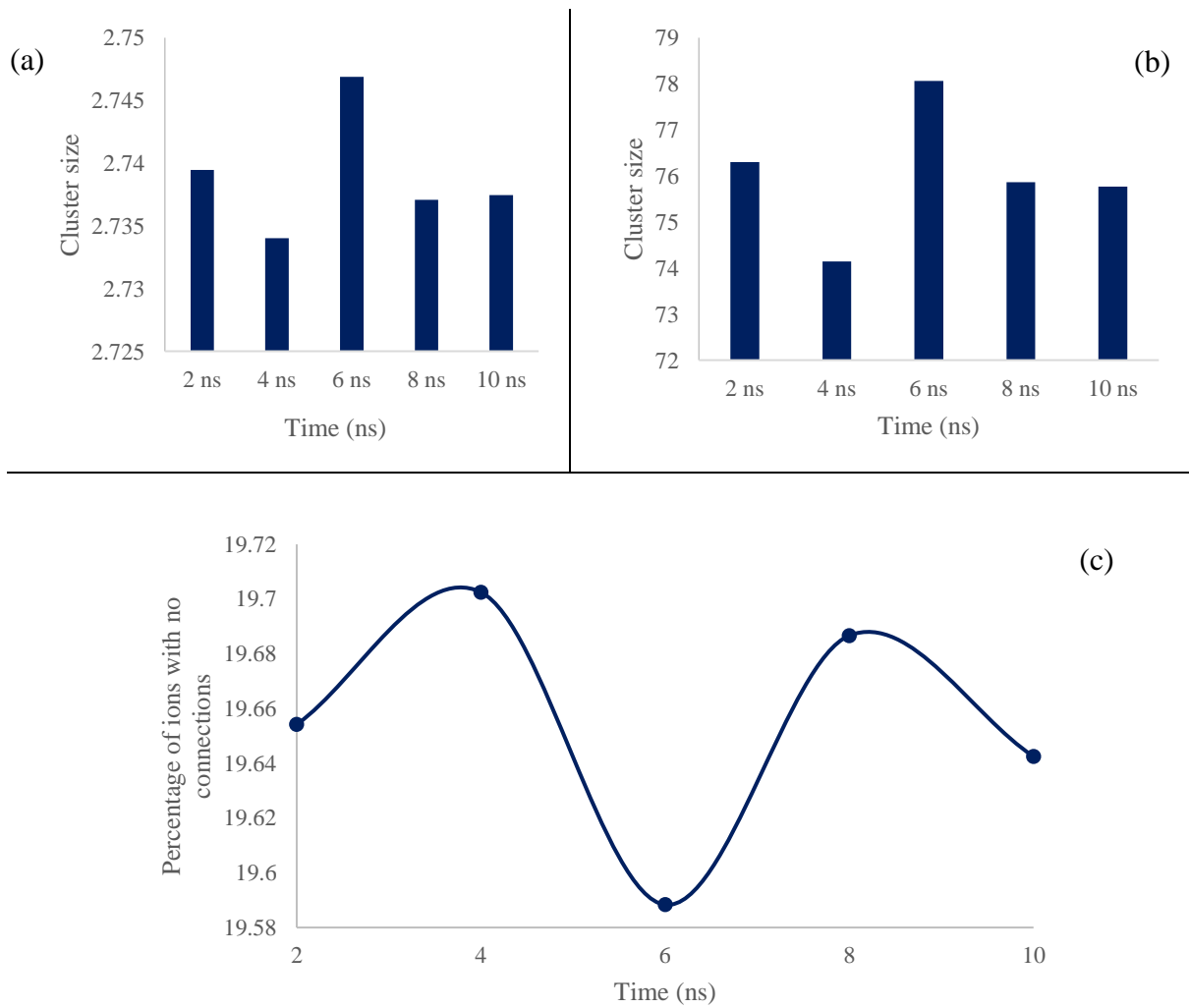


Figure 5.21 12 molal solution: (a) average number of potassium unit included in a finite size cluster through the 10 ns of simulation; (b) average number of potassium unit included in the largest detected cluster through the 10 ns of simulation; (c) average number of potassium unit not showing any connection at all through the 10 ns of simulation, normalised as a function of the total number of potassiums.

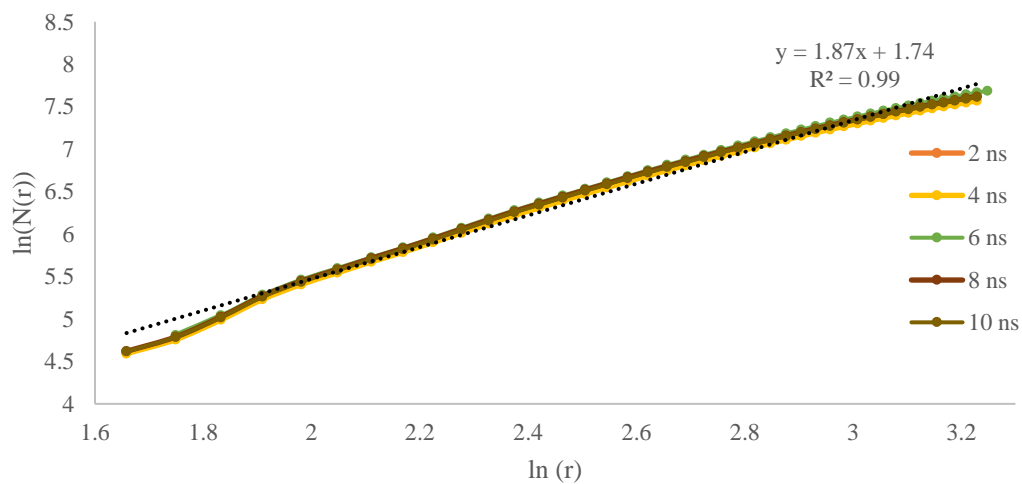


Figure 5.22 Fractal dimension of the largest finite cluster in solution for a 12 molal box

5.2.5 Comparison of Molalities

Trying to summarise the behaviour of all the different molal solutions, it is interesting to notice that the percentage of ions not involved in connection appears to decrease with the increase of the concentration, and it spans from 28 to 19.6%, with 8.4 % interval. This trend is shown in Figure 5.23.

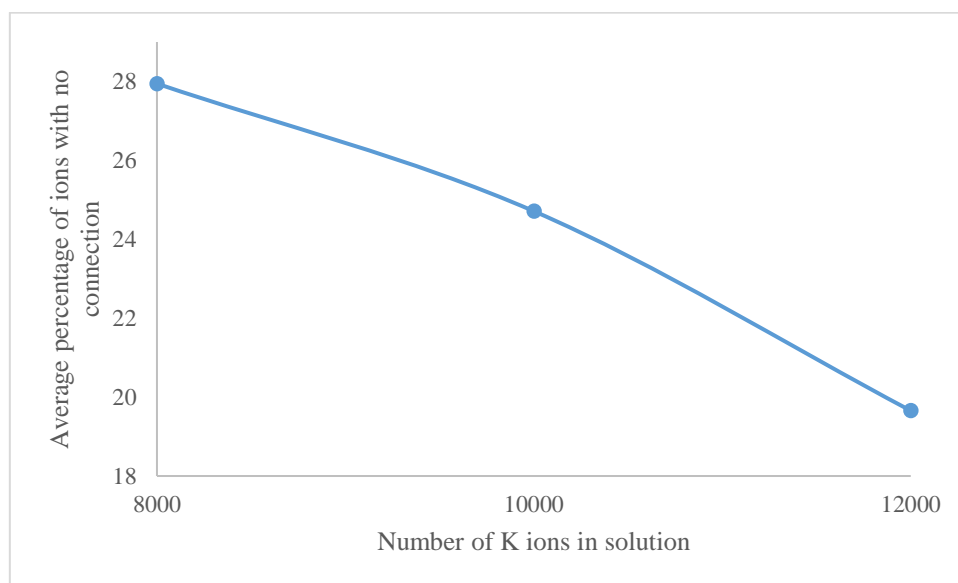


Figure 5.23 Percentage of 'single unit' cluster as a function of total number of potassium ions

The system appears to form a plethora of clusters with various shape and dimensions. The majority of clusters, though are highly hydrated chains that appear to fold to include water in 'pockets', as visible from Figure 5.25.

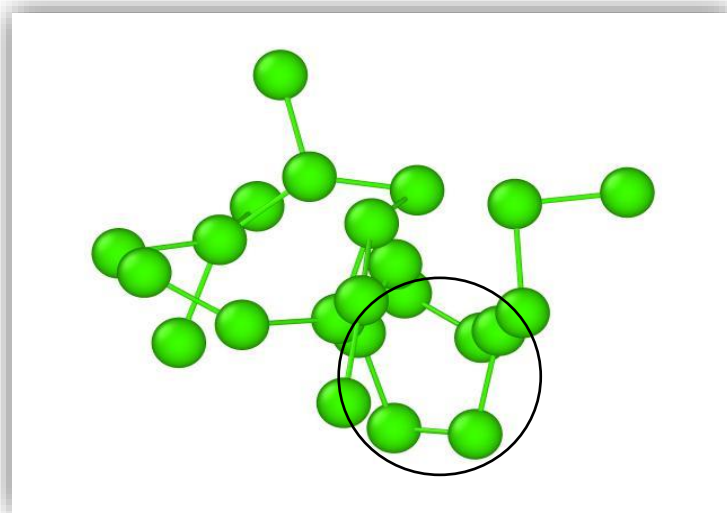


Figure 5.24 Isolated medium-sized cluster. Picture shows only potassiums in green.

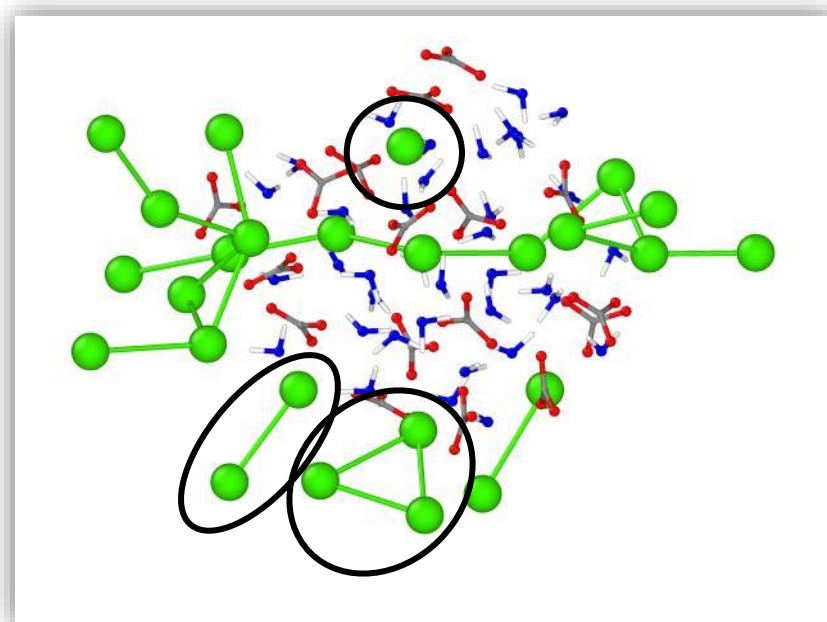


Figure 5.25 Collection of clusters in various shapes and sizes, with potassium ions shown in green. At the top of the figure, highlighted in a black circle is an isolated ion, the middle of the figure shows the biggest cluster, a long chain with a few folds. At the bottom of the figure, highlighted in black circles, are a pair and a triangle-shaped cluster.

Figure 5.24 shows one of the biggest, better organised clusters detected in a 12m solution. In this case, the chain scrunches itself in the formation of an almost 3-D structure, but with visible holes and gaps, as the analysis of the fractal dimension suggested. The structure resembles the so-called DOLLOPs (dynamically ordered liquid-like oxyanion polymer, a form of stable

prenucleation mineral clusters that are considered to be small liquid-like ionic polymer clusters) in calcium carbonate.

Therefore, it does not appear, in the timeframe analysed, it is possible to identify any nuclei. The next step will be to check if any of those small-sized clusters resemble, in any way an organised crystalline structure.

5.3 Manhattan distance

The 'Manhattan distance' refers to a geometry in which the conventional distance function or metric of Euclidean geometry is substituted with a new metric in which the distance between two points is the sum of their Cartesian coordinates' absolute differences ^[19].

In \mathbb{R}^2 , the Manhattan distance between two points is given by

$$d = |x_1 - x_2| + |y_1 - y_2| \tag{5.2}$$

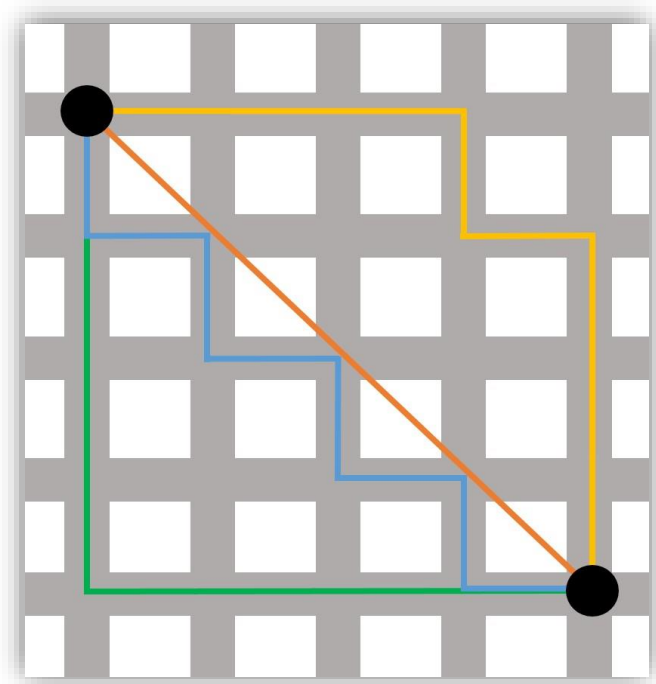


Figure 5.26 Orange Euclidean distance, green, light blue and yellow Manhattan distances

5.3.1 Reference Systems

The standard coordination of potassiums with respect to the oxygens of the nitrate group (respectively six for calcite and nine for aragonite) of the ions in the solutions is compared to crystal reference structures. The aim of this work is to check similarities in a high dimensional parameter space by using a cluster analysis technique. A nitrate was assumed to be coordinated to a potassium if the oxygen atoms of the anion were 3.5 Å or less from the cation. For each potassium ion surrounded by six or nine oxygens, discrete probability distributions were calculated and represented by the vectors P_α and P_β , respectively for the distances and angles. Measurements of the crystalline similarity to known references included

$$s_\alpha = \|P_\alpha(d) - P_\alpha^{ref}(d)\| \quad (5.3)$$

$$s_\beta = \|P_\beta(\theta) - P_\beta^{ref}(\theta)\| \quad (5.4)$$

where the average probability distributions $P_\alpha^{ref}(d)$ and $P_\beta^{ref}(\theta)$ are vectors of identical length for the reference crystal (shown for crystals at 300K in Figure 5.27/5.29). The metric used is the Manhattan one, described in the previous section.

In contrast to the references, the geometric ordering of the atoms differs less in s_α and s_β values. As a result, a genuine amorphous material should have average $s(\alpha)$ and $s(\beta)$ values that are not zero and almost equal.

We define the order of a structure in comparison with the perfect crystalline system by the number of standard deviation its distance and angles differ from the perfect crystal. We analysed only ions with distances and angles equal or less than three standard deviations from the reference crystal.

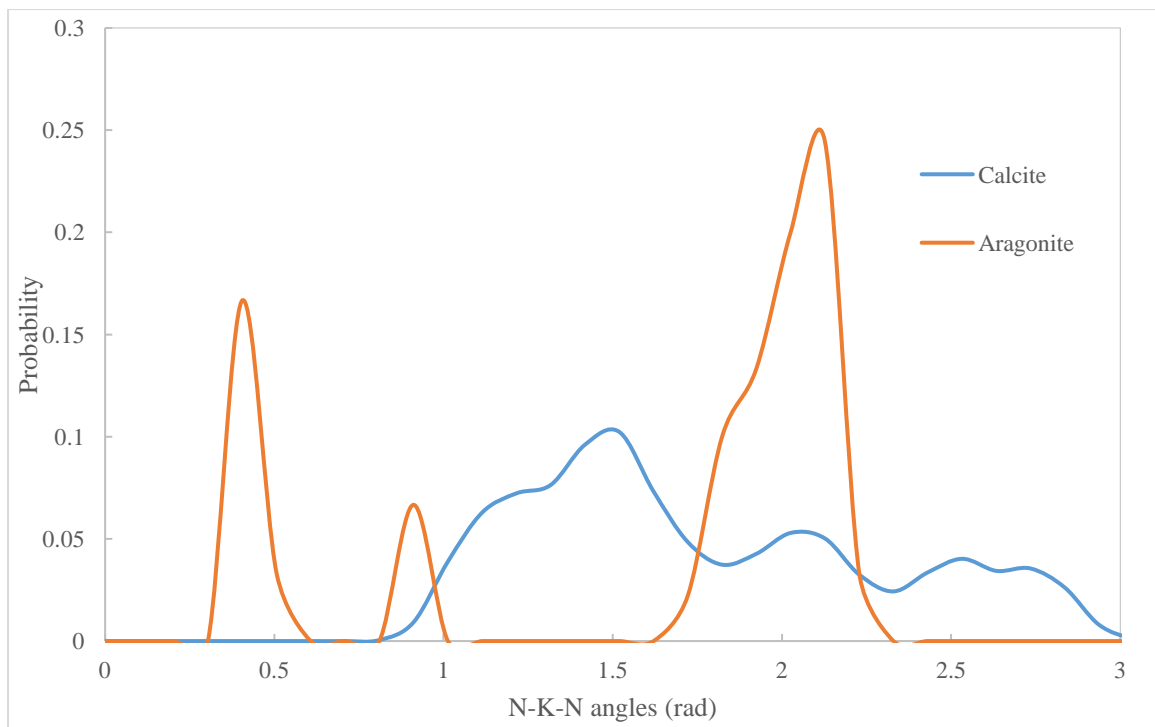


Figure 5.27 Angles reference

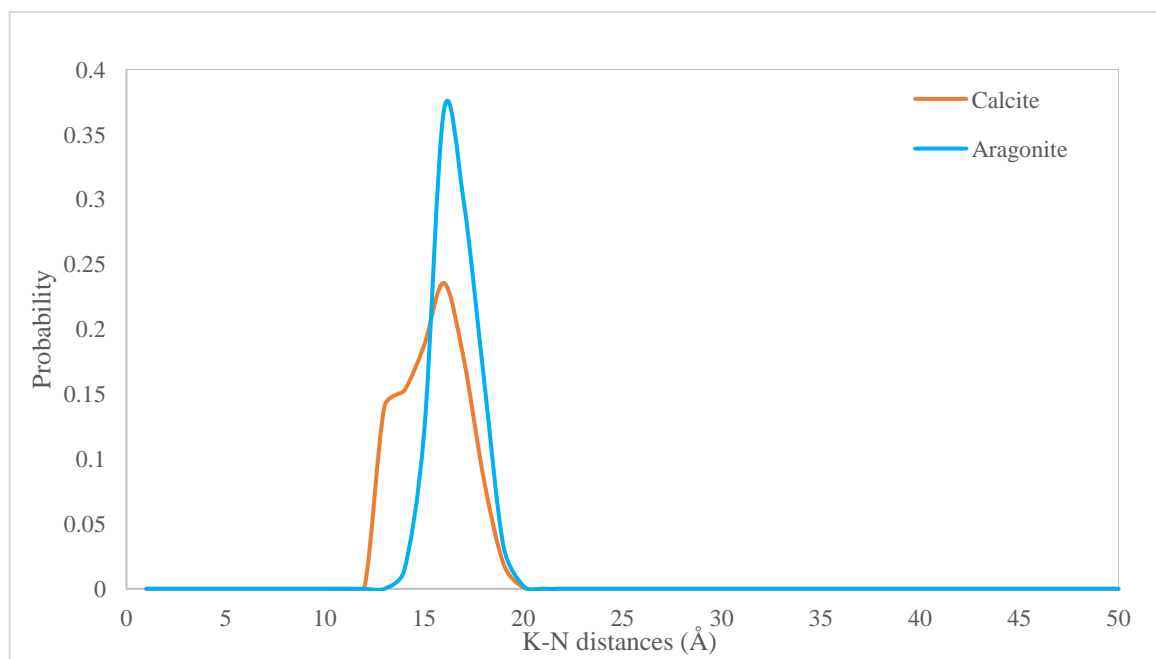


Figure 5.28 Distances reference K-N

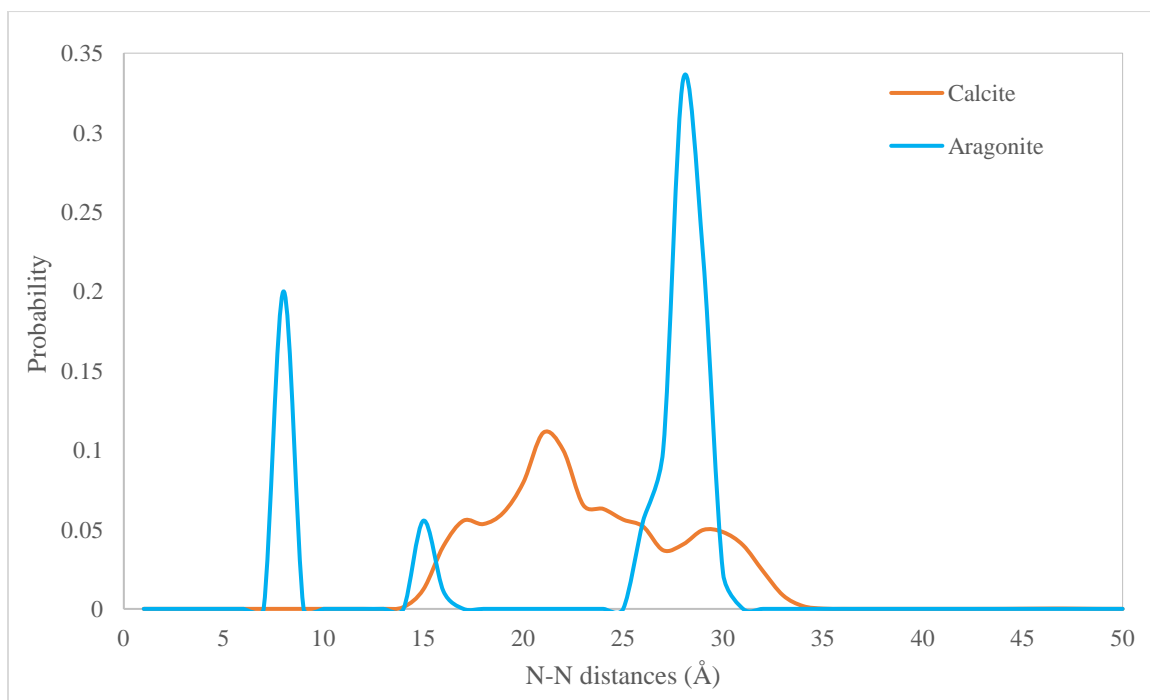


Figure 5.29 Distances reference N-N

5.3.2 Average Polymorphs

In this section, we analyse the mean value of the Manhattan distance difference. As previously discussed, for a perfect crystal the average is close to zero.

Table 5.8 shows the results for a 6 molal clustered solution. This system was run only for 2 nanoseconds, as the intention was to capture the system before it had the opportunity to rearrange itself. In this case, the average is very close to zero, with a deviation only in the fourth decimal digit. Therefore, the system shows almost no sign of any proto-cluster or $\text{KNO}_3(n)$ units with a geometry like crystalline KNO_3 . There is a slight preference for the calcite structure over the aragonite one.

For the other molalities, both numbers vary though the simulation time. We can see in some cases a large fraction of those potassium with 6 or 9 neighbouring oxygen resemble the crystal structures. Calcite seems to have on average smaller values even when considering three standard deviations.

Table 5.8 Mean fractions of the Manhattan distance difference for calcite and aragonite within 1 and 3 standard deviation from the mean

	Average Calcite				Average Aragonite			
	1 Standard Deviations		3 Standard Deviations		1 Standard Deviations		3 Standard Deviations	
	0-2 ns	8-10 ns	0-2 ns	8-10 ns	0-2 ns	8-10 ns	0-2 ns	8-10 ns
6m clustered	0.0001	-	0.0006	-	0.0002	-	0.0008	-
8m	0.0791	0.0234	0.4480	0.0723	0.1469	0.0440	0.8166	0.0941
10m	0.0963	0.0954	0.5220	0.5203	0.1779	0.1763	0.8754	0.8753
12m	0.1079	0.0154	0.5751	0.0827	0.1997	0.0287	0.9103	0.1310

5.3.3 8 molal solution

Figures 5.30 and 5.31 show the Manhattan separation N-N versus the N-K-N angle for both calcite (Figure 5.30) and aragonite (Figure 5.31) respectively for the 8 molal solution. In these graphics the z value represents the number of K with 6 or 9 Oxygen coordinated that are within the number of standard deviations indicated on the x and y axis of the value of N-K-N angle and N-N separation respectively. Figure 5.30 shows that, during the first 2 ns of the simulation all the potassiums coordinated with six oxygens are distributed within three standard deviations of the calcite structure, with a higher concentration in the radius of 2.5 standard deviations. The area in the 0.5 standard deviation radius appears to contain the highest number of entries.

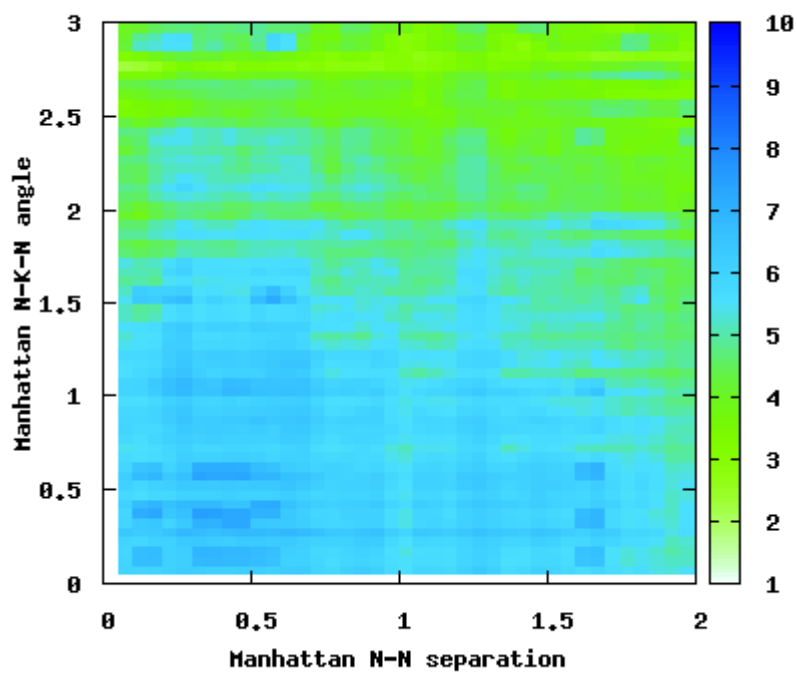
Moving towards the end of the simulation, at 10 ns it appears that all the numbers are still contained in three standard deviations; however, the area where the concentration is higher is much more limited this time, with an average radius of 0.5 standard deviation. The rest of the points are then clustered in areas with higher concentration, but the behaviour is not as continuous as the previous case. The aragonite polymorph shows a similar behaviour, however, as shown in Figure 5.31, the probability of occurrence of an aragonite-like structure seems higher than the calcite equivalent: all the entries are condensed in a 2 standard deviation radius, with a higher prevalence in the one standard deviation radius. This system does not seem to be as symmetrical as the previous one.

Moving toward the end of the simulation the total number of potassium coordinated with 9 oxygens seems to increase, but not the local order in respect to the oxygens.

The area of interest, in fact, keeps being included in the 2.5 standard deviation radius.

Calcite

0-2 ns



8-10 ns

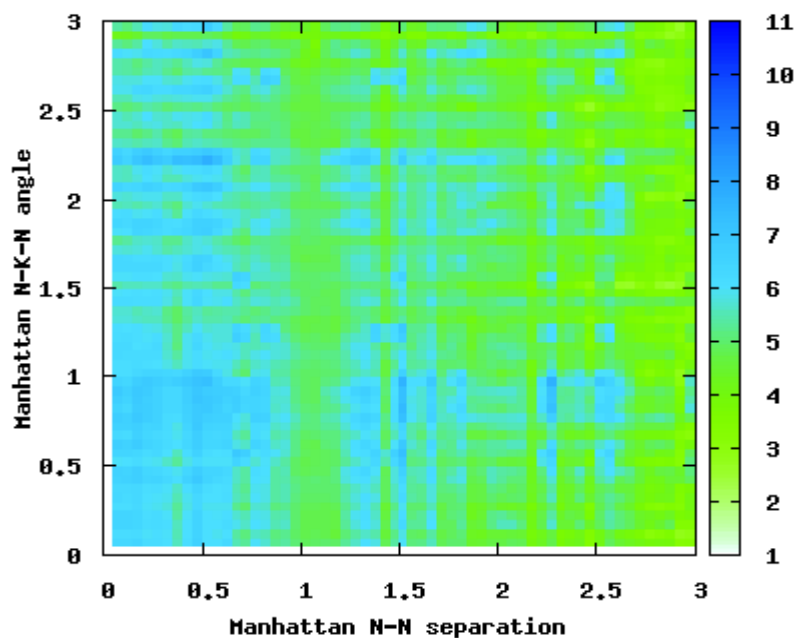
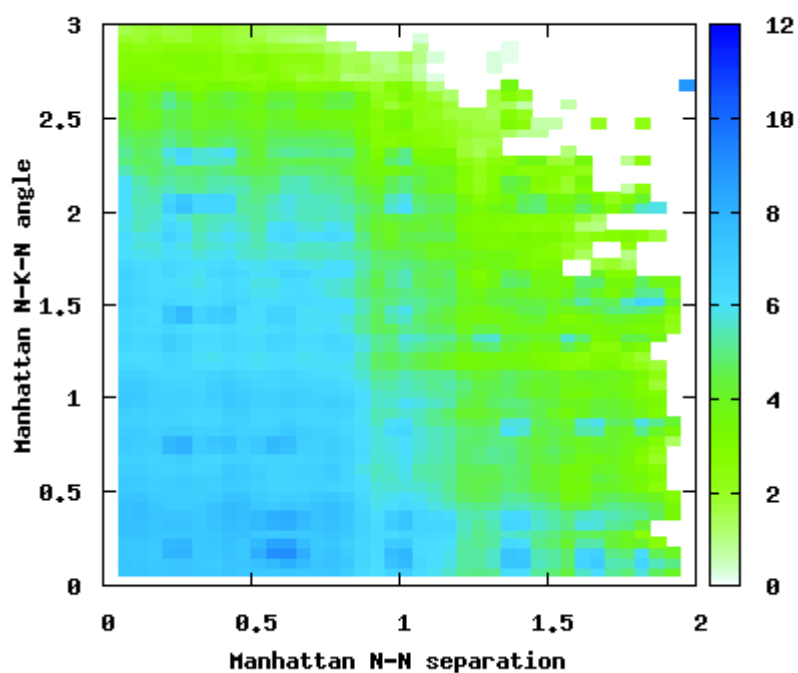


Figure 5.30 $s(\alpha)$ vs $s(\beta)$ for calcite in a 8 molal solution after 2 and 10 ns of simulation. The areas of more intense blue represent the combination of standard deviation with the highest occurrence of polymorph resemblance.

Aragonite

0-2 ns



8-10 ns

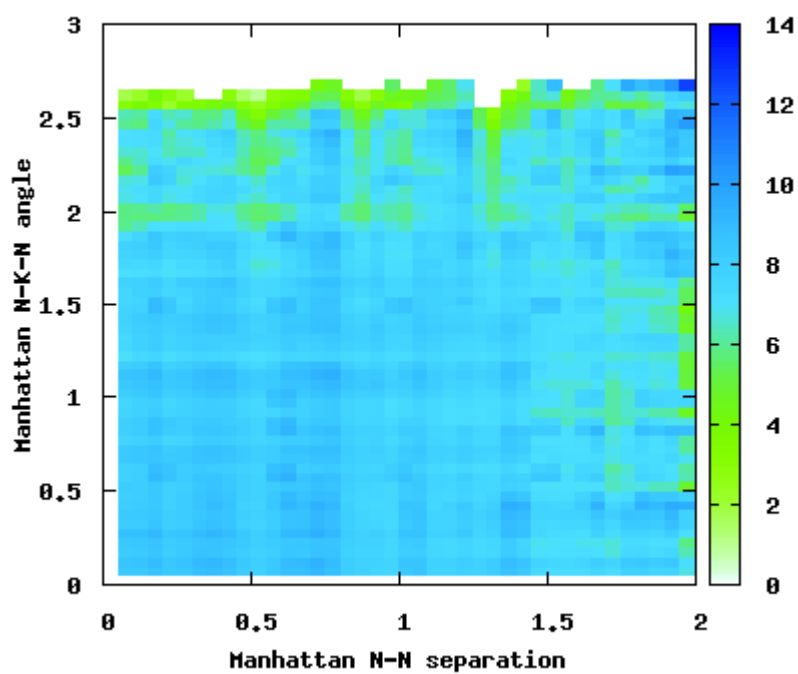


Figure 5.31 *s(a)* vs *s(b)* for aragonite in a 8 molal solution after 2 and 10 ns of simulation. The areas of more intense blue represent the combination of standard deviation with the highest occurrence of polymorph resemblance.

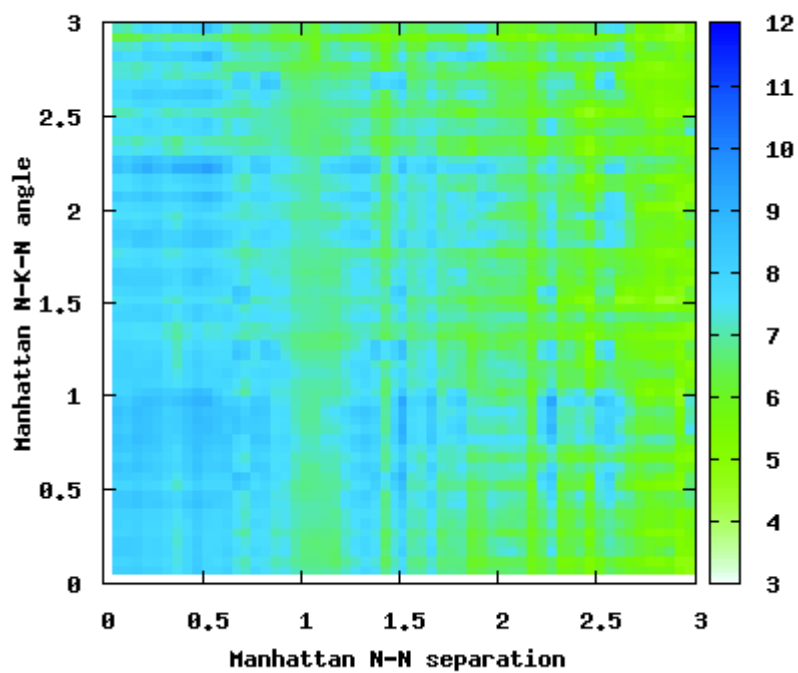
5.3.4 10 molal solution

For the first two nanoseconds of the simulation, as shown in Figure 5.32, all of the potassiums coordinated with six oxygens are spread within three standard deviations, while the radius of the region with a greater concentration is only two standard deviations. The remaining points subsequently group together in areas of higher concentration, however the pattern is not as continuous as it was in the first situation. By the conclusion of the simulation, this behaviour matches the 8-molal instance (10 ns). This suggests that, regardless of concentration, this may be the highest organised state a solution may achieve. At the simulation's end, this pattern is almost unaltered (10 ns).

Similar behaviour is seen by the polymorph of aragonite. Similar to the other examples, this system does not appear to be highly symmetrical, creating larger density clusters in areas with varying x/y values. The calcite level does not alter significantly during the course of the experiment, and neither does the aragonite.

Calcite

0-2 ns



8-10 ns

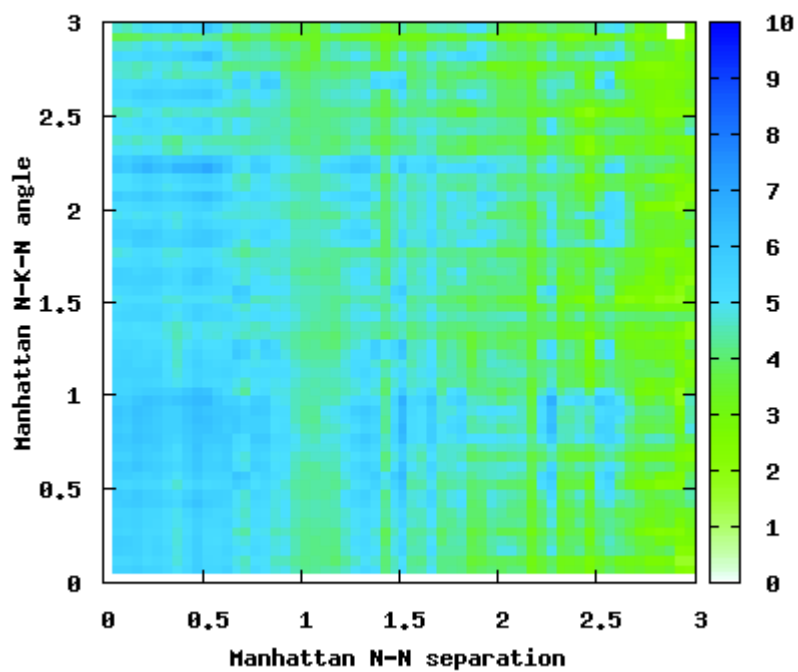
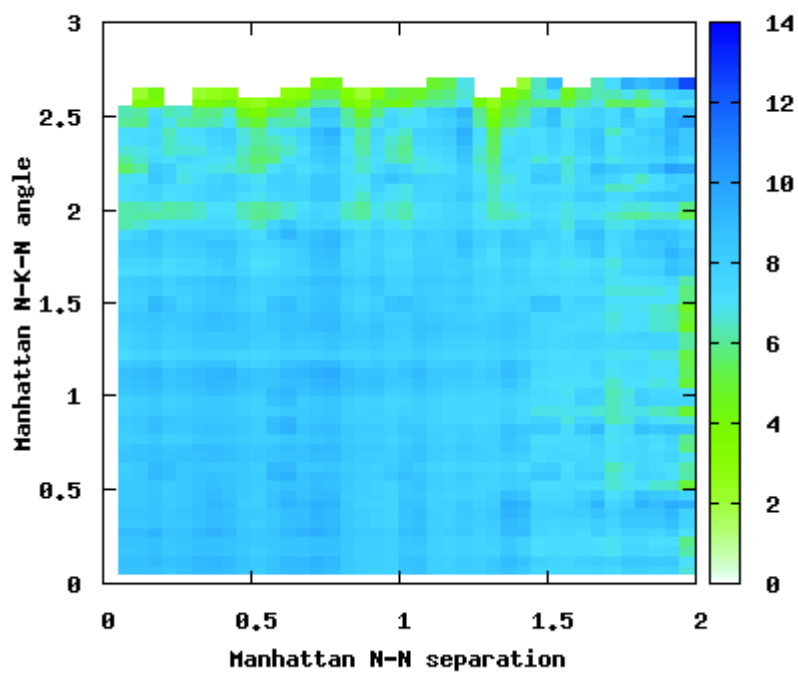


Figure 5.32 *s(a)* vs *s(b)* for calcite in a 10 molal solution after 2 and 10 ns of simulation. The areas of more intense blue represent the combination of standard deviation with the highest occurrence of polymorph resemblance.

Aragonite

2 ns



10 ns

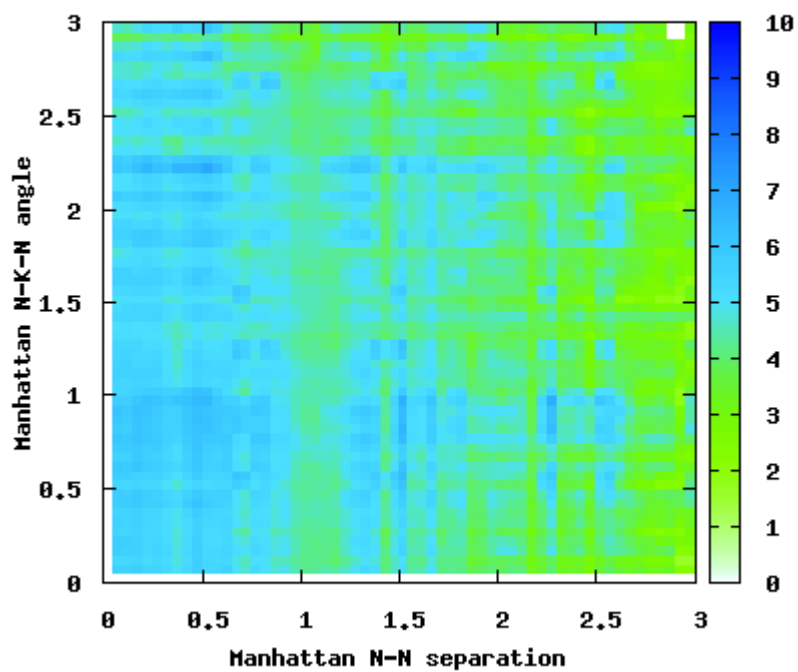


Figure 5.33 $s(a)$ vs $s(b)$ for aragonite in a 10 molal solution after 2 and 10 ns of simulation. The areas of more intense blue represent the combination of standard deviation with the highest occurrence of polymorph resemblance.

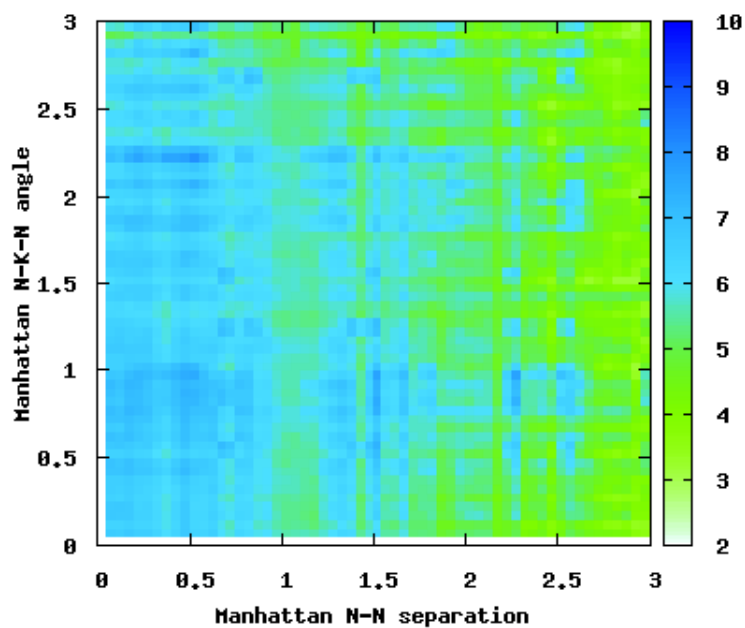
5.3.5 12 molal solution

Figure 5.34 shows that, for the first 2 ns of the simulation all the potassiums coordinated with six oxygens are distributed within three standard deviations. However, the area where the concentration is higher is limited to a radius of 0.5 standard deviation. The rest of the points are then clustered in areas with higher concentration, but the behaviour is not as continuous as the previous case. This behaviour resembles the 8 molal case, towards the end of the simulation (10 ns). This leads to the idea, that, perhaps that is the most ordered structure a solution could reach no matter what the concentration. This trend is barely unchanged at the end of the simulation (10 ns).

The aragonite polymorph shows a similar behaviour. As the previous cases, this system does not seem to be very symmetrical, forming clusters of higher density at regions with different x/y values. As for the calcite, even the aragonite does not show a significant change through the simulation time.

Calcite

0-2 ns



8-10 ns

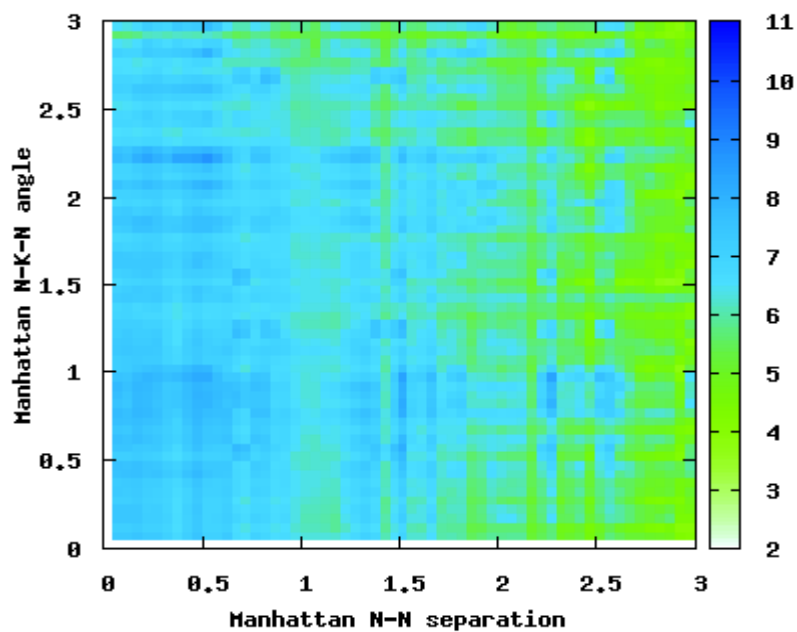
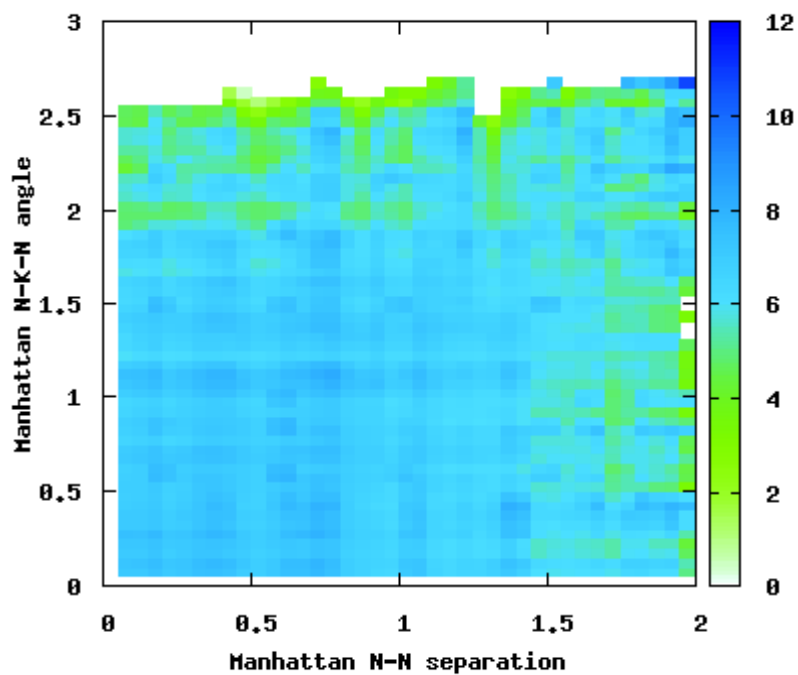


Figure 5.34 $s(\alpha)$ vs $s(\beta)$ for calcite in a 12 molal solution after 2 and 10 ns of simulation. The areas of more intense blue represent the combination of standard deviation with the highest occurrence of polymorph resemblance.

Aragonite

0-2 ns



8-10 ns

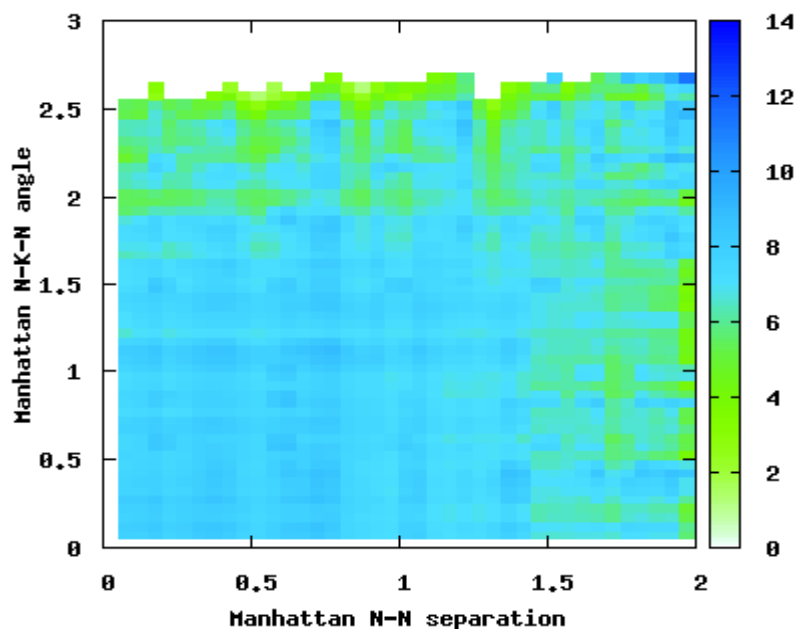


Figure 5.35 s(a) vs s(β) for aragonite in a 12 molal solution after 2 and 10 ns of simulation. The areas of more intense blue represent the combination of standard deviation with the highest occurrence of polymorph resemblance.

5.3.6 Polymorphs resemblance

By analysing the six- coordinated potassium (with respect to the oxygens), it is possible to identify and visualise highly coordinated potassium units. Figure 5.36 shows a potassium with a hybrid coordination in-between the standard calcite and aragonite ones. It is, in fact surrounded by eight oxygens belonging to nitrate groups, equally distributed between bi-dentate coordination and mono-dentate coordination.

What is interesting to highlight from this Figure is that the first shell of solvation of the potassium ion contains three water molecules. This brings the total coordination of the potassium with respect to the oxygens (from both the nitrate group and water) to a total of 11: we are visualising the numerical description of the RDF reported in Section 5.1.1.

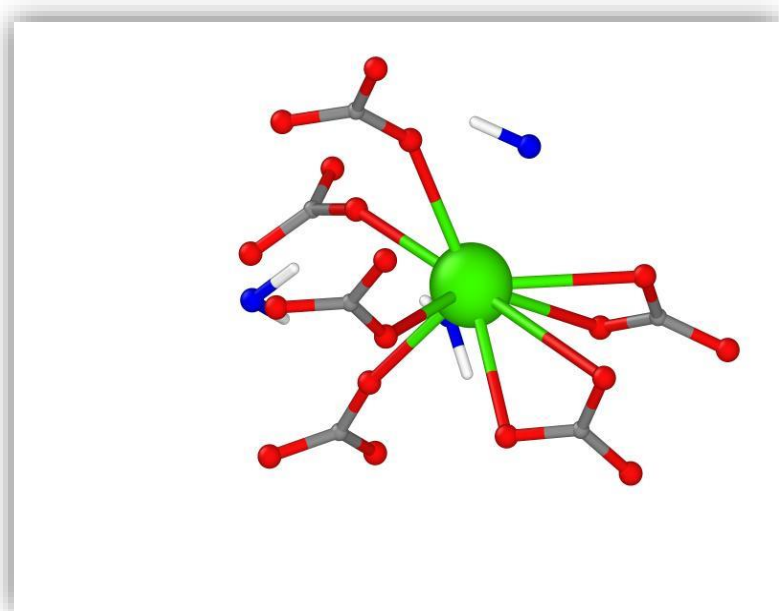


Figure 5.36 intermediate coordination 8 oxygen of NO_3 and 3 water oxygens

In a similar manner, it is possible to identify both aragonite like and calcite like polymorphs, reported in Figures 5.36/5.41.

Figure 5.37 shows a calcite-like structure with all the nitrate groups sharing only one oxygen to create the bond with the potassium core (monodentate). Out of the six total connected oxygens four are on the xy plane and two perpendicular to the plane (z axis). The first hydration shell consist of five water molecules, which brings, again, the total coordination number up to 11. Those water molecules, however appear to be away from the central core, giving the impression that the structure might, in fact, be partially dehydrated. This will require,

for a longer simulation period, a further analysis of the distance to check the oxygen of the water further from the organised structure.

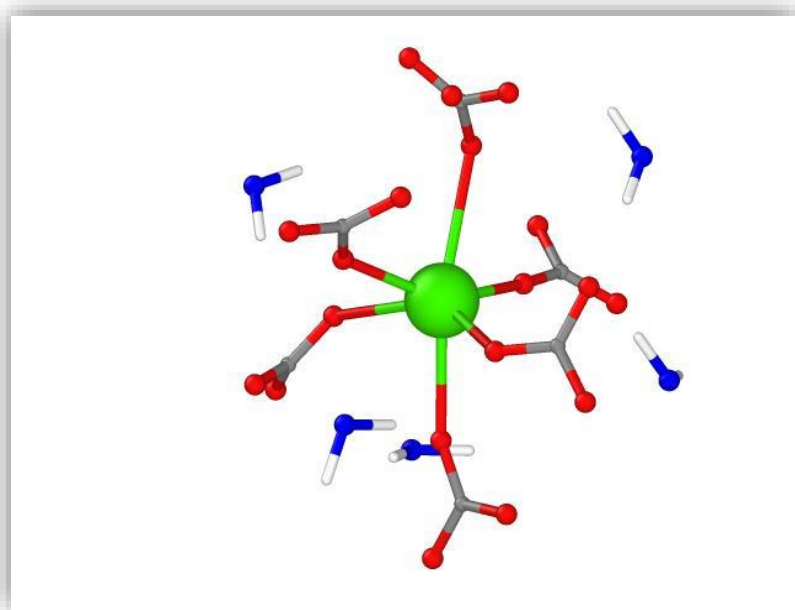


Figure 5.37 Calcite like with only monodentate binder oxygens. Total oxygen coordination 11

Figure 5.38 shows the coordination polyhedron of only the central potassium and the oxygens of the nitrate groups. This shows that the structure appears to be quite regular, as expected from a proto-nucleus.

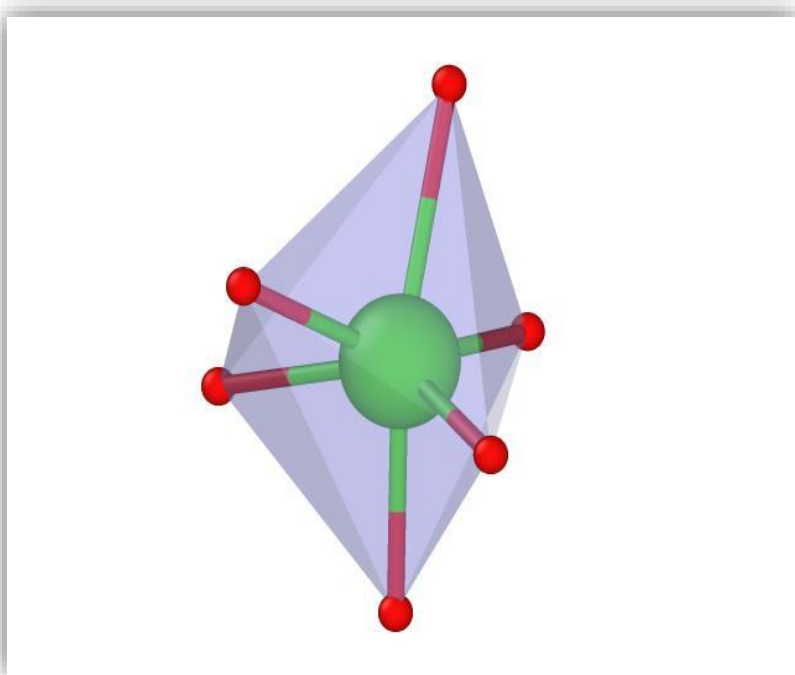


Figure 5.38 Coordination polyhedron of Figure 5.37

Figure 5.39 shows a calcite like unit, this time with the four oxygens in the xy plane coming from two nitrate groups (bidentate). The same unit is also reported in Figure 5.40, viewed from the z -axis, to enhance the denticity.

As in the previous case five water molecule constitute the first hydration shell and the total coordination of the potassium in respect to all the oxygens adds up to 11.

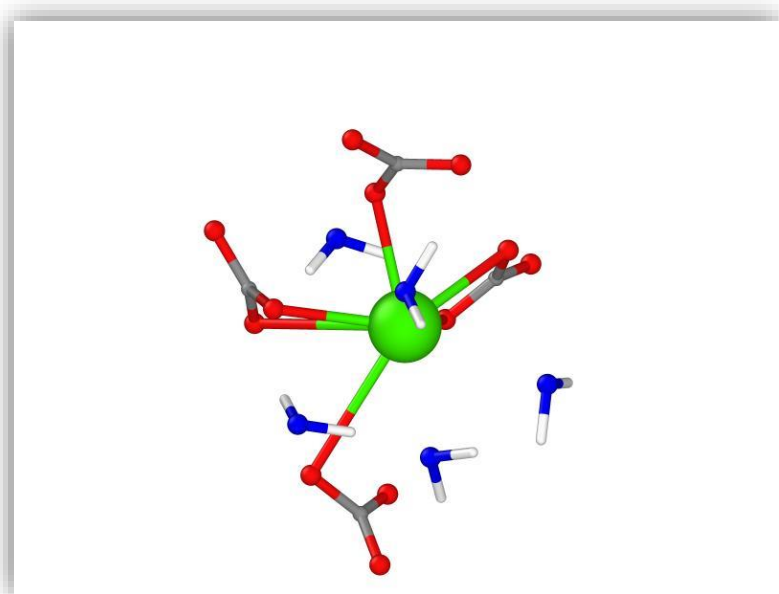


Figure 5.39 Mono and bi-dentate calcite on xy plane

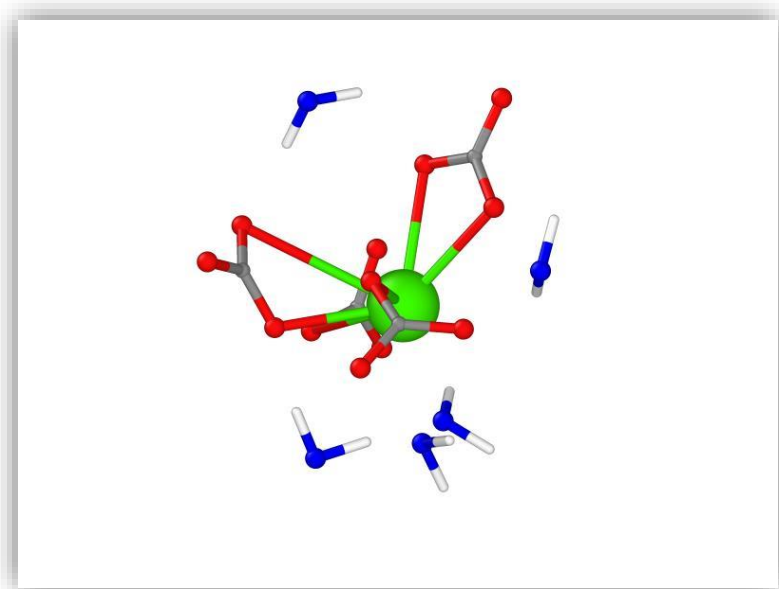


Figure 5.40 Mono and bi-dentate calcite on z axis

Finally, figure 5.42 shows an aragonite like structure. The nine oxygens are divided in the following way: six come from 3 nitrate groups, all of them sharing two oxygens each (bidentate), and the other three come from three more nitrate groups sharing only one oxygen each (monodentate). Again the first hydration shell consists of only two water molecules, bringing the total coordination to 11.

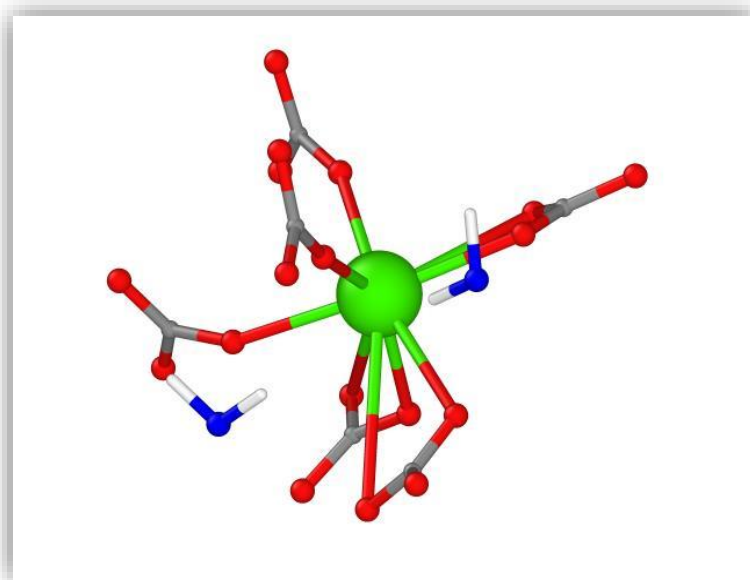


Figure 5.41 Aragonite-like structure. Total coordination sums up to 11.

5.3.7 Conclusions

Based on the preceding work, one may draw the conclusion that many of the 6- and 9-coordinated systems have a structure that is similar to the perfect crystal; however, this could be because nitrate crystals have a larger structural variety (natural disorder). It may still be possible for them to have water coordination while they are in these units, which makes it more difficult for them to match the crystal structure.

There is no sign that nuclei are developing since there is no progression over time towards a higher number of crystal-like units or an increase in their overall order. As a result, there is no evidence that nuclei are forming in the timeframe analysed. Going to higher order of magnitude timeframe could give a better insight of the system, however given the resources and the purpose of this work we have considered the analysed timeframe bounteous.

5.4 References

- [1] J. E. Helt, M. A. Larson, *Effects of temperature on the crystallization of potassium nitrate by direct measurement of supersaturation*, 1977, *AIChE Journal* (Vol. **23**, No. 6), 822-820;
- [2] V. Fantauzzo, S. R. Yeandel, C.L. Freeman, J.H. Harding, *A transferable force-field for alkali metal nitrates*, 2022, *J. Phys. Commun.*, **6**,055011;
- [3] X. Wu, F.R. Fronczek, L.G. Butler, *Structure of LiNO₃: Point Charge Model and Sign of the ⁷Li Quadrupole Coupling Constant*, *Inorg. Chem.*, 1994, **33**, 1363;
- [4] L. Martínez, R. Andrade, E. G. Birgin, J. M. Martínez, *PACKMOL: A package for building initial configurations for molecular dynamics simulations*, *Comput Chem*, 2009, **30**, 2157–2164;
- [5] I.T. Todorov, W. Smith, *THE DL POLY 4 USER MANUAL*, Version 4.02.0, 2011;
- [6] D. Kashchiev, *Nucleation*, Elsevier, 2000;
- [7] R. Benages-Vilau, T. Calvet, M.À. Cuevas-Diarte, *Polymorphism, crystal growth, crystal morphology and solid-state miscibility of alkali nitrates*, *Crystallography Reviews*, 2014, **20**:1, 25-55;
- [8] T. Dunn, F. Meldrum, 2023, to be submitted;
- [9] E.J. Freney, L.A.J. Garvie, T.L. Groy, P.R. Buseck, *Growth and single-crystal refinement of phase-III potassium nitrate, KNO₃*, *Acta Cryst.*, 2009, **B65**:659–663;
- [10] B. Mandelbrot, *The fractal geometry of nature*, Macmillan, 1983;
- [11] B. Mandelbrot, *How Long is the Coast of Britain? Statistical Self-Similarity and Fractional Dimension*, *Science*, 1967, **156** (3775): 636–8;
- [12] K. Falconer, *Fractal Geometry*, 2003, Wiley. p. 308;
- [13] A. Alexanderson, *Benoit Mandelbrot: In his own words*, *Mathematical people: profiles and interviews*, 2008, AK Peters. p. 214. ISBN 978-1-56881-340-0.
- [14] B. Mandelbrot, *Fractals and Chaos*, Springer. p. 38;
- [15] A. Sharifi-Viand, M. G. Mahjani, M. Jafarian, *Investigation of anomalous diffusion and multifractal dimensions in polypyrrole film*, *Journal of Electroanalytical Chemistry*, 2012, **671**: 51–57;
- [16] H. Sagan, *Space-Filling Curves*, 1994, Springer-Verlag. p. 156;
- [17] A. Balay-Karperien, *Defining Microglial Morphology: Form, Function, and Fractal Dimension*, Charles Sturt University, 2004, p. 86;
- [18] H. von Koch, *On a continuous curve without tangents constructible from elementary geometry*, Edgar, 2004, pp. 25–46;
- [19] P.E. Black, *Manhattan distance*, *Dictionary of Algorithms and Data Structures*, 2019.

Chapter 6

Growth of KNO_3

The subject of the study of this chapter will be the molecular control of crystal nucleation and growth of potassium nitrate. It will start by giving an overview of the experimental reasons that lead to the set-up of the simulations included in this chapter and it will explain the methodology choice based on preliminary results obtained using classical MD (which has been used extensively during the entire work).

6.1 Purpose of this work

It has been stressed during the previous chapter that homogeneous nucleation is a rare event, and from the computational point of view, even the creation of a confined environment is not of any help when it comes to make the process statistically more probable.

The first approach has been, therefore, to start from a pre-existent surface. This would act as an homogeneous nucleant, and allows us to perform an ‘in medias res’ simulation: we are assuming that we take control of the experimental droplet after the first nucleation has taken place. By using this *snapshot* of the system as our starting configuration, we have then performed classical molecular dynamics over the system. The following section will give more details about the system.

6.2 Creation of KNO_3 slabs

Various surfaces of potassium nitrate have been cleaved using METADISE^[1], which considers the crystal as a block made up of a stack of planes periodic in two dimensions and parallel to the defect (surface).

6.2.1 Methodology

METADISE starts from an assumption: only those ions close to the defect will need to relax from their lattice sites. Therefore, the blocks are split into two regions. Region 1, the inner region, contains those ions close to the defect while region 2, the outer region, incorporates ions more distant from the defect.

The ions in region 1 are allowed to relax to their mechanical equilibrium. Those in region 2 are fixed at their bulk lattice sites. The energy and forces on the ions are calculated within the Born model of solids^[2]. This uses a potential model which includes long range electrostatic terms and short range interactions.

The specific surface energy is defined as the energy per unit area required to transform a bulk region into a surface region. The surface energy is thus given by:

$$\gamma = \frac{U_{surf} - U_{bulk}}{A} \quad (6.1)$$

In (6.1) U_{surf} is referred to the energy of region I of a surface calculation; U_{bulk} is referred to the energy of an equivalent number of bulk ions; and A is one of the two surface areas cleaved.

Tasker^[3] defined three types of surface. Type I surfaces are composed of stoichiometric layers and thus have no dipole perpendicular to the surface (*Figure 6.1*, top). Type II surfaces are composed of multi-layer repeat units which have no dipole (*Figure 6.1*, middle). Type III surfaces have a multi-layer repeat unit and have a dipole perpendicular to the surface (*Figure 6.1*, bottom). In order to calculate the surface energy, there must be no dipole perpendicular to the surface. Such a dipole would lead to a divergent surface energy^[7].

Because of the lack of experimental data, the calculated surface energies of a crystal are very difficult to compare. However, one strategy is to evaluate the morphology. This can be either at thermodynamic equilibrium or controlled by kinetic growth.

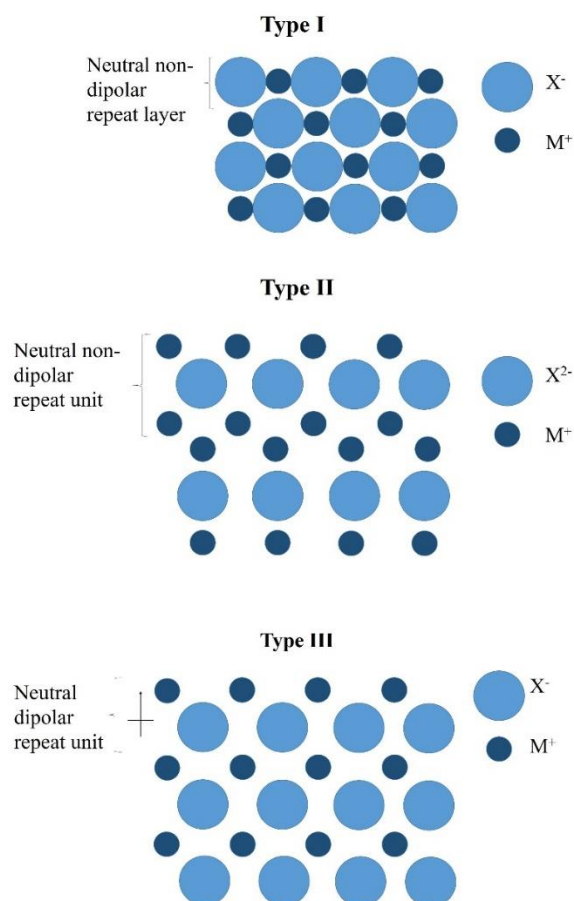


Figure 6.1. Definition of the three types of surfaces according to Tasker^[3,5]

6.2.2 Results

Various surfaces of KNO_3 have been cleaved using the methodology described in the previous section, with attention paid to data available in literature (see Chapter 2, section 2.4.3).

The goodness of the results has been tested by comparison with ab-initio calculations performed using CASTEP^[10], using the following parameters

Table 6.1. CASTEP parameters

Cut-off energy	800 eV
K-point grid	8 8 8
Spacing	0.001 \AA^{-1}

The Monkhorst-Pack^[6] k-point grid was set as 8 8 8 with a spacing of 0.001 \AA^{-1} .

The results obtained for KNO₃-aragonite are highlighted in Table 6.2. There is no experimental data available about the relative energy of the surfaces, but previous DFT calculation^[8] confirm the energetic order obtained in this work.

Table 6.2 Comparison between surface energy obtained with DFT and force field from this work. Surfaces are listed by their energy values (ranked from the lowest to the highest)

	Fitted force field	DFT
	J·m⁻²	
0 0 1	0.237	0.199
1 0 0	0.246	0.250
1 1 0	0.276	0.297
0 1 0	0.310	0.344

Calcite and ferroelectric phases are supposed to behave, according to the literature^[9], like calcium carbonate, with {104} being the most stable surface. The calcitic phase presents a non-full occupancy of the sites, therefore studies with the ferroelectric polymorph have been conducted here.

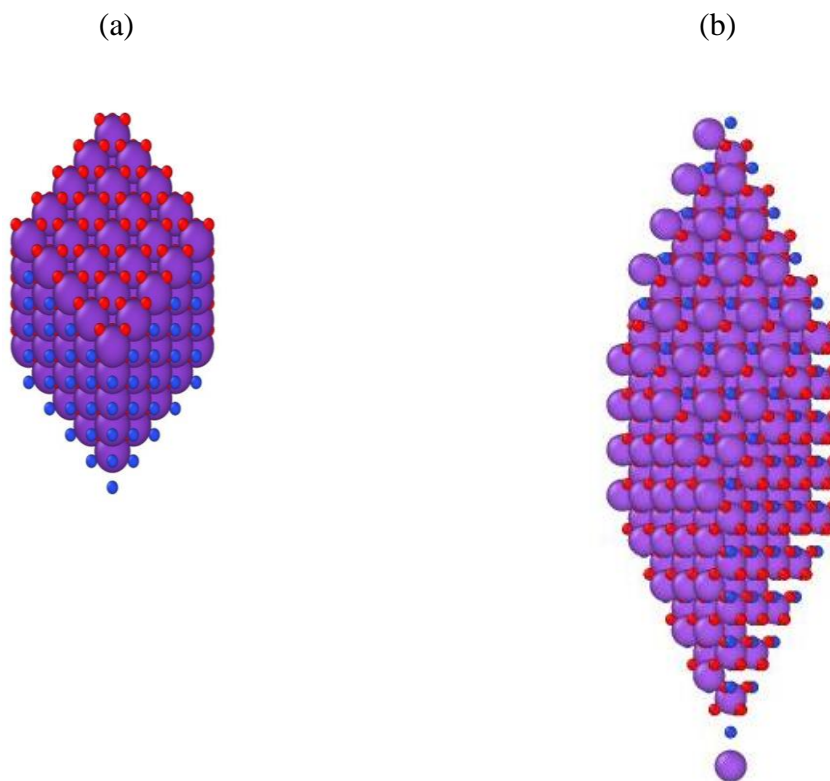


Figure 6.2 (a) ferroelectric potassium nitrate, (b) aragonite potassium nitrate

6.3 Classical Molecular Dynamics

With the use of classical molecular dynamics, simulations of the possible behaviour of crystal nucleation and growth have been performed on aragonite- KNO_3 .

The most stable surface cleaved using the methodology described in the previous section, $\{001\}$ has been put in contact with saturated solutions of KNO_3 .

6.3.1 Methodology

Molecular dynamics simulations were performed using the DL_POLY^[9] code. We performed canonical ensemble calculations over a temperature interval from 1 to 300 K in order to relax the simulation box and let the system equilibrate itself. A Nosé-Hoover^[35,36] thermostat with a relaxation time of 0.1 ps was used. The time step was set to 0.5 fs. The selected number of time steps was 50000 (25 ps), of which 10000 (5 ps) were used as an equilibration period, where the temperature was scaled from 1 to 300 K. This interval has been proven sufficient to reach convergence. A temperature-scaling interval of 10 K was used, whilst the radial distribution function (RDF) was collected every 1000 time steps, using a bin width of 0.1 Å to obtain the plot. The Ewald summation real space cut-off was set to 8.0 Å, whilst the width of the Verlet shell was 1 Å. The Ewald sum precision was set to a relative error of 10^{-5} . In order to calculate the long ranged electrostatic (Coulombic) potentials the Smoothed Particle Mesh Ewald (SPME^[11]) summation method was used. The grid for the k-vector summation was set with dimensions of 8x8x8, and α , the Ewald splitting parameter, set to 0.36037 \AA^{-1} . Isothermal-isobaric (NPT) ensemble calculations were performed using the Nose-Hoover NPT ensemble, with the pressure set to 1 atm and the temperature set to 300 K. The thermostat and barostat relaxation times were 0.1 ps. Other parameters were set as for the NVT simulation.

6.3.2 Results

A slab of $\langle 0 0 1 \rangle$ potassium nitrate with the size of $120 \times 109 \times 180 \text{ \AA}$ has been cleaved and put in contact with various solutions of potassium nitrate (namely 3.5, 4.3 and 5 molal).

Figure 6.3 shows the initial configuration for the 5 molal case. Water is not displayed for clarity. After running this simulation box with the specification listed in previous section, it was possible to notice that, swiftly (1.5 ns), the ions in the solution would approach the surface. Simulations have been ran at three fixed values of temperature (100, 200 and 300 K). These have shown that the solution tends to crystallise on top of the existing surface with a behaviour that is influenced by temperature and concentration.

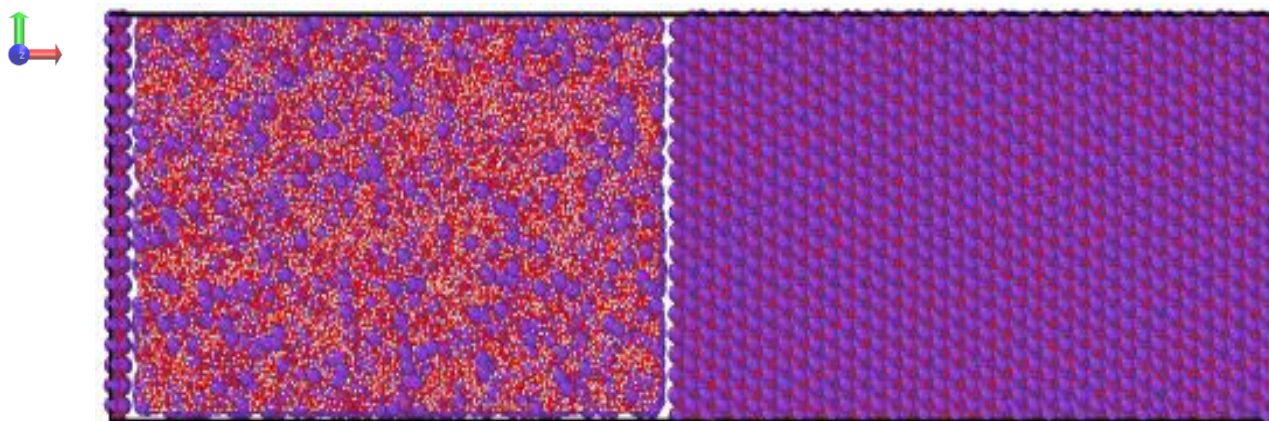


Figure 6.3. Simulation box of $\langle 001 \rangle$ KNO_3 surface in contact with high concentration KNO_3 solution. Red arrow indicates the x, green y, and blue z axis.

At low temperature, (100/200 K) the system appears to freeze, while at 300 K it shows a tendency for the ions to layer, although with no apparent order, on the surface.

Because the simulation is run as an NVT ensemble, while the ions layer on the surface, the space once occupied by the solution becomes empty, as it is possible to see from Figure 6.4

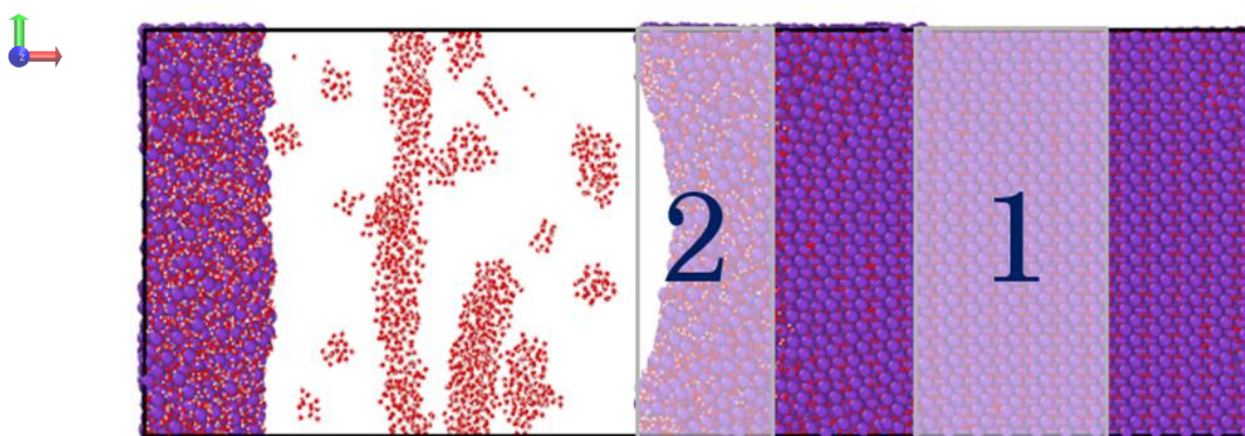


Figure 6.4. Simulation box of $\langle 001 \rangle$ KNO_3 surface in contact with a high concentration KNO_3 solution after 2 picoseconds run in the NVT ensemble. Red arrow indicates the x, green y, and blue z axis.

The structure is periodic along the x -axis, therefore the ions on the left-hand side of the box should be considered belonging to the top of the surface on the right-hand side.

It is possible to identify two separate regions in Figure 6.4: the one defined as (1) represents the centre of the slab and it clearly shows a retained crystalline structure, however the region of new growth, identified as (2) does not appear as ordered and it also shows the presence of encapsulated water.

6.3.2.1 Analysis of the radial distribution function (RDF)

Analysis of the radial distribution function of the two sections might help understanding their nature.

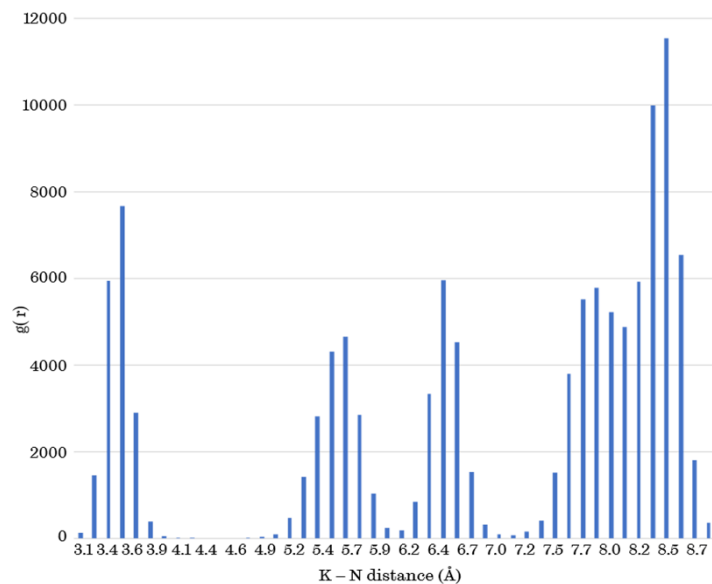


Figure 6.5. RDF for the zone 1 reported in Figure 6.4

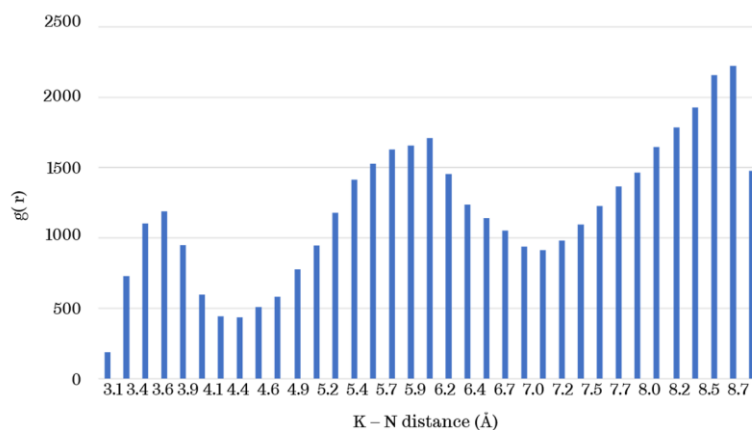


Figure 6.6. RDF for the zone 2 reported in Figure 6.4

Figure 6.5 shows the RDF of the region marked as (1) in Figure 6.4, as we expected, there are clear peaks that resemble the crystalline structure. In contrast, Figure 6.6 shows the RDF of the region marked as (2) in Figure 6.4. In this case, there is barely any trace left of clear peaks, and as we expected, the region appears to be amorphous.

6.4 Constant Chemical Potential Molecular Dynamic (C μ -MD)

The results obtained with the classical MD analysis demonstrate a common limitation of the technique. Classical MD can be subjected to size limitations; being based on empirical potentials, it can typically study systems of size up to $10^4 - 10^9$ atoms. Another limitation, which is especially relevant when trying to simulate rare events such as nucleation, is the relatively small time scales that can be simulated. All those limitations become particularly dramatic in the simulation of phase transformations, as for the crystal growth from solution. As the crystallisation proceeds, the solution is depleted and this causes a change in its chemical potential, which affects the growth process itself^[14-16]. Therefore, it is reasonable to think that this might have affected the results presented in the previous section. To try to eliminate those effects, sizeable finite-size corrections are required. This will make the simulation results more reliable and comparable with the experimental results.

One of the most common methods to account for these effects is to use a numerical approach to prevent such finite size problems, which means effectively to sample the configurations in the Grand-Canonical (GC) ensemble^[17-31]. In this case we decided to use a recently developed approach, constant chemical potential molecular dynamics^[32].

6.4.1 Methodology

Figure 6.7 shows the standard set-up for a constant-chemical potential MD simulation: on the left we can see a crystal region, with solid density n^C , while on the other side of z_I we can see the transition Region (TR), of length ζ .

The TR is extended so that when $z > z_I + \zeta$, the density approaches its bulk value, n^B ^[12].

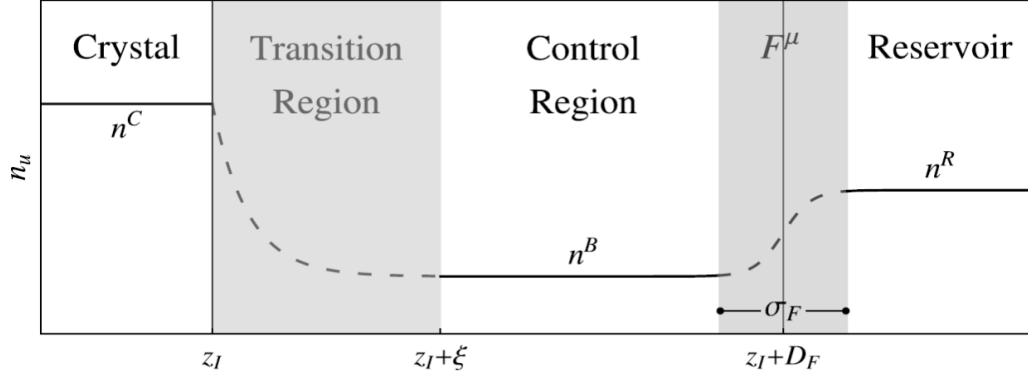


Figure 6.7. Scheme of a standard constant chemical potential molecular dynamics simulation. Reproduced with permission from [12]

The concentration profile, n_u changes inside the TR, as determined by the crystallisation kinetics and the diffusivity of the liquid, and cannot be predicted with high confidence a priori^[27].

The aim is to establish the target concentration in a section of the solution volume, defined as Control Region (CR), while the rest of the solution is used as a molecule reservoir. To control the solution density, an external force, F^μ , is applied at a fixed distance (D_F) from the moving crystal interface. F^μ acts as a membrane, regulating the flux of molecules between the CR and the reservoir, in order to maintain the former at a constant concentration.

To keep the solution environment around the developing crystal interface stable, the force is delivered at a constant distance from the interface. The external force is defined as

$$F_i^\mu(z) = k_i(n_i^{CR} - n_{0i})G(z, Z_F) \quad (6.2)$$

where the bell-shaped function $G(z, Z_F)$ is not zero close to the force centre and provides a harmonic-like force acting on solution molecules at a set distance DF from the solid to correct for instantaneous CR density, n_i^{CR} variations from the desired n_{0i} . The species of interest are denoted by i , and k_i is a force constant that acts on them. We evaluate n_i^{CR} as where n_i is the total number of species and V^{CR} is the volume of CR, then n_i^{CR} ^[27]:

$$n_i^{CR} = \frac{1}{V^{CR}} \sum_{j=1}^{N_i} \theta(z_j) \quad \begin{cases} 1 & \text{if } z_j \in CR \\ 0 & \text{otherwise} \end{cases} \quad (6.3)$$

$$G_w(z - Z_F) = \frac{1}{4w} \left[1 + \cosh \left(\frac{z - Z_F}{w} \right) \right]^{-1} \quad (6.4)$$

G_w has a peak intensity proportional to w^{-1} and a width proportional to w . In the $z \sim Z_F$ case, G_w is the only z -value that is not zero. F^μ is not a conserving force; hence, there is no one formulation of the potential function that will lead to Equation 6.3. It separates the solute and solvent into two distinct forces or interactions. Both species affect the chemical potential of the solution, so controlling their concentration is crucial. Since the barostat method ensures that the concentration of the other species will quickly reach equilibrium, treating more than one population to F^μ in NPT simulations is unnecessary. If NVT dynamics is taken into consideration, then F^μ should have impacts on both the solute and solvent species. In other words, there is a finite amount of time, F^μ , that the chemical potential may be maintained before the reservoir is depleted due to further crystallisation. So that F^μ may function well during the period of interest, it is crucial to keep this time limitation in mind and construct the simulation box accordingly^[27].

To summarise, the C μ -MD set up consists of the following steps^[27]:

1. In order to examine the distribution of solvent molecules within the box, the solid-liquid interface point z_I is determined dynamically.
2. The CR position is modified in accordance with the revised force centre Z_F , which is kept at a constant distance, D_F , from z_I .
3. Using (6.5), it is possible to derive the densities, n_i^{CR}

$$n_i^{CR} = \frac{1}{V^{CR}} \sum_{j=1}^{N_i} \theta(z_j) \quad (6.5)$$

4. The MD equations of motion (and the external forces) are integrated.

Simulations have been carried using LAMMPS^[33,42] interfaced with PLUMED^[34-36].

The initial temperature was set to 0 K and ramped up to 300 K during the equilibration period. We set a time step of 0.5 fs for the equilibration then 1 fs for the production run and a PPPM^[26] long range coulombic interactions solver with an accuracy of $1.0 \cdot 10^5$. All non-bonded interactions were subjected to a cut-off of 9 Å. Simulations were carried out in the NVT ensemble using a Nosé-Hoover thermostat^[37,38] at 300 K. In the following sections, pictures have been produced using VMD^[39] and OVITO^[40].

6.4.2 Moving interface

Standard C μ -MD was been developed using urea (a molecular system)^[32]. As described in the previous section it was engineered to guarantee that the interface would move as the solution crystallises on the surface. The process has been further extended to ionic system using NaCl^[41] as the model system. The main difference between the two examples in the literature is that the urea crystallisation process is rough, and the crystal grows quickly into the control region, therefore the need to develop the ‘moving interface’. On contrary, sodium chloride’s crystallisation process proved to be slow and, in the case of the simulation, the new crystal does not grow into the control region during τ_F . The moving interface has not been tested for ionic system before being applied to KNO₃. The next section will report the results obtained by testing this methodology using potassium nitrate in its trigonal ferroelectric form.

6.4.2.1 KNO₃ ferroelectric

Figure 6.8 shows the C μ -MD simulation of a {104} surface cut of calcite-potassium nitrate. The simulation has been performed at 300 K and the concentration of the control region set up equal to 5 molar. For clarity, the figure only shows the potassium cores from the slab and the potassium from the solution (water and nitrates are hidden). The upper section of the picture shows the initial configuration of the simulation. In the picture, we can also identify three red lines: the one crossing the middle of the slab represents its centre. The two parallel lines adjacent to the reservoir delimit the control region, whose concentration, as previously mentioned has been set up for a value (5M) which according to the literature^[20] is close to the minimum value at which we expect to see crystallisation. The bottom section of the picture shows the same system after 0.25 ns of simulation. It is possible to see a shift of the atoms on the z axis as the position of the centre of the slab no longer corresponds with the initial one. However, there is also a clear dissolution process starting at the interface.

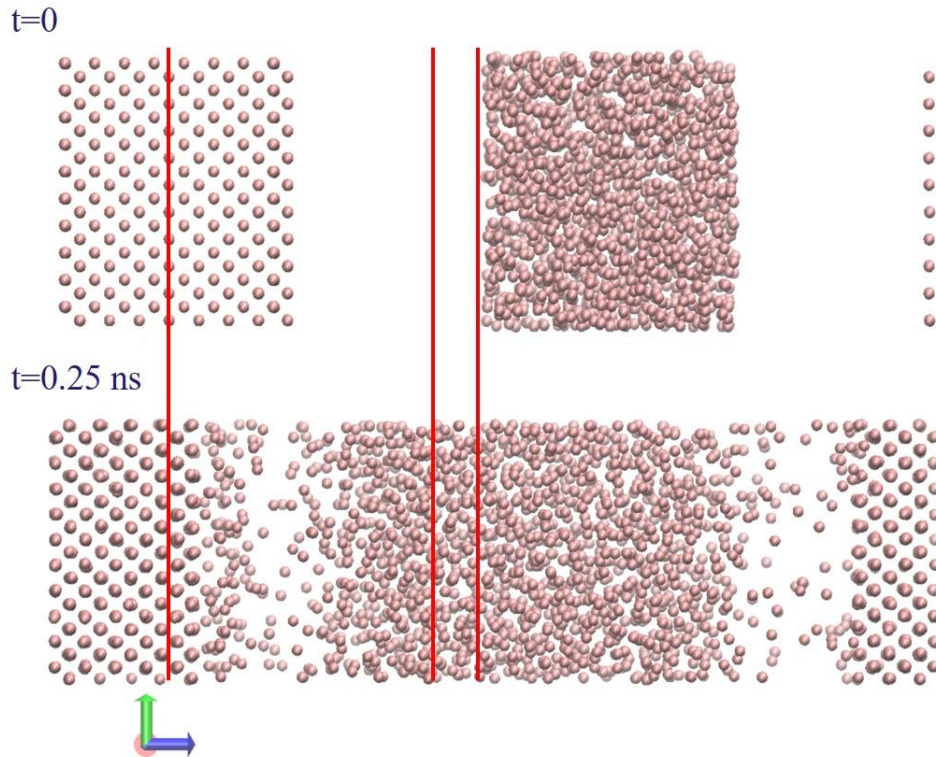


Figure 6.8. $C\mu$ -MD simulation of a KNO_3 -calcite slab, at the beginning of the application of the forces and after 0.25 ns. Red line on the left hand side shows the centre of the slab while the two parallel lines in the middle show the control region (concentration set to 5 M). For clarity, figure shows only the potassium cores (red balls).

Figure 6.9 shows the evolution of the density (expressed in atoms per cubic nanometre) as a function of time in the control region. It is possible to see that, while the water's concentration value stabilise over an average for the solution, the nominal concentration for potassiums and nitrates does not change. This trend is also confirmed by Figure 6.10, which shows the potential bias for both potassiums and nitrates. This value is expected to decrease to zero. This is clearly an artefact of the simulation, since, based on Figure 6.8 it is actually possible to see the ion flow from the reservoir to the control region.

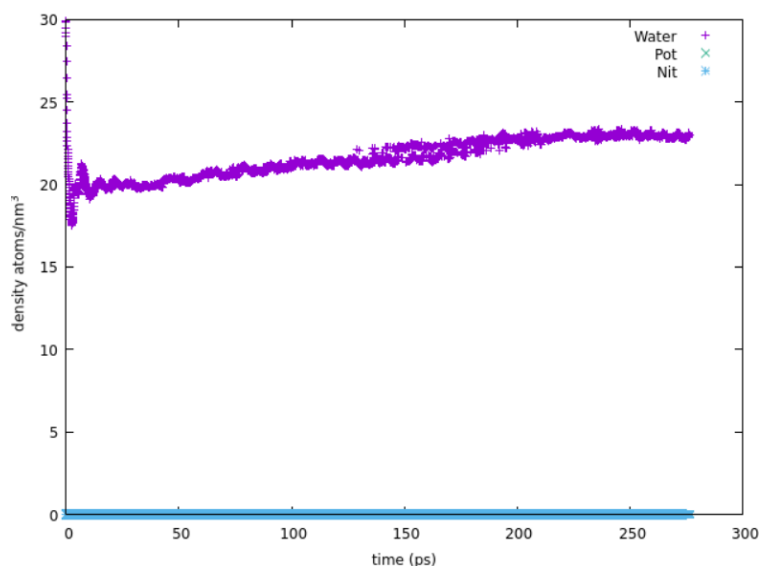


Figure 6.9. Evolution over time (ps) of water (purple symbols), potassium (green symbols) and nitrogen (light blue symbols) concentration expressed as number of ions per cubic nanometre. The potassium and nitrate lines are both equal to zero for the whole simulation and therefore overlap perfectly.

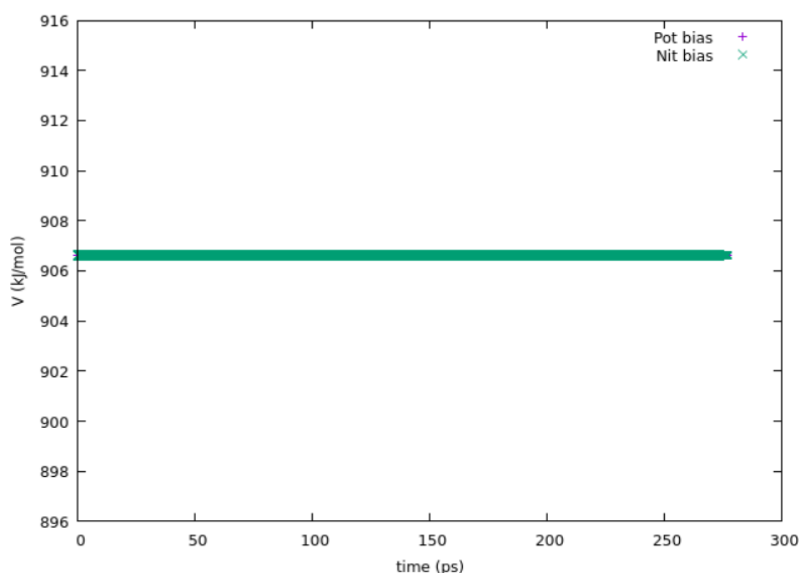


Figure 6.10. Evolution over time (ps) potassium (green symbols) and nitrogen (light blue symbols) potential bias (kJ/mol). The two quantities have constantly the same value and overlap perfectly.

6.4.3 Fixed interface

To overcome the issues stated in the previous section and since it has been proved to work effectively for sodium chloride, it has been decided to try a fixed interface approach. As the name suggests, in this case the control region position does not move accordingly to the expansion (in case of crystallisation) or contraction (in case of dissolution) of the slab. The issue that this could cause is, if the system nucleates swiftly, the crystal would rapidly grow

into the control region, thus destroying the whole set-up. Based on the preliminary study it appears that potassium nitrate might grow quickly, however experimental set-up is not in agreement with the simulation result. Because of this discrepancy and with the idea in mind that the results of the classical MD might be artificial, we decided to proceed by testing the fixed interface.

6.4.3.1 KNO_3 ferroelectric

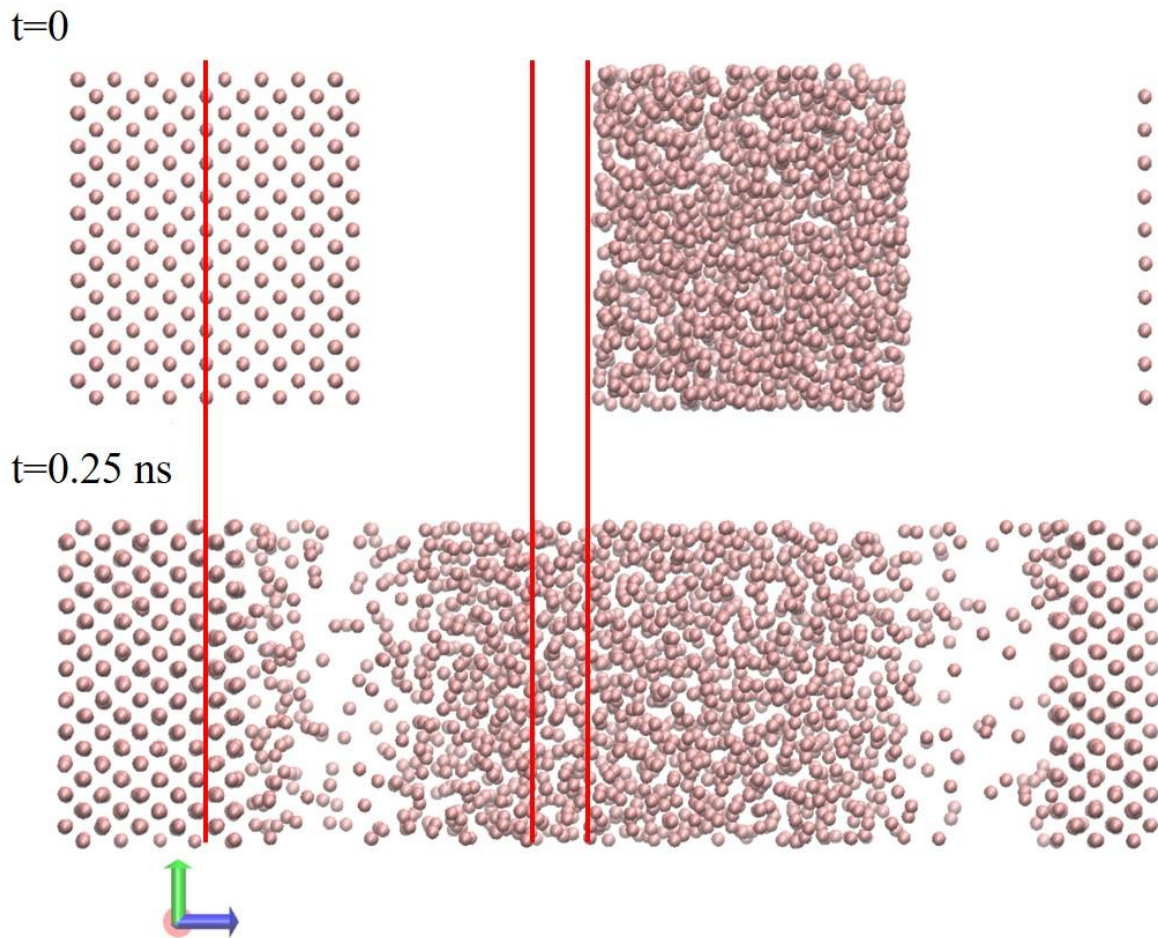


Figure 6.11. $C\mu$ -MD simulation of a KNO_3 -calcite slab, at the beginning of the application of the forces and after 1 ns. Red line on the left hand side shows the centre of the slab while the two parallel lines in the middle show the control region (concentration set to 5 M). For clarity, figure shows only the potassium cores (red balls).

In this case, as it is possible to see from Figure 6.11, the application of constraining forces at the centre of the slab avoided its drifting in the z direction. This allows us to compare the initial and final configuration even visually. The red line at the left-hand side of the figure shows the centre of the slab for both systems and because of the periodicity in z we can see a layer of ions belonging to the surface at the right-hand side of the picture. This is again, showing only the

potassium cores of the slab and the reservoir, for clarity. The two red lines in the middle of the picture enhance the control region, whose concentration was set to 7 M. We can clearly see, after 3 ns that most of the slab does dissolve. We can see the behaviour of the fixed interface from Figure 6.12. After the initial adjustment the concentration of the ions, it reaches the target concentration for both the water and the ions in solution. Figure 6.13 confirms the trend, where it is possible to see the potential bias fluctuating around zero.

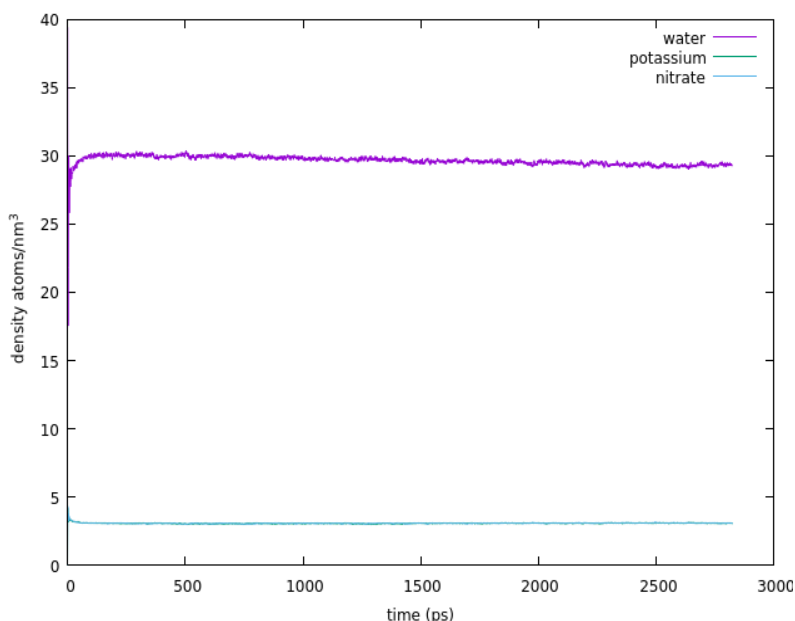


Figure 6.12. Evolution over time (ps) of water (purple symbols), potassium (green symbols) and nitrogen (light blue symbols) concentration expressed as number of ions per cubic nanometre.

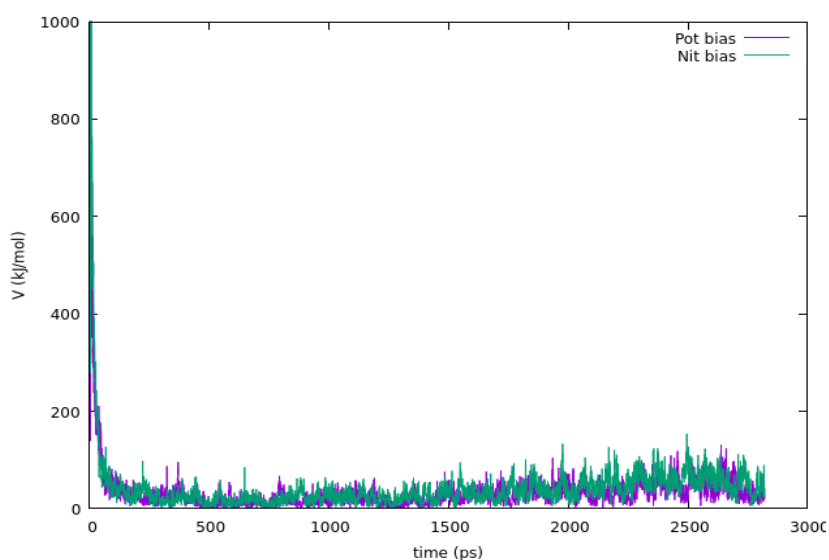


Figure 6.13. Evolution over time (ps) potassium (green symbols) and nitrogen (light blue symbols) potential bias (kJ/mol).

6.4.3.1.1 Collective variables analysis

To analyse this system we have made use of a particular collective variable: the sixth order Steinhardt parameter^[38], referred to as q_6 . Steinhardt parameters are a group of variables based on spherical harmonics that are used to investigate the local atomic environment. These variables have been widely used for a variety of purposes, including the differentiation of crystal structures, the identification of solid and liquid atoms, and the detection of defects. This parameter allow us to measure the degree to which the first coordination shell around an atom is ordered. As it is possible to see from Figure 6.14, the mean value of q_6 lies in a symmetrical position in the diagram, which means the system is ordered.

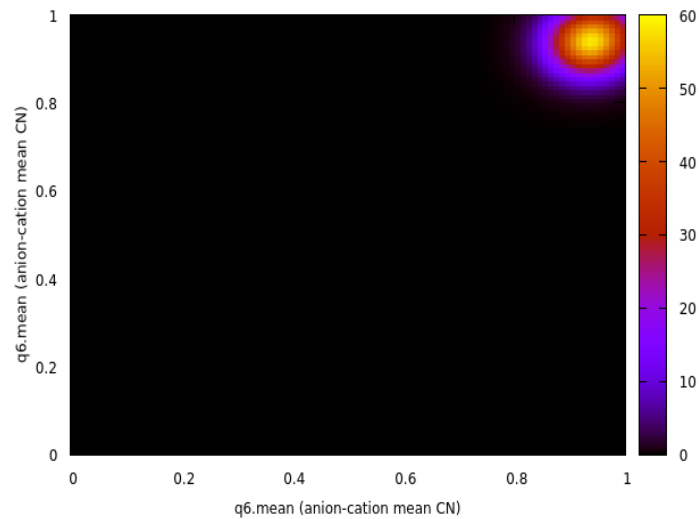


Figure 6.14. q_6 mean (anion-cation) of the system depicted in Figure 6.11 at the beginning of the simulation

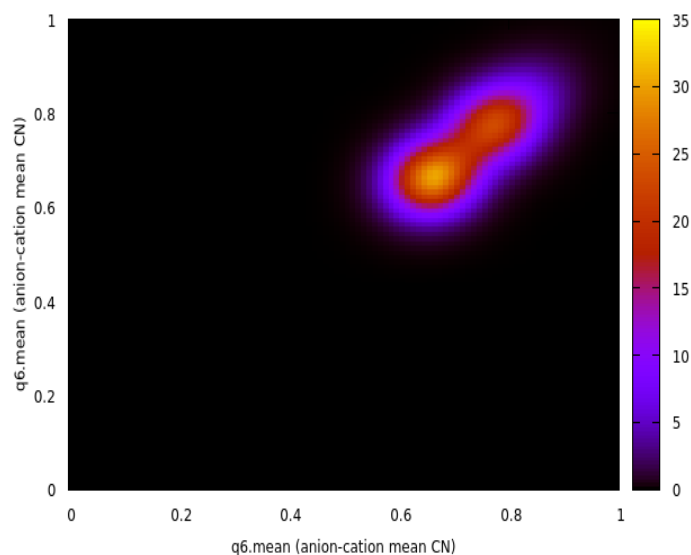


Figure 6.15. q_6 mean (anion-cation) of the system depicted in Figure 6.11 after 1 ns

Shifting to the end of the simulation, this mean stops being symmetric and it spreads: we can recognise the formation of the amorphous phase from this shape, as shown in Figure 6.15.

6.4.3.1.2 Results

Dissolution of KNO_3 –calcite can be explained from different points of view and it has been observed as well on preliminary studies. It has been proven, as well, to affect more the unstable polymorphs (phase I and II). It could be due, as well by the energetic implication coming from the unbalanced surface to bulk energy ratio, which could be potentially resolved by extending the box dimension in the direction of periodicity.

6.4.3.2 KNO_3 aragonite

To overcome the size problem, when testing KNO_3 -aragonite we made use of a slab 180 Å long in the z direction, and the total length of the cell was set to 607 Å. Out of the total length of the cell the reservoir occupies 100 Å and its concentration has been set to 12 M. For this set up, we did not put the reservoir in contact with pure water. Instead, we decided to create a less concentrated solution. The purpose of this was to avoid any possible initial dissolution due to

the fact that the surface, for the early stage of the simulation, and before the Fermi forces would have moved the ions in the control region, would have been in contact with pure water.

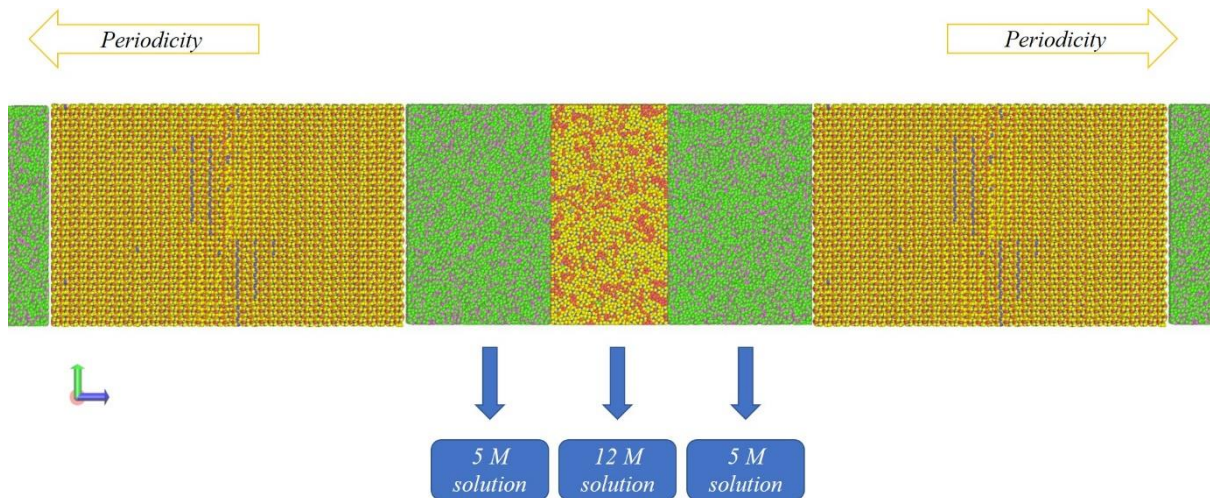


Figure 6.16. Set up for a Cu -MD simulation of a KNO_3 -aragonite slab. On the right-hand side we can see the slab, in contact with a low concentration solution (5 M) and then the reservoir (15M). Because of the system's periodicity the reservoir is in the middle of two low concentration solutions.

We decided to check, then, two different scenarios: in the first case, we set up the control region at a concentration equal to 2 molar: in this case we would expect to see dissolution. For growth, we set up another system with control region concentration equal to 7 molar. The next sections will discuss in detail the two set ups

6.4.3.2.1 Control Region 2 M

Figure 6.17 shows a zoom on the slab for the configuration at the beginning and after 3 ns. The picture only shows the potassium cores. The black lines at the left and right-hand side enhance the edge of the surface. After 3 ns the slab has lost, symmetrically on both sides, one layer of potassiums, confirming the expectation of dissolution. The black box enhances the missing layer.

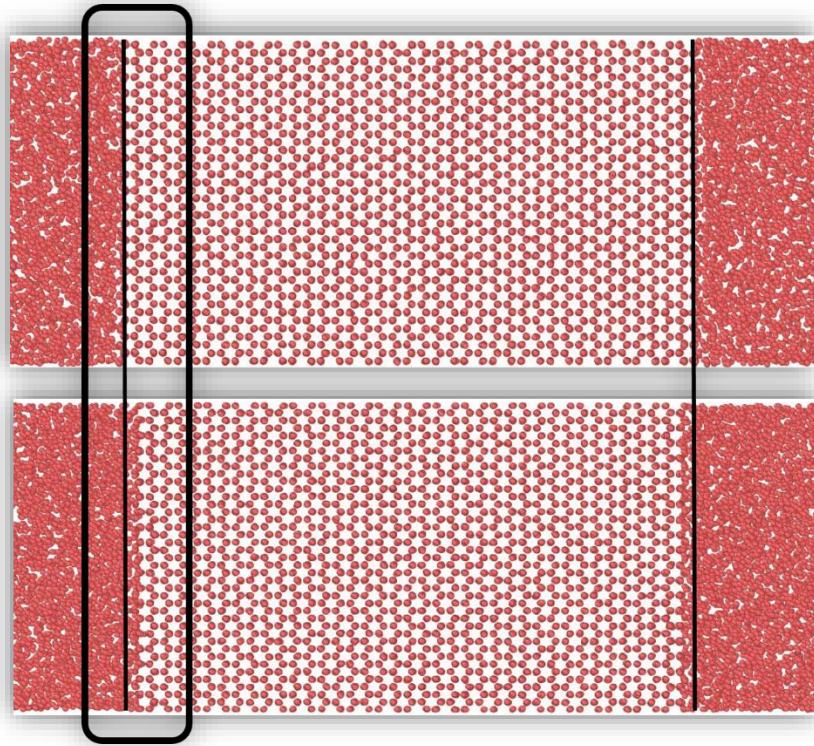


Figure 6.17. *Cμ*-MD simulation of a KNO_3 -aragonite slab, at the beginning of the application of the forces and after 3 ns. Black lines underline the very last layer of the surface. Black box on the right hand-side enhances the dissolution process.

6.4.3.2.1.1 Water ordering

Figure 6.18 shows, on the left-hand side the concentration for hydrogens and oxygens of the water inside the reservoir. Because the concentration of potassium nitrate is nearly doubled compared to the control region, the water concentration is lower than the control region. Around bin size of 2500 it is possible to see the Fermi wall and the ion drift. The concentration becomes stable in the control region and then it is possible to see a peak right next to the surface. The water concentration swiftly goes to zero inside the bulk and the behaviour is repeated symmetrically on the other side of the slab.

Figure 6.19 and 6.20 show close ups of the water level near the Fermi wall and the surface, as they change over time.

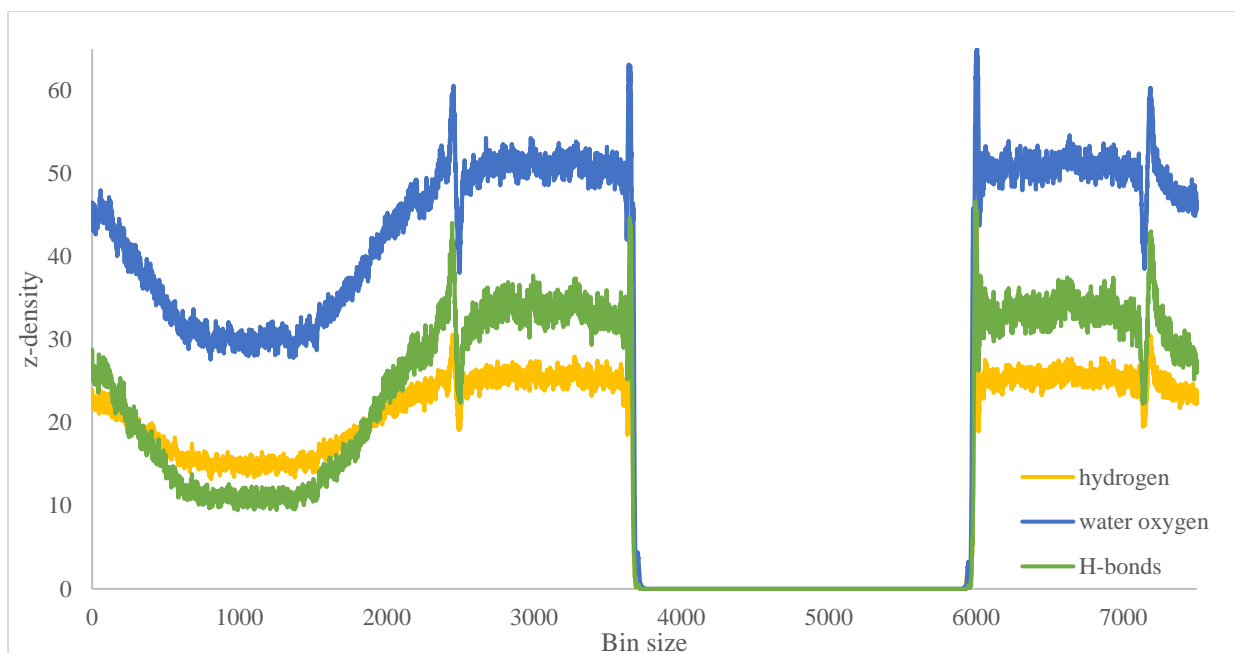


Figure 6.18. *z*-density as a function of the bin size for hydrogen (yellow lines) and oxygen of the water (blue line). Green line represents the hydrogen bond density.

From Figure 6.19 we can see that as soon as the concentration reaches its target value in the control region, the amount of water flowing in diminishes. Figure 6.20, however, shows the water density and how its value spikes close to the surface, before going to zero inside the slab. This spike can be justified considering the interaction water would create with the ions sitting on the surface.

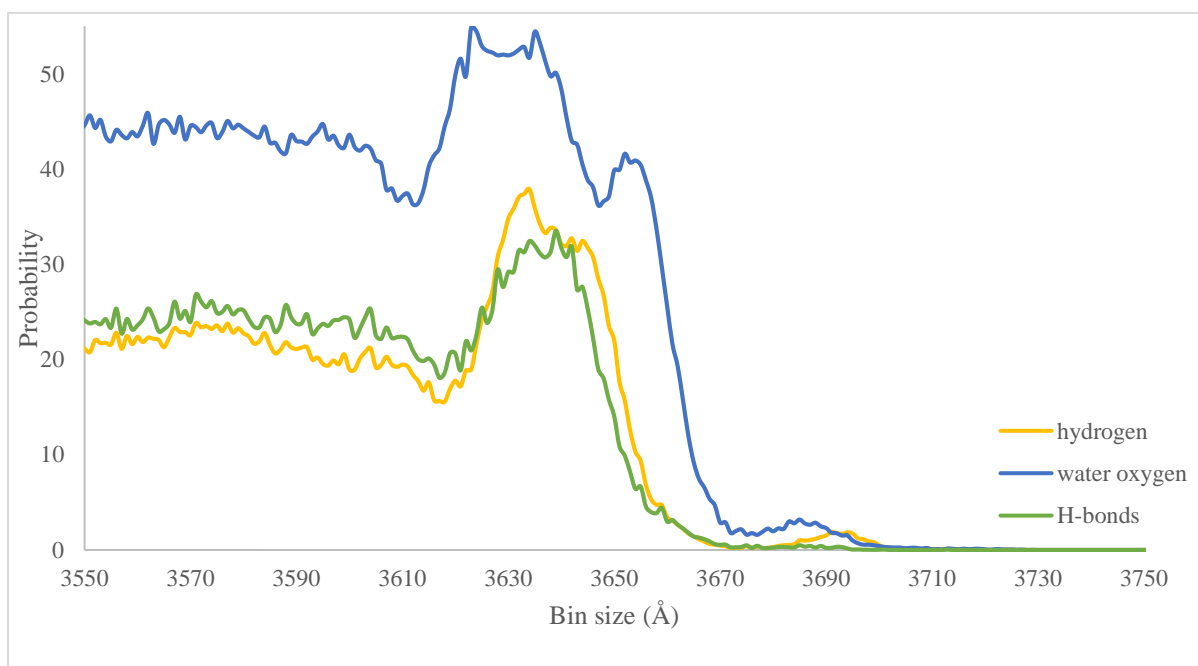


Figure 6.19. Close up next to the surface of the *z*-density as a function of the number of bins for hydrogen (yellow lines) and oxygen of the water (blue line). Green line represents the hydrogen bond density

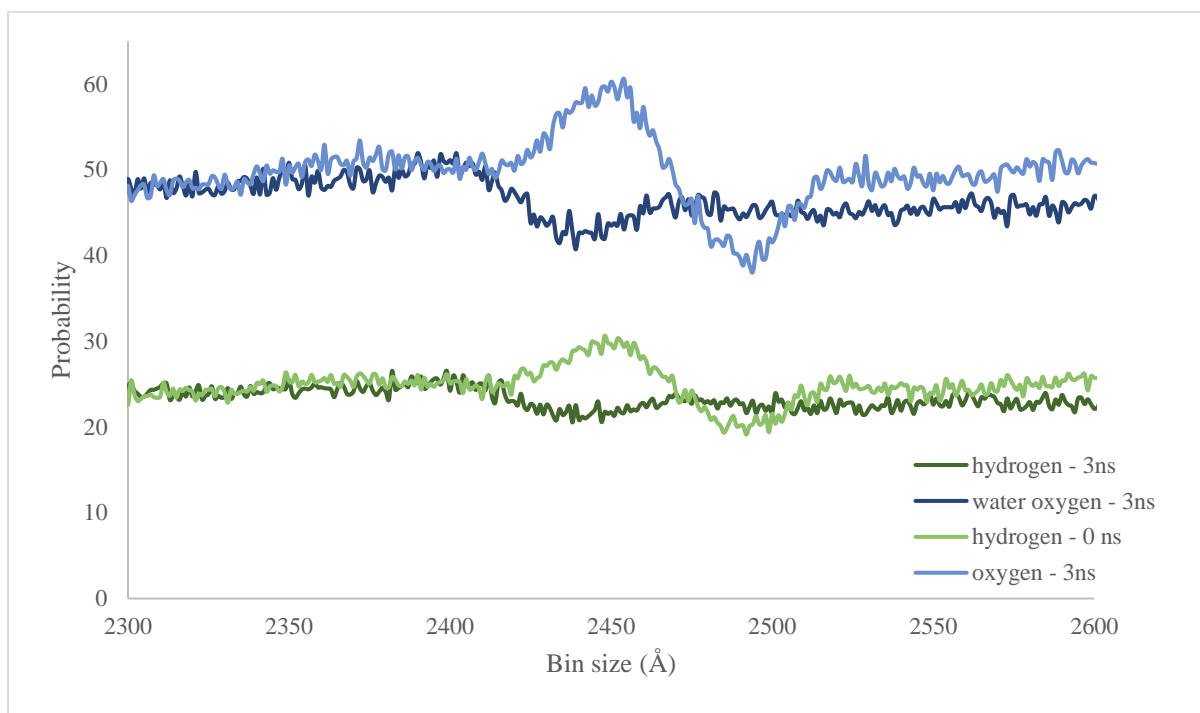


Figure 6.20 Close up next to the Fermi wall of the z -density as a function of the number of bins for hydrogen (green lines) and oxygen of the water (blue lines). Green line represents the hydrogen bond density

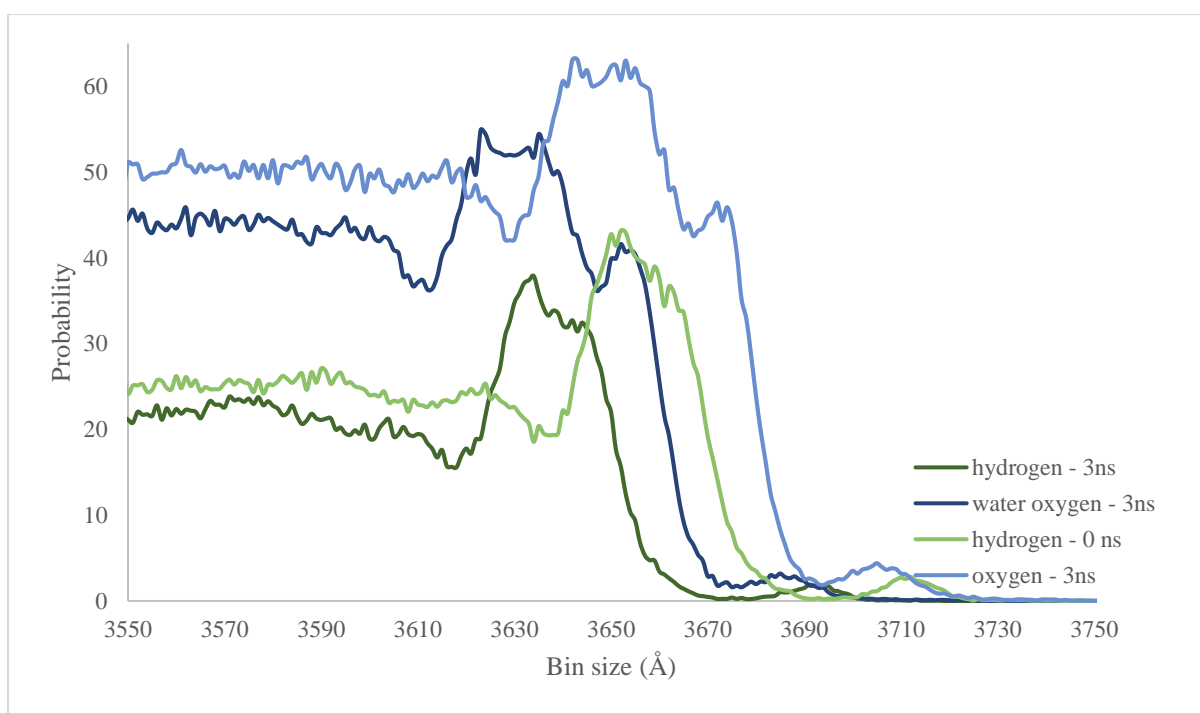


Figure 6.21. Close up next to the surface of the z -density as a function of the number of bins at the beginning of the application of the forces and after 3 ns of simulation, for hydrogen (light green, beginning, dark green after 3ns) and oxygen of the water ((light blue, beginning, dark blue after 3ns).

6.4.3.2.1.2 z-density analysis

Figure 6.22 shows the behaviour of all the potassium nitrate's ions throughout the entire simulation box. We can clearly identify the ordered slab and the variation of the concentration in the different area of the C μ -MD set-up. Figure 6.23 shows a close-up of the surface. We can see the peaks getting less neat as the surface approaches the solution: this already gives an idea of how soluble potassium nitrate is, since the very top layer loses ions (dissolves) very quickly. Figure 6.24 shows a comparison of the nitrogen behaviour over time, this shows some of the bulk peak centred in almost the same position and by counting the total number we can see that the very last one is missing. This quantifies what we were able to see visually from Figure 6.17. The system is clearly dissolving.

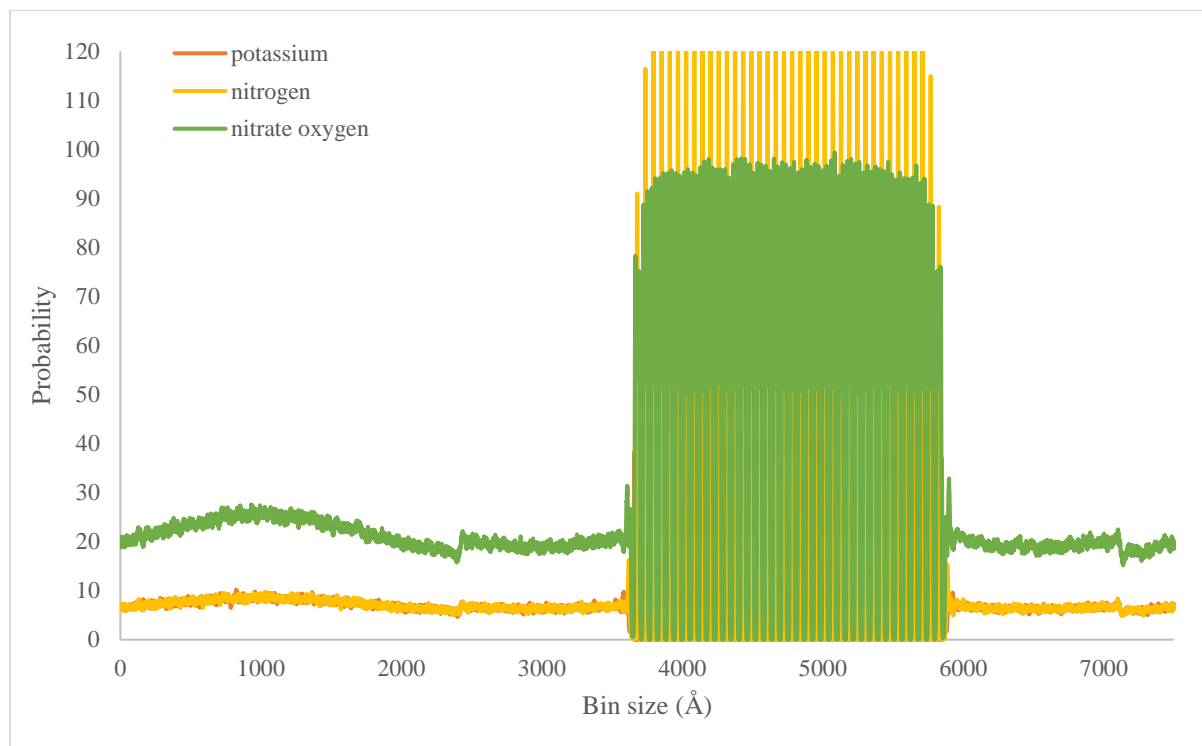


Figure 6.22. z-density as a function of the number of bins for potassium (yellow lines), nitrogen (orange line) and oxygen of the nitrate (green line).

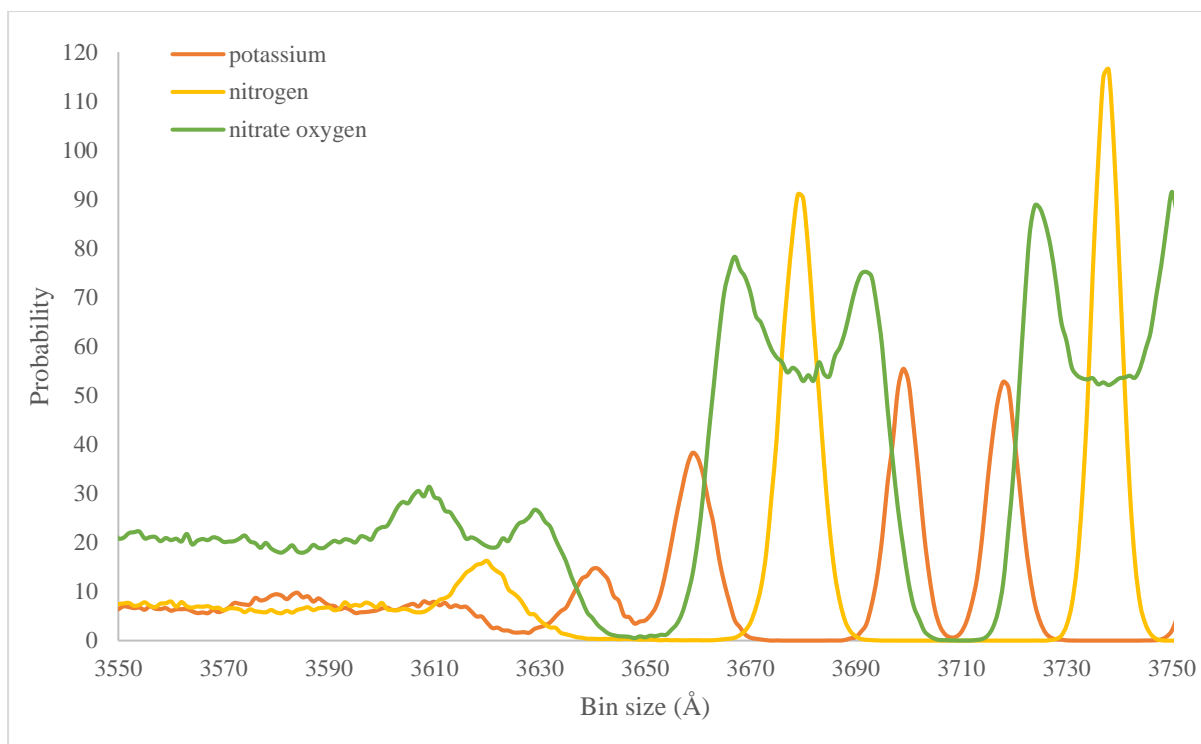


Figure 6.23. Close up next to the surface of the z-density as a function of the number of bins for potassium (yellow lines), nitrogen (orange line) and oxygen of the nitrate (green line).

In this case, the system appears very symmetrical and analyzing the right/left-hand side shows a similar behaviour.

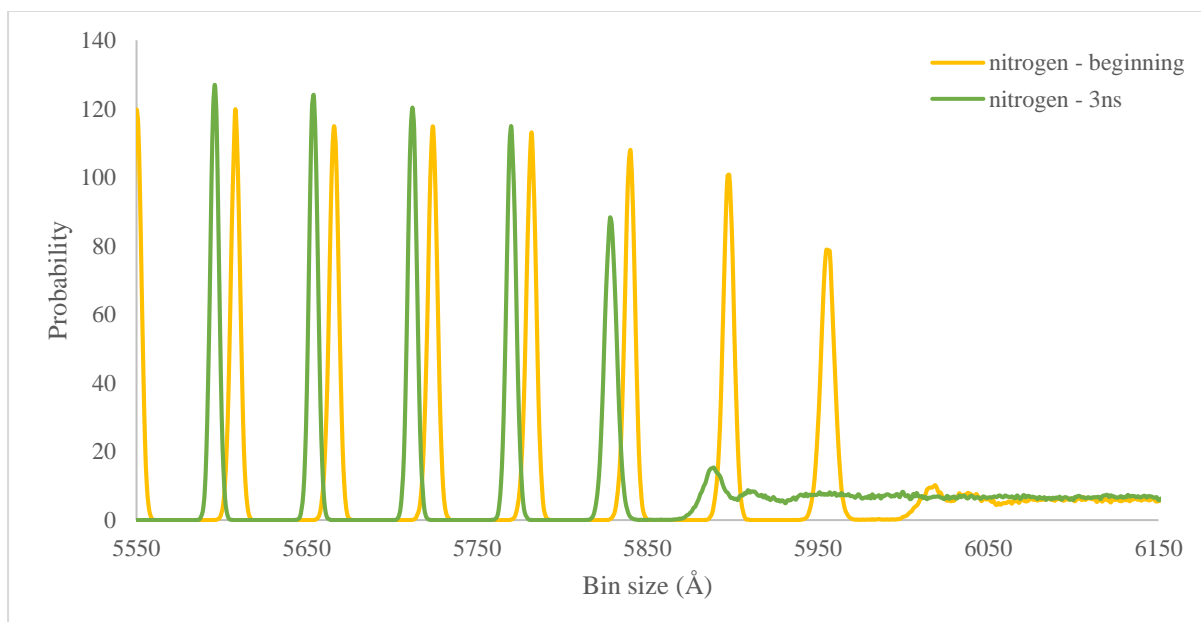


Figure 6.24. Close up next to the surface of the z-density as a function of the number of bins for nitrogen. Yellow line represents the system at the beginning of the application of the forces, the green line after 3 ns of simulation.

6.4.3.2.2 Control Region 7 M

When it comes up to the 7 molar control region case the result is not as neat and evident as in the previous case. To have a better idea, this time, Figure 6.25 shows all the ions present in solution. Before adding the constant chemical potential, the system had to be equilibrated using classical MD *NPT* ensemble at 300 K. In this timeframe, the system had time to adjust the last layer. As we can see, from the left hand side of the picture, indicated with a black circle, some nitrates have already dissolved. The goal here, should be to see whether the target concentration stops the dissolution or not. This is not as easy to visualise, that is why the z-density analysis, in this case gives results that are very helpful in understanding the system.

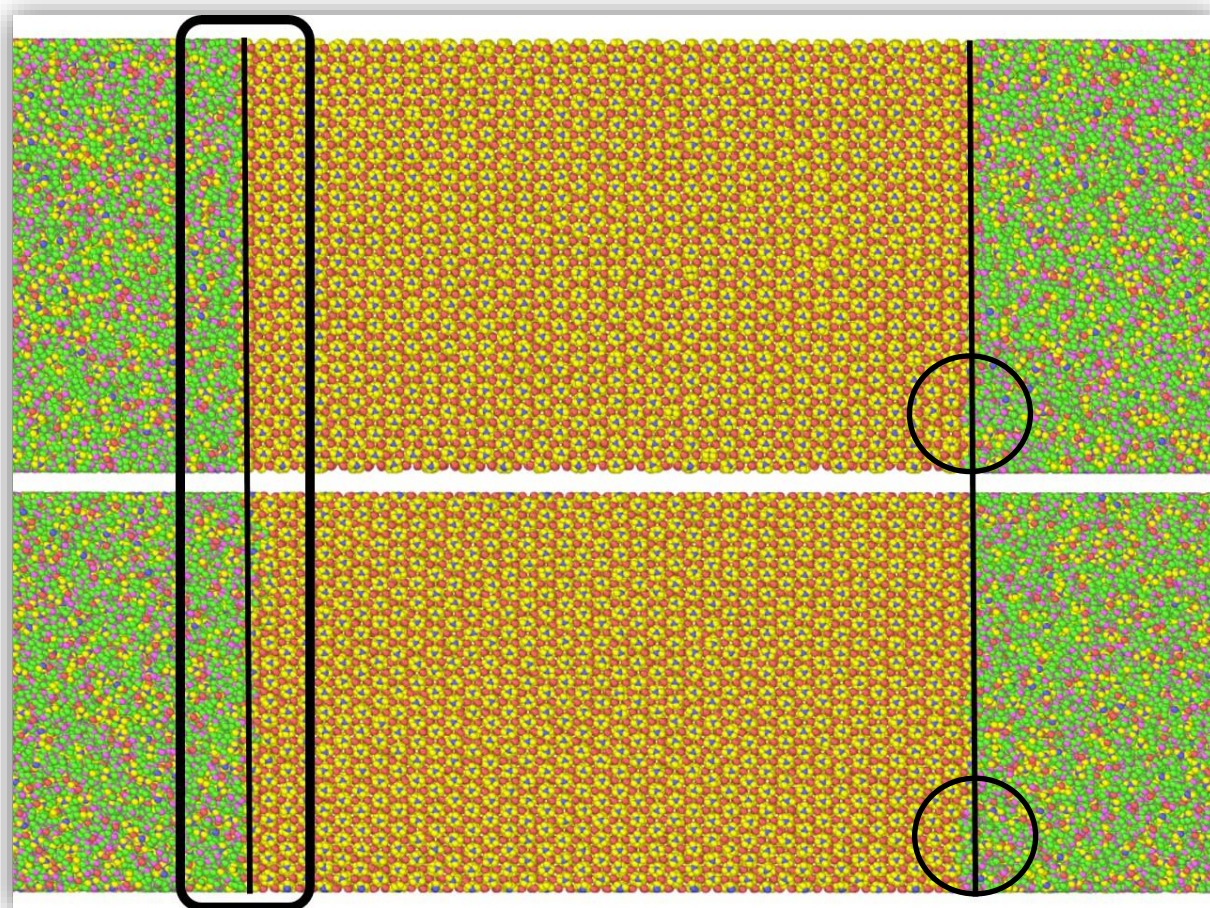


Figure 6.25. *C μ* -MD simulation of a KNO_3 -aragonite slab, at the beginning of the application of the forces and after 3 ns. Black lines underline the very last layer of the surface. Black box on the right hand-side highlights the surface's behaviour.

6.4.3.2.1 Water ordering

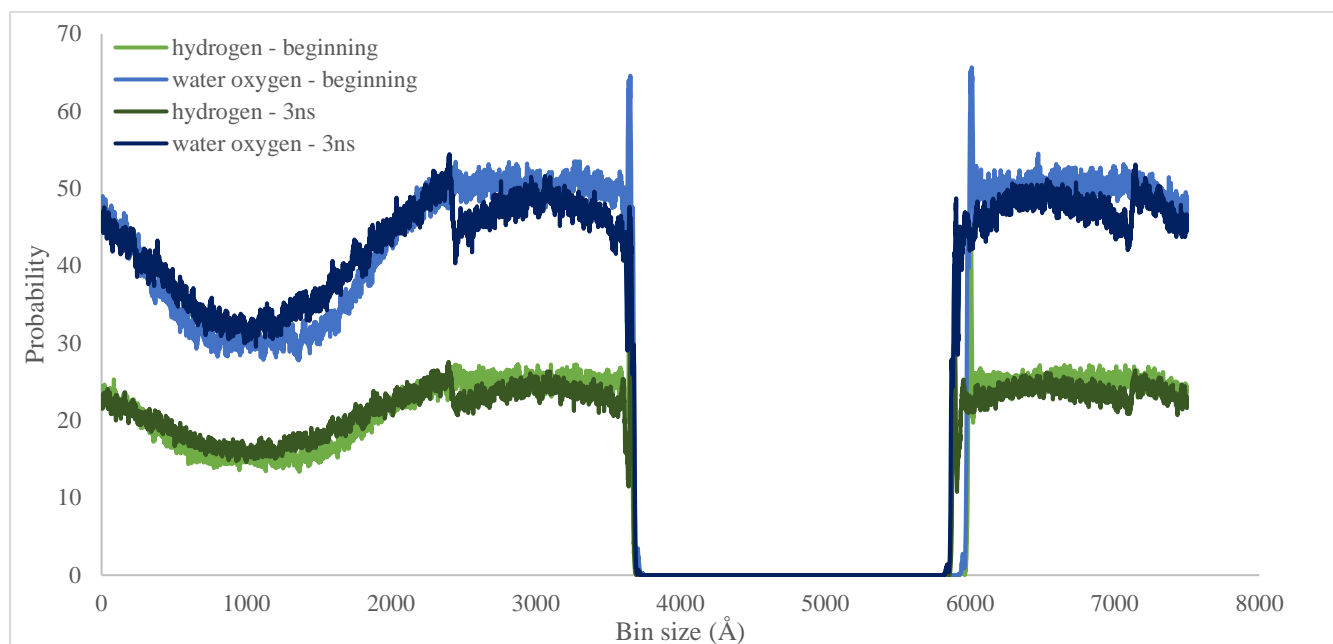


Figure 6.26 z-density as a function of the number of bins at the beginning of the application of the forces and after 3 ns of simulation, for hydrogen (light green, beginning, dark green after 3ns) and oxygen of the water ((light blue, beginning, dark blue after 3ns).

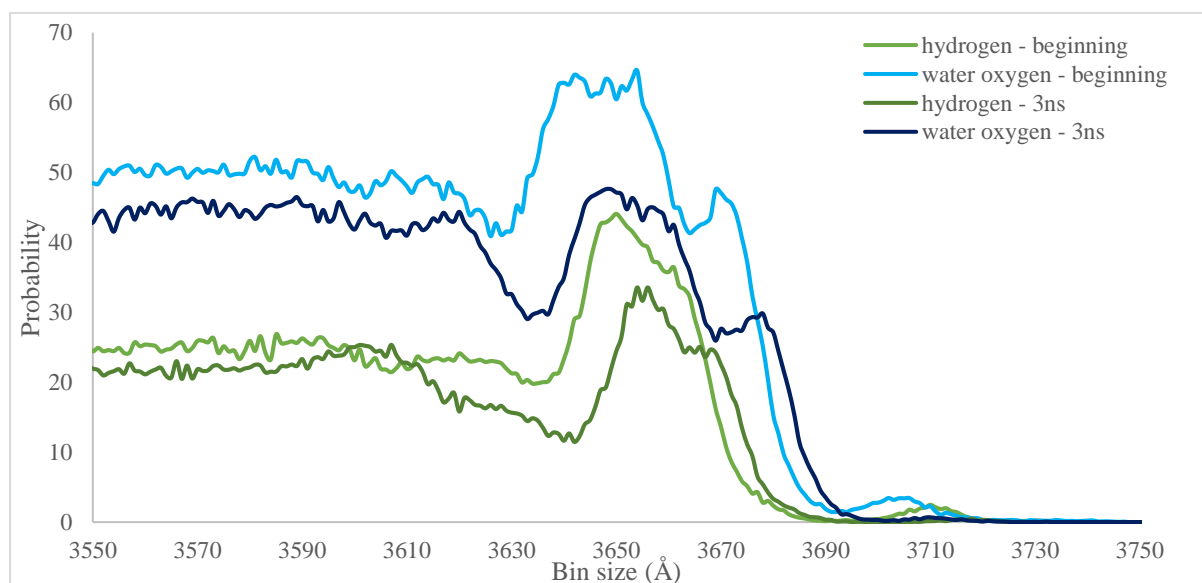


Figure 6.27. Close up next to the surface of the z-density as a function of the number of bins at the beginning of the application of the forces and after 3 ns of simulation, for hydrogen (light green, beginning, dark green after 3ns) and oxygen of the water ((light blue, beginning, dark blue after 3ns).

The water behaviour over time shows very similar behaviour to the previous case and, because the target concentration is much higher this time, the discrepancy between the amount of water flowing is much higher as well. Overall, from a close up, it appears like the surface is losing

water over time, as it is possible to see from Figure 6.26. Analysis of the ions' behaviour would clarify what the surface is going through at this stage.

6.4.3.2.2 z-density analysis

Figure 6.28 shows the nitrogen's behaviour at one of the surfaces. The slab is nitrate terminating, which is the reason why we are analysing nitrate and not potassium. As previously mentioned, what is presented as the 'beginning' of the simulation is actually a system that has already gone through relaxation, so the ions have already had time to approach the surface. We have seen the system interacting with a solution at a concentration not high enough to avoid dissolution, which is what we saw at the very beginning. This layer of partially dissolved nitrates, however, based on Figure 6.25 is reincorporating the lost nitrates: the system is filling its gaps. To quantify the variation, each layer contains 760 nitrogens. The peak at the beginning integrates for 110 ions, while the one after for 170 ions.

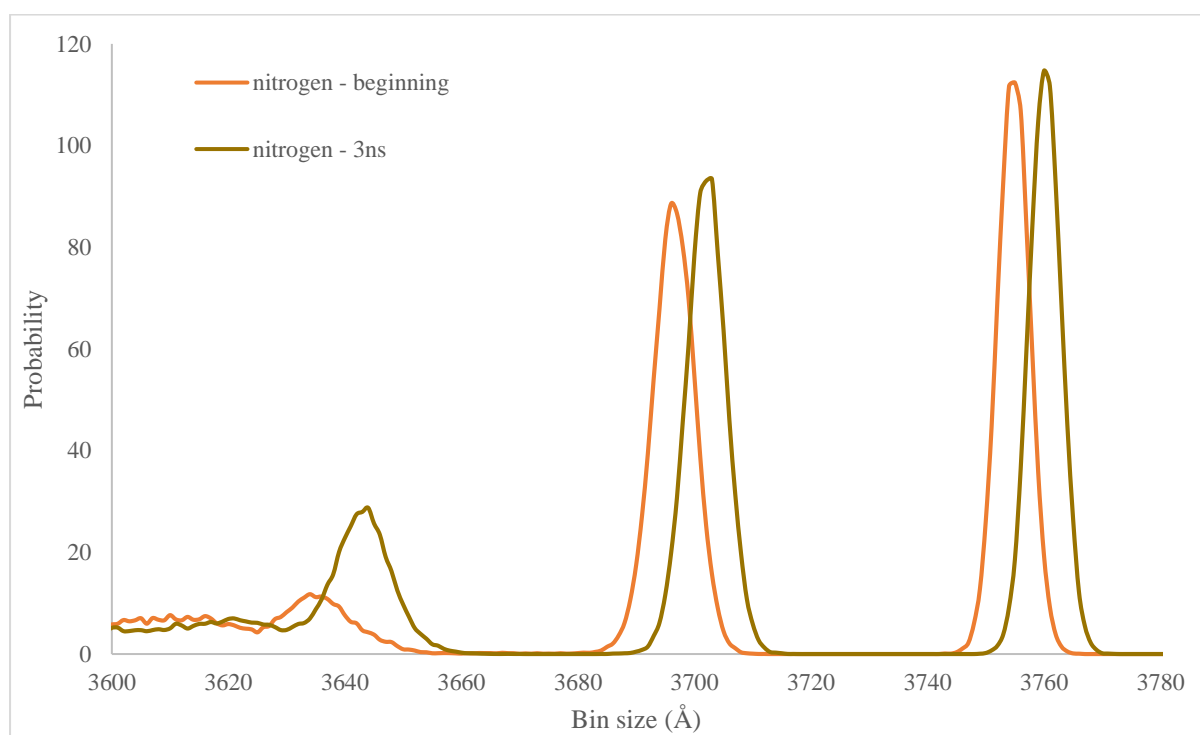


Figure 6.28. Close up next to the surface of the z-density as a function of the number of bins for nitrogen. Yellow line represents the system at the beginning of the application of the forces, the green line after 3 ns of simulation.

6.5 Final considerations and future work

We can conclude that, based on the results obtained with constant chemical potential molecular dynamics, the results obtained with classical molecular dynamics might have been an artifact. There is no experimental evidence of the ability of potassium nitrate to nucleate with a rate as quick as the one we might have derived from classical MD simulation. The $C\mu$ -MD correctly represents the high solubility of potassium nitrate. At the stage of this work, we cannot confirm clearly the growth behaviour. This behaviour is in agreement with the sodium nitrate case. It looks like the growth rates for the two systems are similar, which would need further studies to be confirmed. Based on the primary results however, we can confirm the correctness of the choice to apply fixed-distance control regions: the growth is slow enough to allow this methodology to be used successfully. There is evidence of order forming but that should be confirmed with much longer period simulations. That would allow considering in a more precise way, from the statistical perspective, the system's behaviour.

6.6 References

- [1] N.H. de Leeuw, G.W. Watson, S.C. Parker, *Atomistic simulation of adsorption of water on three-, four-, and five-coordinated surface site of magnesium oxide*, J Chem Soc Faraday Trans, 1996, 92, 2081–209;
- [2] P.W. Tasker, The stability of ionic crystals, J Phys C, 1979, **12**, 4977–4983;
- [3] G.W. Watson, P.M. Oliver, S.C. Parker, *Computer simulation of the structure and stability of forsterite surfaces*, Phys Chem Minerals, 1997, **25**, 70–78;
- [4] H. J. Monkhorst, J. D. Pack, *Special points for Brillouin-zone integrations*, Phys. Rev. B, 1976, 13, 5188;
- [5] R. Benages-Vilau, T. Calvet, M.À. Cuevas-Diarte, *Polymorphism, crystal growth, crystal morphology and solid-state miscibility of alkali nitrates*, Crystallography Reviews, 2014, **20**:1, 25-55;
- [6] J.K. Nimmo, B.W. Lucas, *The crystal structures of γ - and β -KNO₃ and the α - γ - β phase transformations*, Acta Cryst., 1976, B-**32**:1968–1971;
- [7] W. Smith, T.R. Forester, *DL_POLY_2.0: A general-purpose parallel molecular dynamics simulation package*, J. Molec. Graphics, 1996, 14 136
- [8] M. Salvalaglio, C. Perego, F. Giberti, M. Mazzotti, M. Parrinello, *Molecular-dynamics simulations of urea nucleation from aqueous solution*, Proc. Natl. Acad. Sci., 2015, **112**, E6;
- [9] J. W. Schmelzer, A. S. Abyzov, *Crystallization 2012 Proceedings of the 10th International Symposium on Crystallization in Glasses and Liquids Goslar, Germany, September 23–26, 2012*, J. Non-Cryst. Solids, 2014, **384**, 2;
- [10] R. Grossier, S. Veessler, *Reaching One Single and Stable Critical Cluster through Finite-Sized Systems*, Cryst. Growth Des., 2009, **9**, 1917
- [11] H. L. Yau, S. Y. Liem, K.-Y. Chan, *A contact cavity-biased method for grand canonical Monte Carlo simulations*, J. Chem. Phys., 1994, **101**, 7918;
- [12] A. Papadopolou, E. D. Becker, M. Lupkowski, F. van Swol, *Molecular dynamics and Monte Carlo simulations in the grand canonical ensemble: Local versus global control*, J. Chem. Phys., 1993, **98**, 4897;
- [13] C. Lo, B. Palmer, *Alternative Hamiltonian for molecular dynamics simulations in the grand canonical ensemble*, J. Chem. Phys., 1995, **102**, 925;
- [14] T. Çağın and B. M. Pettitt, *Grand Molecular Dynamics: A Method for Open Systems*, Mol. Phys., 1991, **72**, 169;
- [15] G. C. Lynch, B. M. Pettitt, *Grand canonical ensemble molecular dynamics simulations: Reformulation of extended system dynamics approaches*, J. Chem. Phys., 1997, **107**, 8594;
- [16] R. Delgado-Buscalioni, P. V. Coveney, *USHER: An algorithm for particle insertion in dense fluids*, J. Chem. Phys., 2003, **119**, 978;
- [17] H. Wang, C. Hartmann, C. Schütte, L. Delle Site, *Chemical potential of liquids and mixtures via adaptive resolution simulation*, Phys. Rev. X, 2013, 011013;
- [18] R. Potestio, S. Fritsch, P. Español, R. Delgado-Buscalioni, K. Kremer, R. Everaers, D. Donadio, *Hamiltonian Adaptive Resolution Simulation for Molecular Liquids*, Phys. Rev. Lett., 2013, **110**, 108301;
- [19] R. Potestio, P. Español, R. Delgado-Buscalioni, R. Everaers, K. Kremer, D. Donadio, *Monte Carlo adaptive resolution simulation of multicomponent molecular liquids*, Phys. Rev. Lett., 2013, **111**, 060601;

- [20] D. Mukherji, K. Kremer, *Coil–Globule–Coil Transition of PNIPAm in Aqueous Methanol: Coupling All-Atom Simulations to Semi-Grand Canonical Coarse-Grained Reservoir*, *Macromolecules*, 2013, **46**, 9158;
- [21] S. Piana, M. Reyhani, J. D. Gale, *Simulating micrometre-scale crystal growth from solution*, *Nature*, 2005, **438**, 70;
- [22] S. Piana, F. Jones, J. Gale, *Assisted Desolvation as a Key Kinetic Step for Crystal Growth*, *J. Am. Chem. Soc.*, 2006, **128**, 13568;
- [23] D. Cheong, Y. Boon, *Comparative Study of Force Fields for Molecular Dynamics Simulations of α -Glycine Crystal Growth from Solution*, *Cryst. Growth Des.*, 2010, 10, 5146;
- [24] J. Anwar, D. Zahn, *Uncovering Molecular Processes in Crystal Nucleation and Growth by Using Molecular Simulation*, *Angew. Chem.*, 2011, Int. Ed. 50, 1996;
- [25] M. Salvalaglio, T. Vetter, F. Giberti, M. Mazzotti, M. Parrinello, *Uncovering Molecular Details of Urea Crystal Growth in the Presence of Additives*, *J. Am. Chem. Soc.*, 2012, **134**, 17221;
- [26] M. Salvalaglio, T. Vetter, M. Mazzotti, M. Parrinello, *Controlling and Predicting Crystal Shapes: The Case of Urea*, *Angew. Chem.*, 2013, **52**, 13369;
- [27] C. Perego, M. Salvalaglio, M. Parrinello, *Molecular dynamics simulations of solutions at constant chemical potential*, *J. Chem. Phys.*, 2015, **142**, 144113;
- [28] S. Plimpton, *Fast Parallel Algorithms for Short-Range Molecular Dynamics*, *J. Comput. Phys.*, 1995, **117**, 1–19;
- [29] The PLUMED consortium. Promoting transparency and reproducibility in enhanced molecular simulations, *Nat. Methods* 16, 670 (2019);
- [30] G.A. Tribello, M. Bonomi, D. Branduardi, C. Camilloni, G. Bussi, *PLUMED2: New feathers for an old bird*, *Comp. Phys. Comm.*, 2014, **185**, 604;
- [31] M. Bonomi, D. Branduardi, G. Bussi, C. Camilloni, D. Provasi, P. Raiteri, D. Donadio, F. Marinelli, F. Pietrucci, R.A. Broglia, M. Parrinello, *PLUMED: a portable plugin for free energy calculations with molecular dynamics*, *Comp. Phys. Comm.*, 2009, **180**, 1961;
- [32] S. Nose', *A unified formulation of the constant temperature molecular dynamics methods*, *J. Chem. Phys.*, 1984, **81**, 511;
- [33] W. G. Hoover, *Canonical dynamics: Equilibrium phase-space distributions*, *Phys. Rev. A: At., Mol., Opt. Phys.*, 1985, **31**, 1695;
- [34] W. Humphrey, A. Dalke, K. Schulten, *VMD: visual molecular dynamics*, *J. Mol. Graphics*, 1996, **14**, 33–38;
- [35] A. Stukowski, *Visualization and analysis of atomistic simulation data with OVITO—the Open Visualization Tool*, *Modelling Simul. Mater. Sci. Eng.*, 2010, **18**, 015012;
- [36] A. Finney, M. Salvalaglio, *Multiple pathways in NaCl homogeneous crystal nucleation*, *Faraday Discuss.*, 2022, **235**, 56-80;
- [37] A. P. Thompson, H. M. Aktulga, R. Berger, D. S. Bolintineanu, W. M. Brown, P. S. Crozier, P. J. Veld, A. Kohlmeyer, S. G. Moore, T. D. Nguyen, R. Shan, M. J. Stevens, J. Tranchida, C. Trott, S. J. Plimpton, *LAMMPS - a flexible simulation tool for particle-based materials modeling at the atomic, meso, and continuum scales*, *Comput. Phys. Commun.*, 2022, **271**, 108171;

[38] P. J. Steinhardt, D.R. Nelson, M. Ronchetti, *Bond-orientational order in liquids and glasses*, Phys. Rev. B, 1983, **28**, 784

Chapter 7

Behaviour of Potassium Nitrate on Self-Assembled Monolayer surfaces

This chapter explores how self-assembled monolayers, whose nature will be explained in the following section, may alter the nucleation process of potassium nitrate. Previous work^[1] has proved that this system appears to work as an effective catalyst for calcium carbonate. Given the similar geometric structure of the nitrate group to the carbonate group (already stressed in the previous chapters), the idea behind this work was to examine any similarity, or difference, between how the two systems (carbonate and nitrate) respond to the presence of SAMs.

7.1 Introduction

The behaviour of clusters of potassium and nitrate ions in water can be influenced by various factors, including surface chemistry, substrate concentration, solubility, flexibility, and topology. Atomic-scale defects represents a class of nucleant that has not been deeply investigated yet. Work contained in this chapter naturally follows the two previous ones: in Chapter 5, we have tried to nucleate potassium nitrate from homogeneous solution, Chapter 6 tried to add a nucleant to an homogeneous system (KNO₃ slabs). In this chapter, the aim is to investigate the significance of atomic-scale defects in a flexible self-assembled monolayer surface and their effect on the behaviour of ion clusters. We used molecular dynamics simulations to estimate the diffusion coefficients of ion clusters around different topological surface features and obtain ionic radial distribution functions around these features of interest.

7.1.1 Self-Assembled Monolayers (SAMs)

We define a self-assembled monolayer (SAM) as an assembly of organic molecules. These organic molecules are fixed to a surface via strong adsorption. Weak interactions between the chains then organise them with respect to each other.^[2,3] The connection with the base substrate can be weak or strong (proper adsorption) either way that is usually enough to stabilise the system and allow the chain-to-chain interactions to take place. Figure 7.1 shows the classical

structure of a SAM. We can identify the head group (shown in yellow). Common head groups are thiols, silanes, carboxylic acids and other organic moieties with the ability to be functionalised, oxidised-reduced, and protonated/deprotonated.

SAMs are formed through the chemisorption of "head groups" from the vapour or liquid phase onto a substrate, followed by the slow organisation of "tail groups"^[4,5,6]. At low molecular density on the surface, adsorbate molecules form a disordered mass of molecules or an ordered two-dimensional "lying down phase,"^[4] whereas at higher molecular coverage, crystalline or semi crystalline structures form on the substrate surface over minutes to hours.^[7] The "head groups" form on the substrate, while the "tail groups" form in the solution. Nuclei of densely packed molecules form and grow until the surface of the substrate is covered in a single monolayer. Because of van der Waals interactions^[2,8], the monolayer packs tightly, lowering its own free energy.^[2]

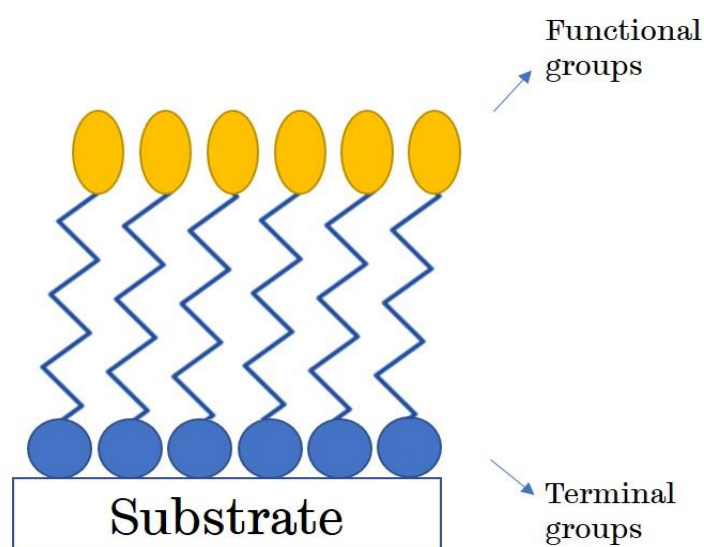


Figure 7.1. Schematic representation of a SAM. Blue balls represents the terminal group, yellow balls the head group, zig-zag lines the organic chains.

It is challenging to characterise surfaces with efficient nucleating qualities, despite the prediction from classical nucleation theory that numerous surfaces should encourage nucleation and crystallisation. Certain surfaces have a significant affinity for the crystallising species and can facilitate nucleation. This might be via an epitaxial matching, in which the developing crystal and substrate have a good lattice fit, or if the surface is charged, its presence can accelerate local supersaturation and speed up the nucleation process. Surface flaws like

faults, pits, or fractures on nucleants may boost localised ion concentrations and encourage nucleus development.

Surface defects can be formed because of "pits" in the underlying substrate and can appear as a vacancy or step defect. In nature, this might be caused by corrosion or erosion of the substrate prior to the assembly of SAMs on the surface^[9]. A vacancy defect is a full offset in the substrate, but a step defect contains a few sequential steps in the offset, resulting in a slope-like structure. Figure 7.2 depicts the two flaws.

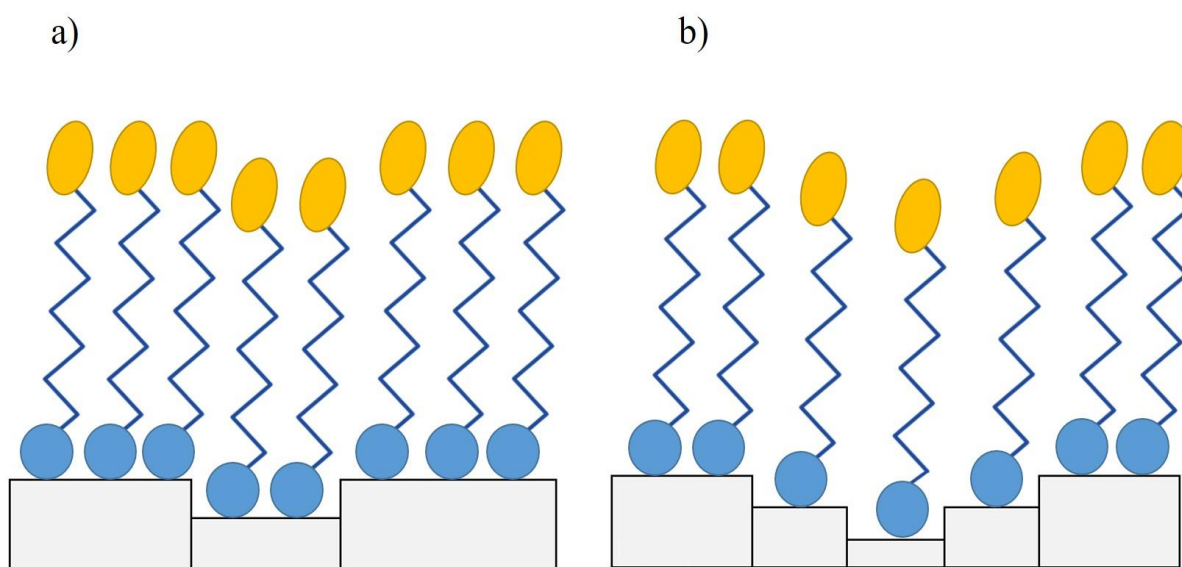


Figure 7.2: Different types of surface defects in SAM surfaces: a) Vacancy and b) Step defect

Since they enable simple modification of surface chemistry, charge, and flexibility in both computational and experimental contexts, self-assembled monolayers (SAMs) provide a versatile platform for studying how surfaces influence the substrate's behaviour.

7.1.2 SAMs with calcium carbonate

SAMs have been proved to accelerate crystallisation in calcium carbonate^[10,11,12]. The addition of nanoscale surface defects has also been analysed and proved to enhance crystallisation, for some bio molecular systems^[13,14]. The process of CaCO_3 nucleation on alkanethiol SAMs as a model system for biomineralisation processes in living things has been extensively studied.^[10] It has been shown^[11] that, for calcium carbonate, some defects (called 'active defects'), can affect the ionic surface diffusion. The authors suggest that these topological features could promote ion clustering and, as a result, increase the local ionic concentration at specific surface

sites. By showing how the presence of microscopic atomic-scale faults may affect a surface's function in the process of heterogeneous nucleation, the study helps to define what makes a surface an effective nucleating agent.

7.2 Methodology

In this work, we followed the same methodology applied in the work of Marinova et al.^[1] Systems were generated in collaboration with V Marinova to produce the input files and force field terms. Details of the force-field will be given in the following sections.

Only one type of defect has been investigated here, the one that the authors have reported to be the most efficient in concentrating calcium carbonate ions. Because potassium nitrate nucleates at much higher concentrations than calcium carbonate, the ratio of potassium nitrate to water has been increased compared to previous values^[1].

7.2.1 Introduction of defects

Surface defects in the monolayers were created by removing atoms from the Au(111) surface. A layer of Au(111) is placed on top of a layer of argon atoms to provide a non-reactive underlayer in which to apply and anchor SAMs chains.

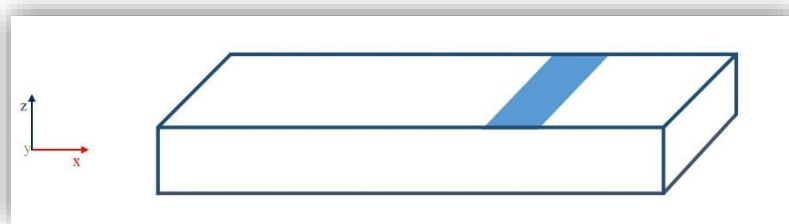


Figure 7.3 Schematic representation of the defect on the xy plane

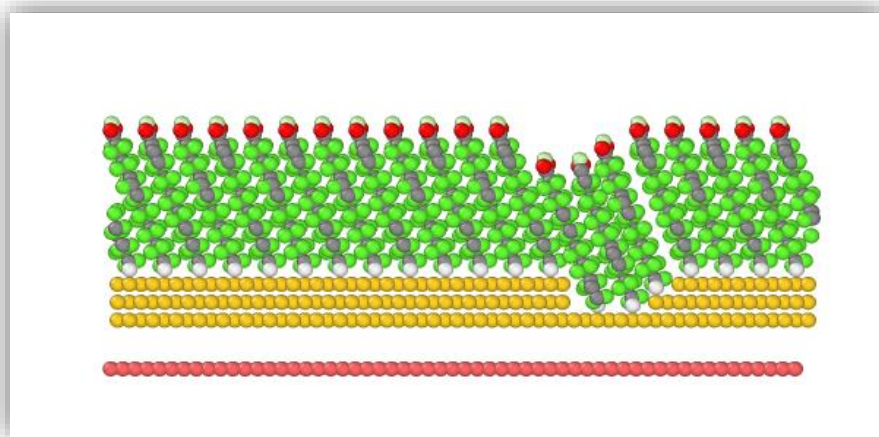


Figure 7.4. Figure 7.4. A vacancy defect in 16-MHDA SAM. The three yellow layers represent gold atoms. Their role is to anchor the SAMs at various heights, thus generating the defect. Underneath it is possible to see a red layer (argon) that operates as a barrier for the molecules and ions moving across the periodic boundaries of box.'

In particular, the role of gold is to create the defects in the SAM: the argon layer remains flat, while the chain connects one another in an offset manner. Figure 7.3 shows the type of vacancy used in this work. This vacancy is extended parallel to the xy plane as shown in Figure 7.4.

The role of the argon layer is to block unwanted interactions between the SAM layer and the solution in the direction of periodicity (z -axis)

The aim was to determine the mean square displacement (MSD) and use it to calculate the average diffusion coefficient for said cluster.

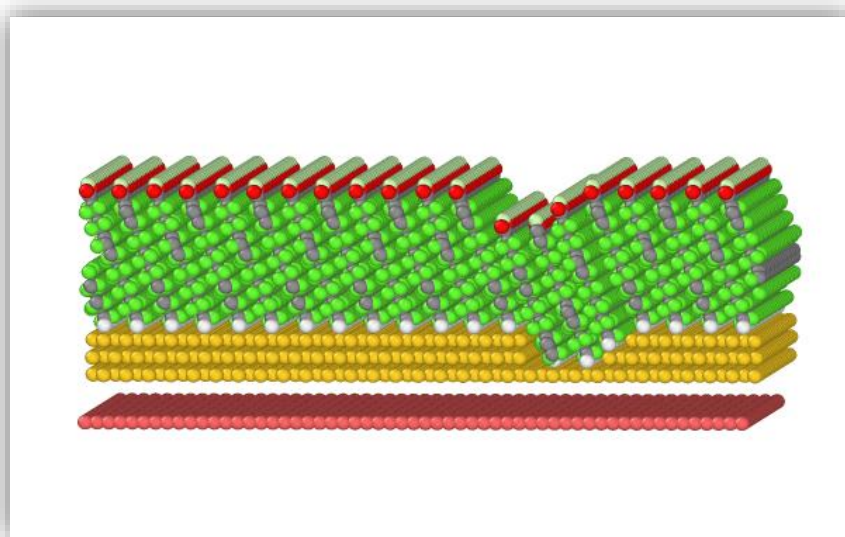


Figure 7.5 Vacancy defect of 16-MHDA SAM on the xy plane

7.2.2 Simulation set-up

We used, as a building block for the SAM structure, chains of 16-mercaptohexadecanoic acid, whose chemical formula is $\text{HS}(\text{CH}_2)_{15}\text{COOH}$ as shown in Figure 7.5:

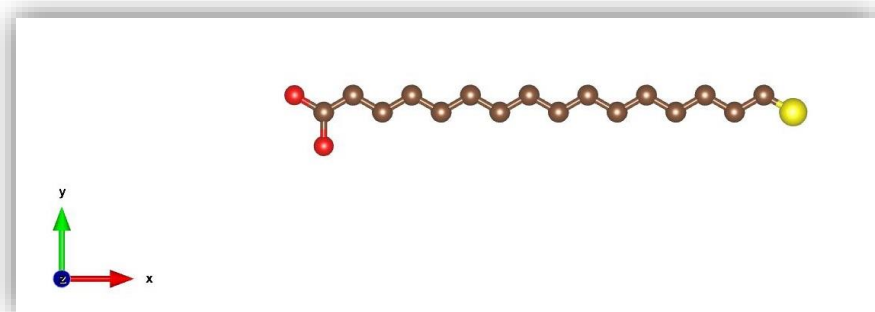


Figure 7.6 Chain of 16-mercaptohexadecanoic acid

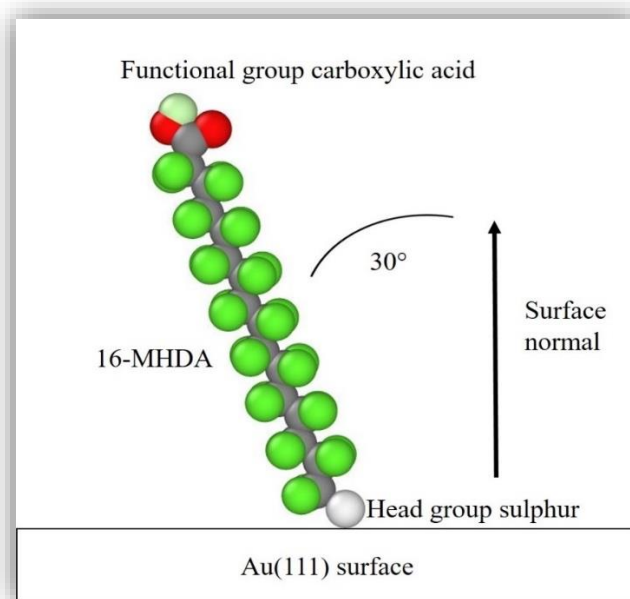


Figure 7.7 Single chain of 16-mercaptohexadecanoic acid on a SAM surface set-up

340 alkanethiol molecules were used to create self-assembled monolayer surfaces on an $80 \times 80 \text{ \AA}$ grid on an Au(111) surface utilising 16-MHDA as a building block. The 30 degree angle of the chains with respect to the normal to the surface plane (shown as the z -axis in Figure 7.2) was maintained throughout the system^[15,16] In the xy -plane, a gap of 4.98 \AA was maintained between the sulphur atoms. Figure 7.3 show a cross-section of the defect in the xz -plane,

whereas Figure 7.4 and Figure 7.5 show a schematic of the defect running parallel to the y-axis.

A box of potassium nitrate in water solution has been placed about 5 nm above the SAM surface. Surface defects were created by removing underlying gold atoms, resulting in a vacancy defect. Figures 7.8(a) and 7.8(b) show the two SAM surfaces.

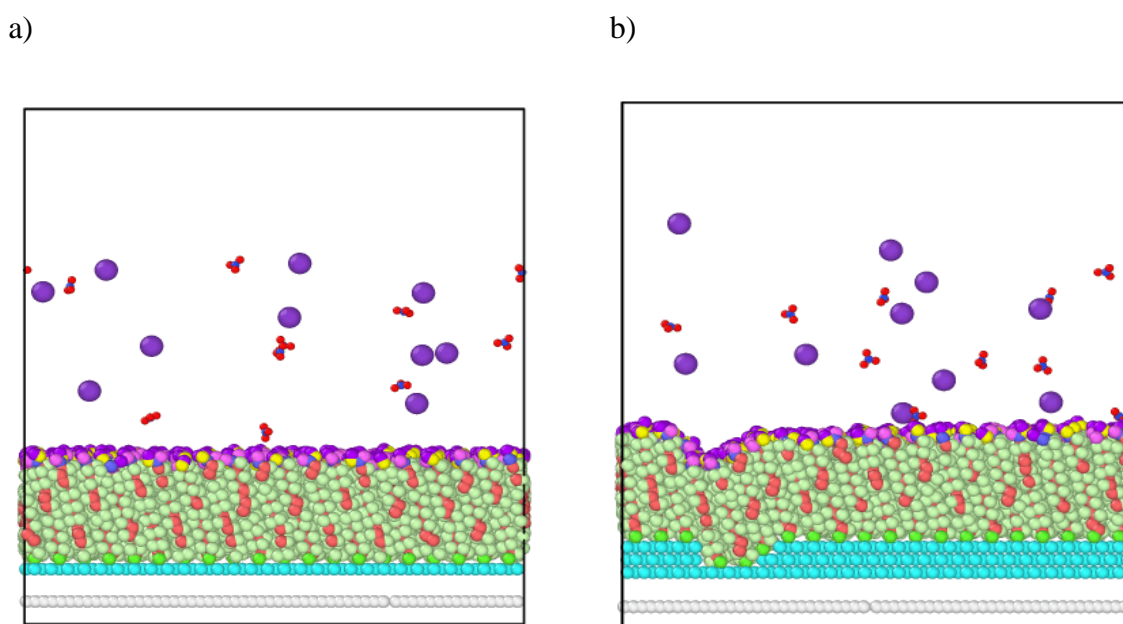


Figure 7.8 a) Flat SAM surface and b) Vacancy defect SAM surface with a box of water and Potassium Nitrate. Water is not displayed.

7.2.2.1 Force-field parameters

The conventional ANTECHAMBER process was used to parametrise the organic component, the chains of 16-MHDA, in line with the AMBER force field.^[17,18,19] The neutral parametrisation of the chains means that the functional carboxylic groups are uncharged ($-\text{COOH}$). The pH of the majority of experimental settings is one where we would expect the functional groups to ionise ($-\text{COO}^-$) but the same number of potassium ions has been added to the simulation box to neutralise the charges. The main focus of this work remains to study how surface flexibility works in conjunction with variable surface topography. We can thoroughly examine the impact of these factors by preventing strong Coulombic interactions that might cloud the interpretation of the data by simplifying the surface chemistry. The overlap between 16-MHDA and the Au under-layer at faults was avoided via non-bonded Au interactions.^[20] For those atoms, the interactions were estimated using the typical Lorenz-Berthelot mixing

rules.^[21, 22] The Lorenz-Berthelot mixing rules were also applied to generate interactions between the 16-MHDA chains and water, as well as interactions between the 16-MHDA chains and the oxygen on the nitrate ion. AMBER carboxylic C-atom interactions were used to simulate the non-bonding interactions between SAM chains and nitrogens from the nitrate group. Finally, non-bonded interactions between the carboxylic oxygens in the SAM functional group and potassium ions were parameterised using the procedure outlined by Freeman et al^[23].

7.2.2.2 Molecular dynamics set-up

Molecular dynamics (MD) simulations were performed using both the DL_POLY 4^[32] and LAMMPS^[24,25] codes with a time step of 1 fs and a PPPM^[26] long range Coulombic interactions solver with an accuracy of 1.0×10^{-5} . All non-bonded interactions were subjected to a cut-off of 9 Å. Simulations were carried out in the NVT ensemble using a Nosé-Hoover thermostat^[27,28] at 300 K and a relaxation time of 200 ps. All the configurations have been built using Packmol^[33].

7.2.2.2.1 SAMs-water simulations

Both flat and defective SAMs surface were equilibrated with a box of water. The simulations were run for an initial period of 200 ps, to allow the system to relax and the water to equilibrate its density. The simulation was then restarted for a further period of 2 ns.

7.2.2.2.2 Ion cluster at SAMs defect in water

Clusters of potassium nitrate were positioned close to the SAM surface and run as MD simulations. Simulations were run with varying sized clusters from 10 formula units up to 50 formula units, as reported in Table 7.1 (which gives the concentrations for the various solutions).

Initially the cluster structure was relaxed for 100 ps in water. The next step was running the full configuration of flat/defective SAMs and the solution for 0.5 ns (which is referred to as the

‘initial study’ in the following section) and then for a total of further 3.5 ns (referred to as ‘further studies’).

Table 7.1 Concentrations expressed in number of moles per litre of solution for the boxes containing different amount of KNO_3

	Molality (number of moles of solute (n)/mass of solvent (kg))
10 KNO_3	0.032
20 KNO_3	0.063
30 KNO_3	0.095
40 KNO_3	0.127
50 KNO_3	0.159

7.2.3 Diffusion coefficient calculations

A diffusion coefficient for the ions was calculated for the charged system using a mean squared displacement (MSD). Figure 7.9 shows the diffusion coefficient derived from the slope of a matching MSD plot for the time step section between 2 ns and 30 ns in each production run. We did an interquartile range (IQR) analysis on the 3D MSD values across the cluster to derive an average cluster diffusion coefficient that is consistent with the overall cluster behaviour. Figure 7.10 shows an example of this approach. The graphic shows the mean value of the cluster diffusion coefficient (in red) as well as all individual ion diffusion data points (in blue). The diffusion of many ions that are orders of magnitude greater than the dataset's median (shown in green) would distort the mean cluster diffusion. These points belong to individual ions that have separated from the cluster and must thus be omitted from the ionic cluster's diffusion coefficient calculation. In our results, we employ the IQR (in brown) to identify which points are to be omitted and give the revised mean (in orange). OVITO was used to create the simulation pictures in this study^[34]. Python 3 was used for trajectory analysis^[35].

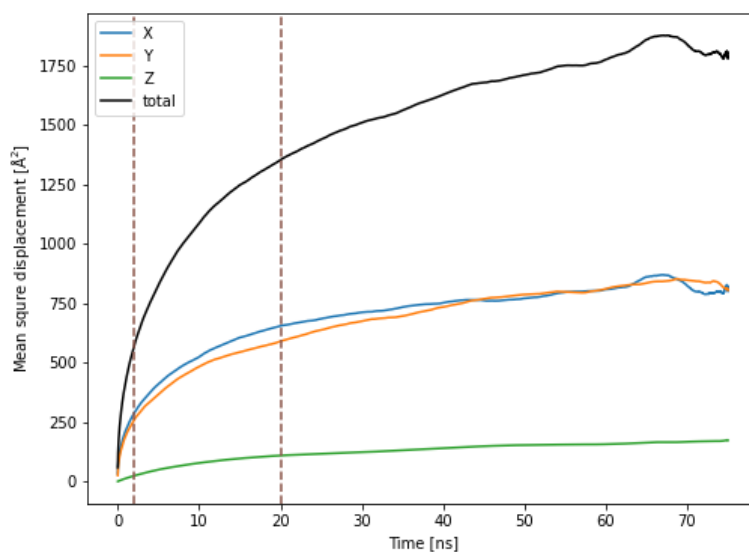


Figure 7.9 Example of an MSD plot of an ion broken into x -, y - and z -components. The region used for the calculation of diffusion coefficients is marked in red.

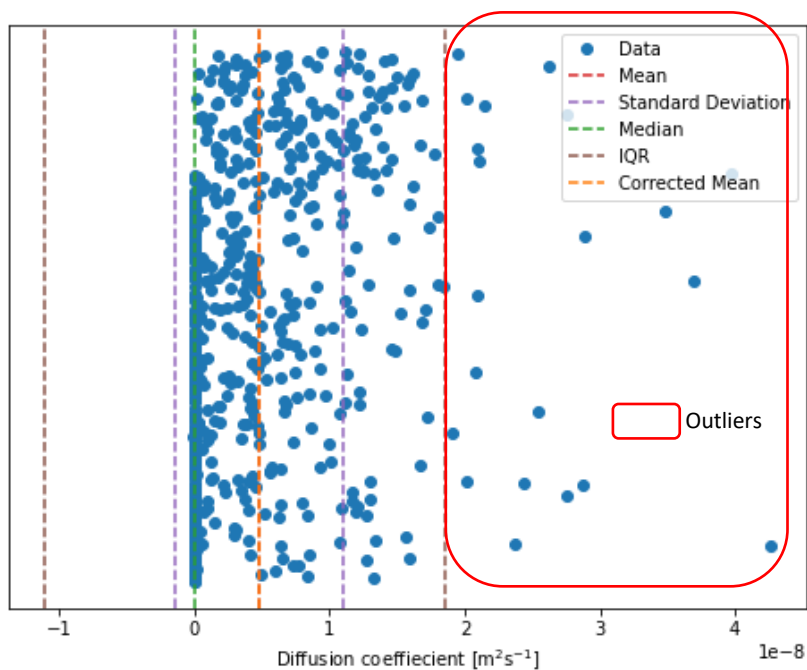


Figure 7.10 Interquartile range analysis on the diffusion coefficients of ions within a cluster. The analysis identifies some outliers, as marked on the plot, which are removed from the mean cluster diffusion coefficient to obtain a corrected mean.

7.3 Results

The work here is divided into five sections: first, we have the study on the neutral SAMs surface, divided into three sections, two preliminary studies for the neutral flat and defective studies and the follow-up for the defective surface. The final section contains the results for the charged SAMs surfaces (flat and defective).

7.3.1 Neutral SAMs, Preliminary Studies - Flat SAM

This section is dedicated to the preliminary study regarding flat SAMs and a single vacancy configuration SAMs.

Simulations have been performed using DL_POLY 4 for a short amount of time, equal to 0.5 ns. The interaction of potassium nitrate with the SAM can be seen graphically in Figure 7.11. The whole solution relaxed onto the SAM surface, as shown in Figure 7.11(a), removing the vacuum gap from the starting configuration. Potassium nitrate ions relax with the aqueous solution in all configurations, coming closer to the SAM surface. However, there is not a noticeable grouping of ions on the SAM surface.

Potassium nitrate ions were concentrated in the bottom half of the fluid in the initial setup for the simulation with 10 Potassium Nitrate ions (Figure 7.11(b)), bringing them closer to the SAM surface. By doing this, the intention was to provide the opportunity for the ions to stay close to the surface rather than drift off. Despite the closer starting condition the ions still did not cluster on the surface but remain in the solution. This is most likely because the ions and SAM surface interact only weakly, and as a result, the ions have little reason to travel towards the surface from elsewhere in the solution. Visually, as seen in Figure 7.12, as nitrate approaches the surface, the oxygen molecule will interact with the hydrogen in the functional group, but potassium has a stronger interaction with nitrate and displays no contact with the surface.

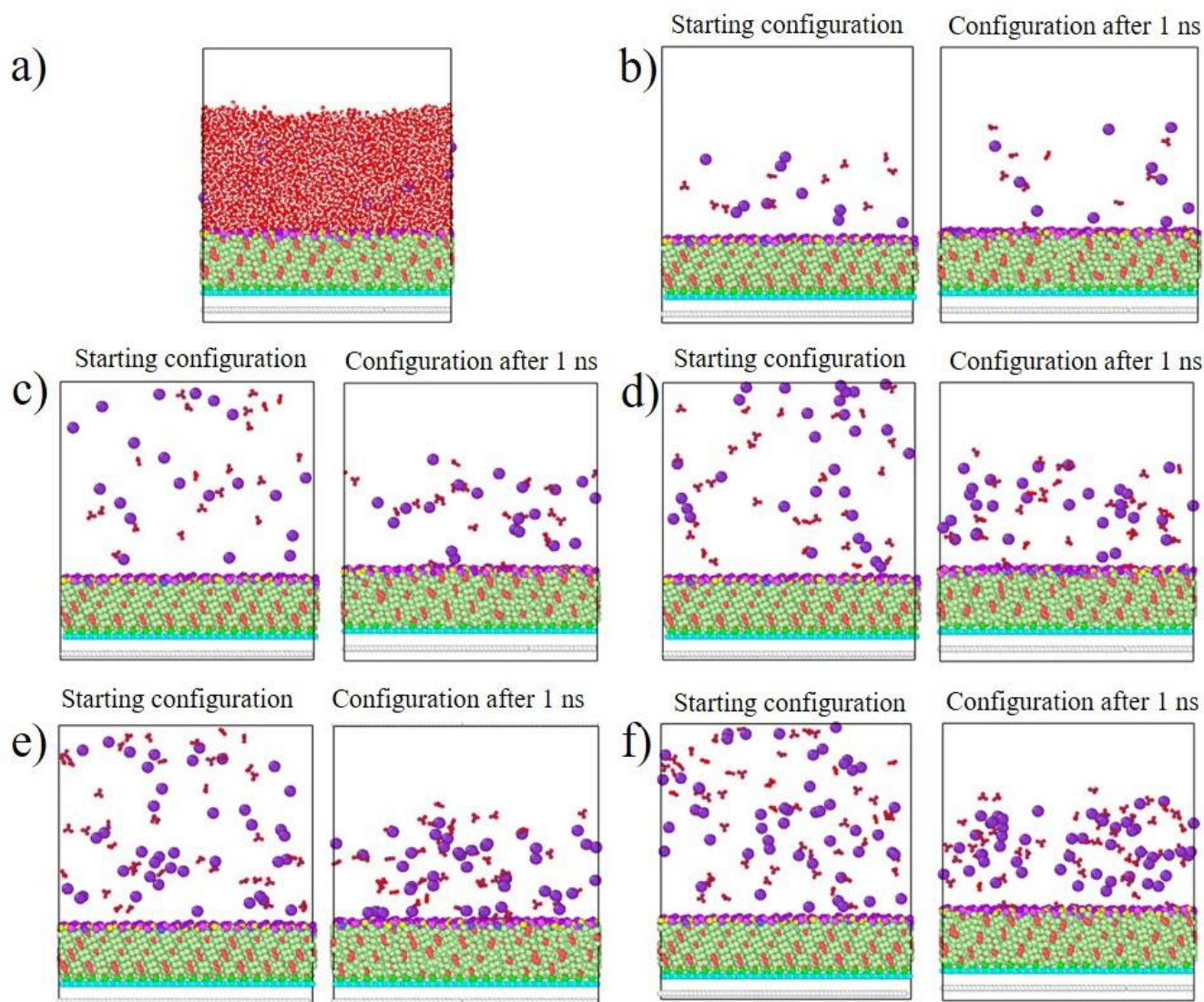


Figure 7.11: a) Configuration of system after 1 ns with water visualised and configurations containing b) 10, c) 20, d) 30, e) 40, f) 50 Potassium Nitrate Ions before and after 1 ns. For figures b) to f) water molecules not shown for clarity.

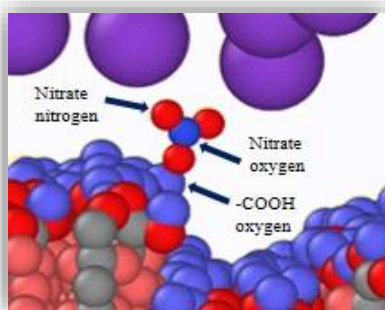


Figure 7.12 Nitrate on the SAM surface

7.3.1.1 Analysis of the radial distribution function (RDF)

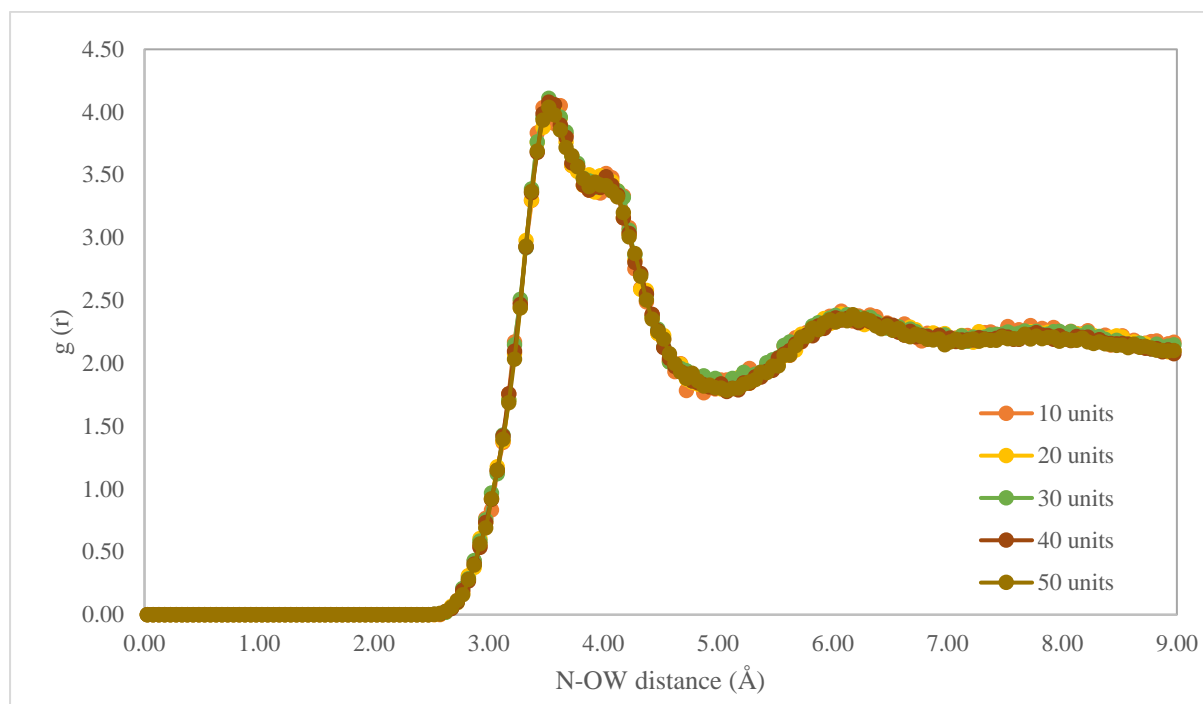


Figure 7.13 RDF of the interaction between nitrogen of the nitrate group and oxygen of the water

Figure 7.13 shows the RDF of the interaction between nitrogen of the nitrate and oxygen of the water. It shows little to no variation with the concentration through the simulation. All the curves appear to have the same trend. This means that the entire nitrate appear to be as solvated as it would be in a pure solution.

Figure 7.14 shows the RDF for the nitrogen of the nitrate group to the oxygen of the carboxylic acid. The centre of the peak is constant and the shape is the same through all the concentrations although the intensity appears to vary randomly with the concentration, which suggests no link between the concentration and surface interaction. Integration of the first peak of the RDFs confirms numerically what is possible to see from the pictures. Coordination with the water seems unchanged with respect to pure solution and coordination with respect to the surface is close to zero. These results point to random variance, which is most likely caused by nitrate passing close to the surface rather than significant interactions.

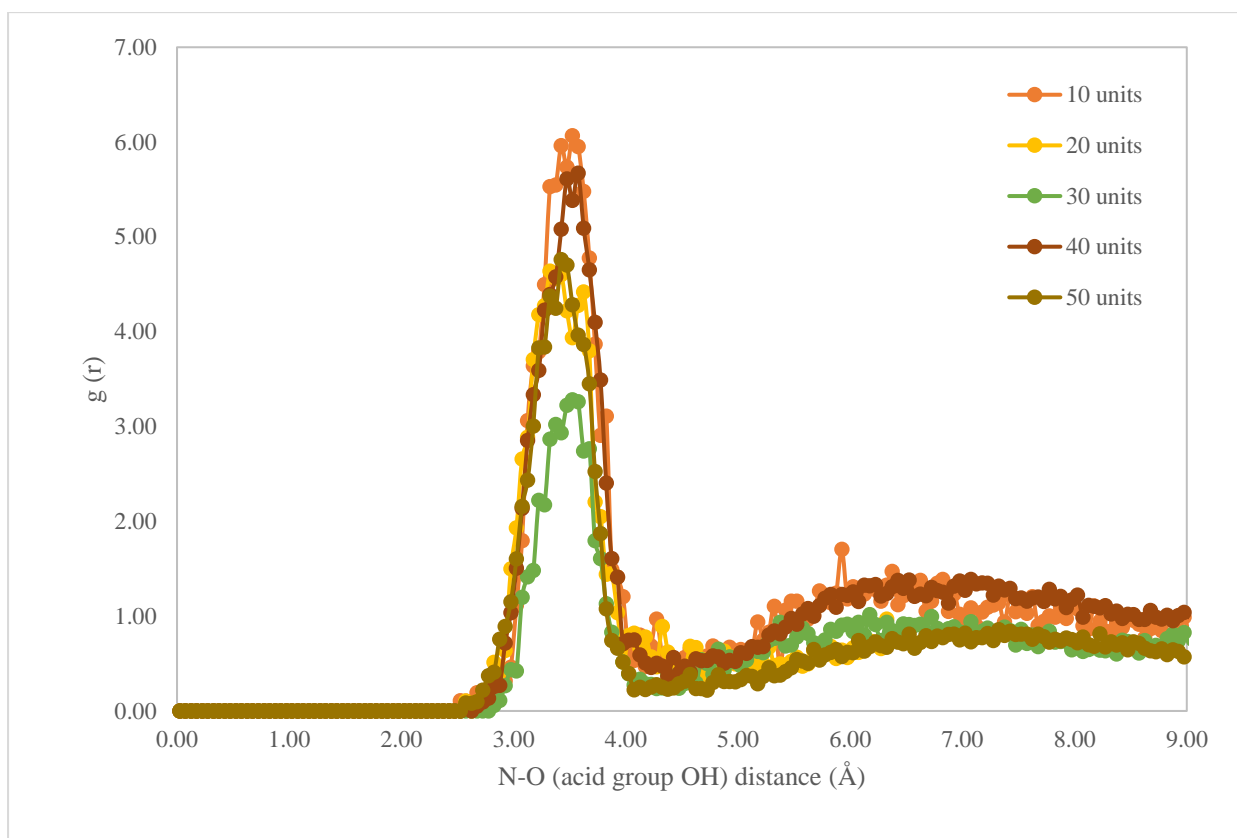


Figure 7.14 RDF of the interaction between nitrogen of the nitrate group and oxygen of the carboxylic head group of the 16-MDHA chains

Table 7.2 Coordination number for the nitrogen of the nitrate group in respect of the oxygen of the water and oxygen of the carboxylic head group of the 16-MDHA chains, for the various concentration solutions.

Pair	Number of potassium nitrate ions in configuration	Coordination number
N-OW	10	11.169
	20	10.733
	30	10.628
	40	11.076
	50	10.969
N-oh	10	0.0106
	20	0.0094
	30	0.0062
	40	0.0110
	50	0.0104

7.3.2 Neutral SAMs, Preliminary Studies - Defective SAM

The visual behaviour of potassium nitrate with the defective SAM is shown in Figure 7.15. To stimulate contact between the ions and the SAM surface, the potassium nitrate ions were concentrated closer to the SAM surface in all configurations. Regardless of the beginning configuration, the ions disperse throughout the water solution in all situations, with the SAM having minimal effect on their ultimate placements. There is also no discernible grouping of ions on the SAM surface. This is the same behaviour as the flat surface, demonstrating that the vacancy defect has no additional influence at this stage of the simulation.

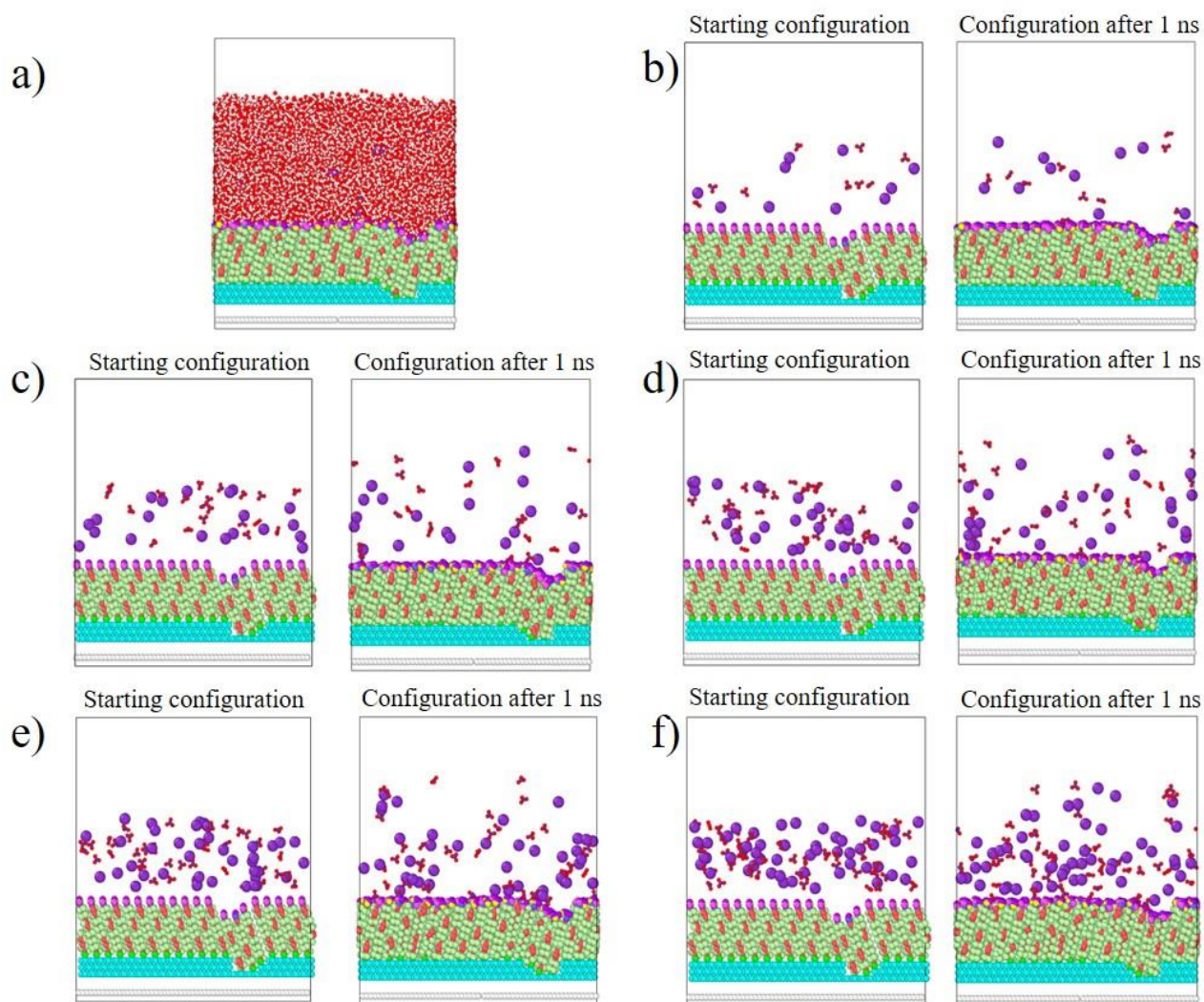


Figure 7.15 (a) Configuration of system after 0.25 ns with water visualised and configurations containing b) 10, c) 20, d) 30, e) 40, f) 50 Potassium Nitrate Ions before and after 0.25 ns. Except for (a), which depicts the whole system, the water molecules have been eliminated for clarity.

7.3.2.1 Analysis of the radial distribution function (RDF)

The RDF of the interaction between nitrogen and water oxygen is shown in Figure 7.16. It suggests minimal to no fluctuation with concentration throughout the simulation. The curves all appear to follow the same pattern. This indicates that all of the nitrate seems to be solvated as it would be in a pure solution.

Figure 7.17 depicts the RDF for the nitrogen of the nitrate group to the oxygen of the carboxylic acid. Despite the fact that the intensity appears to change randomly, the peak's centre and shape stay similar across all concentrations: for each concentration, in a random matter, the nitrogens get closer to and further away from the surface. Again, the numerical confirmation of what is visible in the images comes from the integration of the first peak of the RDFs. Coordination with water appears to remain unchanged as compared to pure solution, and coordination with the surface appears to be almost non-existent, for the time frame analysed.

Table 7.3 Coordination number for the nitrogen of the nitrate group in respect of the oxygen of the water and oxygen of the carboxylic head group of the 16-MDHA chains, for the various concentration solutions.

Pair	Number of potassium nitrate ions in configuration	Coordination number
N-OW	10	11.025
	20	11.200
	30	11.199
	40	11.010
	50	11.219
N-oh	10	0.0066
	20	0.0039
	30	0.0115
	40	0.0125
	50	0.0065

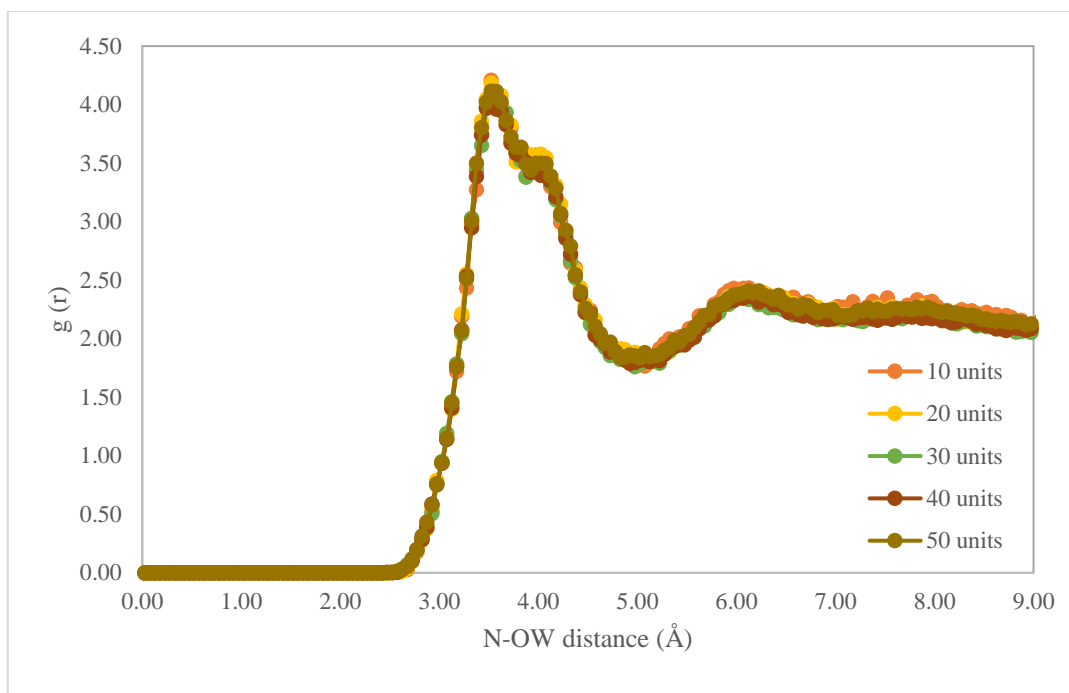


Figure 7.16 RDF of the interaction between nitrogen of the nitrate group and oxygen of the water

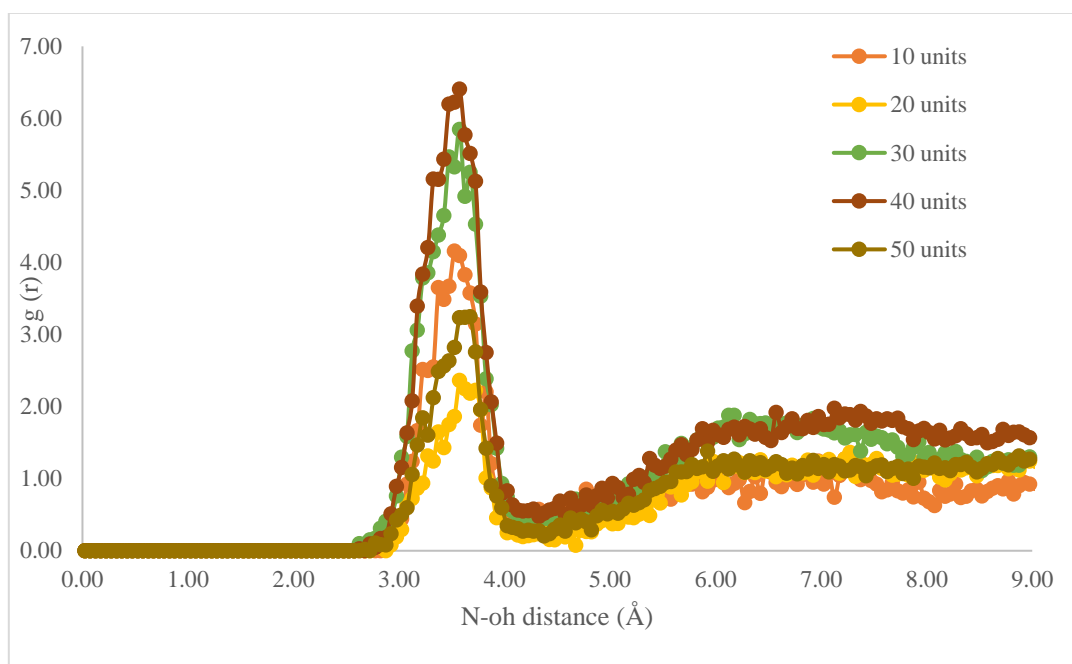


Figure 7.17 RDF of the interaction between nitrogen of the nitrate group and oxygen of the carboxylic head group of the 16-MDHA chains

7.3.3 Further studies on defective SAM

To provide more confidence in the results of the previous section, some of the simulations were transferred to LAMMPS and run for a total of 3 ns. Figure 7.18 shows the starting configuration selected, the highest concentration previously studied with a defect.

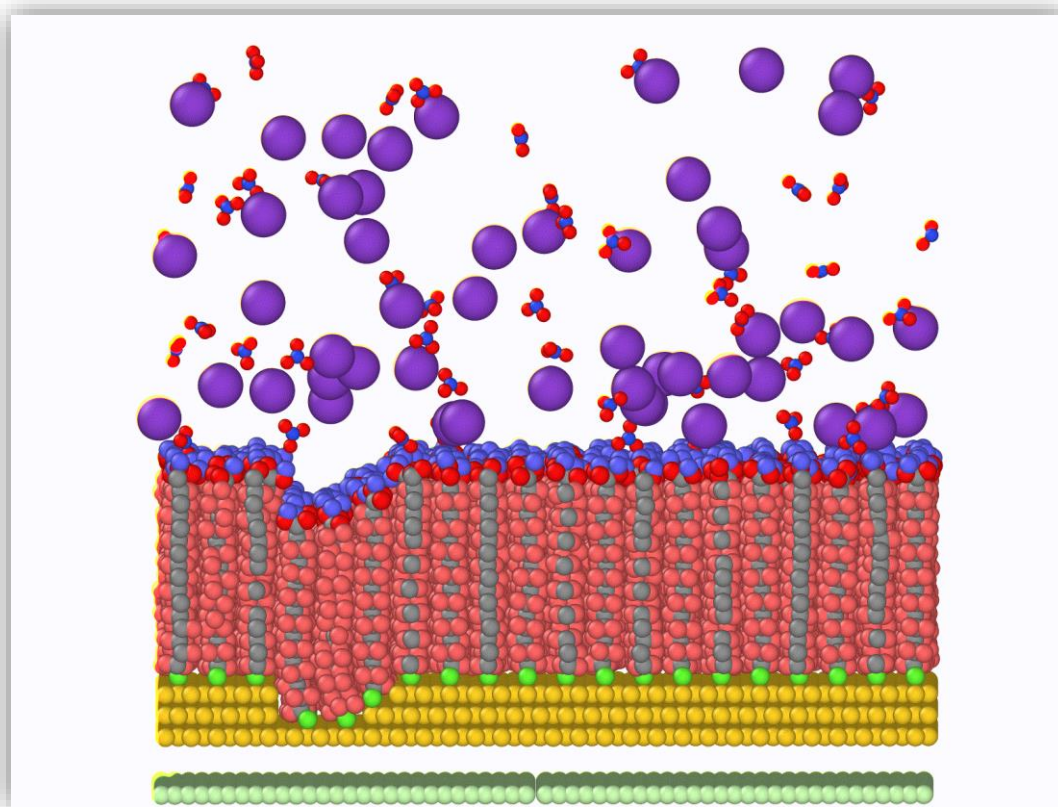


Figure 7.18 Starting configuration, in LAMMPS, for defective SAMs surface and 50 KNO_3 . Picture does not include water.

7.3.3.1 Analysis of the radial distribution function (RDF)

Figure 7.19 shows the RDF of the interaction nitrogen of the nitrate-oxygen of the water, while Figure 7.20 shows the RDF of the interaction nitrogen of the nitrate-oxygen of the carboxylic head group. Table 7.4 shows the coordination number obtained by the integration of the first peak of each RDF. Comparison with the first 0.5 ns of simulations shows that though the simulation the affinity of the nitrate group for the SAM surface does increase quite drastically. As we have noticed for the pure solution case, even this time the nitrogen can accommodate a maximum number of oxygens that does not change (nine). What changes is the nature of those

oxygens: when there is no interaction with the surface the nitrogen of the nitrate is fully hydrated, as it approaches the surface it starts pushing this water away, getting closer and creating ‘bonds’ with the surface.

Table 7.4 Coordination number for the nitrogen of the nitrate group in respect of the oxygen of the water and oxygen of the carboxylic head group of the 16-MDHA.

	Coordination number		
	K-OW	K-oh	total
50 KNO3	5.7	3.3	9

7.3.4 Charged SAMs

Based on the results obtained in the previous section, which showed little interaction between the neutral SAM and the nitrates, it was decided to consider the role of the head group’s charges in nucleation. This is the equivalent of changing the pH of the solution, experimentally.

All the–COOH head groups were artificially deprotonated for the simulation and the appropriate amount of potassium ions has been added to neutralise the surface. As for the previous case, simulations were performed with a flat and a defective SAMs surface. The results obtained for each simulation set up will be discussed in details in the following sections.

7.3.4.1 Flat SAM

To analyse nucleation in the system, a cluster of potassium nitrate was used as a starting point for the simulations, as shown in Figure 7.21. As can be seen from Figure 7.22 the cluster does not remain clustered: all the ions are generally diffusing freely through the solution, and no longer in one unit.

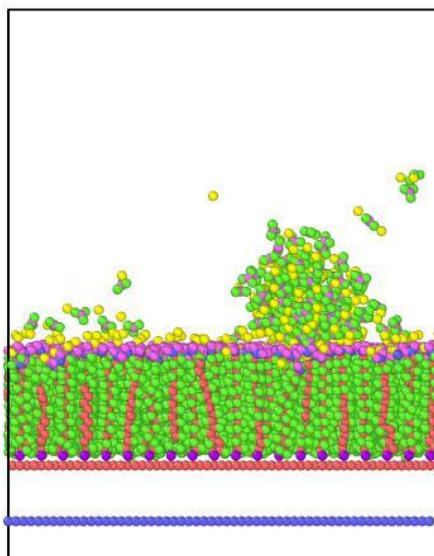


Figure 7.19 Clustered KNO_3 on a flat, charged, SAM surface. Starting configuration for the simulation. Water not displayed for clarity.

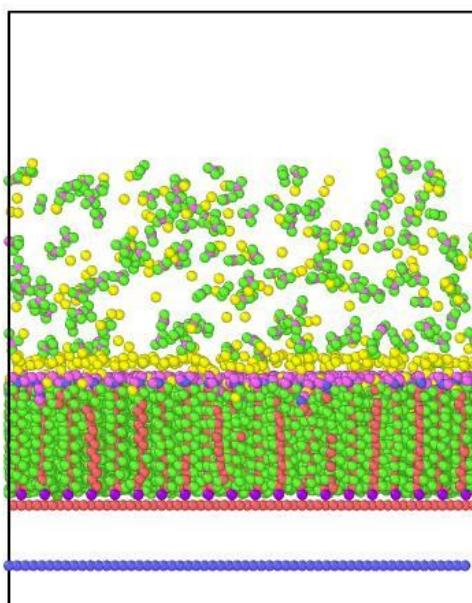


Figure 7.20 Cell of Figure 7.19 after 30 ns of nvt run. Water not displayed for clarity.

7.3.4.1.1 Analysis of the radial distribution function (RDF)

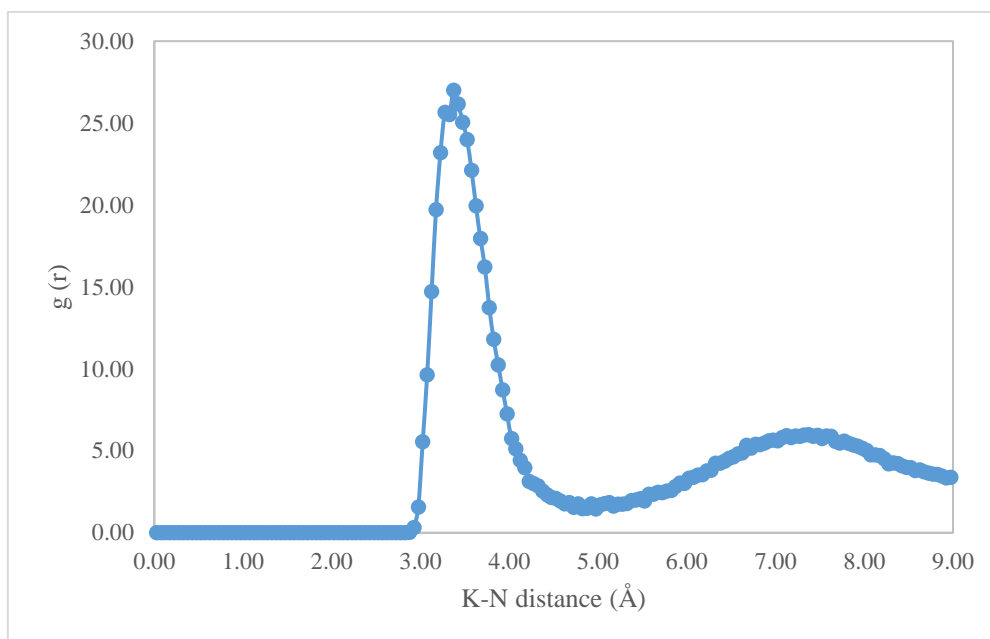


Figure 7.21 RDF for the potassium to nitrogen interaction for the solution on top of a flat SAM surface.

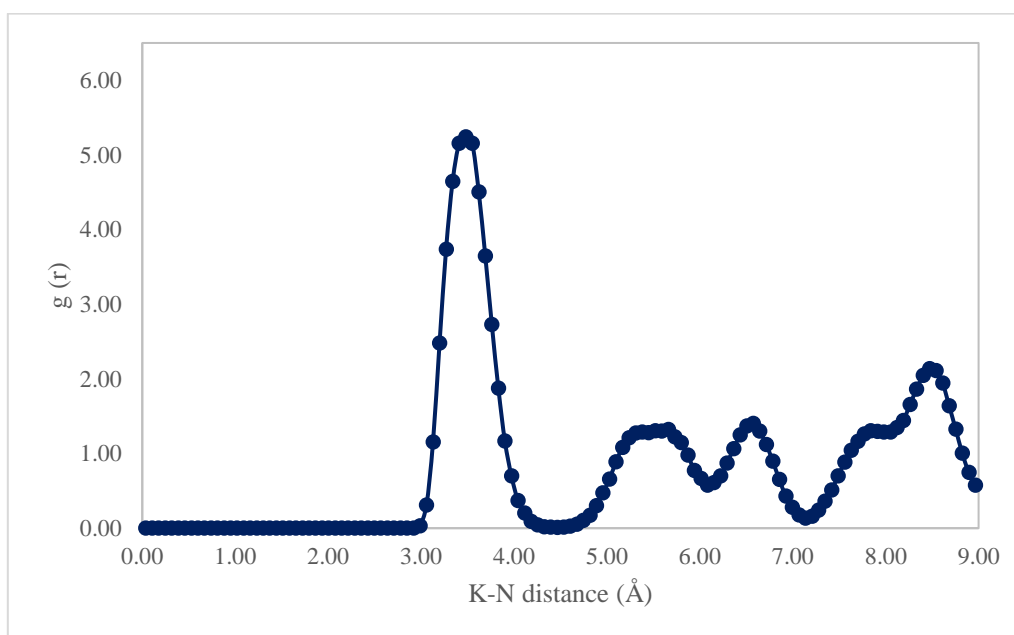


Figure 7.22 RDF for the potassium to nitrogen interaction for potassium nitrate – aragonite.

The analysis of the interaction of the potassium ions with the nitrogens in the solution shows a clear, neat, single peak. This proves that each potassium is not able to expand its organisation of the surrounding water further than a single shell. The peak is centred at 3.5 Å, and presents a shape similar to the one of potassium in an aragonitic system, as it is possible to see by comparison to Figure 7.24, although none of the longer-range structure is present.

7.3.4.1.2 Mean-square displacement analysis

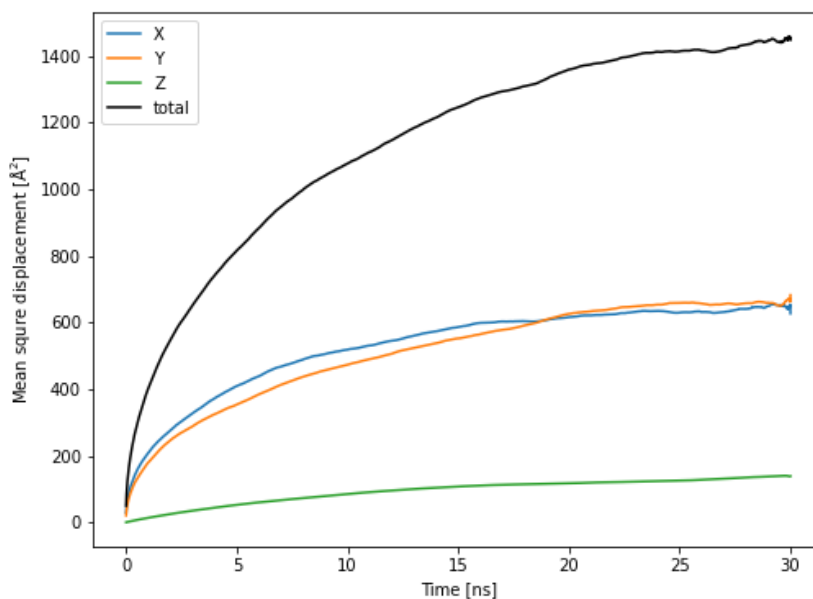


Figure 7.23 MSD of K ions on a flat SAM surface. The blue line represents the x-, the orange line the y- and the green line the z- components. The black line shows the total MSD

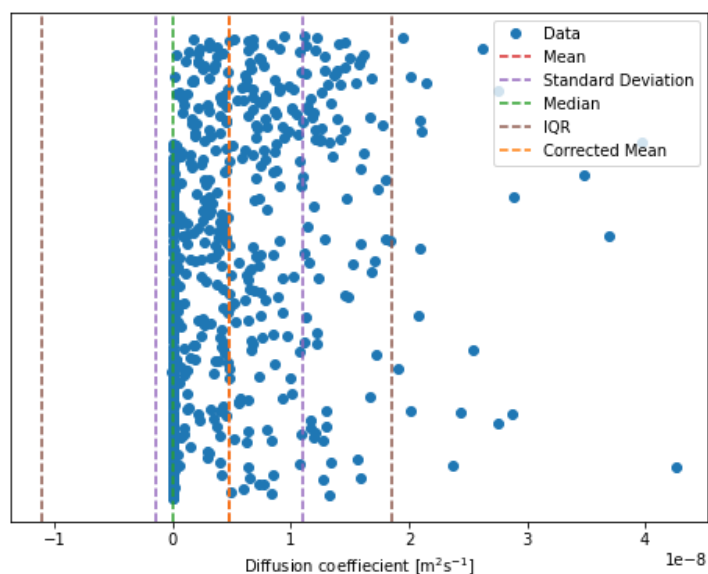


Figure 7.24 IQR analysis for K ions on a flat SAM surface. Blue dots represent the data set, red dashed line the mean, purple dashed line the standard deviation, green dashed line the median, brown dashed line the interquartile range and orange dashed line the corrected mean

Figures 7.23 and 7.24 show the analysis on the potassium ions. The mean square displacement shows that the particles in the system do not have a large degree of freedom in z. They primarily move in the xy plane and the curves for the two axis plateau after approximately 10 ns. In this period of time, on average, the particles do move, otherwise, after 15 ns they do not have longer range diffusion. We can imagine the whole surface as being divided into four quadrants and

the majority of the particle composing a ‘cluster’ appear to be confined in that region, it appears as if they are limited in this energetic well.

Figure 7.24 confirms that there are only a few ions able to freely escape the surface; the majority cannot diffuse away from the surface. This behaviour is in agreement with what shown in literature for calcium carbonate. Figure 7.25 and 7.26 show the analysis on the nitrogen ions.

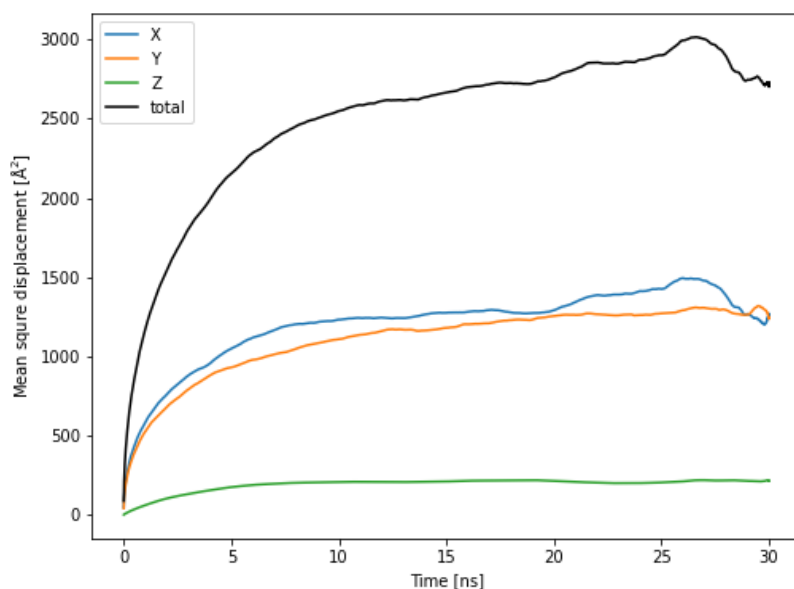


Figure 7.25 MSD of nitrogen ions on a flat SAM surface. The blue line represents the x-, the orange line the y- and the green line the z(-) components. Black line shows the total MSD.

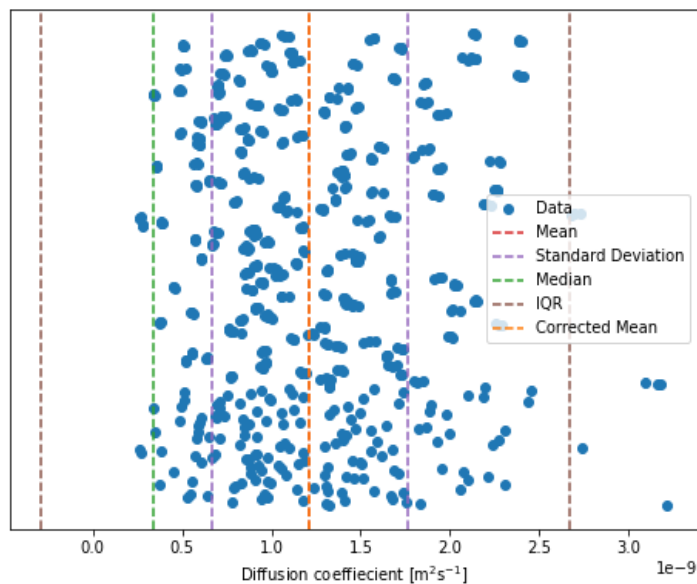


Figure 7.26 IQR analysis for nitrogen ions on a flat SAM surface. Blue dots represent the data set, red dashed line the mean, purple dashed line the standard deviation, green dashed line the median, brown dashed line the interquartile range and orange dashed the correct mean

The nitrate ions show an enhanced tendency to diffuse along the z-axis compared to the potassiums. They appear to move faster and have longer range diffusion. The potassium ions appear to have some clustering and are restricted in moving in z. This suggests that some layering of ions i.e. stern layer is occurring but the layer is mobile on the xy plane.

7.3.4.1.3 Cluster analysis

In order to understand the behaviour of potassium nitrate in solution, cluster analysis has been performed. Table 7.5 shows the average coordination for the ions in solution, which is less than 2. It means that, on average, each potassium ion connects and loses connection with another potassium ion, similarly to the previous case. Table 7.5 also reports the number of ions included in the largest finite cluster, which represents less than 3% of the total ions in solution. On the other hand, almost 50% of the total ions appear to form no connection at all.

Table 7.5 Statistics about the cluster connection in a potassium nitrate solution sitting on a flat SAM surface.

	Total number	Percentage
Average Coordination	1.71	-
Largest finite cluster	12.69	2.6%
Ion with no connections	206.10	42%

The average radius of gyration appears to increase over time as it is possible to see from Figure 7.27. After it reaches a maximum, it tends to fluctuate regularly. The behaviour of the curve beyond 30 ns suggest that there might be a large cluster breaking into two and reforming.

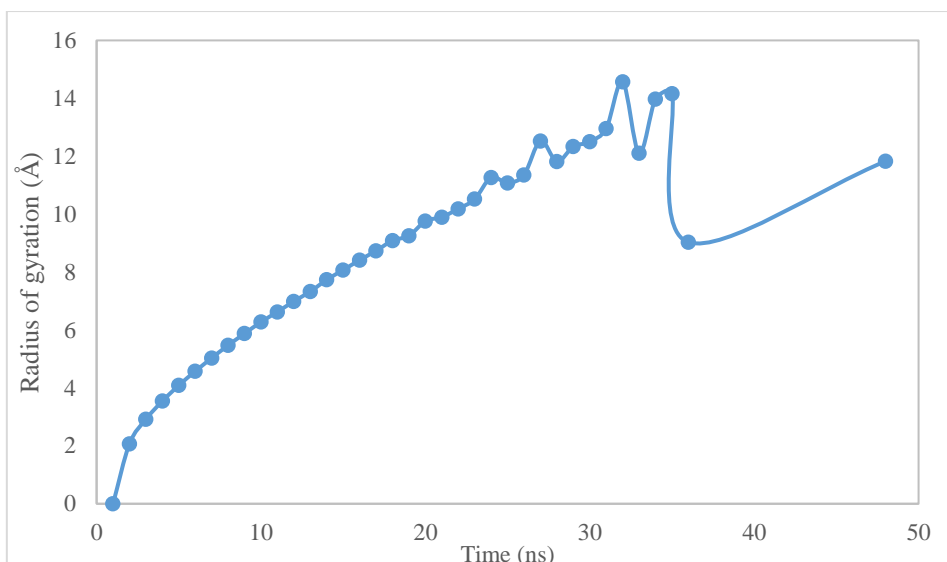


Figure 7.27 Radius of gyration over time

Figure 7.28 shows the logarithm of the number of connections as a function of the radius of a cluster, it presents a slope of 1.6, which indicates that the cluster have a low density 2-D shape, and can be imagined as a flat surface with holes and gaps.

The behaviour of the radius of gyration over time can be interpreted with the potassium ions approaching the surface and spreading over it. This causes the formation of what can be considered a flat cluster, which eventually separates in two different units. The behaviour can also come from the drifting of said ions in and out the surface.

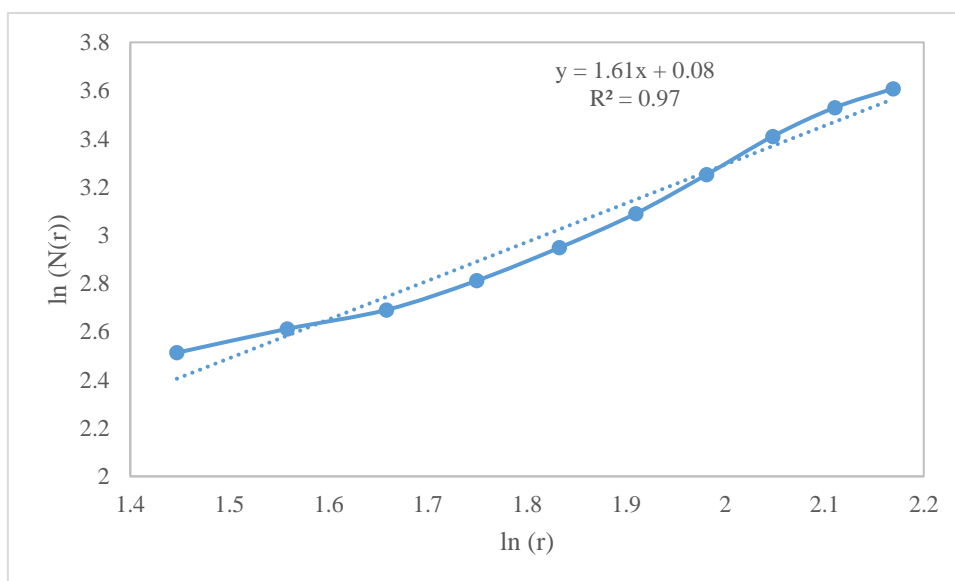


Figure 7.28 Fractal dimension of the average finite cluster in solution for a solution of KNO_3 sitting on a flat SAM surface

Figure 7.29 shows the average number of potassium in a cluster versus its probability of existence (normalised). The probability, overall, decreases exponentially, which is good agreement with the expected behaviour of a system following the classical nucleation theory.

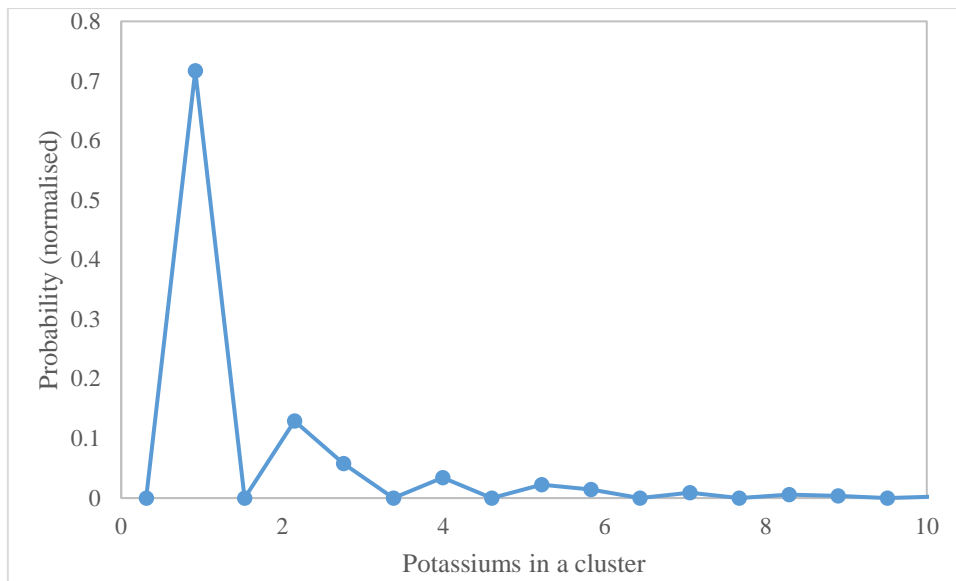


Figure 7.29 Number of potassium in a cluster vs probability (normalised)

7.3.4.2 Defective SAM

As can be seen in Figure 7.31, again, the cluster does not remain unchanged. All of the ions can be seen approaching the surface and generally diffusing through the solution.

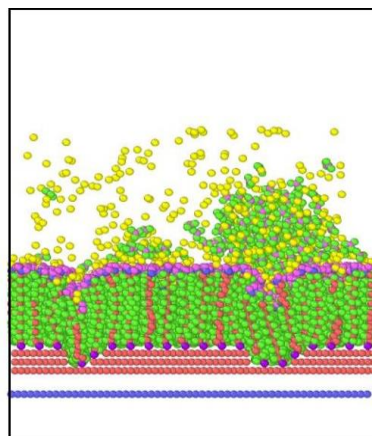


Figure 7.30 Clustered KNO_3 on a defective, charged, SAM surface. Starting configuration for the simulation

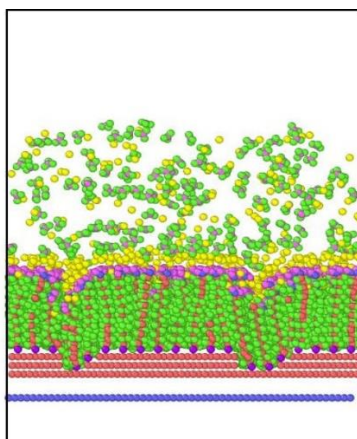


Figure 7.31 Cell of Figure 7.30 after 30 ns nvt run

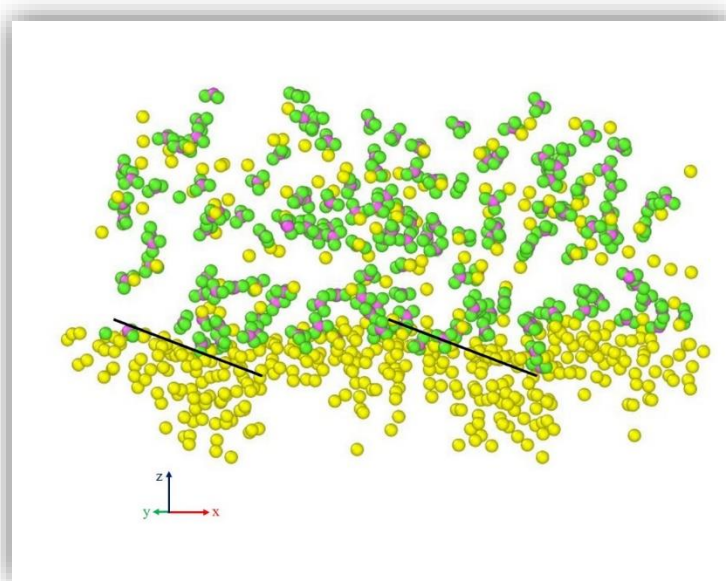


Figure 7.32 Cell of Figure 7.30 after 30 ns nvt run. Only KNO_3 displayed. Black line show the defects on the xy plane

7.3.4.2.1 Analysis of the radial distribution function (RDF)

The analysis of the interaction of the potassium ions with the nitrogens in the solution shows a double peak not as neat as the previous case. Again, this shows that each potassium is not able to expand its organised coordination further than a single shell. The top-split peak, in this case, presents a shape similar to the one of potassium in a trigonal ferroelectric system, as it is possible to compare with Figure 7.34. The RDF of the solution on the SAM surface shows a first peak that is much shorter than the crystalline system, but also compared with the flat-SAM.

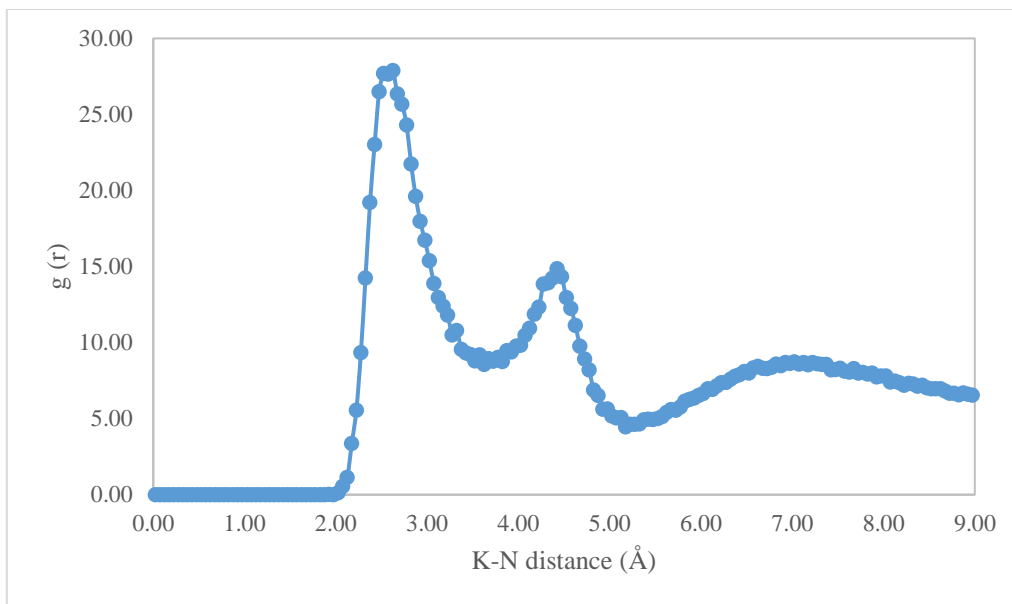


Figure 7.33 RDF for the potassium to nitrogen interaction for the solution on top of a defective SAM surface.

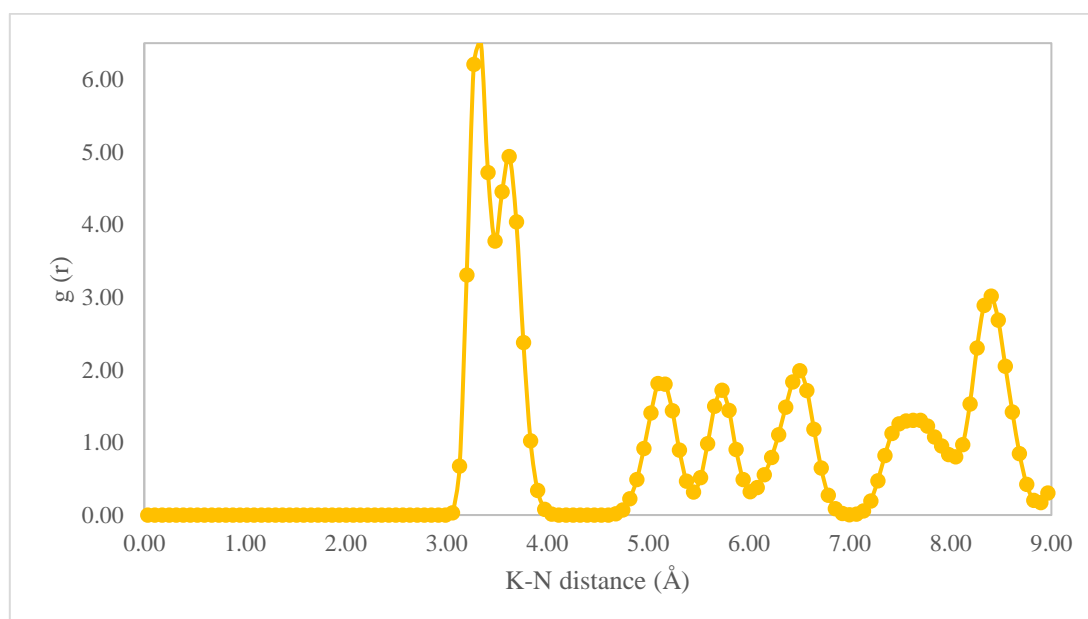


Figure 7.34 RDF for the potassium to nitrogen interaction for potassium nitrate - calcite.

7.3.4.2.2 Mean-square displacement analysis

Also, for this system, the mean square displacement indicates that there is little degree of freedom in z for the particles in the system. They primarily move in the xy plane, and the curves for both axes reach a plateau after approximately 10 ns.

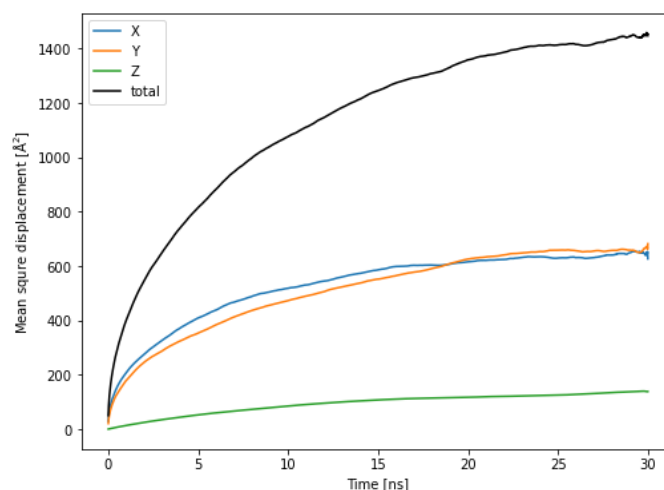


Figure 7.35 MSD of K ions on a defective SAM surface. The blue line represents the x-, the orange line the y- and the green line the z(-) components. Black line shows the total MSD

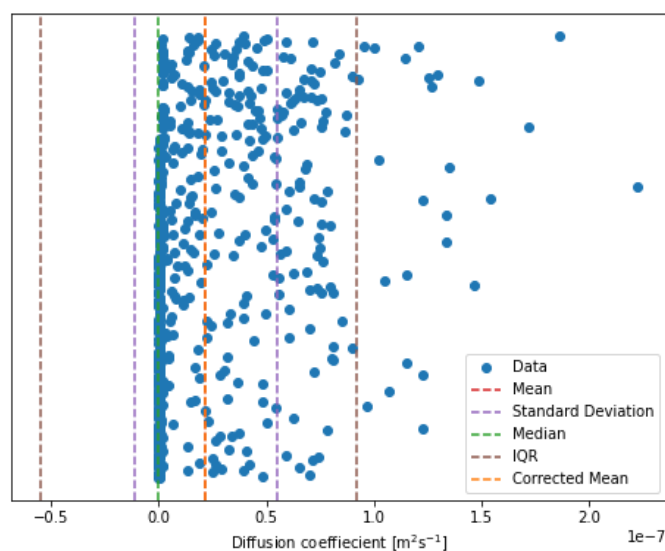


Figure 7.36 IQR analysis for K ions on a flat SAM surface. Blue dots represent the data set, red dashed line the mean, purple dashed line the standard deviation, green dashed line the median, brown dashed line the interquartile range and orange dashed the corrected mean

We may picture the entire surface divided into four quadrants, with the majority of the particles constituting a 'cluster' appearing to be restricted in that region, as if they are constrained in this energy well. Figure 7.36 shows that just a few ions may readily depart the surface, whereas the bulk cannot diffuse away from the surface.

Figures 7.37 and 7.38 show the analysis of the nitrogen motion. In addition, in this case, the nitrate ions are less likely than potassium ions to propagate along the z-axis. Figure 7.38 shows that the majority of the ions prefer to stick to the original clustered configuration when we analyse the initial configuration with all of the ions combined.

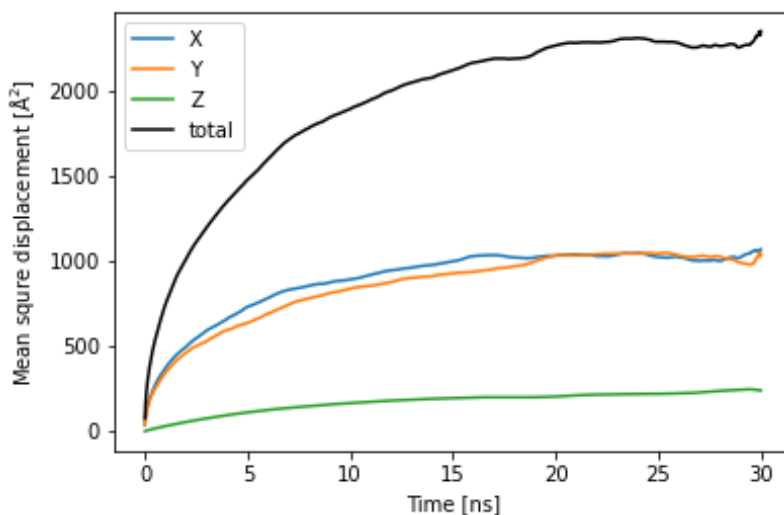


Figure 7.37 MSD of nitrate ions on a defective SAM surface. The blue line represents the x-, the orange line the y- and the green line the z(-) components. Black like shows the total MSD

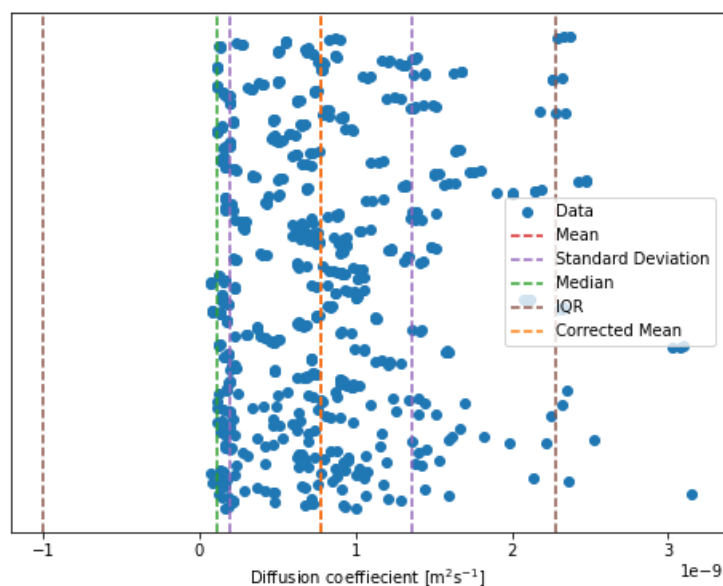


Figure 7.38 IQR analysis for nitrate ions on a defective SAM surface. Blue dots represent the data set, red dashed line the mean, purple dashed line the standard deviation, green dashed line the median, brown dashed line the interquartile range and orange dashed the correct mean

7.3.4.2.3 Cluster analysis

The average coordination for the ions in solution is less than 2, as shown in Table 7.6. That indicates that each potassium ion interacts and disconnects with another potassium ion on average. The table also shows the number of ions in the biggest finite cluster, which accounts

for less than 3% of the total ions in solution. On the other hand, over half of all ions appear to have no connection at all.

Table 7.6 Statistics about the cluster connection in a potassium nitrate solution sitting on a flat SAM surface.

	Total number	Percentage
Average Coordination	1.7051	
Largest finite cluster	17.56	3.5%
Ion with no connections	208.1	42%

The average radius of gyration for clusters appears to increase over time, as it is possible to see from Figure 7.39. After it reaches a maximum, it tends to increase/decrease regularly.

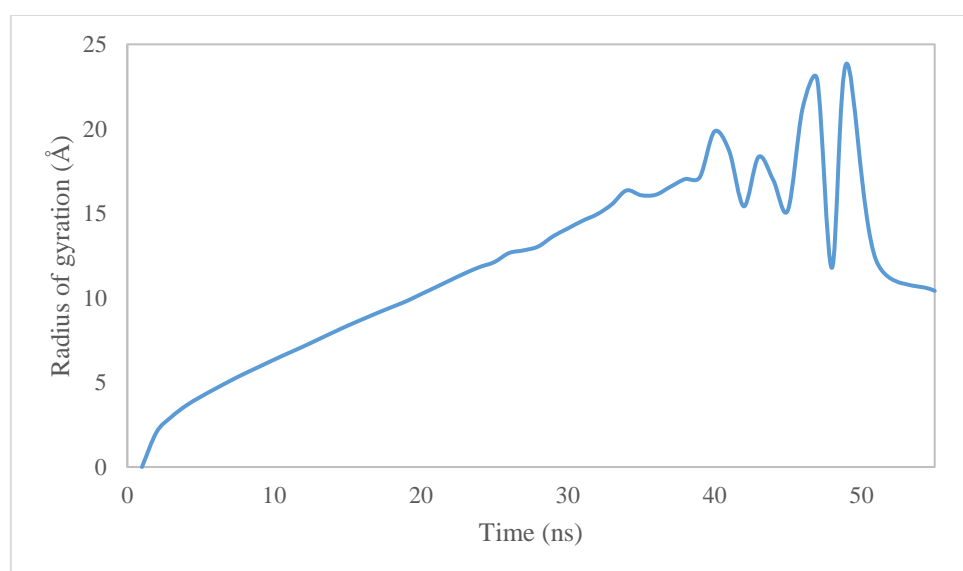


Figure 7.39 Radius of gyration over time

Figure 7.40 shows the logarithm of the number of connections as a function of the radius of a cluster, it presents a slope of 1.6, which indicates that the cluster is probably a not very dense 2-D one, and can be imagined as a flat surface with holes and gaps.

Even in this case, the behaviour of the radius of gyration over time can be explained by potassium ions coming and diffusing over the surface. This results in the creation of a flat cluster, which ultimately divides into two distinct groups. The activity can also be caused by ions moving in and out of the surface.

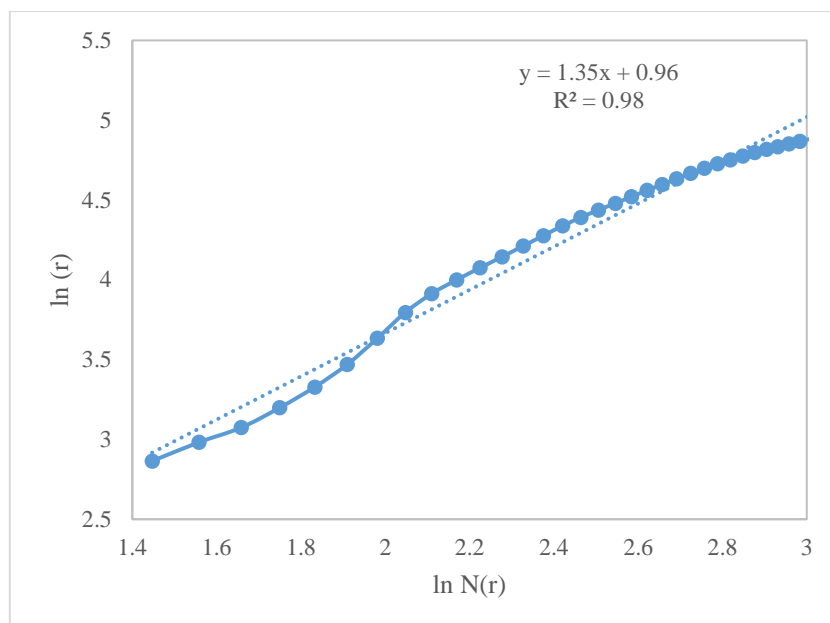


Figure 7.40 Fractal dimension of the average finite cluster in solution for a solution of KNO_3 sitting on a flat SAM surface

Figure 7.41 shows the average number of potassium in a cluster versus its probability of existence (normalised). The probability, overall, decreases exponentially, which is in good agreement with the expected behaviour of a system following the classical nucleation theory.

Its behaviour is basically the same as the flat charged surface. The defect appears to generate little to no difference.

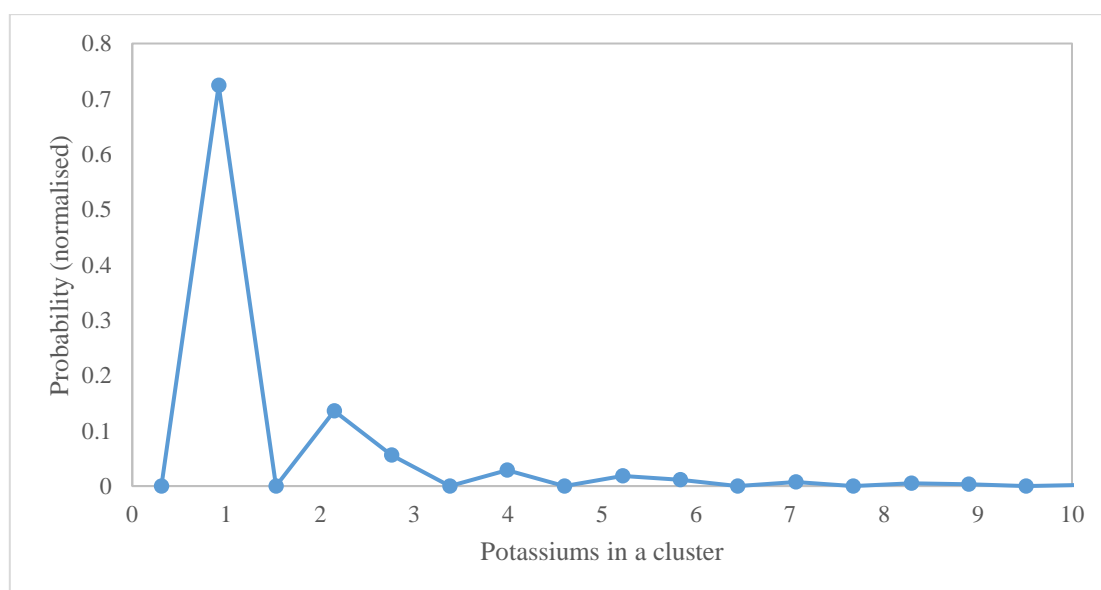


Figure 7.41 Number of potassium in a cluster vs probability (normalised)

7.4 Conclusions

Calcium carbonate solutions outperform potassium nitrate solutions in terms of organisation on the SAM surface. Recent research has demonstrated that the crystallisation of calcium carbonate on carboxyl-terminated SAMs follows classical nucleation theory, with nucleation on the surface growing into a crystal^[29]. Analysis of the RDF shows that there is a weaker potassium nitrate ion interaction with the SAM surface, since there is little organisation.

In recent research^[1], certain defects are hypothesised to facilitate ion clustering, raising solute concentration at particular places and facilitating surface nucleation. The behaviour of potassium nitrate seen in this study does not correspond to these data since the ion distributions in solution are very similar for both surfaces. This might be due to the weak interactions between the ions and the SAM functional group, which have less impact on the ions and so have a considerably smaller effect than if these interactions were stronger.

Calcium carbonate has a lower solubility in water than potassium nitrate, having a solubility of around 0.013 g/L at 25°C compared to 383 g/L^[30, 31]. As a result, a large local concentration of potassium nitrate must be reached to lead to nucleation. Therefore our system may be limited by the general solubility.

The comparison with calcium carbonate, again, shows that the energy barrier, and in particular the ΔG term does not contribute, for potassium nitrate, as significantly as it does for calcium carbonate. The system does tend to aggregate but not to reorganise into a crystalline form.

7.5 Appendix: force field parameters

Tables 7.7 and 7.8 report the values used in this work, respectively for all the non-bonded and bonded type of interactions.

Table 7.7 Non-bonded interactions

Lennard-Jones	ϵ (eV)	σ(Å)
C ₃ - C ₃	0.004748	3.39961
C ₃ - C	0.00420798	3.39974
C ₃ - O _H	0.006581	3.23316
C ₃ - O	0.006575	3.1799
C ₃ - H _C	0.0018	3.02437
C - C	0.003733	3.39958
C - O _H	0.005839	3.23297
C - O	0.00583	3.17984
C - H _C	0.001593	3.02491
O _H - O _H	0.009127	3.06654
O _H - O	0.009123	3.01315
O _H - H _C	0.002497	2.85771
O - O	0.009111	2.95997
O - H _C	0.00249	2.80488
H _C - H _C	0.000677	2.65083
O _w - O _w	0.00674	3.16549
C ₃ - O _w	0.005657	3.28255
C - O _w	0.005016	3.28253
O _H - O _w	0.007843	3.11602
O - O _w	0.00783631	3.06273
H _C - O _w	0.00213658	2.90816
C ₃ - Au	0.00283275	3.1673
C - Au	0.00251174	3.16729
O _H - Au	0.0039275	3.00077

O - Au	0.00392396	2.94749
H _C - Au	0.00106987	2.79291
K - O _W	0.011207	3.00195
C ₃ - N _N	0.00592642	3.37481
C - N _N	0.00525483	3.37479
O _H - N _N	0.008217	3.20827
O - N _N	0.008209	3.15498
H _C - N _N	0.002238	3.00042
C ₃ - O _N	0.009986	3.0748
C - O _N	0.008854	3.0748
O _H - O _N	0.013845	2.9083
O - O _N	0.013832	2.8549
H _C - O _N	0.003771	2.7004

Buckingham	A(eV)	$\rho(\text{\AA})$	C(eV \AA^6)
K - O _N	220.6	0.3678	0
K - N _N	4990000000000	0.0939	0
O _N - O _N	44806	0.2066	31
O _N - O _W	225677	0.18661	29
O _N - H _W	577.7	0.22635	0
K - O	261	0.3678	0
K - O _H	1999.8	0.27151	0
K - C	0.3678	0.12	0
K - C ₃	120000000	0.12	0

Table 7.8 Bonded interactions

Harmonic	k_2 (eV Å⁻²)	r_0 (Å)	
C ₃ - C ₃	13.042	1.5375	
C ₃ - C	13.567	1.524	
C ₃ - H _C	14.33	1.0969	
C - O _H	17.342	1.3513	
C - O	27.642	1.2183	
O _H - H _O	16.098	0.973	
C ₃ - S	13.042	1.845	
O _W - H _W	22.965	1.012	
N _N - O _N	20.24465	1.255	
Angle-bending	k_θ (eV rad⁻²)	θ_0 (deg)	
C ₃ - C ₃ - C ₃	2.726	111.51	
C ₃ - C ₃ - H _C	2.006	109.8	
C ₃ - C ₃ - C	2.743	111.04	
C ₃ - C - O _H	2.964	112.73	
C ₃ - C - O	2.921	123.2	
C - C ₃ - H _C	2.032	108.77	
C - O _H - H _O	2.162	106.55	
O _H - C - O	3.289	122.1	
H _C - C ₃ - H _C	1.707	107.58	
H _W - O _W - H _W	1.645	113.24	
O _N - N _N - O _N	6.617	120	
Dihedrals	k_ϕ (eV)	n	δ(deg)
C ₃ - C ₃ - C ₃ - C ₃	0.0078	3	0
C ₃ - C ₃ - C ₃ - C ₃	0.0087	1	180

$C_3 - C_3 - C_3 - C_3$	0.0108	2	180
$C_3 - C_3 - C_3 - H_C$	0.0069	3	0
$C - C_3 - C_3 - H_C$	0.0067	3	0
$C_3 - C - O_H - H_O$	0.0997	2	180
$O - C - C_3 - H_C$	0.0347	1	0
$O - C - C_3 - H_C$	0.0035	3	180
$O - C - O_H - H_O$	0.0824	1	0
$H_C - C_3 - C_3 - H_C$	0.0069	3	0

Out of plane	k_2 (eV \AA^{-2})	k_4 (eV \AA^{-4})
$N_N - O_N - O_N - O_N$	13.647	360

7.6 References

- [1] V. Marinova, C. L. Freeman, J.H. Harding, *Significance of atomic-scale defects in flexible surfaces on local solvent and ion behaviour*, Faraday Discuss., 2022, **235**, 289–306;
- [2] J.C. Love, L.A. Estroff, J.K. Kriebel, R.G. Nuzzo, G.M. Whitesides, *Self-Assembled Monolayers of Thiolates on Metals as a Form of Nanotechnology*, Chem. Rev., 2005, **105** (4), 1103–1170;
- [3] S.M. Barlow, R. Raval, *Complex organic molecules at metal surfaces: bonding, organisation and chirality*, Surface Science Reports, 2003, **50** (6–8), 201–341;
- [4] D.K. Schwartz, *Mechanisms and Kinetics of Self-Assembled Monolayer Formation (2001). "Mechanisms and kinetics of self-assembled monolayer formation*, Annu. Rev. Phys. Chem., 2001, **52**, 107–37;
- [5] F. Schreiber, *Structure and growth of self-assembling monolayers*, Progress in Surface Science, 2000, **65** (5–8), 151–257;
- [6] G. Wnek, G.L. Bowlin, *Encyclopedia of Biomaterials and Biomedical Engineering*, Informa Healthcare, 2004, 1331–1333;
- [7] J.G. Vos, R. J. Forster, T.E. Keyes, *Interfacial Supramolecular Assemblies*, Wiley, 2003, 88–94;
- [8] A. Kaifer, *Supramolecular Electrochemistry*, Coral Gables, 2001, Wiley VCH. 191–193.
- [9] J.P. Bucher, L. Santesson, K. Kern, *Thermal Healing of Self-Assembled Organic Monolayers: Hexane- and Octadecanethiol on Au(111) and Ag(111)*, Langmuir, 1994, **10**, 979 – 983;
- [10] C. L. Freeman, J. H. Harding, D. M. Duffy, *Simulations of calcite crystallization on self-assembled monolayers*, Langmuir, 2008, **24**, 9607–9615.
- [11] J. Aizenberg, A. J. Black, G. M. Whitesides, *Controlling local disorder in self-assembled monolayers by patterning the topography of their metallic supports*, Nature, 1998, **394**, 868–871;
- [12] C. L. Freeman, Q. Hu, M. H. Nielsen, J. Tao, J. J. De Yoreo, J. H. Harding, *Surface selectivity of calcite on self-assembled monolayers*, J.Phys. Chem. C, 2013, **117**, 5154–5163;
- [13] K. Sprenger, Y. He, J. Pfaendtner, *Probing How Defects in Self-assembled Monolayers Affect Peptide Adsorption with Molecular Simulation*, in *Foundations of Molecular Modeling and Simulation*, Springer, Singapore, 2016, 21–35;
- [14] G. Chong, I. U. Foreman-Ortiz, M. Wu, A. Bautista, C. J. Murphy, J. A. Pedersen, R. Hernandez, *Defects in Self-Assembled Monolayers on Nanoparticles Prompt Phospholipid Extraction and Bilayer-Curvature-Dependent Deformations*, J. Phys. Chem. C, 2019, **123**, 27951–27958;
- [15] C. Vericat, M. E. Vela, R. C. Salvarezza, *Self-assembled monolayers of alkanethiols on Au(111): surface structures, defects and dynamics*, Phys. Chem. Chem. Phys., 2005, **7**, 3258–3268;
- [16] A. Ulman, *Formation and Structure of Self-Assembled Monolayers*, Chem. Rev., 1996, **96**, 1533–1554;

- [17] J. Wang, R. M. Wolf, J. W. Caldwell, P. A. Kollman, D. A. Case, *Development and testing of a general amber force field*, *J. Comput. Chem.*, 2004, **25**, 1157–1174;
- [18] J. Wang, W. Wang, P. A. Kollman, D. A. Case, *Automatic atom type and bond type perception in molecular mechanical calculations*, *J. Mol. Graphics Modell.*, 2006, **25**, 247–260;
- [19] P. Raiteri, J. D. Gale, *Water Is the Key to Nonclassical Nucleation of Amorphous Calcium Carbonate*, *J. Am. Chem. Soc.*, 2010, **132**, 17623–17634;
- [20] P. K. Ghorai, S. C. Glotzer, *Molecular Dynamics Simulation Study of Self-Assembled Monolayers of Alkanethiol Surfactants on Spherical Gold Nanoparticles*, *J. Phys. Chem. C*, 2007, **111**, 15857–15862;
- [21] H. A. Lorentz, *Ueber die anwendung des satzes vom virial in der kinetischen theorie der gase*, *Ann. Phys. Chem.*, 1881, **248**, 127–136;
- [22] D. Berthelot, *Sur le mélange des gaz*, *C. R. Hebd. Seances Acad. Sci.*, 1898, 1703–1855;
- [23] C. L. Freeman, J. H. Harding, D. J. Cooke, J. A. Elliott, J. S. Lardge, D. M. Duffy, *New Forcefields for Modeling Biomineralization Processes*, *J. Phys. Chem. C*, 2007, **111**, 11943–11951;
- [24] S. Plimpton, *Fast Parallel Algorithms for Short-Range Molecular Dynamics*, *J. Comput. Phys.*, 1995, **117**, 1–19;
- [25] A. P. Thompson, H. M. Aktulga, R. Berger, D. S. Bolintineanu, W. M. Brown, P. S. Crozier, P. J. Veld, A. Kohlmeyer, S. G. Moore, T. D. Nguyen, R. Shan, M. J. Stevens, J. Tranchida, C. Trott, S. J. Plimpton, *LAMMPS - a flexible simulation tool for particle-based materials modeling at the atomic, meso, and continuum scales*, *Comput. Phys. Commun.*, 2022, **271**, 108171;
- [26] R. W. Hockney, J. W. Eastwood, *Computer Simulation Using Particles*, Hilger, 1988, Bristol;
- [27] S. Nose', *A unified formulation of the constant temperature molecular dynamics methods*, *J. Chem. Phys.*, 1984, **81**, 511;
- [28] W. G. Hoover, *Canonical dynamics: Equilibrium phase-space distributions*, *Phys. Rev. A: At., Mol., Opt. Phys.*, 1985, **31**, 1695;
- [29] C. L. Freeman, Q. Hu, M. H. Nielsen, J. Tao, J. J. De Yoreo, J. H. Harding, *Surface Selectivity of Calcite on Self-Assembled Monolayers*, *J. Phys. Chem. C*, 2013, **117**-10, 5154-5163;
- [30] N. C. f. B. Information. "PubChem Compound Summary for CID 10112, Calcium Carbonate." <https://pubchem.ncbi.nlm.nih.gov/compound/Calcium-carbonate> (accessed 5 May, 2022).
- [31] N. C. f. B. Information. "PubChem Compound Summary for CID 24434, Potassium Nitrate." <https://pubchem.ncbi.nlm.nih.gov/compound/Potassium-nitrate> (accessed 5 May, 2022).
- [32] W. Smith, T.R. Forester, *DL_POLY_2.0: A general-purpose parallel molecular dynamics simulation package*, *J. Molec. Graphics*, 1996, **14**, 136;
- [33] L. Martínez, R. Andrade, E. G. Birgin, J. M. Martínez, *PACKMOL: A package for building initial configurations for molecular dynamics simulations*, *Comput Chem*, 2009, **30**, 2157–2164;

- [34] A. Stukowski, *Visualization and analysis of atomistic simulation data with OVITO—the Open Visualization Tool*, *Modelling Simul. Mater. Sci. Eng.*, 2010, **18**, 15-12;
- [35] G. Van Rossum, F. L. Drake, *Python 3 Reference Manual*, CreateSpace, Scotts Valley, CA, 2009, 242.

Chapter 8

Conclusions and Future work

During the course of this study, we discussed the necessity of a reliable and transferable force-field for the nitrates of alkali metals. This force-field would be applicable to all nitrates, including solid solutions. The order of stability of the polymorphs for each alkali nitrate is reproduced by our force-field, and so are the crystal structures of the polymorphs, as well as the elastic and dielectric properties of the materials, when these are accessible. It is always possible to produce stable phonon spectra (i.e., no imaginary modes). The model also performs well as a function of temperature, accurately recreating the experimental lattice expansion and demonstrating, if applicable, how the structures might convert into disordered forms as a result of the thermally induced rotation of the nitrate groups.

This force-field has been evaluated in the research of the behaviour of a variety of solutions, at different molalities. It is worth noting that the percentage of ions not involved in connection appears to decrease in all of the situations. It would appear that the system forms a variety of clusters, each of which has its own distinct form and dimensions. The vast majority of clusters, however, are made up of highly hydrated chains that appear to fold in such a way as to incorporate water into "pockets."

According to the results of the study of the fractal dimension, the chain in this scenario scrunches itself up into the form of what is virtually a three-dimensional structure, but it also has obvious flaws and gaps. The structure is quite similar to the so-called DOLLOPs that are found in calcium carbonate.

As a result, it does not appear that any nuclei can be identified in the time-frame being studied. The subsequent phase will consist of determining whether any of those clusters of a smaller size resemble an organised crystalline structure in any way. This could lead to another piece of work following the present. Longer timeframe studied could possibly lead to the visualisation of some clustering occurring.

The previous research may lead one to conclude that many of the 6- and 9-coordinated systems have a structure that is close to the ideal crystal; however, this could be because nitrate crystals have a greater structural variation (natural disorder). When they are in these units, there is still

a possibility that they will have water coordination, which makes it more difficult for them to match the crystal structure.

There is no indication that nuclei are developing because there is no movement over time towards a bigger number of crystal-like units or an increase in their overall order. This indicates that there is no evidence that nuclei are growing. As a direct consequence of this, there is no evidence to suggest that nuclei are being formed.

In the section that is dedicated to the application of constant chemical potential, in the process of trying to nucleate potassium nitrate on a homogeneous slab, we can conclude that the results obtained with classical molecular dynamics might be an artefact. There is no experimental evidence to support the hypothesis that potassium nitrate shows the ability to nucleate at a pace comparable to the one that we may have predicted using classical MD simulation. On a similar subject, the high solubility of potassium nitrate is accurately represented by the constant chemical potential molecular dynamics. We are unable to establish with absolute certainty the growth behaviour at this level of the process. This pattern of activity is consistent with the sodium nitrate investigation. It seems as though the growth rates for the two systems are comparable; nevertheless, this hypothesis would need to be confirmed by additional research. However, based on the primary results, we can confirm that the choice to apply fixed-distance control regions was the right one: the growth is slow enough to make it possible to use this methodology successfully. There are indications that order is building, but this should be validated using simulations conducted over significantly longer time periods. That would make it possible to think about the behaviour of the system in a more precise manner, from a statistical point of view. The fact that this methodology has never been used before on an ionic system, in which the anion is not composed of a single atom that has been ionised, was a limitation for the study. Because of the challenges presented by the spinning of the nitrates, in conjunction with the high solubility of the system, this configuration turned out to be more articulated than was originally anticipated. As a result, the time available for the investigation is somewhat restricted, which opens the door to the possibility of additional research.

Previous stages of the setting up process have involved using pure water immediately in contact with the slab. This has shown that, by the time the right concentration is reached we see dissolution.

To avoid such an issue an intermediate molarity value between one where dissolution is expected and the one where growth is expected. Even in this case it was possible to notice an

initial readjustment of the slab. It appears that potassium nitrate is a very soluble salt and therefore, for this system in particular it would be advised to create a solution in contact with the slab that is already above the supersaturation value.

When a surface of a SAM is used in place of the slab of potassium nitrate, it is important to note that calcium carbonate solutions perform better than potassium nitrate solutions in terms of organisation on the SAM surface. This is something that should be kept in mind. Crystallisation of calcium carbonate on carboxyl-terminated SAMs has been shown to follow the classical nucleation theory pathway, with nucleation occurring on the surface and developing into a crystal. Due to the lack of organisation, an analysis of the RDF reveals that the interaction between the potassium nitrate ion and the SAM surface is significantly weaker than expected.

Because the ion distributions in solution are so comparable between the two surfaces, the behaviour of potassium nitrate that was observed in this study does not correspond to the data that were collected. This may be caused by the weak contacts between the ions and the SAM functional group, which have less of an effect on the ions and a smaller effect overall than if these interactions were stronger.

It could be possible that defects that were not classified as very successful for calcium carbonate may influence the ions and solution. Because of the different charges between the two species there is a chance that a different behaviour might be observed. Another interesting point of study could be investigating a hypothetical species with a charge between the two (e.g. +1.5). While this does not have any experimental counterpart, it could be beneficial in the setting up of the methodology itself.